Open-Science Materials Acceleration Platforms for Clean Energy Material Design Spaces

Maria Politi

A dissertation

Submitted in partial fulfillment of the

Requirements for the degree of

Doctor of Philosophy

University of Washington

2024

Reading Committee:

Lilo D. Pozzo, Chair

Stuart B. Adler

David A. C. Beck

Daniel T. Schwartz

Program Authorized to Offer Degree:

Chemical Engineering

© Copyright 2024

Maria Politi

University of Washington

Abstract

Open-Science Materials Acceleration Platforms for Clean Energy Material Design Spaces

Maria Politi

Chair of the Supervisory Committee:

Lilo D. Pozzo

Department of Chemical Engineering

Conventional materials synthesis schemes can be labor and time-intensive, which significantly impedes the pace of new materials discovery and their applications. To achieve innovative solutions to global challenges, such as climate change and an ever-growing sustainable energy demand, a new paradigm of science movement arose in the past five years to adapt traditional materials science workflows to ones with the potential to accelerate the pace of materials discovery. This novel approach to science has been called *"Materials Acceleration Platforms"* (MAPs) or *"Self-driving Laboratories"* (SDLs) and it relies on autonomous robotic systems designed to conduct scientific experiments and research with minimal human intervention. However, new initiatives of MAPs are still too costly, and their rigid design limits their implementation. It is also essential to acknowledge and address the diverse needs and challenges of different scientific fields. In this context, open-hardware principles have allowed the use of

laboratory automation to be more accessible and more easily implemented for a variety of applications. In this work, workflows with various levels of automation of experimental and computational tasks are presented implementing a combination of off-the-shelf open-source robotic platforms, high-throughput, small scale characterization tools, and custom open-hardware solutions. A semi-automated protocol was designed for the synthesis, physical and electrochemical characterization of novel electrolytes based on deep eutectic solvents and organic redox active molecules for use in electrochemical storage systems. Next, a human-in-the-loop SDL was developed to explore a large design space for the investigation of CdSe nanoparticles' optical properties at a fraction of the time compared to traditional techniques. This work implements a repurposed multi-tool, open-hardware 3D printer platform, Jubilee, reconfigured for sonochemical processing. Furthermore, data-driven methods were also used to obtain a holistic view of the space and learn trends in the data based on all variables tested. Finally, a new python-based control library for Jubilee is presented, along with the broadening of tool library with new synthesis, processing, and characterization tools. These efforts enabled the creation of closed-loop workflows, such as the benchmarking protocol for SDLs, an autonomous color-mixing problem. These tools hold immense scientific and educational value for both new materials discovery and more interdisciplinary skill development. The increased access through low-costs solution will broaden the application space of this new science paradigm, empowering a larger number of (materials) scientists to take advantage of the precision of automation, and enabling automation tools to be included in hands-on educational curricula.

TABLE OF CONTENTS

LIST OF FIGURES

LIST OF TABLES

ACKNOWLEDGEMENT

I wish to deeply thank my advisors Dr. Lilo Pozzo, Dr. David Beck, and Dr. Stuart Adler for your mentorship over the past five years of graduate school. Your continuous support, guidance, and encouragement throughout my PhD journey have been invaluable. Your expertise and insightful feedback have been invaluable in shaping my experience and this dissertation. I am also grateful for allowing me to explore, to grow, and for believing in me. You have all been a great inspiration. I also would like to thank my committee members and all other collaborators I had the great opportunity to work with during my time at UW.

I would like to thank past and present Pozzo research group members, especially Claire Benstead, Dr Kacper Lachowski, Dr. Shayna Hillburg, and Dr. Sage Scheiwiller. You have all been such a great support system and great company in these past five years. My experience as a graduate student would not have been the same without you all. Thank you to past members of the Adler research group as well as all the amazing people of the Beck research group. I would also like to thank all the amazing UW Chemical Engineering and UW Chemistry graduate students I had the opportunity to interact with during my PhD. You have made my years in Seattle memorable and have helped me survive grad school, you've all been a source of support and inspiration, I am forever grateful.

I acknowledge the financial support of the National Science Foundation through NSF-CBET grant no. 1917340, the Data Intensive Research Enabling Clean Technology (DIRECT) National Science Foundation (NSF) National Research Traineeship (DGE-1633216), and the UW Molecular Engineering Materials Center, a Materials Research Science and Engineering Center (Grant No. DMR-1719797). I acknowledge the use of facilities and instrumentation supported by the U.S. National Science Foundation through the Major Research Instrumentation (MRI) program

(DMR-2116265), as well as by the University of Washington, Department of Chemical Engineering.

I am grateful to my family, for your love, encouragement, and for believing in me. To my mum, for having been an amazing role model and the reason I was able to accomplish all of I've done so far. To my friends near and far, your love and support have been essential, I am eternally grateful to have you all in my life. To Evan and his family, your companionship has been a source of strength throughout this journey, without you I would not be where I am today.

DEDICATION

To all the incredible, strong women who have graced my life, you've been such an inspiration. Your support has been invaluable.

Chapter 1. INTRODUCTION

1.1 CHEMICAL DESIGN SPACES

The area of material discovery through automated protocols and instrumentation in the field of chemistry, material science, and molecular science is an ever-evolving space deeply rooted in combinatorial chemistry. This latter discipline has seen its advent in the late 1980s-early 1990s, focused predominantly on medicine and new biochemically active compounds. [1] In fact, the ability to synthesize and screen large numbers of compounds simultaneously in a systematic and efficient manner has quickly become a powerful tool for drug discovery and materials science. The appeal of this strategy is its ability to rapidly generate large libraries of compounds. First, these property databases are obtained by combining various building blocks, reagents, and reaction conditions, all in a high-throughput manner. Next, these libraries can be queried to identify molecules with desired properties. One of the main advantages of combinatorial chemistry is its ability to explore chemical space more efficiently and comprehensively than traditional one-at-a-time synthesis methods. Additionally, it can provide insights into structure-activity relationships and lead optimization. However, the high-throughput nature of combinatorial chemistry can also lead to a large number of false positives, and screening processes can be time and resource intensive. Nonetheless, with recent advances in automation and machine learning, combinatorial chemistry is becoming an increasingly powerful tool for several research fields, such as molecular recognition, catalysis, drug discovery, energy materials and materials science. [2]

The design space of new material discovery is extremely vast and unstructured, making the generation and optimization of new compounds a challenging and time-consuming task. [3] In fact, in order to capture a relevant phenomenon, several conditions might need to be concurrently varied. These can include species' concentration, temperature and pressure conditions, molecular

structure and functionalization, solvents, sequence for the addition of reagents, and reaction time. [4,5] However, this list is not nearly exhaustive. In fact, the number of variables to be changed during an experimental campaign will depend on the desired outcome, experimental and characterization capabilities, costs of operation and materials, as well as data management and analysis strategies. There are two types of research approaches that can be implemented with high-throughput experimentation. These are dependent on the task at hand, whether it is exploratory or based on the optimization of a target property or structure. The first involves the selection of a set of conditions that involve the synthesis of new materials, or combinations of components that have not been previously tested. In this case there's an inherent uncertainty related to the design space, as it depends on the set of initial condition and the number of total samples deemed necessary to make an initial inference on the outcome of the experimental campaign. Generally, it is desired to have a diverse set of parameters with which one can more broadly capture the available design space. However, this can necessitate testing a larger number of samples. On the other hand, the latter strategies are based on the improvement of a selected material property or target structural feature. This is usually based on known experimental outcomes and tends to have more targeted design spaces. [4] This assumes a more in-depth knowledge of the material of interest and requires higher domain knowledge.

Traditional design of experiments (DoE) techniques usually involves simple factorial design for a selected number of test variables, the definition of the parameters range and selection of the total number of experiments able to be completed in the predisposed timeline. The results are then analyzed, and the process is repeated given the new information learned from the previous campaign. While successful, this process can quickly become prohibitive when the number of input variables to test is increased. [6] In fact, there is an exponential growth of total number of

experimental samples to test for every variable added to the investigation. [7] Thankfully, new data-driven strategies can aid in achieving a more manageable number of samples and overall experimental campaign, while simultaneously providing more insight on the chemical space under investigation.

1.2 Data-Driven Strategies

To draw parallels to combinatorial chemistry strategies, it is important to define metrics to find lead compounds for each target application. These candidates are defined as those that possess the best activity in specific target metrics, which depend on the final application. However, it is not always known which properties are going to be more strongly correlated with the final experimental outcome. As humans we are restricted to visualize parameter spaces in low dimensions and at times lack a more holistic view necessary to draw better conclusions. There is an estimated chemical space of 10^{60} possible unique candidates, the large majority of which is virtually unexplored. [8] While presenting an opportunity to find functional materials to solve current global challenges, the vastness of chemical space highlights the need to move into new scientific paradigms, even past the "Big Data-driven" approach. [9,10]

Thanks to technological and computation advances of the last few decades, it is now possible to access and learn from a larger chemical space using computational algorithms. The widespread implementation of machine learning algorithms in several realms of science and the increase in achievable computing power promise to increase the speed of new materials discovery. In fact, the integration of artificial intelligence (AI), algorithms with human-like intelligence able to problem-solve, can be leveraged to create adaptable decision-making policies for faster design and synthesis of new materials. This approach has the potential to further innovate experimental paradigms and increase research productivity. [11–16] In particular, a class of machine learning

algorithms that are suitable for this self-optimization task are based on active learning. Namely, Bayesian optimization (BO) [17] has gained significant traction and popularity in many materials' science and chemical spaces. [9,18–25] This class of algorithms provides a more advanced approach DoE through an iterative process in which any subsequent iterations are guided by the knowledge gained from previous experimental results. This, in turn, allows convergence towards a final target in a faster and optimized manner. [6,26] Using these algorithms can significantly improve on the overall learning of each experimental campaign as they are able to handle high dimensional data more easily and can also reduce the overall experimental cost, both from a material consumption to a total number of samples required to reach an optimized state.

To create a more streamlined process for experimental design with minimum user interaction, it is paramount to combine physical experimental automation with reliable and efficient data analysis strategies. Without the aid of faster and automated data classification, the bottleneck of the high-throughput sample synthesis and screening process would simply be shifted from the experimental tasks to the feature recognition and modeling steps. Machine learning algorithms have proven to be effective tools that can aid the performance of the classification step and increase its efficiency. However, most of the time these algorithms are still application-dependent and not easily generalizable to other material spaces. The implementation of these automated analysis tasks is also necessary to allow the implementation of new AI algorithms for more autonomous experimental campaigns. Without further development of more system-agnostic algorithms able to extract metrics of success after each experimental testing, the implementation of automated and autonomous design of experiment will be limited and not able to achieve its full potential in fields of new material design

Again, the application of new DoE strategies to chemical exploration promises to accelerate the development of new materials. However, the design of new materials is known to be inherently a multivariate task requiring solutions aiming at the simultaneous optimization of several target properties. Multi-objective optimization (MOOP) strategies have become increasingly popular, especially in the drug discovery field. [27–29] However, these techniques rely on available predictive frameworks, databases or molecular simulations providing a variety of measured or estimated properties for the chemicals used. Furthermore, MOOP systems need to be coupled with medium or high-throughput strategies to best achieve the desired outcome of faster identification of materials with desired properties. Without these experimental infrastructures, the bottleneck of the task would simply shift onto the sample formulation and testing phase.

Finally, regardless of the optimization task at hand, these new data-driven methods are not meant to replace the human role in the research process, but are tools aimed to augment and enrich the capabilities of researchers. In fact, by reducing the need for human-intensive tasks and allowing more time for hypothesis formulation, for more creative ways to find scientific solutions, and to converge faster towards better performing materials for the unprecedented global issues.

1.3 Laboratory Automation, From Data to Materials

Conventional materials synthesis schemes can be labor and time-intensive, which significantly impedes the pace of new materials discovery and their applications. Moreover, to achieve new solutions to global challenges, such as climate change and an ever-growing sustainable energy demand, a new movement arose in the past five years to adapt traditional materials science workflows to ones that have the potential to accelerate the pace of materials discovery. [30] This new approach to science has been called *"Self-driving Laboratories"* and it relies on autonomous robotic systems designed to conduct scientific experiments and research with

minimal human intervention. Furthermore, it integrates both computation and physical cutting-edge technologies such as artificial intelligence, robotics, and advanced sensors to perform tasks traditionally carried out by scientists. [7,30–34] Another definition of these autonomous systems is *"Materials Acceleration Platforms"* (MAPs). These have emerged as integrated ecosystems incorporating not only automation, and artificial intelligence (AI), but also highlight the implementation of databases, scheduling, and orchestration along with human creativity and intuition as crucial components for speeding up the discovery, optimization, and use of new materials. [26] Through the use of experimental data automation, as well as machine learning algorithms, self-driving labs streamline experimentation processes, enhance efficiency, and can reduce human error in experimental campaigns. These autonomous laboratories have the potential to revolutionize various fields, by accelerating the pace of discovery and enabling round-the-clock experimentation without the limitations of human availability. Moreover, the use of robotic platforms also promises to eliminate batch variability due to human errors, allowing to track and quantify systematic errors, leading to more reproducible procedures. Finally, while being used almost interchangeably in the community, there can be slight differences in emphasis between SDLs and MAPs, as the latter one conveys a more specific focus on materials research and innovation within the broader context of self-driving labs. Nonetheless, in this Thesis the two terms will be used as synonyms to describe autonomous, experiment-performing system. The main advantage of these platforms is the possibility to investigate broader experimental spaces for both synthesis and parameter optimization. Robotic platforms have been successfully applied to synthesize organic compounds of pharmaceutical interest, [35–37] nanomaterials, [38–45] materials science, [46] chemistry, [35,47,48] biotechnology, [37,49,50] among others. However, MAPs still present some limitations, such as 'rigid' designs (i.e., only useful for specific reactions or applications) and

the high upfront cost of implementation in the laboratory. This limits incentives to integrate such platforms, and most wet-lab researchers still rely on low-throughput, time intensive workflows. [51] The highest benefit of SDLs will be achieved by closed-loop design approaches, in which the experimental campaign is conducted completely without human intervention by relying on AI agents for data analysis and decision-making, and robotic platforms for all the physical sample manipulation and characterization. However, especially in materials science context, it can be more cost-effective and appropriate to initially design a semi-automated workflow with a human-in-the-loop type of approach. In this case, it is still possible to make use of AI-based technologies for the design of experiment and laboratory automation platforms for the time-intensive manual steps, but the research is tasked with connecting and shuttling the samples between different stages of the experimental workflow. This can be a more practical solution if the objective is to accelerate the material discovery process or as an initial proof of concept for a new experimental campaign.

Combinatorial chemistry paradigms have been more commonly implemented in industry and at the commercial scale. Similarly, the application of high-throughput experimentation systems and automation platforms has been more limited at the broader academic scale primarily due to economic reasons. [1] However, this trend was present at the beginning of the development of this new way of carrying out experiments in the biochemistry and medical field. As more and more companies decided to adopt these strategies, the technology and instrumentation costs started to decrease, making it possible for research groups from different institutions to take on this synthesis and analysis route. It is known that industry plays a crucial role in addressing the challenges posed by the required hardware and software for SDLs. In fact, currently experimental automation has been more commonly implemented in biological science and medicinal chemistry thanks to a larger commercial push on technological development. [7] Unfortunately, the realm of

inorganic chemistry and materials science is still lagging as most of their characterization techniques still rely on high-fidelity, single-sample type of protocols. Nonetheless, there has been a recent increase in manufacturers that offer off-the shelf automated instrumentation for a variety of processing and materials characterization. However, most academic research groups and institutions still rely on very few simple semi-automated equipment. The focus is usually the sample formulation, while the processing and characterization are still performed in a low-throughput manner. To contrast these limitations and lower the barrier of entry to these technologies for a more wide-spread use of automation systems, academic groups have been making use of open-source hardware (OSH) systems. [52,53] These are physical devices whose designs are made publicly available for anyone to replicate, modify, distribute, and manufacture. This aims to be the physical complement to open-source software. Both movements emphasize transparency and collaboration, allowing individuals and organizations to freely access, improve, and share products, in this case hardware, without restrictive licenses or proprietary constraints. The openness of these designs fosters innovation, encourages community involvement, and promotes interoperability among different hardware components and systems. [54] Some examples of open-hardware designs in the research context include solutions the adaptation of 3D printers and platforms, [55–57] platforms for modular automated workflows, [51] liquid handling systems (e.g., pipetting robot platforms, pipettes, and autosamplers), [57–63] and imaging, [64–67] to name a few. These examples of automated and semi-automated tools with multi-use and application-agnostic features make for a more accessible and affordable system for increasing the throughput of material discovery.

Finally, besides lowering the cost entry point of these systems, to make these materials acceleration platforms more prevalent, more approachable, and implemented by a broader

community, there needs to be a mindset shift. While there can be a high up-front time and resource commitment into transforming a traditionally low-throughput protocol into an automated one, the use of these autonomous systems can increase the pace at which new materials are discovered, as well as allow the research to focus on higher-level scientific questions. [7] To truly achieve the goal of making SDLs ubiquitous in chemistry and materials science laboratories, there is a need for the development of standardized hardware designs and equipment communication protocols, as well broader availability of easily reproducible, openly available designs.

1.4 Goals and Objectives

The main goal of this thesis is to showcase the use of data-driven strategies in combination with open-source and open-hardware laboratory automation platforms to create low-cost self-driving labs for new material discovery in the realm of energy-related applications and optical materials. As the thesis builds up, the level of automation and data-driven strategies used in each workflow presented will increase, to culminate in a fully autonomous task based on open-source and open-science tools. First, Chapter 2 will cover the fundamentals of several experimental and computational techniques used throughout the thesis. Experimental tools will focus on electrochemical characterization techniques, spectroscopic techniques, and thermal analysis techniques. On the other hand, computational techniques will cover active learning algorithms, particularly Bayesian Optimization. Next, Chapter 3 will discuss the investigation of a new class of organic designer solvents called deep eutectic solvents (DESs) as battery electrolytes. This chapter will cover the development and implementation of a semi-automated workflow for the solvents' synthesis, physical and electrochemical characterization based on a combination of off-the-shelf laboratory automation platforms and high-throughput, small scale characterization tools. Chapter 4 will then focus on the inclusion of organic redox active compounds into the DES-based

electrolytes for use in redox-flow batteries as an alternative to current water-based solutions for this energy storage technology. Next, Chapter 5 will showcase a human-in-the-loop SDL for the synthesis of CdSe quantum dots. The workflow makes use of a combination of an open-hardware solution for the sample processing and high-throughput characterization tools allowing for a 4D design space to investigate at a significantly reduced fraction of the time compared to traditional techniques. Data-driven methods were also used to obtain a holistic view of the space and learn trends in the data based on all variables tested. Next, Chapter 6 will focus on the development of an open-source and open-hardware, modular, and closed-loop laboratory automation platform based on a repurposed, tool-changing 3D printer. Its implementation for autonomous workflows will be evaluated based on a benchmarking protocol for SDLs, an autonomous color-mixing demo. Finally, Chapter 7 will summarize the work presented in the previous chapters and discuss the outlook for self-driving labs, specifically in the realm of open-source and open-hardware tools. The appendix section will showcase a collection of smaller open-science products: an open-source, automatic data classification software based on convolutional neural networks; an open-source and open-hardware platform for high-throughput IR bolometry measurements to determine phase-transition temperatures of materials; open-hardware tools for mixing solutions hosted in SLAS standard microplates based on haptic motors and an electromagnet tool for picking up and moving small objects in a laboratory automation platform.

1.5 REFERENCES

1. Borman, stu. Combinatorial chemistry. *Chem. Eng. News* **76**, 47–67 (1998).
2. Bing, Y. & Zhang, B. Analytical Issues in Combinatorial Chemistry. in *Analytical Methods in Combinatorial Chemistry* 1–11 (2010).
3. Gómez-Bombarelli, R. *et al.* Automatic chemical design using a data-driven continuous representation of molecules. *ACS Cent. Sci.* **4**, 268–276 (2018).

4. Maier, W. F., Stowe, K. & Sieg, S. Combinatorial and high-throughput materials science. *Angewandte Chemie - International Edition* **46**, 6016–6067 (2007).
5. Xue, D. *et al.* Accelerated search for materials with targeted properties by adaptive design. *Nat. Commun.* **7**, (2016).
6. Houben, C. & Lapkin, A. A. Automatic discovery and optimization of chemical processes. *Curr. Opin. Chem. Eng.* **9**, 1–7 (2015).
7. Abolhasani, M. & Kumacheva, E. The rise of self-driving labs in chemical and materials sciences. *Nature Synthesis 2023 2:6* **2**, 483–492 (2023).
8. Kirkpatrick, P. & Ellis, C. Chemical space. *Nature* **432**, 823 (2004).
9. Miguel Hernández-Lobato, J., Requeima, J., Pyzer-Knapp, E. O. & Aspuru-Guzik, A. *Parallel and Distributed Thompson Sampling for Large-Scale Accelerated Exploration of Chemical Space*. (2017).
10. Hey, T., Tansley, S. & Tolle, K. *The Fourth Paradigm: Data-Driven Discovery*. (2009).
11. Aspuru-Guzik, A. & Persson, K. *Materials Acceleration Platform: Accelerating Advanced Energy Materials Discovery by Integrating High-Throughput Methods and Artificial Intelligence*. https://www.cifar.ca/wp-content/uploads/MissionInnovationIC6Report.pdf (2018).
12. Pyzer-Knapp, E. O. *et al.* Accelerating materials discovery using artificial intelligence, high performance computing and robotics. *NPJ Comput Mater* **8**, (2022).
13. Liu, J. & Hein, J. E. Automation, analytics and artificial intelligence for chemical synthesis. *Nature Synthesis* **2**, (2023).
14. Xie, Y., Sattari, K., Zhang, C. & Lin, J. Toward autonomous laboratories: Convergence of artificial intelligence and experimental automation. *Prog Mater Sci* (2022) doi:10.1016/j.pmatsci.2022.101043.
15. McCullough, K., Williams, T., Mingle, K., Jamshidi, P. & Lauterbach, J. High-throughput experimentation meets artificial intelligence: A new pathway to catalyst discovery. *Physical Chemistry Chemical Physics* **22**, 11174–11196 (2020).
16. Kulik, H. J. & Sigman, M. S. Advancing Discovery in Chemistry with Artificial Intelligence: From Reaction Outcomes to New Materials and Catalysts. *Acc Chem Res* **54**, 2335–2336 (2021).
17. Jones, D. R., Schonlau, M. & Welch, W. J. Efficient Global Optimization of Expensive Black-Box Functions. *Journal of Global Optimization* **13**, 455–492 (1998).
18. Shahriari, B., Swersky, K., Wang, Z., Adams, R. P. & De Freitas, N. Taking the human out of the loop: a review of Bayesian optimization. *Proc. IEEE* **104**, 148–175 (2016).
19. Liang, Q. *et al.* Benchmarking the performance of Bayesian optimization across multiple experimental materials science domains. *NPJ Comput Mater* **7**, (2021).
20. Slautin, B. N. *et al.* Bayesian Co-navigation: Dynamic Designing of the Materials Digital Twins via Active Learning.
21. Adams, F., Mcdannald, A., Takeuchi, I. & Gilad Kusne, A. Human-in-the-loop for Bayesian autonomous materials phase mapping. doi:10.1016/j.matt.2024.01.005.

22. Vaddi, K., Chiang, H. T. & Pozzo, L. D. Autonomous retrosynthesis of gold nanoparticles via spectral shape matching. *Digital Discovery* **1**, 502–510 (2022).
23. Schmidt, J., Marques, M. R. G., Botti, S. & Marques, M. A. L. Recent advances and applications of machine learning in solid-state materials science. *npj Computational Materials* vol. 5 Preprint at https://doi.org/10.1038/s41524-019-0221-0 (2019).
24. Sun, S. *et al.* A data fusion approach to optimize compositional stability of halide perovskites. *Matter* **4**, 1305–1322 (2021).
25. Burger, B. *et al.* A mobile robotic chemist. *Nature* **583**, 237–241 (2020).
26. Flores-Leonar, M. M. *et al.* Materials Acceleration Platforms: On the way to autonomous experimentation. *Curr Opin Green Sustain Chem* **25**, 100370 (2020).
27. Cummins, D. J. & Bell, M. A. Integrating Everything: The Molecule Selection Toolkit, a System for Compound Prioritization in Drug Discovery. *J. Med. Chem* **59**, 7010 (2016).
28. Nicolaou, C. A. & Brown, N. Multi-objective optimization methods in drug design. *Drug Discov Today Technol* **10**, (2013).
29. Cruz-Monteagudo, M., Borges, F. & Cordeiro, M. N. D. S. Desirability-Based Multiobjective Optimization for Global QSAR Studies: Application to the Design of Novel NSAIDs with Improved Analgesic, Antiinflammatory, and Ulcerogenic Profiles. (2008) doi:10.1002/jcc.20994.
30. Delgado-Licona, F. & Abolhasani, M. Research Acceleration in Self-Driving Labs: Technological Roadmap toward Accelerated Materials and Molecular Discovery. *Advanced Intelligent Systems* **5**, (2023).
31. Bennett, J. A. *et al.* Autonomous reaction Pareto-front mapping with a self-driving catalysis laboratory. *Nature Chemical Engineering* **1**, 240–250 (2024).
32. Epps, R. W., Volk, A. A., Ibrahim, M. Y. S. & Abolhasani, M. Universal self-driving laboratory for accelerated discovery of materials and molecules. *Cell Press* **7**, 2541–2545 (2021).
33. MacLeod, B. P. *et al.* Self-driving laboratory for accelerated discovery of thin-film materials. *Sci Adv* **6**, (2020).
34. Seifrid, M. *et al.* Autonomous Chemical Experiments: Challenges and Perspectives on Establishing a Self-Driving Lab. *Acc Chem Res* **55**, 2454–2466 (2022).
35. Coley, C. W. *et al.* A robotic platform for flow synthesis of organic compounds informed by AI planning. *Science* **365**, 1–9 (2019).
36. Chan, C. Y. *et al.* Accelerating drug discovery via organs-on-chips. *Lab Chip* **13**, 4697 (2013).
37. Caschera, F. *et al.* Automated Discovery of Novel Drug Formulations Using Predictive Iterated High Throughput Experimentation. *PLoS One* **5**, (2010).
38. Li, J. *et al.* Autonomous discovery of optically active chiral inorganic perovskite nanocrystals through an intelligent cloud lab. *Nature Communications 2020 11:1* **11**, 1–10 (2020).

39. Chan, E. M. *et al.* Reproducible, High-Throughput Synthesis of Colloidal Nanocrystals for Optimization in Multidimensional Parameter Space. *Nano Lett* **10**, 1874–1885 (2010).
40. Vikram, A., Brudnak, K., Zahid, A., Shim, M. & Kenis, P. J. A. Accelerated screening of colloidal nanocrystals using artificial neural network-assisted autonomous flow reactor technology. *Nanoscale* **13**, 17028–17039 (2021).
41. Epps, R. W., Felton, K. C., Coley, C. W. & Abolhasani, M. Automated microfluidic platform for systematic studies of colloidal perovskite nanocrystals: towards continuous nano-manufacturing. *Lab Chip* **17**, 4040–4047 (2017).
42. Abdel-Latif, K. *et al.* Self-Driven Multistep Quantum Dot Synthesis Enabled by Autonomous Robotic Experimentation in Flow 2000245 (1 of 13). *Adv. Intell. Syst* **3**, (2021).
43. Salley, D. *et al.* A nanomaterials discovery robot for the Darwinian evolution of shape programmable gold nanoparticles. doi:10.1038/s41467-020-16501-4.
44. Zhao, H. *et al.* A robotic platform for the synthesis of colloidal nanocrystals. *Nature Synthesis* **2**, 21 (2023).
45. Li, J., Tu, Y., Liu, R., Lu, Y. & Zhu, X. Toward "On-Demand" Materials Synthesis and Scientific Discovery through Intelligent Robots. *Advanced Science* **7**, (2020).
46. Ren, F. *et al.* Accelerated discovery of metallic glasses through iteration of machine learning and high-throughput experiments. *Sci Adv* **4**, (2018).
47. Coley, C. W., Eyke, N. S. & Jensen, K. F. Autonomous Discovery in the Chemical Sciences Part I: Progress. *Angewandte Chemie - International Edition* **59**, 22858–22893 (2020).
48. Caramelli, D. *et al.* Discovering New Chemistry with an Autonomous Robotic Platform Driven by a Reactivity-Seeking Neural Network. *ACS Cent Sci* **7**, 1821–1830 (2021).
49. King, R. D. *et al.* The automation of science. *Science (1979)* **324**, 85–89 (2009).
50. Coutant, A. *et al.* Closed-loop cycles of experiment design, execution, and learning accelerate systems biology model development in yeast. *PNAS* (2019) doi:10.1073/pnas.1900548116.
51. Eggert, S., Mieszczanek, P., Meinert, C. & Hutmacher, D. W. OpenWorkstation: A modular open-source technology for automated in vitro workflows. *HardwareX* **8**, e00152 (2020).
52. Powell, A. Democratizing production through open source knowledge: From open software to open hardware. *Media Cult Soc* **34**, 691–708 (2012).
53. Blow, N. Lab automation: tales along the road to automation. *Nature Methods 2008 5:1* **5**, 109–112 (2008).
54. Definition (English) - Open Source Hardware Association. https://www.oshwa.org/definition/.
55. Jones, R. *et al.* RepRap-The Replicating Rapid Prototyper Proof for review only RepRap-The Replicating Rapid Prototyper. : *Robotica* **29**, 177–191 (2011).
56. Zhang, C., Wijnen, B. & Pearce, J. M. Open-Source 3-D Platform for Low-Cost Scientific Instrument Ecosystem. *SLAS Technol* **21**, 517–525 (2016).

57. Baas, S. & Saggiomo, V. Ender3 3D printer kit transformed into open, programmable syringe pump set. *HardwareX* **10**, e00219 (2021).
58. Carvalho, M. C. & Murray, R. H. Osmar, the open-source microsyringe autosampler. *HardwareX* **3**, 10–38 (2018).
59. Keesey, R., LeSuer, R. & Schrier, J. Sidekick: A Low-Cost Open-Source 3D-printed liquid dispensing robot. *HardwareX* **12**, e00319 (2022).
60. Nejatimoharrami, F., Faina, A. & Stoy, K. New Capabilities of EvoBot: A Modular, Open-Source Liquid-Handling Robot. *SLAS Technol* **22**, 500–506 (2017).
61. Bravo-Martinez, J. Open source 3D-printed 1000 lL micropump. *Hardware X* (2018) doi:10.1016/j.ohx.2017.08.002.
62. Faiña, A., Nejati, B. & Stoy, K. EvoBot: An Open-Source, Modular, Liquid Handling Robot for Scientific Experiments. doi:10.3390/app10030814.
63. Open-Source Liquid Handler | OTTO. https://openliquidhandler.com/.
64. Bhom, A. AMi: A GUI-based, open-source system for imaging samples in multi-well plates. *Acta Crystallogr F Struct Biol Commun* **75**, 531–536 (2019).
65. Pineda, D., Pérez, J., Gaviria, D., Ospino-Villalba, K. & Camargo, O. MEDUSA: An open-source and webcam based multispectral imaging system. (2022) doi:10.1016/j.ohx.2022.e00282.
66. Regan, B., Kinahan, D., Daly, P., O'kennedy, R. & Collins, D. Design and fabrication of a low-cost wireless camera imaging system for centrifugal microfluidics. *HardwareX* **11**, e00259 (2022).
67. Jonveaux, L. Arduino-Like Development Kit for Single-Element Ultrasound Imaging. *Journal of Open Hardware* (2017) doi:10.5334/joh.2.

Chapter 2. EXPERIMENTAL METHODS AND RELATED THEORY

2.1 Electrochemical Characterization Techniques Fundamentals

2.1.1 *Electrochemical Impedance Spectroscopy*

EIS is a non-destructive technique that allows for the separation of specific contributions to cell resistance via timescale based on the response of the cell to a sinusoidal voltage or current perturbation. Practically speaking, EIS is performed by sweeping through a wide range of frequencies at a single small perturbation amplitude.[1] Figure 2.1 shows an examples schematic of the relationship between input and output signals.

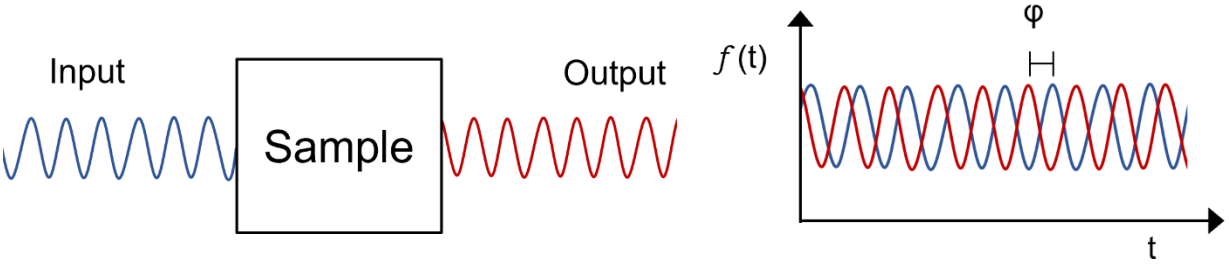

Figure 2.1 Example schematic of an EIS measurement where a sinusoidal input is applied to a sample and a sinusoidal output is measured (Left). Representation of output and input sinusoidal as a function of time. Most of the time there is a phase shift between the two which is informative of processing that happening in the sample (Right).

EIS experiments can be run in either potentiostatic or galvanostatic mode, by indicating which input signal is generated. In the former case, a voltage input is used, whereas the latter one uses a current input. The definition of impedance, Z, is the ability of a circuit element to resist flow of electrical current. It is defined as follows:

$$Z = \frac{V(t)}{I(t)} = \frac{\mathrm{V_o}\sin(\omega t)}{\mathrm{I_o}\sin(\omega t + \varphi)} = Z_o \frac{\sin(\omega t)}{\sin(\omega t + \varphi)} \qquad 2.1$$

Here $V(t)$ refers to the voltage perturbation in V; $I(t)$ is the current sinusoidal perturbation in A; ω is the angular frequency in rad; φ is the phase shift; Z_o is the impedance magnitude expressed in Ω. The impedance can also be expressed as a complex number as follows:

$$Z = \frac{V(t)}{I(t)} = \frac{V_o\, exp(j\omega t)}{I_o exp\,(j\omega t\, - \phi)} = Z_o[cos(\varphi) + j\, sin(\varphi)] \qquad 2.2$$

In this thesis, EIS was implemented to capture the ionic conductivity of deep eutectic solvents. In fact, at the highest frequencies probed, the electrode current becomes almost entirely capacitive, such that the measured cell impedance (Z) becomes ohmic, with resistance inversely proportional to the ionic conductivity of the solvent. Thus, EIS can be used to isolate ionic conductivity in a system with unknown or variable electrode characteristics, such as the one implemented for the electrochemical characterization of DES (Chapter 3). Once the measurement is completed, the data is visualized using a Nyquist plot, (Figure 2.2) in which the negative imaginary component $(-Z_{im})$ of the impedance is plotted against the real component (Z_{re}). The point at which the impedance curve first intersects the axis of the real component is extracted as the ohmic resistance of the system.

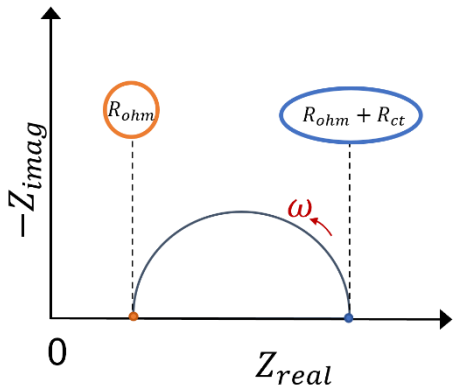

Figure 2.2 Example Nyquist plot in which the (negative) Imaginary component of the Impedance is plotted against the Real component. The shift on the x-axis represents the value of the ohmic resistance (orange dot), whereas the other end of the semicircular shape represents the combined ohmic and charge transfer resistance (blue dot). In this case, the frequency (ω) of the input sinusoidal increases moving right to left.

2.1.2 *Cyclic Voltammetry*

Cyclic voltammetry (CV) was performed to investigate the possibility of undesired electrochemical side reactions in regions between the limiting reduction and oxidation potentials of the DES electrolytes. This technique is the most commonly used to study electrochemical properties of analytes in solutions. The measurement input consists of a linearly ramped voltage at a constant scan rate, between a starting potential E_1 and a switching potential E_2.[2] Generally, this process is repeated in cycles of forward ($E_1 \rightarrow E_2$) and backward ($E_2 \rightarrow E_1$) scans. Figure 2.3 left, shows an example of a CV voltage input plotted with respect to time.

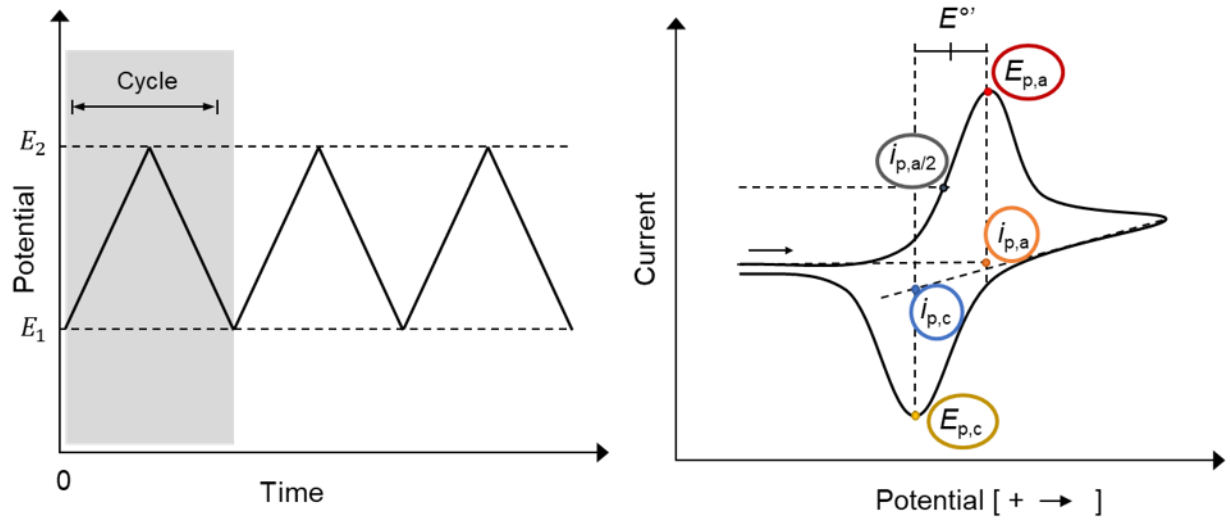

Figure 2.3 Left) Example input voltage for cyclic voltammetry as a function of time. Right) Example resulting *i*-*V* curve of a cyclic voltammogram. Some basic curve features are noticed on the graph, such as standard potential, $E^{o\prime}$, peak anodic and cathodic voltages, $E_{p,j}$ and peak anodic and cathodic currents, $i_{p,j}$.

An ideal electrolyte would be one that does not show electrochemical activity withing the application operating window, also referred to as the electrochemical stability window. Therefore, we would expect a relatively flat line from a cyclic voltammogram. However, if there is a redox active species in solution, the resulting voltammogram resembles more the one depicted Figure 2.3 (right), also known as a 'duck-shape curve'. A typical experimental set up for CV involves a three-electrode cell in which the potential is monitored between the working electrode (W.E.) and at the reference electrode (R.E.), whereas the current is flown between the W.E. and a counter electrode (C.E.), Figure 2.4.

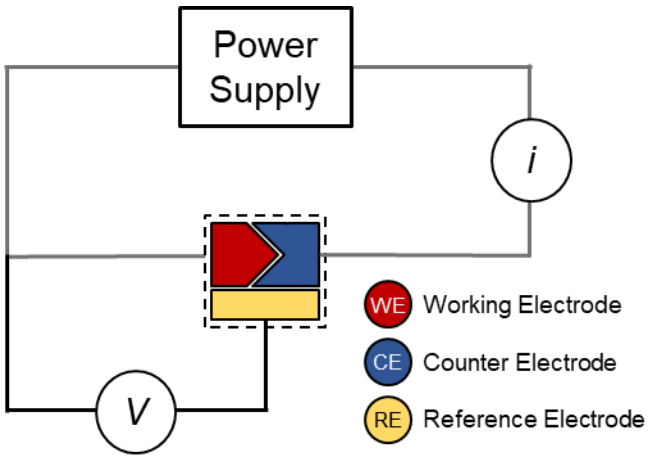

Figure 2.4 simplified schematic depicting a 3-electrode cell. Here, the potential is monitored between the working electrode (W.E.) and at the reference electrode (R.E.), whereas the current is flown between the W.E. and a counter electrode (C.E.).

2.1.3 *Chronopotentiometry*

Chronopotentiometry is a measurement that involves a series of current holds of set values and the measurement of the sample's voltage response. [3] The current input is maintained for several seconds as the voltage response will equilibrate towards the end of the measurement. The potential of the last two seconds of every current step is averaged and extracted for analysis. Linear fit of the current steps and potentials is obtained from plots of current density vs. potential in both the positive and negative regions. From these, the potential at zero current is calculated as follows:

$$E_i = -\frac{intercept}{slope}; i = a, c \qquad 2.3$$

Here, the subscripts refer to the anodic (a) and cathodic (c) potential limits. Multi-step constant chronopotentiometry was implemented in Chapter 3 to determine the limiting reduction and oxidation potentials of the DES electrolytes. The use of chronopotentiometry to obtain these potentials has been proposed and reported previously for liquid electrolytes as fast and accurate estimates for comparisons, which facilitates data collection and analysis in the high-throughput

pipeline.[4] The potentials at the line of zero current are the estimated limiting reduction and oxidation potentials for the DES electrolyte. Figure 2.5 shows example chronopotentiometry data and their analysis using the procedures described above.

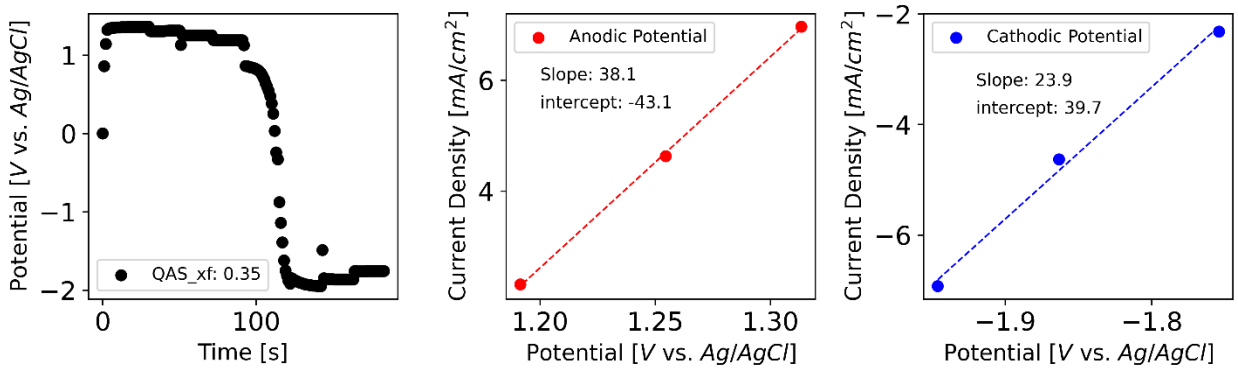

Figure 2.5 Example Chronopotentiometry analysis for the extraction of the Anodic and Cathodic Potentials for the DES formed by Choline Chloride and Ethylene Glycol (0.35: 0.65 molar fraction) sample. Left) Overall Chronopotentiometry measurement. Center) Average of the last 2 seconds for each of the positive current steps (excluding the conditioning step). Right) Average of the last 2 seconds for each of the negative current steps (excluding the conditioning step). The anodic and cathodic potential are obtained using equation 2.3.

2.2 Spectroscopic Techniques

The optical properties of a material provide information on how it interacts with light. The characterization of these properties can provide significant insight into the material's structure, size, and composition. In this section, two spectroscopy techniques involving the determination of the amount of light absorbed and emitted by materials. When light is shined on a material, part of it is absorbed and part of it is scattered. Before we dive a little deeper in the techniques, Figure 2.6 showcases all the possible mechanisms in which a molecule can convert or dissipate the energy that it has absorbed to transition one (or more) of its electrons from a ground state to an excited one. [5]

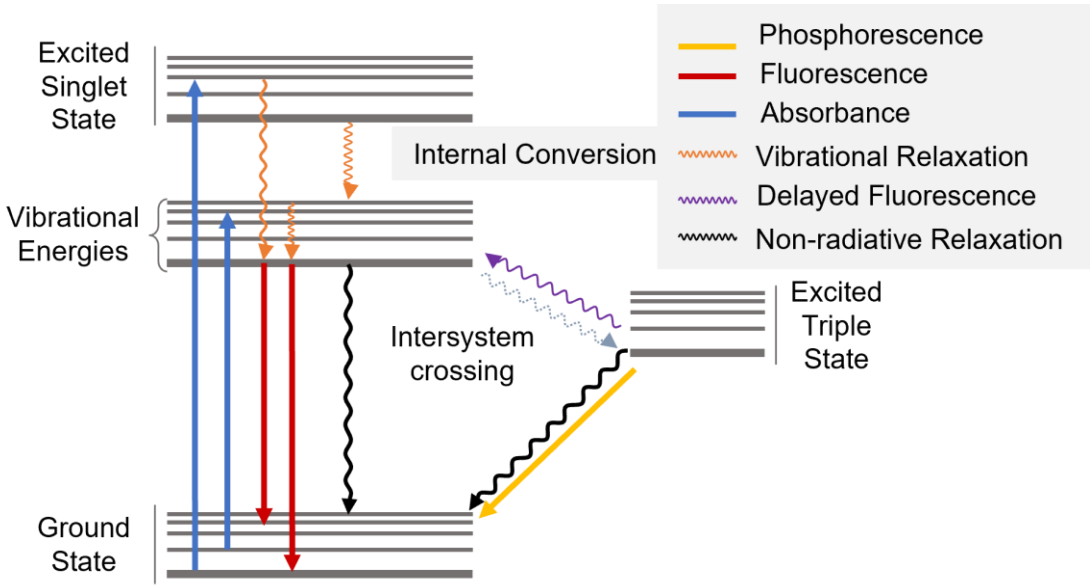

Figure 2.6 Energy diagram depicting several of the possible mechanism in which a molecule can dissipate the energy that it has absorbed to transition from a ground state to an excited one. The y axis indicates increasing energy.

2.2.1 *Ultraviolet-Visible Spectroscopy*

Ultraviolet-visible (UV-Vis) spectroscopy is a non-destructive technique for the determination of optical properties of matter. Generally, UV-Vis spectroscopy that measures the amount of light absorbed by a material as a function of the light's energy (i.e., light's wavelength).[6] Most commonly we define absorbance, A, or optical density as follows:

$$A = \log_{10}\left(\frac{I}{I_0}\right) \qquad 2.4$$

Here I_0 refers to the intensity of the incident light, whereas I refers to the intensity of light that passed through the sample. A schematic of a basic UV-Vis spectrometer is set up can be seen in Figure 2.7. Here, light from a source is passed through a monochromator, which isolates light possessing a specific wavelength, prior to hitting the samples to be characterized. Finally, the amount of light that was able to pass through is measured using a photodetector.

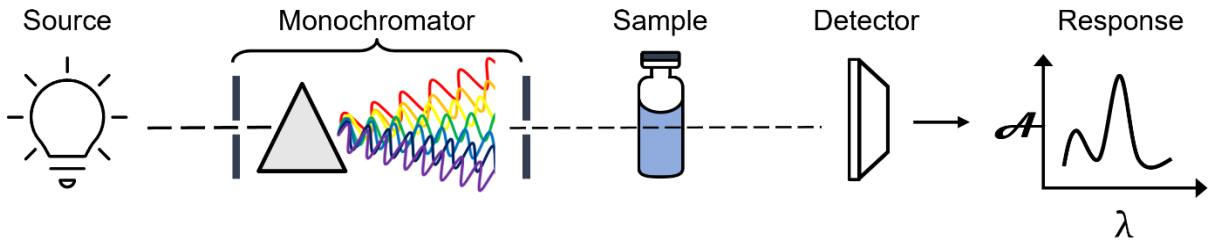

Figure 2.7 Example schematics for a UV-Vis spectrometer.

The absorbance response of semiconducting nanoparticles, such as those discussed in Chapter 5, can be used to infer structural information about the material based on the peak absorbance location (wavelength). Furthermore, the peak intensity can also be used to quantify the concentration of nanoparticles in solution. [5]

When looking at mixtures or species in solution, it is important to determine the absorption contribution of the solvent and that of the solute, which most of the time is the material of interest. To do so, a UV-Vis measurement of the pure solvent should be collected and subtracted from the spectrum obtained for the solution. Moreover, the amount of light absorbed by a sample is also proportional to the sample's concentration. *Beer's Law* expresses this relationship in the following form:

$$A = \epsilon C l \qquad 2.5$$

Here, ϵ refers to the extinction coefficient, a material-dependent property which indicates how strongly the material can absorb light. This quantity is usually measured on a molar basis and is expressed in units of $M^{-1}cm^{-1}$. C is the sample's concentration expressed in M $\left[\frac{mol}{L}\right]$, while l is the pathlength of light through the sample's cell expressed in cm. A similar technique to UV-Vis absorption is light extinction spectroscopy. While the measurement and the experimental set up are the same, this technique measures the total amount of light absorbed over all wavelengths. [7]

Another important use for UV-Vis spectroscopy application is the determination of species' concentration in solution. In fact, using *Beer's Law* it is possible to create calibration curves of samples with known species' composition, given the linear relationship between the sample's absorbance and its concentration. Figure 2.8 shows an example curve used to spectroscopically determine the maximum solubility of an organic molecule, 4-hydroxy TEMPO, dissolved in a deep eutectic solvent formed by acetylcholine chloride and ethylene glycol at a 1:4 ratio, respectively. The peak absorbance value for each spectral curve is extracted using a peak finding algorithm in Python, [8] and subsequently plotted against its concentration. As expected, the resulting data follows a linear trend, and its slope can be used to estimate the amount of solute found in samples of unknown concentration.

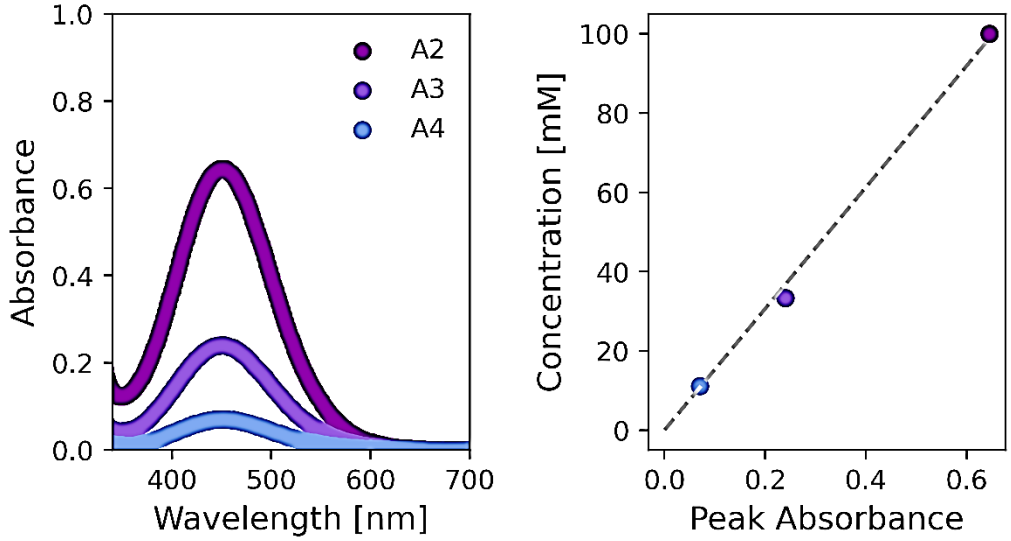

Figure 2.8 Example Uv-Vis absorption spectra for the determination of the maximum solubility of 4HOT in AcChCl:EG at a 1:4 ratio (Left) and resulting spectroscopic calibration curve (Right) obtained using *Beer's Law (*equation 2.5).

Another way of assessing the absorbance of a sample is by measuring the fraction of light transmitted through it. [7] Transmittance is defined as follows:

$$T = \frac{I}{I_0} \tag{2.6}$$

Here, I represents the transmitted light; I_0 is the incident light; T is transmittance, the transmitted light reported as a percentage value. On the other hand, absorbance is the reciprocal of transmittance:

$$A = -\log_{10} {}^{1}/_{T} \tag{2.7}$$

This technique can be used to assess the color of materials, surface defects, and coatings.

Photoluminescence Spectroscopy

The process of photoluminescence refers to the optical excitation and successive relaxation of exited states, generated from light absorption, and their recombination which generates a fluorescence emission to allow the excited electrons to return to its ground state. In this case, it is possible to measure the number of photons emitted as a function of energy (or wavelength). To do so, the instrumental set up is similar to the one for UV-Vis spectroscopy. Figure 2.9 shows a simplified schematic of a photoluminescence spectrometer. In this case the detector is placed perpendicular to the incident light. This instrument configuration minimizes the influence of incident light as any measured signal would have to be generated in the samples. In practice, some incident light can scatter and be measured at high angles. However, this makes the intensity of emission not an absolute value.

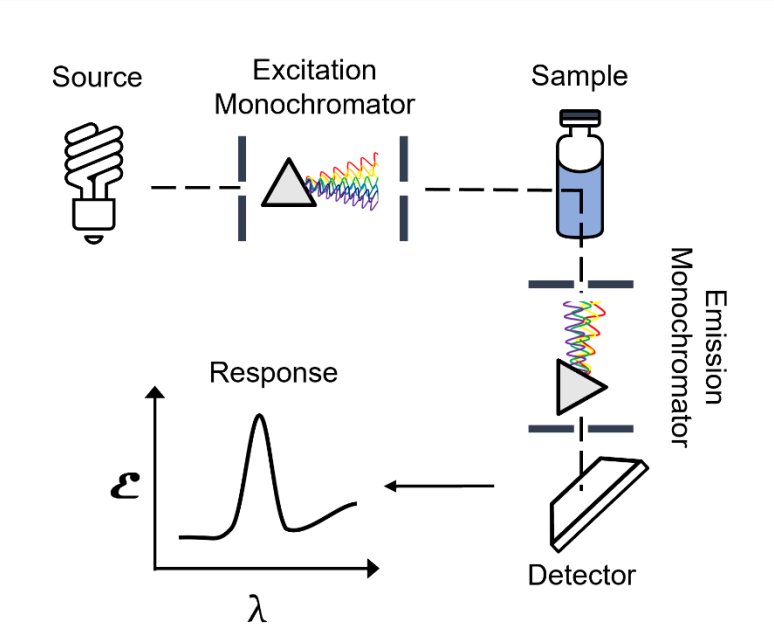

Figure 2.9 Example schematics for a photoluminescence spectrometer.

The photoluminescence response of semiconducting nanoparticles, such as those discussed in Chapter 5, can provide crucial information about the particle's surface such as passivation, as well as band gap energy.[5]

2.3 PHYSICAL PROPERTIES CHARACTERIZATION

2.3.1 *Phase Transition Temperature*

2.3.1.1 Differential Scanning Calorimetry & Differently Thermal Analysis

Performing thermal analysis of organic samples is an integral part of materials characterization. This is routinely used to determine melting/boiling points, phase transitions, to assess sample purity, and thermal stability, which are all key features to a few research and technology areas including the development of pharmaceuticals, advanced materials, and foods. The industry standards for this type of analysis are usually based on differential scanning calorimetry (DSC) and differential thermal analysis (DTA), both of which measure thermal differences of a reference and a sample material under identical thermal cycles. On one hand, DTA

tracks the samples temperature difference with respect to a reference while they are subject to a heating or cooling cycle. DSC instead measures changes in heat flow rate between the sample and the reference material. This is done through a calorimetric calibration which converts temperature differences among the two elements and converts them into a heat flow. [9] Figure 2.10 depicts example schematics for a DTA (left) and DSC (right) instrumentation.

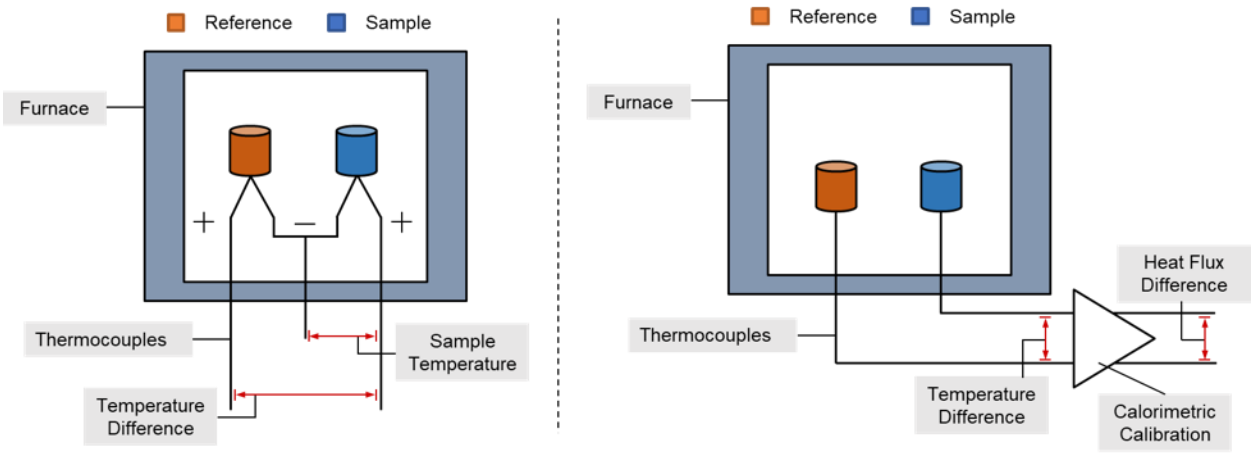

Figure 2.10 Simplified schematics of a differential thermal analysis (DTA) instrument (Left) and a differential scanning calorimeter (DSC) (Right). The main difference between these systems is the type of thermal properties that is record, temperature, and heat flux, respectively.

Both techniques can provide information on physical changes which are temperature dependent. In fact, it is not only possible to detect melting point of substances, which refer to changes from a solid state to a liquid one, but they can also measure freezing points, which instead refer to changes from a liquid to a solid state. In the case of deep eutectic solvents, a class of green designer solvents with desirable properties for a wide variety of applications, it is important to detect the composition of the eutectic point. In the literature, the freezing temperature of DES

solvents are commonly reported using differential scanning calorimetry (DSC) in the cooling cycle. Figure 2.11 shows an example of DSC curve for three chloride-based DES.

However, DSC is a low-throughput technique that can take upwards of 60 minutes per sample. While additional instrumentation could be added to increase the throughput of these measurements, such as an autosampler, the technology is currently not conducive to high-throughput experimentation or suitable for the exploration of large design spaces such as DES system.

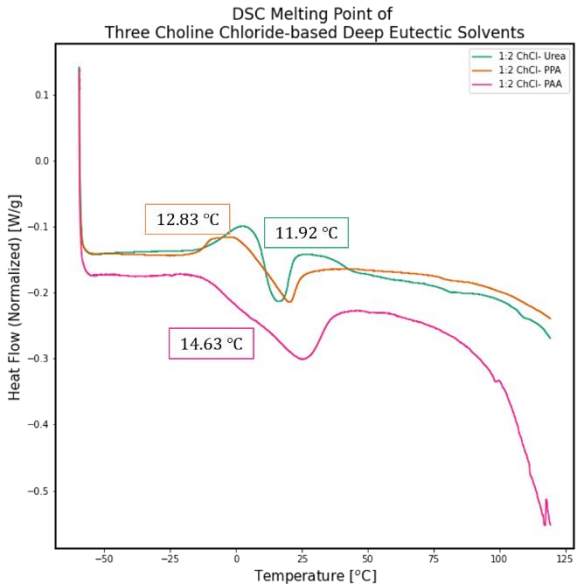

Figure 2.11 Results of freezing point determination for three Choline Chloride-based Deep Eutectic Solvents using differential scanning calorimetry.

2.3.1.2 IR Bolometry

While DSC and DTA allow for accurate and precise results, measurements can take upwards of an hour per sample to complete. This becomes extremely time-consuming and expensive to run for large sample sets. Recently, the concept of optically determining melting points and other thermal properties with an infrared (IR) camera has been proposed.[10] IR cameras, also called thermal sensors, detect emission of thermal energy from objects and convert it into an

electrical signal. This technology is similar to a bolometer, a thermal detector which measure radiated energy through an electrical resistance thermometer.[11] This technique is non-destructive and does not require contact with the object under measurement. Based on this idea, an open-hardware and related software were design for parallel thermal imaging, called PhasIR (Figure 2.12).[12,13]

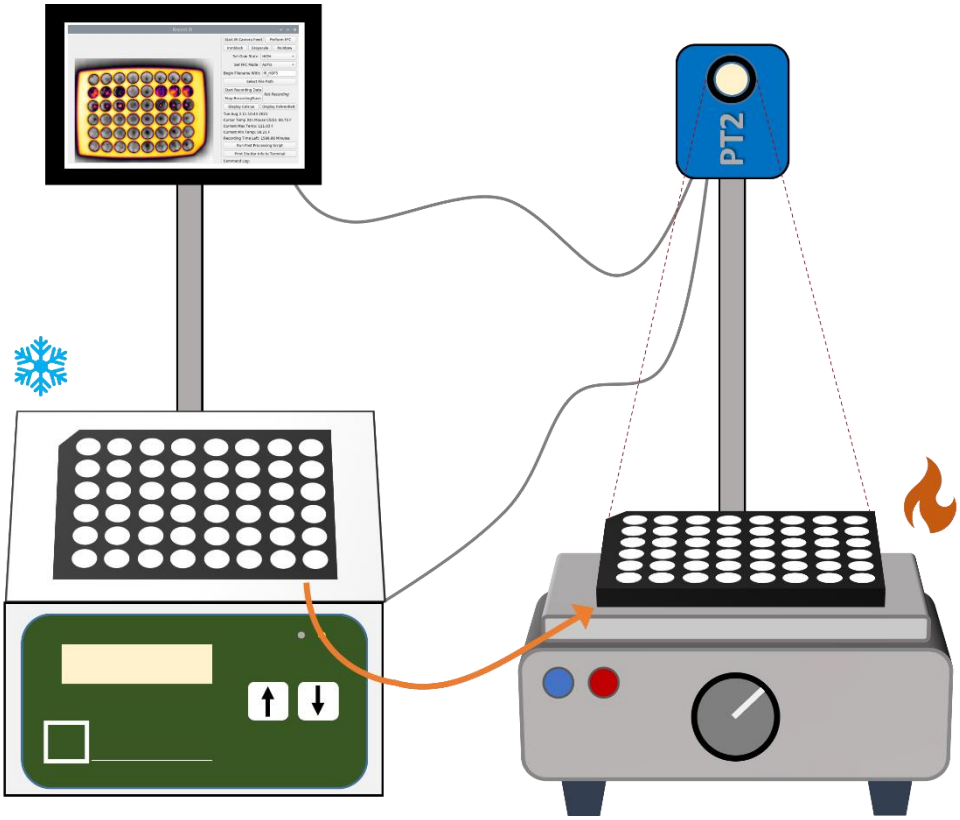

Figure 2.12 PhasIR schematics. The system is composed of a Raspberry Pi microcomputer, a FLIR LEPTON 3.5 IR camera, and aluminum multi-well plates as the basic elements, a Peltier plate (left) for cooling the samples prior to imposing a heating cycle using a standard hot plate (right).

The PhasIR system consists of a Raspberry Pi microcomputer, a FLIR LEPTON 3.5 IR camera, and aluminum multi-well plates as the basic elements. Its functionality is remarkably similar to differential thermal analysis (DTA). However, instead of the thermocouples used in DTA, the temperature of the plate and sample are measured using an IR camera during heating,

and the onset of melting is determined by the ΔT curve between the reference (metal well plate) and the sample temperatures.

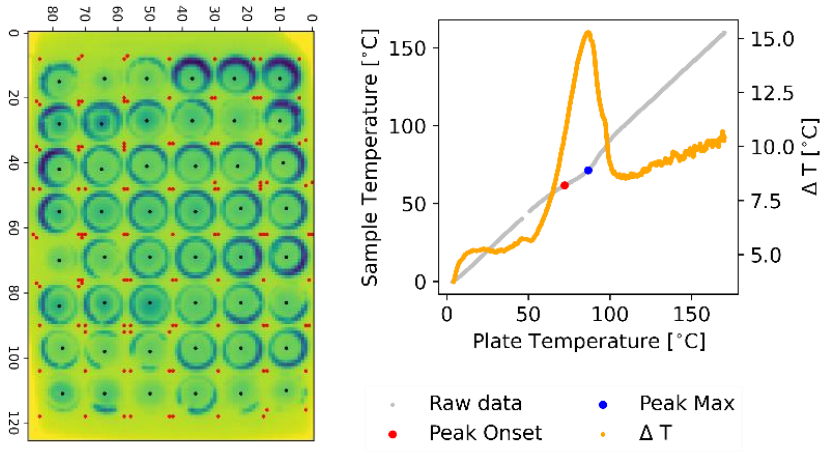

Figure 2.13 Left) Example 48-well well plate with centroid and plate temperature identification obtained through the PhasIR Image Analysis module. The black marker identifies the centroid of the well, whereas the red marked are used as the reference plate temperature for each well. Right) Melting point for the $35\,mol\%$: 65 mol % choline chloride: N, N-dimethylurea sample. The temperature was recorded using the PhasIR system. The melting point is defined as the onset (red marker) of the $\Delta T = T_{plate} - T_{sample}$ curve (yellow)

An example plot can be seen in Figure 2.13, right. Here, the temperature of the samples and the aluminum plate are encoded in the pixel value composing the frames collected by the Lepton IR camera. The sample temperature is obtained from averaging the pixel values across a circular region around the centroid of each well, across all frames of the video. For each well identified in the image, the plate temperature is averaged over four equidistantly points placed diagonally with respect to the well centroid. An example image of the metal 48-well plate with centroid and plate position identification obtained through the PhasIR *Image Analysis* module can be found in Figure 2.13, left. Next, the samples and plate are heated from a low temperature and the temperature of the sample (T_{sample}) is plotted with respect to the temperature of the plate (T_{plate}). For the majority of the heating process, there is a linear relationship between the two

temperatures. However, when samples melt, there is a discontinuity in this plot due to the abrupt change in the thermal conductivity of the sample. Thus, for each sample in the plate, the onset of the phase transition event is obtained from the onset of the peak formed by the $\Delta T = T_{plate} - T_{sample}$ curve. The peak onset is determined using the SciPy peak finding algorithm.[8]

The infrared bolometry technique used in the PhasIR system is well suited for fast screening of up to 96 samples simultaneously in ~10 minutes. On the other hand, it is unfortunately difficult to identify phase transitions in the PhasIR system during cooling cycles (freezing) due to the slow cooling rates of Peltier plates and the variable nucleation rates of different DES samples. Therefore, reported phase transitions in this work correspond to the 'first onset of melting' for the samples evaluated, which may not always correspond to the complete homogeneous melting of DES samples.

2.4 Active Learning

The widespread implementation of machine learning algorithms in several realms of science and the increase in achievable computing power promise to increase the speed of new materials discovery. Active learning is a subfield of machine learning and artificial intelligence in which an algorithm iteratively learns and improves its performance as it experiences new instances of the search design space. The algorithm can autonomously formulate and test new hypotheses, based on its knowledge obtained from previous results, as part of its learning process. [14] Implementing these algorithms allow for more advanced design of experiment approaches and smarter investigation of the chemical space at hand. In particular, Bayesian optimization (BO) strategies have gained significant traction and popularity in many materials' science and chemical spaces. [15] Its broad implementation stems from its ability to optimize high-dimensional, complex, and noisy tasks.

2.4.1 *Bayesian Optimization*

Bayesian optimization (BO) is a commonly used class of algorithm that allows for advanced design of experiments planning. The main advantage is the learning strategy implemented by optimizer, which takes the form of an iterative process in which any subsequent experimental iteration (e.g., sample composition to test) is guided by the knowledge gained from previous experimental results. This, in turn, allows convergence towards a final target in a faster and optimized manner.

In its simplest form, BO is a global optimization strategy used to maximize (or minimize) a function with unknown closed-form expression, usually called a black-box function. This usually does not take on any specific functional form (e.g., a linear correlation between inputs and outputs) and their objective is either not directly accessible or known. [15] Examples of these scenarios are extremely common in science as the exact mechanisms that govern an outcome might not be straightforward to learn or it might be challenging to decouple the effect that each design variable has on the system. To circumvent this limitation, BO generates a probabilistic surrogate model to relate the inputs and outputs, while simultaneously trying to maximize (or minimize) the black-box function, Equation 2.8. [16]

$$x^* = argmax_{x \epsilon X}\ f(x) \qquad 2.8$$

Where f is the black-box function of interest, x are the inputs of the system, and x^* represents the optimal candidate that satisfies the optimization task. Since the relationship between inputs and outputs is not explicitly known, there is a need to approximate it using a surrogate model. In most cases, the chosen modeling function is based on *a Gaussian Process (GP).*[17] This is a regression technique based on a probabilistic model that estimates the objective black-box function by fitting a distribution of functions, each of which takes the form of a *Gaussian distribution*, $f(x)$, a

symmetric, continuous probability distribution with set mean μ and variance κ.[17] The GP model can be fully characterized by its prior distribution, a representation of what is known about the possible functional form before any observation is made. After data has been acquired, the posterior distribution is computed, which revises the assumptions about the functions based on the new knowledge. Figure 2.14 depicts an example of a gaussian process.

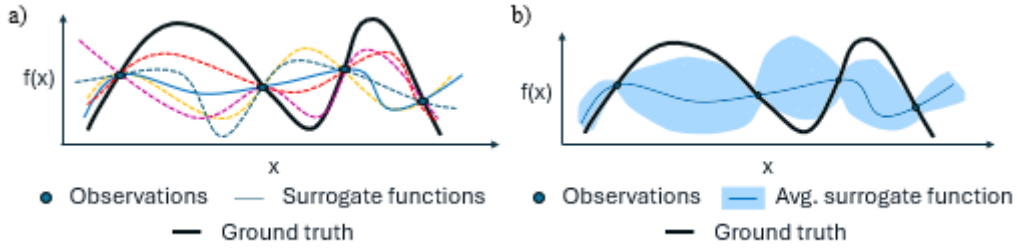

Figure 2.14 a) Example of a Gaussian Process. The black-box ground truth function (solid black line) and the known observations (markers) are initially approximated using a collection of random functions (dashed lines). b) Representation of the same GP process, using its average functional form(solid blue line) and corresponding uncertainty region (blue shaded regions). The uncertainty is higher for points further from the observations and lower for known inputs and outputs.

The black-box ground truth function (solid black line) and the known observations (markers) are initially approximated using a collection of random functions (dashed lines). The predicted value of $f(x)$ at each value x is then represented using the mean of the surrogate gaussian functions (solid blue line), along with the corresponding uncertainty region (blue shaded regions). Those are defined by the kernel function, also known as the covariance function. [18] Initially, the form of the average function composing the prior distribution is taken randomly, and iteratively updated, the posterior, as new inputs and outputs are queried. The main advantage of this approach is that a GP provides probabilistic predictions that also contains information on the point's uncertainty. This tends to be higher for points further from the observations and lowers lower for the known inputs and outputs.

Once again, as an active learning algorithm, BO iteratively tries to learn the design variables' relationship. To do so, it implements an acquisition function, used to quantify the benefit of evaluating each point in the design space, that will intelligently suggest strategies for querying the input space with higher uncertainties. A common acquisition function for Bayesian Optimization is the *expected improvement (EI)*, Equation 2.9 . [15] This is a function that models the expectation that the new queried $f(x)$ will exceed a threshold corresponding to the best observation so far, see Equation 2.9 .for the Eis utility function, $u(x)$

$$u(x) = max(0,\ f(x^*) - f(x)) \qquad 2.9$$

This utility function is evaluated for every point x in the domain to generate the *probability of improvement*. The new suggested x value to query will be the one with the higher probability of improvement, therefore the local maximum in the curve seen in Figure 2.15

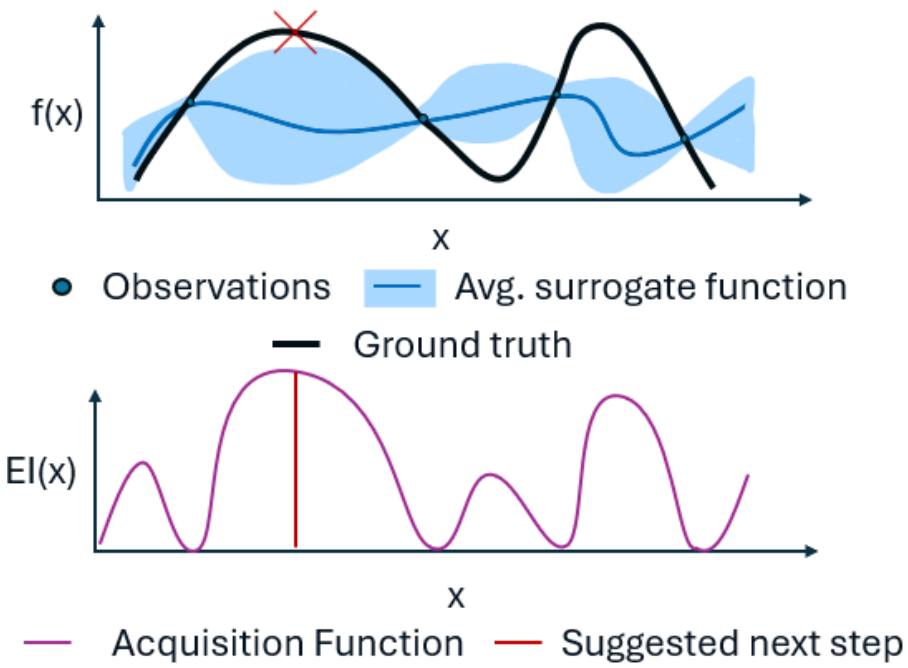

Figure 2.15 The corresponding *expected improvement* function (bottom plot) evaluated for the GP (top plot). The red line and the x marker indicated the maximum expected probability and the next input point to query, respectively.

In this case, the suggested new input point to query is the one corresponding to a local maximum in the EI function, red line and x marker. This allows the algorithm to compute a trade-off between *exploring* a new region of the design space or *exploiting* the model's confidence of the most likely area of the input design will meet the requirements of the task. [15]

The final component of a BO is the scoring strategy. This is a function that is used to evaluate each point to satisfy the optimization task, Equation 2.8. In Chapter 6, the Euclidean distance of the queried point and x^* as follows:

$$d(a,b) = \sqrt{\sum_{i=1}^{n} (a_i - b_i)^2} \qquad 2.10$$

In this case, the optimization task is a minimization on, so Equation 2.8 will be $argmin()$ instead. Finally, the BO algorithm will then iteratively run the following steps :

1. Generate the next point to query using the acquisition function
2. The proposed point (input) is evaluated based on its outcome (output)
3. The current input and output observations are then added to the dataset used to then update the surrogate model of the system.

This loop is repeated until a condition is met, either the optimization task is met, or the total number of possible iterations is exhausted. While the application of this methodology is straightforward, the algorithm assumes that the output of the model is a single scalar value which can be correctly computed. For example, this can be the distance metric in Equation 2.10 . The evaluation selected for the conducting an optimization task using BO will affect the chances of converging towards the correct objective. Unfortunately, it is not always simple to find the right metric of evaluation for every system. In this thesis, this type of optimization task will be used in Chapter 6 to run a self-driving lab task of autonomous color matching. A BO algorithm will be

tasked to learn how to create target color. The algorithm will be coupled with a robotic platform to physically mix stock colors and evaluate the resulting sample color.

2.5 REFERENCES

1. Orazem, M. E. & Tribollet, B. *Electrochemical Impedance Spectroscopy*. (Wiley, 2008).
2. Elgrishi, N. *et al.* A Practical Beginner's Guide to Cyclic Voltammetry. (2017) doi:10.1021/acs.jchemed.7b00361.
3. Bard, A. J., Faulkner, L. R. & White, H. S. *Electrochemical Methods*. (Wiley, 2022).
4. Dave, A. *et al.* Autonomous Discovery of Battery Electrolytes with Robotic Experimentation and Machine Learning. *Cell Rep Phys Sci* **1**, (2020).
5. Bera, D., Qian, L., Tseng, T.-K. & Holloway, P. H. Quantum Dots and Their Multimodal Applications: A Review. *Materials* 2260–2345 Preprint at https://doi.org/10.3390/ma3042260 (2010).
6. Harris, D. C. & Bertolucci, M. D. *Symmetry and Spectroscopy- An Introduction to Vibrational and Electronic Spectroscopy*. (Oxford University Press, Inc., 1978).
7. Horvath, I. T., Colinet, P. & Vetrano, M. R. Assessment of the light extinction spectroscopy technique for submicron particle characterization. *Powder Technol* **291**, 375–382 (2016).
8. scipy.signal.find_peaks. https://docs.scipy.org/doc/scipy/reference/generated/scipy.signal.find_peaks.html.
9. Gallagher, P. K. *Handbook of Thermal Analysis and Calorimetry*. vol. 1 (1998).
10. Kawakami, K. Parallel thermal analysis technology using an infrared camera for high-throughput evaluation of active pharmaceutical ingredients: A case study of melting point determination. *AAPS PharmSciTech* **11**, 1202–1205 (2010).
11. Richards, P. L. Bolometers for Infrared and Millimeter Waves. *J Appl Phys* **76**, 1 (1994).
12. Rodriguez, J. *et al.* PhasIR: An Instrumentation and Analysis Software for High-throughput Phase Transition Temperature Measurements. *Journal of Open Hardware* **5**, (2021).
13. Politi, M. & Rodriguez, J. phasIR: Python modules for high-throughput measurement of melting point using IR bolometry. *GitHub* https://github.com/pozzo-research-group/phasIR (2021).
14. Settles, B. *Active Learning*. (2012).
15. Jones, D. R., Schonlau, M. & Welch, W. J. Efficient Global Optimization of Expensive Black-Box Functions. *Journal of Global Optimization* **13**, 455–492 (1998).
16. Vaddi, K., Chiang, H. T. & Pozzo, L. D. Autonomous retrosynthesis of gold nanoparticles via spectral shape matching. *Digital Discovery* **1**, 502–510 (2022).
17. Rasmussen, C. E. & Williams, C. K. I. Gaussian Processes for Machine Learning. *Gaussian Processes for Machine Learning* (2005) doi:10.7551/MITPRESS/3206.001.0001.
18. 1.7. Gaussian Processes — scikit-learn 1.5.0 documentation. https://scikit-learn.org/stable/modules/gaussian_process.

Chapter 3. HIGH-THROUGHPUT DESIGN OF DEEP EUTECTIC SOLVENTS ELECTROLYTES

This chapter contains work from the following publication and the author would like to acknowledge the contributions of the coauthors:

Rodriguez, J. Jr[*]; Politi, M[*]; Adler, S.; Beck, D. A.; Pozzo, L.D. High-throughput and Data-driven Strategies for the Design of Deep Eutectic Solvent Electrolytes. *Mol. Syst. Des. Eng* **2022**, 7, 933-949. https:// 10.1039/d2me00050d

[*] These authors contributed equally to this work

3.1 INTRODUCTION & MOTIVATION

Deep Eutectic Solvents (DES) are a new class of green designer solvents which are inexpensive, nontoxic, and do not require further purification and create no waste. These samples are composed of two or more materials that, when mixed at specific molar ratios, exhibit significantly greater depression of their melting point than one would predict assuming an ideal liquid solution. [1] Abbott et al. identified several types of DES, including many that are formed by combination of a quaternary ammonium halide salt (QAS) with a molecular hydrogen bond donor (HBD) at specific molar ratios.[2] These solvents share similarities in several physical and electrochemical properties with ionic liquids (ILs), salt-like materials with melting points below 100 ℃. The main appeal of DES stems from their low vapor pressure, low flammability, good ionic conductivities and a wide stable electrochemical potential window compared to current aqueous systems. [3,4] Thanks to these characteristics, they have found several applications, from electroplating and metal recycling, [5–11] to CO_2 capturing, [12–17] gas separations, [18,19] extractions and purification processes, [20,21] to name a few. Moreover, deep eutectic solvents have a straightforward synthesis consisting of simply mixing solid components at specific molar ratios and heating until they form a clear and uniform liquid solution. [22] Therefore no solvent is required for their synthesis. In particular, type III DESs are formed of a combination of a quaternary ammonium salt, which

acts as a molecular hydrogen bond acceptor, and a hydrogen bonding species (e.g., polyols, carboxylic acids or amines) at a specific molar ratio, making their experimental design space extremely large.

In fact, there still exists major challenges for the molecular design of ideal DESs electrolytes. The literature states that the total number of possible DES candidates likely exceeds the estimated design space for ILs (estimated at $\sim 10^{18}$ unique anion/cation pairs).[23,24] Yet despite the simple synthesis process for DES, current experimental efforts and methods have been slow at making a significant dent in the exploration of these materials. Thus, computational methods have become a powerful tool to provide insight where experiments may fall short. Unfortunately, a common theme amongst computational studies on DESs is the lack of data available to make significant strides in developing generalized predictive models. Moreover, there is still a lack of chemical diversity in the available experimental literature since many reported DES systems are overwhelmingly based on choline chloride, a commonly used QAS.[25–27] Deeper fundamental understanding of DESs is also necessary, especially when determining their feasibility for use as electrolytes.[28] The strong hydrogen bond network that is formed in DES has direct impacts on several key electrolyte properties, which can be influenced by molecular weight, QAS anions, and the presence of specific functional groups. Still, many of the features that can lead to ideal DES electrolytes may not be intuitive to determine, and therefore the development of this class of materials will require optimization, functional design, and new methods to tackle exploration of the large design space.

In this regard, high-throughput experimentation and data-driven strategies for chemical exploration promise to accelerate the development of new materials, including new electrolytes.[29–32] However, to date these methods have not yet been extensively applied towards development

of DES electrolytes. The design of new materials is known to be inherently a multivariate task requiring solutions aiming at the simultaneous optimization of several target properties. Multi-objective optimization (MOOP) strategies have become increasingly popular, especially in the drug discovery field. [33–35] However, these techniques rely on available predictive frameworks, databases or molecular simulations providing a variety of measured or estimated properties for the chemicals used. Unfortunately, the lack of variety of tested combinations and sparsity in their measured properties in the DES literature hinders the formulation of robust models.

In this chapter, an integrated workflow for the investigation of DES electrolytes for future use in energy-related systems is presented as an example of materials acceleration platform applied to a chemical experimental synthesis. The design space utilized in this chapter was obtained through a previous preliminary cheminformatics approach focused on specific engineering metrics (e.g., chemical similarity, commercial availability). [36] This section of the work was performed by a colleague, Dr. Jaime Rodriguez, and a more in-depth discussion of it can be found in his dissertation. [37] I would like to mention that this was a collaborative project. In fact, the experimental planning and execution was equally shared between Dr. Rodriguez and I, while the data analysis and interpretation of both physical and electrochemical data was conducted by my. Next, the traditional synthesis process for DES has been modified to enable high-throughput sample preparation using open-source, automated liquid handling robotic platforms and custom labware. Electrochemical characterization of the samples is then performed in a high-throughput manner using screen-printed electrodes (SPE) which require minimal sample volume and facilitates data collection and successive analysis. The experimental strategies presented in this chapter can significantly speed up sample preparation for large number of samples and allows for a systematic, combinatorial sequence to explore new formulation of deep eutectic solvent.

3.2 MATERIALS AND METHODS

3.2.1 *Materials*

Again, an initial cheminformatic campaign that was used to identify an initial outline of prospect materials conducted using open-source software and databases. Candidate molecules were first screened for their commercial availability and successively selected through a ranking system based on key engineering metrics. More information on the steps taken to identify the chemical design space for the investigation of new DESs and analogous can be found at the source acknowledged at the beginning of this chapter. [36]

The selected quaternary ammonium salts are as follows. Acetylcholine Chloride (AcChCl) (≥ 99%), Tetraethylammonium Chloride (TEAC) (≥ 98%), Tetrapropylammonium Bromide (TPAB) (98%), and Tetraethylammonium Iodide (TEAI) (98%) were obtained from Sigma Aldrich (Burlington, MA). Choline Chloride (ChCl) (99%) was obtained from Acros Organics (Fair Lawn, NJ). All QASs were dried under vacuum for 24hr upon receipt and were then stored inside an airtight desiccator to prevent significant water uptake.

The selected molecular hydrogen bonding species are as follows. Ethylene Glycol (Certified) was purchased from Fisher Scientific (Hampton, NH). Glycerol (≥ 99 %), Acetamide (~99%), N, N'-dimethylurea (≥ 99%), 3-phenylpropionic Acid (99%), L-serine (≥ 99 %), 4-Amino-4*H*-1,2,4-triazole (99%), and Xylitol (≥ 99%) were purchased from Millipore Sigma (Burlington, MA). Phenylacetic Acid (99%) was purchased from Alfa Aesar (Haverhill, MA). Urea (Ultrapure) was purchased from Thermo Scientific (Hampton, NH). Ethanol (100 Proof) was purchased from Decon Laboratories (Montgomery County, PA). All HBDs were used as received and required no further processing.

3.2.2 *High-Throughput Synthesis of Deep Eutectic Solvents and Analogous*

As previously mentioned, DESs have a relatively simple and straightforward synthesis procedure. However, while some of these components are liquid in their pure form (i.e., ethylene glycol, glycerol, trifluoroacetic acid), the majority are usually solids. While the traditional synthesis approach is suitable for investigating a small number of DES conditions at a time, it quickly becomes inefficient when attempting to explore a broader range of candidates across various molar ratios.

To make use of combinatorial and high-throughput solutions for the formulation of new DESs and analogous samples, the traditional methodology mentioned above was adapted and modified slightly. First, concentrated stock solutions of each QASs and HBDs were prepared using volatile solvents, with either water or ethanol being utilized depending on which yielded the greatest solubility for the starting material. Table 3.1 shows more information on the final concentrations and solvent used for each stock prepared, while Figure 3.1 shows the chemical structure of the selected DES components.

Table 3.1 Concentrated stock solution information for all materials used for the experimental DESs campaign.

Molecular Species	Abbreviation	MW $[\boldsymbol{g/mol}]$	Solvent	HBD Max Conc [M]	Mass $[\boldsymbol{g}]$ for 25mL solution
Ethylene Glycol	EG	62.07	Water	7	10.86
Glycerol	Gly	92.09	Water	7	16.12
Acetamide	Ace	59.07	Water	7	10.34
N,N'-dimethylurea	NNDMU	88.11	Water	7	15.42
3-phenylpropionic acid	PAA	150.17	Ethanol	3	11.26
Urea	U	60.06	Water	7	10.51
L-serine	L-S	105.09	Water	2	5.25
4-Amino-4H-1,2,4-	4AT	84.08	Water	4	8.41
Xylitol	Xyl	152.15	Water	3	11.41
Phenylacetic acid	PAA	136.15	Ethanol	3	10.21
Choline Chloride	ChCl	139.62	Water	4	13.96
Acetylcholine Chloride	AcChCl	181.66	Water	4	18.17

Tetraethylammonium Chloride	TEAC	165.7	Water	3	12.43
Tetrapropylammonium Bromide	TPAB	266.26	Water	2	13.31
Tetraethylammonium Iodide	TEAI	257.16	Water	1	6.429

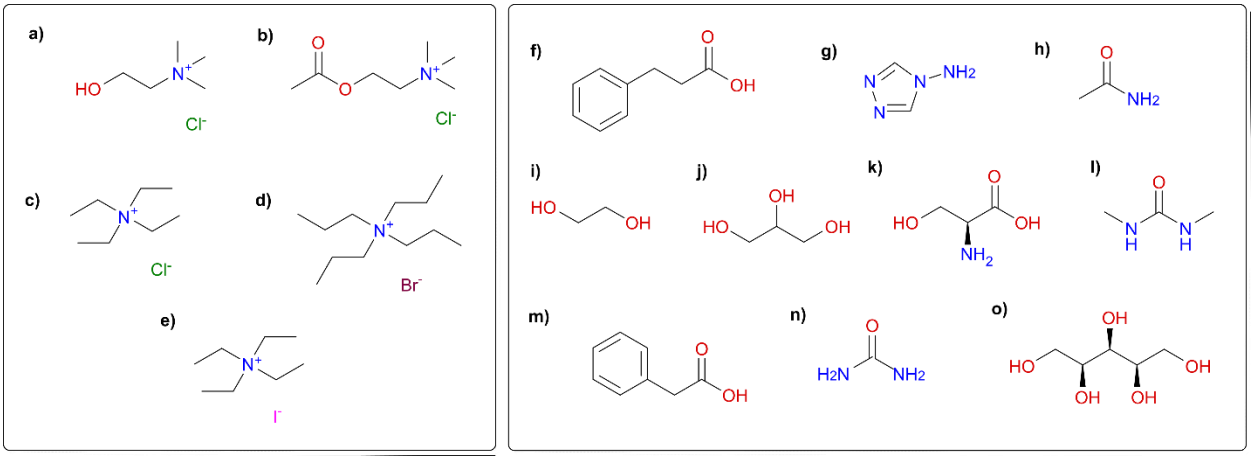

Figure 3.1 Structures of Quaternary Ammonium Salts (Left) and Hydrogen Bond Donors (Right) selected for high-throughput DES synthesis. The depicted molecules are the following: a) Choline Chloride, b) Acetylcholine Chloride, c) Tetraethylammonium Chloride, d) Tetrapropylammonium Bromide, e) Tetraethylammonium Iodide, f) 3-Phenylpropionic acid, g) 4-Amino-4H-1,2,4-triazole, h) Acetamide, i) Ethylene Glycol, j) Glycerol, k) L-serine, l) N,N'-Dimethylurea, m) Phenylacetic acid, n) Urea, o) Xylitol

To automate the mixing of the two DESs components and create a reproducible protocol, the Opentrons OT-2 liquid handling robot was implemented for the sample formulation. This is a relatively inexpensive, open-source and open-hardware materials acceleration platform that can be easily interfaced using simple scripting protocols. The entire procedure, from the determination of the necessary volume of the species in each sample, to the commands for the OT-2 platform, was performed using python scripts executed in Jupyter Notebooks. The samples composition, as well as the protocol containing all hardware specification for the robotic platform are saved in *'.csv'* files for ease in information transfer which is both human and machine readable. Samples can be prepared in a variety of standard multi-well plate formats, as long as the labware of choice follows

SLAS standard sizing. Given the necessity of heating the samples at temperatures above 80℃, custom 48-well wellplates for 2 mL glass scintillation vials were fabricated using a FormLabs Form 3 3-D resin printer. The material of choice for these plates was the FormLabs FLHTAM02 high-temperature resin, which has thermal stability up to 238°C. [38] After the samples are prepared, the volatile carrier solvents are removed through a three-stage process. First, a gentle evaporation step allows the removal of the majority of the carrier solvent. This step makes use of a commercial dehydrator (Cabela's 80L SKU: 2517102), set at 65°C. Samples are processed for 24 hours. Next, the well plates hosting the sample vials are placed in an oven at 100℃ for 30 min. This step is crucial not only to remove any remaining water or ethanol used in the stock preparation, but it helps increase the homogeneity of the final mixture. In fact, some literature sources have noted that heating the DES components 80℃ may result in the formation of area with higher concentration of the QAS, which upon cooling precipitate or cause re-crystallization of the entire sample. [39,40] Preparing the DES in glass vials allows us to incorporate important aspects of their traditional synthesis (i.e. heating to 100℃ or higher), while also aiding in preserving and storing samples for characterization later in the pipeline. Samples are then allowed to cool and successively dried under vacuum at room temperature for 30 min, to remove any potential residual carrier solvent that could remain, and afterwards stored in airtight desiccators until screening and characterization is performed. Figure 3.2 shows a schematic summarizing the high-throughput synthesis workflow.

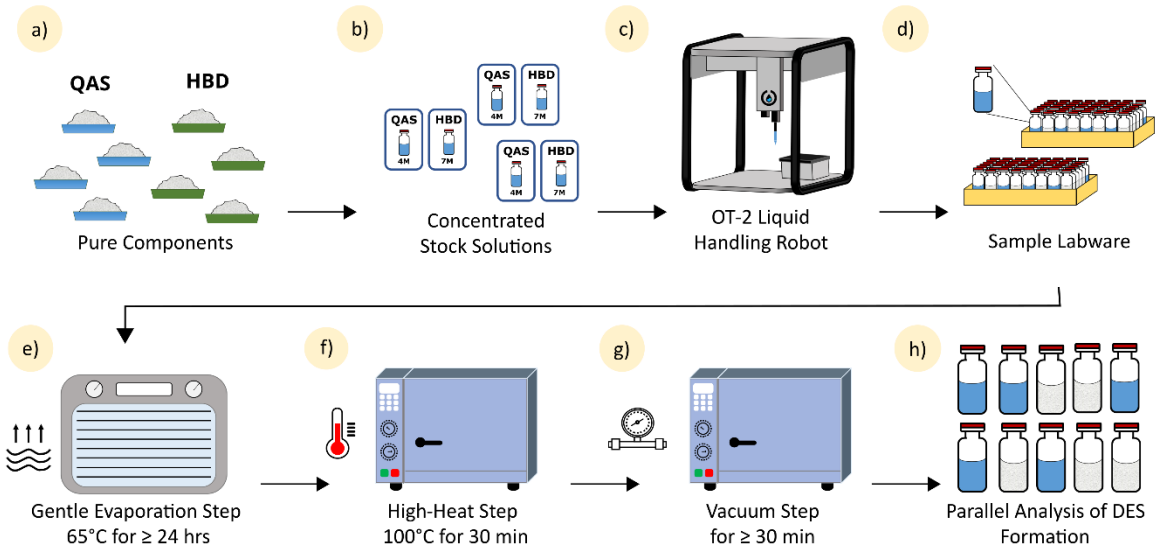

Figure 3.2 Schematic illustration of the proposed high-throughput synthesis protocol for deep eutectic solvents. a) The QASs and HBDs in their pure form. b) Concentrated stock solutions allow for use of MAPs. c) The stocks, labware, and pipette tip racks are loaded onto the OT-2 deck for sample formulation. d) The DES samples are stored in temperature-stable 48-well plates holding glass vials. e) The sample are placed in a dehydrator at 65°C for 24 h to remove the volatile solvents. f) The sample plates are them placed in an over at 100°C for 30 minutes. g) The sample plates then moved into a vacuum for about 30 minutes. h) Samples found in the liquid phase at room temperature are now ready to be characterized.

3.2.3 *High-throughput Determination of Onset of Melting*

The samples' onset of melting was measured using a recently developed high-throughput and open-source thermal analysis system called PhasIR.[41] This system uses IR bolometry to analyzed phase transitions in liquids in a parallel analysis platform. For any binary mixture near a eutectic composition, we expect the solid to liquify over a range of temperatures, starting at the eutectic temperature. Thus, the onset of melting is a good metric for the lowest liquid temperature one can achieve using the chosen mixture, even when the eutectic composition is not known precisely. Given the hygroscopic nature of DES, this sample characterization step was conducted

entirely inside a glovebox for a moisture-free environment. The DES samples were cooled using the Peltier plate of the PhasIR hardware system set at $-10℃$, while the heating process was conducted using a VWR hot/stir plate (NA CAT No: 97042-682) previously set to $200℃$, to achieve a broader temperature range. The samples were loaded on metal 48 or 24 conical-shaped-wells aluminum plates. The overall measurement took approximately 10 minutes per plate to collect. The data was then analyzed using the homonymous Python-based software which can be found on GitHub.[42] For more information on the experimental set up, data collection and analysis using the PhasIR system, please see Chapter 2, section 2.3.1.2.

3.2.4 *High-Throughput Electrochemical Characterization*

All electrochemical characterization techniques were carried out using a Gamry Reference 600 potentiostat along with Metrohm-DropSens DRP-11L screen printed electrodes (SPEs), which were interfaced directly with the Gamry via the Metrohm-DropSens CAC4MMH connector. The DRP-11L is a low cost and disposable compact 3-electrode screen printed cell, making it ideal for working with sample volumes of approximately $100\ \mu L$. The cell, depicted in Figure 3.3, consists of carbon working and counter electrodes and a silver/silver chloride reference electrode. Measurements were conducted only for samples that were liquid at room temperature.

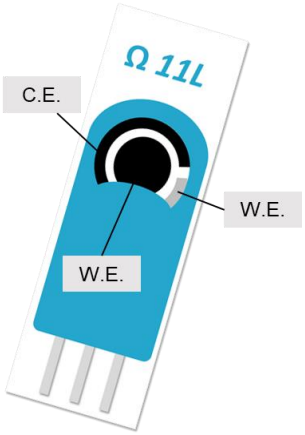

Figure 3.3 Example of DRP-11L Screen Printed Electrode from Metrohm US. The different electrodes composing the electrochemical cell are labeled as follows: working electrode (W.E.); counter electrode (C.E.); reference electrode (R.E.)

3.2.4.1 Multi-step Chronopotentiometry

Multi-step chronopotentiometry was performed to determine the limiting reduction and oxidation potentials of the DES electrolytes. First, a series of four fixed positive currents of $1, 0.75, 0.5,$ and $0.25\ mA$ are applied. These steps are followed by negative currents of the same magnitude. The very first positive and negative steps are held longer, for 15 seconds, as a conditioning step, while each subsequent step is held for 10 seconds with data collected every half second. For more information on the chronopotentiometry data analysis, please see Chapter 2, section 2.1.3.

3.2.4.2Cyclic Voltammetry

Cyclic voltammetry was performed to investigate the possibility of undesired electrochemical side reactions in regions between the limiting reduction and oxidation potentials of the DES electrolytes. Measurements were performed at $100\ mV/s$ scan rate, spanning voltages from $-2\ V$ to $2\ V$, for a total of four complete cycles per sample to ensure equilibration. Moreover, the last 20 points of the forward and reverse scans were used to determine the slope (dI/dV) of

the limiting processes shown in the voltammogram. For more information on the cyclic voltammetry data analysis, please see Chapter 2, section 2.1.2.

3.2.4.3 Electrochemical Impedance Spectroscopy

Electrochemical Impedance Spectroscopy (EIS) was used to determine the ionic conductivity of the DES electrolytes. A small voltage perturbation of amplitude $50\,mV$ was applied to the samples and the frequency was varied from $100\,kHz$ to $100\,Hz$, with 10 points per decade. The impedance data was fit using the open-source package Impedance.py. [43] Due to the unusual geometry of the screen-printed electrochemical cell, a calibration curve was obtained using standards of known conductivity spanning four orders of magnitude to convert the resistance to a quantitative conductivity. The conductivity standards were: $84\,\mu S/cm$, $443\,\mu S/cm$, $1413\,\mu S/cm$, $2764\,\mu S/cm$, and $12880\,\mu S/cm$. These were obtained from Oakton (Vernon Hills, IL) and are all $NaCl$ based solutions. For more information on EIS data analysis, please see Chapter 2, section 2.1.1.

3.3 RESULTS

The selected 10 HBDs and 5 QAS were mixed, with 12 different molar rations per combination of DES components. This yielded a total of 600 samples which were synthesized, processed, and characterized in approximately a month, showing a significant advantage of the implemented high-throughput workflow. After samples were processed through the evaporation, heating, and vacuum steps, it was noted that samples containing ChCl, AcChCl, TEAC, and TPAB as QAS formed liquids at room temperature. All liquid samples were clear and showed a homogeneous phase. In contrast, all samples containing TEAI as a QAS did not form a liquid at room temperature with any HBD combination and therefore were not characterized further.

Similarly, all the samples that used L-serine as the HBD species were found solid at room temperature. So, these were also excluded from electrochemical testing.

3.3.1 *Comparison with Literature Samples*

When developing a new workflow, especially one which uses an adapted protocol to both synthesize and characterize samples, it is important to compare the results from the new experimental campaign with those published in literature. As mentioned before, Choline Chloride-based samples have been some of the most extensively studied DES systems to date. In fact, several of the HBD have been paired with ChCl to form DES.[5,44–47] For this reason, they were used to validate the implemented MAP-based protocol.

The PhasIR measurements were conducted in an argon-filled glovebox to reduce the possible contamination with atmospheric water during the sample's physical characterization. Still, a small portion of measured samples show a phase transition feature close to 0℃, which could be attributed to traces of water in the samples. For example, Figure 3.4 shows PhasIR measurements for the $60\ mol\%$ ChCl sample with acetamide.

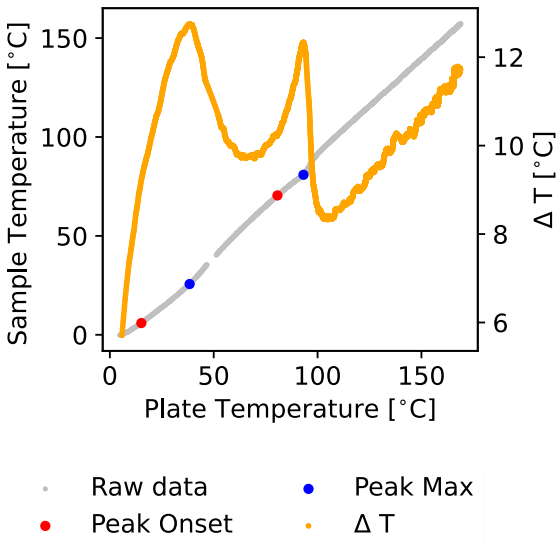

Figure 3.4 Onset of melting determination for the 60 $mol\%$ Choline Chloride with Acetamide. The melting point is defined as the onset (red marker) of the feature in the $\Delta T = T_{plate} - T_{sample}$ curve (yellow). The first peak can be attributed to water present in the sample as the peak onset is found around 0 ℃.

This is the only case in which the feature is so noticeable, in other cases, the 'water feature' is only a small shoulder in the ΔT curve in the lower temperature region of the measurement. Samples which did not show a clear phase transition feature on their PhasIR curve were not included in the final 'phase diagram.' This behavior would signify either a transition temperature is outside of the measurement range of the PhasIR system or the necessity for an instrument with a better resolution. However, in the literature, the freezing temperature of DES solvents is commonly reported using differential scanning calorimetry (DSC) in the cooling cycle. As mentioned previously, DSC is a low-throughput technique that can take upwards of 60 minutes per sample and is therefore not suitable for the exploration of large design spaces such as the one discussed here. In contrast, the PhasIR can characterize upwards of 48 samples simultaneously, with measurement times ranging from 5-10 minutes. However, the identification of phase transitions in the PhasIR system during cooling cycles (freezing) would be extremely challenging due to the slow cooling rates of Peltier

plates and the variability in nucleation rates of the samples. Therefore, the reported phase transitions in this work correspond to the 'first onset of melting' for the samples evaluated, which may not always correspond to the complete homogeneous melting of DES samples.

In fact, for samples containing high ratios of QAS, this phase-transition point often indicates partial melting of a solid sample to a two-phase sample containing a liquid and a dispersed solid. This is clearly outlined by a gray area in the results.

Figure 3.6 shows PhasIR melting-onset diagrams for the urea and N,N'-dimethylurea samples. The eutectic point for the ChCl:urea samples was clearly identified at the expected 1:2 molar ratio, which is consistent with literature reports.[48]

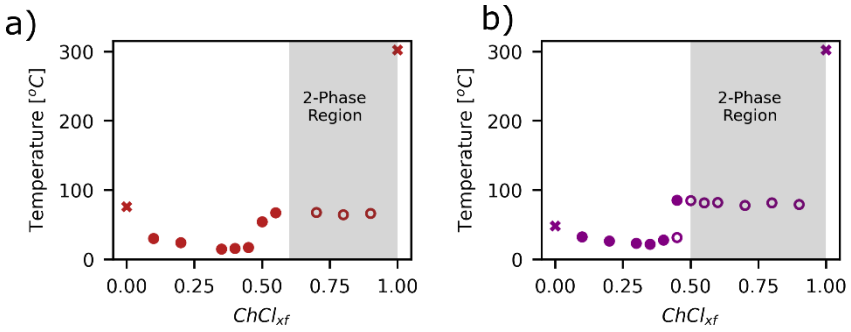

Figure 3.5 Phase diagrams for Phenylacetic Acid (a) and 3-Phenylproprionic Acid (b). The filled circular markers indicate measurements obtained using the PhasIR system, while the unfilled circles represent possible states of incongruent melting. The x-shaped markers indicate literature

The onset-melting diagrams for the two phenyl carboxylic acids can be seen in Figure 3.5 and they both also show a single eutectic temperature depression around the 35 $mol\%$ of choline chloride sample, again in line with samples synthesized using the traditional methodology. [5]

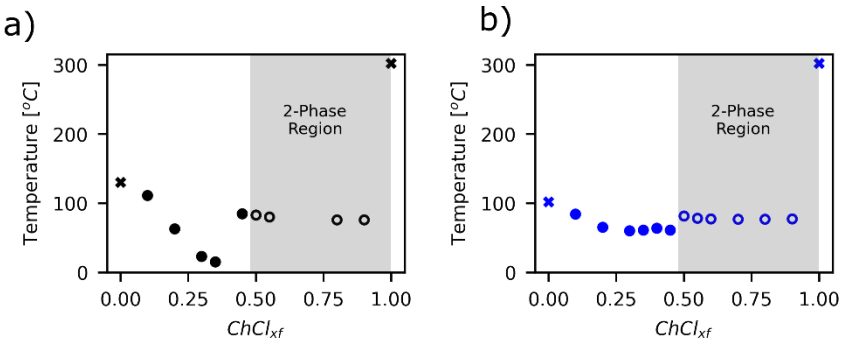

Figure 3.6 Phase diagrams for urea (a) and N,N'-dimethylurea (b). The filled circular markers indicate measurements obtained using the PhasIR system. The x-shaped markers indicate literature

On the other hand, the diagram for N, N'-dimethylurea seems to show a broad low-melting point region followed by a flat two-phase melting region. Unfortunately, it was not possible to measure transition temperature below 0℃ in high-throughput with the PhasIR system due to hardware limitation. Therefore, the diagram for ethylene glycol and glycerol DES could not be obtained as the melting temperature is much lower than can be reliably measured with PhasIR. All the melting diagrams also show complex melting behavior at higher content of QAS. At values above ~55 $mol\%$ of the QAS, there is usually phase separation between a solid QAS dispersion and a mixed QAS/HBD liquid phase as seen in Figure 3.4.

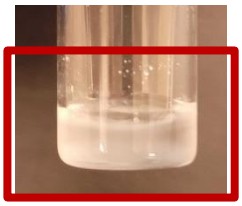

Figure 3.7 Sample composed of the 80 $mol\%$ Choline Chloride with Acetamide. The sample was heated using a hotplate and formed an opaque solution, which is a sign of formation of two phases.

Table 3.2 shows a comparison of the eutectic temperatures measured using the PhasIR system with those reported in the literature. Agreement is generally excellent, with most measurements within ~5°C. Only the DES samples formed between choline chloride and

acetamide and phenylacetic acid, both at a 1:2 ratio (QAS: HBD), show lower values compared to their respective published values. This could again be due to moisture or residual water in the hygroscopic samples, which is known to depress the melting points of DES. Other results obtained for choline chloride samples synthesized using the high-throughput protocol are in great agreement with published values. This supports the use of this high-throughput workflow to investigate the melting temperatures of DES.

Table 3.2 Choline Chloride-based DES Melting point comparison between literature values and those measured in the current publication using the PhasIR system

Ratio	HBD	Current Publication	Literature Values	Source
		[°C]	[°C]	[–]
1:2	Urea	15	12	[48]
1:2	N, N'-Dimethylurea	63.3	70	[48]
1:2	Acetamide	27.5	50	[48]
1:2	Phenylpropionic Acid	21.6	20	[5]
1:2	Phenylacetic Acid	14.5	25	[5]
1:1	Xylitol	3.6	RT	[49]

The ability to screen and identify DES electrolytes in a high-throughput manner with high ionic conductivities and wide electrochemical potential windows is crucial to their performance optimization. However, most electrochemical measurements are still conducted with bulky electrodes and relatively large samples (~10 mL is typical) that are not conducive for screening large design spaces. In this work, we use screen printed electrodes (SPE) that require minimal sample volume (~150 μL) and are ideal for conducting measurements of multiple samples in very short periods of time ($\sim 7\ min/sample$) for all three electrochemical measurements conducted. These SPEs can be interfaced directly with standard electrochemical equipment, converting them into a high-throughput platform for parallel data collection and batch analysis. The DES synthesized in the high-throughput process were then characterized by this high-throughput

electrochemical setup. Once again, only samples that were found to be liquid at room temperature, $(19 - 24\ ℃)$ were characterized. In this case, the 'liquid at room temperature' constraint for the electrochemical charaterization was only enforced in the current workflow due to testing lmitations of the high-throughput set up.

Looking at literature studies of the electrochemical properties of DES, there is still a significant gap in data for DES based on QASs that are not ChCl. Figure 3.8a shows the measured ionic conductivities for the ChCl-based DES and analogous. From the graph, it can be noticed that with greater concentrations of ionic species there is an increase in conductivity, which has been proposed for all DES. [50] It is again important to make a comparison with available literature values for this property to ensure that the sample characterization is correctly implemented in the high-throughput workflows. Table 3.3 summarizes the conductivities of the 1:2 ChCl:HBD samples. In this case, it can be noticed that samples containing ChCl and ethylene glycol, phenylacetic acid or phenylpropionic acid as the HBD, our measurements show similar values to published ones. [5,51,52] On the other hand, the urea- and glycerol-based DES we formulated show elevated conductivities. The increase in conductivity could be due to moisture absorbed from the environment or to residual water from the synthesis process. However, there are discrepancies among literature values for the ChCl-urea DES. [5,52] In fact, even though reported quantities are measured at slightly different temperatures, they differ by an order of magnitude. The values we obtain using the MAP-based workflow are closer to those from Shah et al., while still being higher. [52] Still, there is generally good agreement between conductivities of DES samples produced via our high-throughput workflow and most published results of similar compositions.

Table 3.3 Conductivity measurements of Choline Chloride-based DES and their comparison with reported literature values.

QAS	HBD	Ratio	Literature Values	Current Publication

			Temp	Conductivity	Source	Temp	Conductivity	QAS_{xf}
			[℃]	mS/cm	[−]	[℃]	mS/cm	[−]
ChCl	Phenylacetic acid	1:2	25	0.48	[5]	19-24	0.67	0.35
ChCl	Phenylpropionic acid	1:2	25	0.32	[5]	19-24	0.42	0.3
ChCl	Urea	1:2	30	2.31	[52]	19-24	3.5	0.35
ChCl	Urea	1:2	25	0.75	[5]			
ChCl	Ethylene Glycol	1:2	20	7.61	[51]	19-24	7.32	0.35
ChCl	Ethylene Glycol	1:2	25	7.33	[52]			
ChCl	Glycerol	1:2	20	1.05	[51]	19-24	2.55	0.35
ChCl	Glycerol	1:2	25	1.18	[5,45]			
ChCl	Glycerol	1:2	25	1.75	[52]			
AcChCl	Urea	1:2	40	0.017	[5]	19-24	0.417	0.35

Figure 3.8b shows the measured potential window for the Table 3.3ChCl-based DES and analogous. Current battery electrolytes are mainly based on aqueous solutions, which have operating voltage windows of approximately ~1.23 V, limited by water electrolysis.[53]

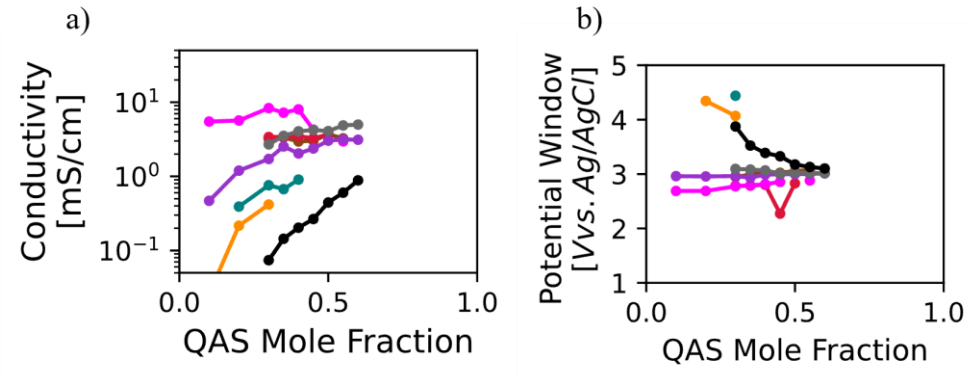

Figure 3.8 Electrochemical measurements of ChCl-based DES and analogous as a function of the QAS mole fraction. a) Plot of ionic conductivity extracted from potentiostatic electrochemical impedance spectroscopy measurements. b) Potential window obtained from chronopotentiometry

ChCl-DES electrolytes tested here show stable potential windows that are at least twice as high as standard aqueous ones (range of 2.5 V to 4.6 V). Once again, due to the lack of diversity in DES composition published in the literature, it is only possible to compare results for samples prepared with choline chloride. Samples in the DES and analogous prepared using the non-traditional

workflow present slightly smaller stable electrochemical potential windows (EPW), when compared to those reported by Li et al. [54] This could again be due to the presence of trace amounts of moisture and/or residual water in the samples that are very hygroscopic. Nevertheless, the potential windows presented in this study compare reasonably well to those reported in the literature for other DES systems, Table 3.4.

Table 3.4 Electrochemical Potential Window (EPW) measurements of Choline Chloride-based DES and their comparison with reported literature values from Li et al. [54]

QAS	HBD	Ratio	Literature Values			Current Publication				
			E_A	E_C	EPW	Temp	E_A	E_C	EPW	QAS_{xf}
			$[V]$	$[V]$	$[V]$	[°C]	$[V]$	$[V]$	$[V]$	$[-]$
ChCl	Urea	1:2	1.54	-2.75	4.29	RT	1.23	-1.85	3.08	0.35
ChCl	EG	1:2	1.26	-2.35	3.61	RT	1.13	-1.66	2.79	0.35
ChCl	Glycerol	1:2	1.38	-2.21	3.59	RT	1.15	-1.78	2.99	0.35
ChCl	Xylitol	1:2	1.66	-2.67	4.33	RT	1.29	-2.23	3.52	0.35

3.3.2 *New DES and Analogous Combinations*

Several samples based on acetylcholine chloride, tetraethylammonium chloride, and tetrapropylammonium bromide as their quaternary ammonium salt results liquid at room temperature and were characterized by their electrochemical properties. Figure 3.9 shows the ionic conductivities of the remaining DES and analogous electrolytes. It is evident that variations in the molar composition in the DES with respect to the QAS and HBD components greatly affect their conductivity, which is related to changes in viscosity and concentration of ionic species.

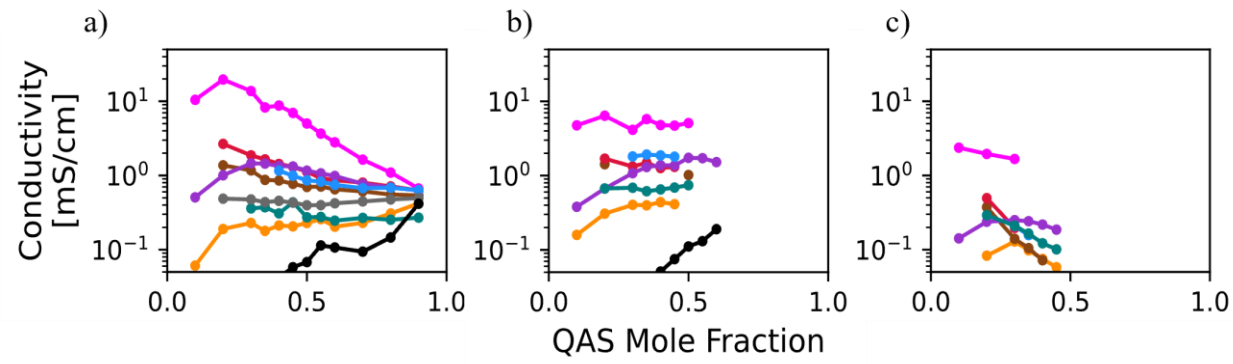

Figure 3.9 Plots of ionic conductivity of DES electrolytes extracted from potentiostatic electrochemical impedance spectroscopy measurements. a) Acetylcholine Chloride (AcChCl), b) Tetraethylammonium Chloride (TEAC), c) Tetrapropylammonium Bromide (TPAB)

The highest conductivities were found in ethylene glycol-based DES, independently of the QAS used, among the combinations tested. The sample at 20 mol % AcChCl having the highest conductivity in the entire dataset at 13.7 mS/cm. Compared to published values of ionic conductivities for DES, this seems to be the highest recorded for this class of materials. In fact, the largest reported conductivity found was for the (3:7) choline chloride-imidazole DES at 12 mS/cm (333K).[55] Conductivities for ethylene glycol-based DES with ChCl, TEAC and TPAB were also relatively large with maximum conductivities of approximately 8.3 mS/cm, 6.4 mS/cm and 2.4 mS/cm, respectively. Typically, DESs based on ethylene glycol are known for possessing relatively high conductivities, as the viscosity of ethylene glycol is very low, and it is one of the few components found in the liquid state in its pure form. On the opposite end, samples based on xylitol possessed the lowest conductivities in the dataset. This is in line with literature as DES with sugar based HBDs, such as xylitol, tend to have significantly higher viscosities. [56] The lowest conductivity recorded, a 0.001 mS/cm, is associated with the xylitol-based DES with 10 mol % TPAB. Comparing the trend of the conductivity among these two HBD extremes (ethylene glycol and xylitol), important distinctions can be made. In the sample containing the sugar HBD, the conductivity has a positive trend towards higher amounts of ammonium salts.

Even though, as previously mentioned, the ChCl DES samples seem to follow this trend, the data collected for the remaining QAS suggests that this behavior is not universal. Notably, there is a significant decrease in ionic conductivity with increasing QAS concentration for AcChCl based DES with ethylene glycol and glycerol. This possibly suggests that increased QAS concentrations result in increased viscosities, which would in turn reduce the conductivity by hindering the mobility of ions in solution. A similar trend is found in the samples based on TPAB, whereas those containing TEAC seem to remain approximately constant or have a slight increase with decrease in HBD concentration. Moreover, previous studies have noted that the conductivity of DES may evolve through a maximum. [57] This is noted particularly with ethylene glycol- and glycerol-based DES, but is also observed in AcChCl and phenylacetic acid, which exhibits a maximum conductivity at 45 mol % AcChCl. In general, most DES and analogous formulated fall within a range slightly above or below 1 mS/cm.

Looking at literature studies of the electrochemical properties of DES, there is still a significant gap in data for DES based on QASs that are not ChCl. Therefore, we are not able to directly compare our results to traditional synthesis routes for samples containing AcChCl, TEAC or TPEB as their QAS. Nonetheless, all samples synthesized using the MAP-based workflow show potential windows above 2.5 V. Within the DES and analogous samples experimentally prepared, xylitol- and phenylacetic acid-based samples show the highest variability with respect to molar composition amongst other samples. The combination between AcChCl and xylitol, shows high potential window of 4.73 V (40 mol % AcChCl), which then drops to 3.14 V at higher QAS concentrations (80 mol % AcChCl). The opposite is found in phenylacetic acid, going from 2.46 V (30 mol % AcChCl) to 3.04 V (50 mol % AcChCl). The remainder of the AcChCl:PAA samples show a relatively constant voltage. Similar trends are found when these HBDs are paired with

TEAC. It is important to note that a few samples that were shown in the conductivity measurements are not reported in the electrochemical potential window. In fact, a few combinations of QASs and HBD, particularly those containing xylitol, were so viscous that the potential required to meet the current at each galvanostatic step was outside the usable range of the potentiostat. Furthermore, we noticed that some samples (e.g., $55\ mol\ \%$ ChCl with Ethylene Glycol, TBAB and 4-Amino-1H,1,2,4-Triazole at all the mole ratios) froze during chronopotentiometry. This could indicate that their melting point was very close to the room temperature. Though only a limited number of samples were measured with TPAB, the potential windows were generally above 3V. The highest potential window measured was 4.9 V for N, N'-Dimethylurea and TPAB at 1:2 mole ratio, which is one of the highest reported in the literature. For most of the samples investigated, the value of the potential window remains approximately constant throughout sample composition for the same combinations of QAS and HBD. This is expected as the stability window of electrolytes is bounded by the electrochemical degradation of species in solution and not on their concentration.

Inspection of the CVs for the candidate electrolytes reveals insights into the correlation of their electrochemical degradation with respect to the QAS and HBD materials. In fact, it can be noted that for HBD that possess similar chemical structure, the CV curves show similar features. Looking at the voltammograms of acetamide and urea, differing only by one amine group, the presence of a peak at negative potentials (around $-1.5\ V\ vs.\ Ag/AgCl$) can be noted, Figure 3.10.

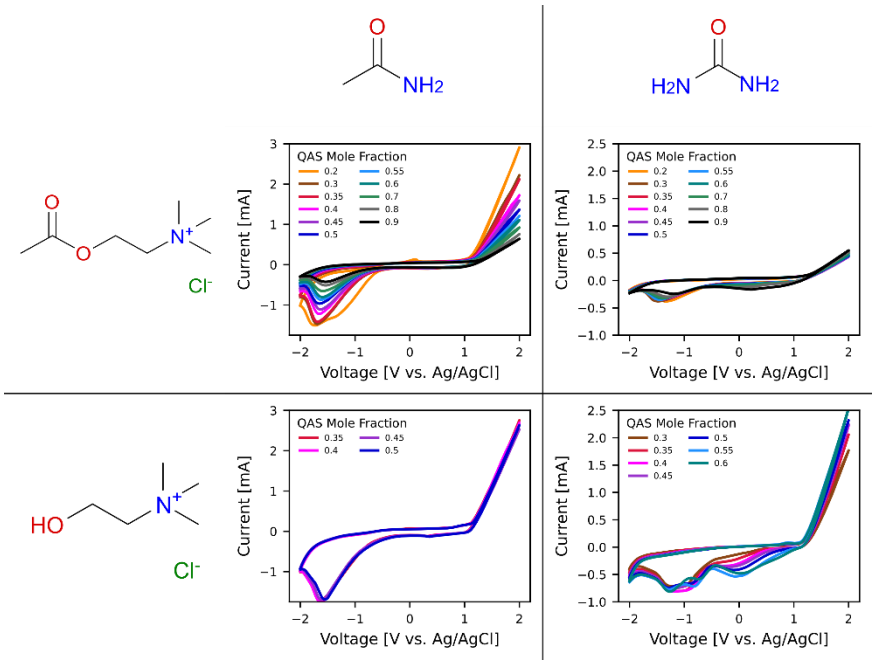

Figure 3.10 Comparison between the cyclic voltammograms of Acetamide (Left) and Urea (Right) in their combinations with Acetylcholine Chloride (Top) and Choline Chloride (Bottom). The two HBD have similar molecular structure and it is possible to show parallel between the CV features in the backward scan. The two QAS both have Chlorine as their halide anion and show similarities

Similar features on the reverse scan of the other amine-containing HBD, N, N'-dimethylurea, can be seen in Figure 3.11.

Looking at all CV collected, it can also be noted that features on the reverse scan are as dependent on the anion of the QAS in the samples. It seems that varying the halide of the QAS has an effect on shifting peak positions. For example, the large feature on the reverse scan seen for Cl^{-1} containing samples found at $0.5\,V\ vs\ Ag/AgCl$ shifts towards more negative potentials for the Br^{-} -based DES and analogous, see Figure 3.11, Figure 3.12, and Figure 3.13.

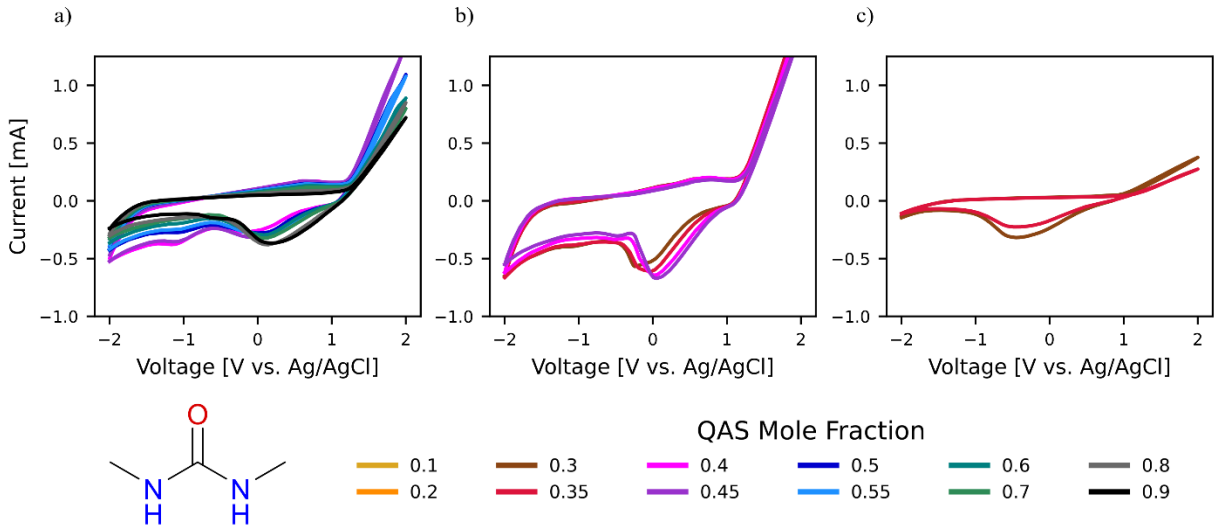

Figure 3.11 Cyclic voltammograms of N,N'-dimethylurea-based DES and analogous as a function of QAS mole fraction. For all measurement, the potential was varied from $-2V$ and $2V$ with a scan rate of $100\ mV/s$ and a total of 4 cycles per sample to ensure equilibration. The position of the feature on the backward scan seems to be dependent on the halide anion of the QAS component. a) Acetylcholine Chloride, b) Tetraethylammonium Chloride, c) Tetrapropylammonium Bromide.

The onset of the anodic limiting processing seems to also differ based on the halide species in the samples. In fact, for all samples containing Br^-, the onset of the limiting potential in the forward scan shifts towards smaller potential, slightly below $1\ V\ vs\ Ag/AgCl$. Contrastingly, for samples containing chloride ions the onset starts at values above $1.1. V\ vs\ Ag/AgCl$. This is in line with the anion's respective oxidation standard potentials. This was previously identified in other published studies involving DES based on choline chloride, where positive limits on the CV stem from the oxidation of Cl^- ions. [58,59] However, studies from Sinclair et al., have also proposed that the reactions at the anode could also be attributed to alcohol oxidation of choline cation. [60] while this could not be excluded, the fact that the limiting processes at positive voltage, regardless of cation salt structure, arise around the same voltage, is more in line with the proposed oxidation of halide salts. In fact, acetylcholine chloride and the alkyl-functionalized ammonium salts also show this feature, while not possessing an alcohol moiety. Sinclair et al, have also investigated reactions

happening at the cathode side. In this case, they indicate the formation of H_2 gas, which could be due to trace amounts of water in the samples and the dehydration of the choline cation. Haerens et al., have also looked into a possible cathodic decomposition reaction of the quaternary ammonium salt. In this case, they propose the formation of radical species. [58] The disparities between these studies shows limited understanding of the processes that limit the potential window of these solvents. This prompts further research and characterization, which could be enabled with the presence of a larger number and broader diversity of data on these designer solvents.

Figure 3.12 and Figure 3.13 depict the voltammograms obtained from the two of the polyol-based DES and analogous, again reinforcing the relationship between HBD structure and CV features on the reverse scan. On the other hand, it is noted that changing the cation component of the quaternary ammoniums salt does not seem to have an influence on the features present in the cyclic voltammograms.

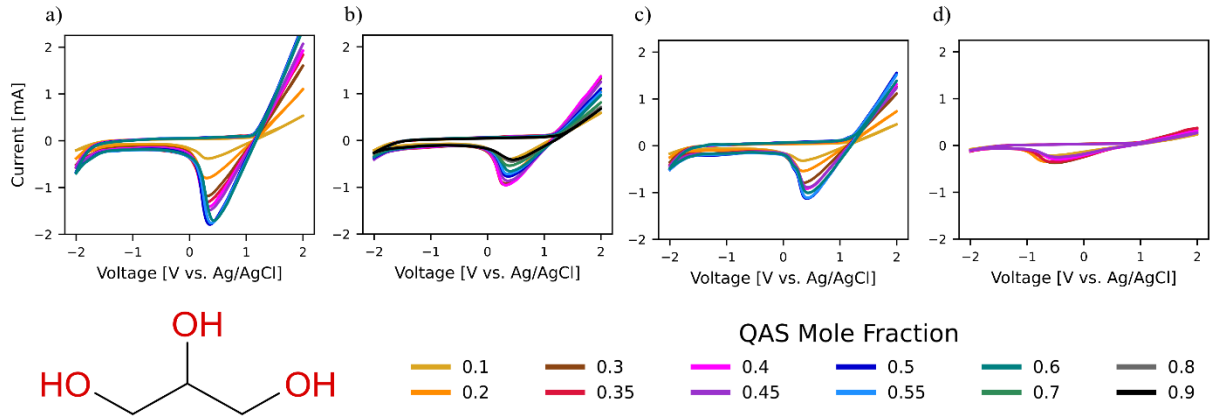

Figure 3.12 Cyclic voltammograms of Glycerol-based DES and analogous as a function of QAS mole fraction. For all measurement, the potential was varied from $-2V$ and $2V$ with a scan rate of 100 mV/s and a total of 4 cycles per sample to ensure equilibration. The position of the feature on the backward scan seems to be dependent on the halide anion of the QAS component. a) Choline Chloride, b) Acetylcholine Chloride, c) Tetraethylammonium Chloride, d) Tetrapropylammonium

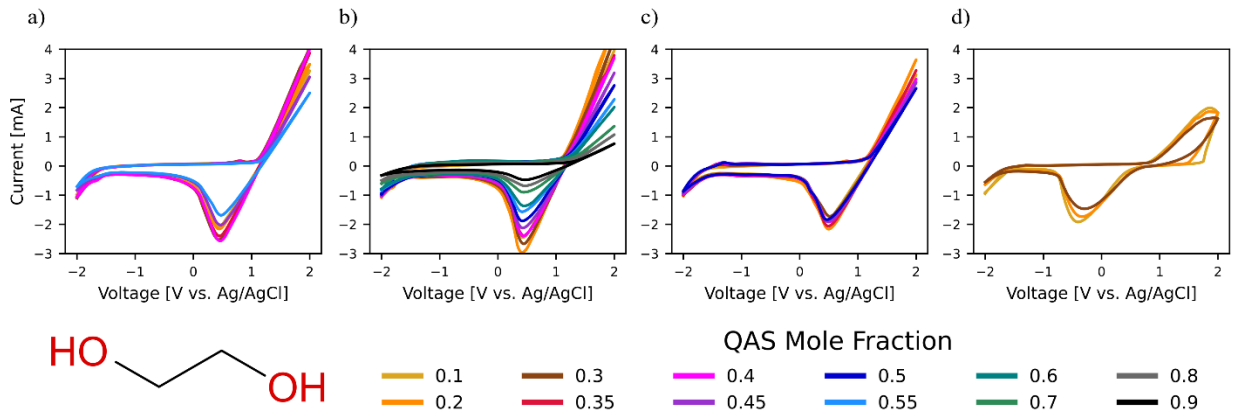

Figure 3.13 Cyclic voltammograms of Ethylene Glycol-based DES and analogous as a function of QAS mole fraction. For all measurement, the potential was varied from $-2V$ and $2V$ with a scan rate of $100\,mV/s$ and a total of 4 cycles per sample to ensure equilibration. The position of the feature on the backward scan seems to be dependent on the halide anion of the QAS component. a) Choline Chloride, b) Acetylcholine Chloride, c) Tetraethylammonium Chloride, d)

Finally, another interesting feature of the CV data is the variation in the slope of the limiting processes (e.g., see Figure 3.13). This quantity seems to have a dependence on the molar composition of the DES samples. To further look into this behavior, the slope at both anodic and cathodic limits were extracted and, when plotted against the QAS mole fraction, the data seem to follow trends matching those of the sample's conductivity (compare Figure 3.9 with Figure 3.14).

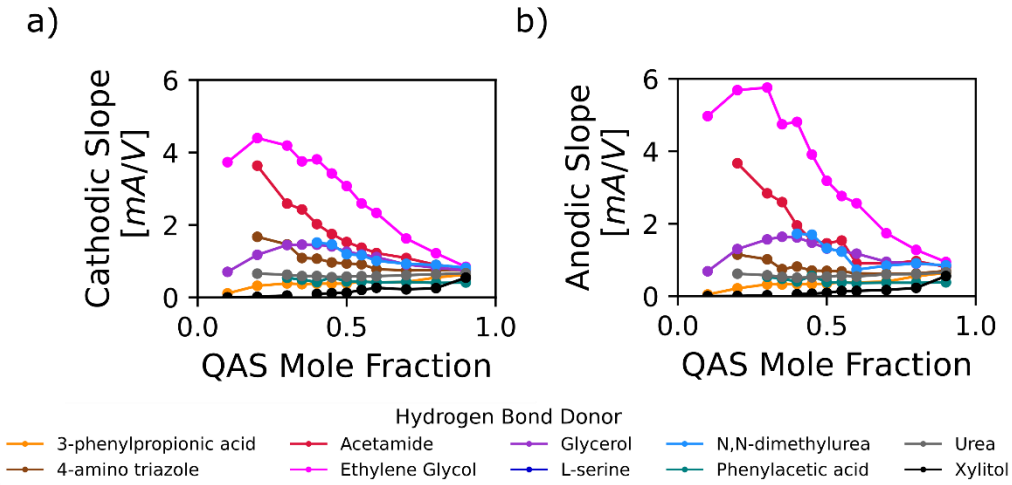

Figure 3.14 Limiting slope extracted from the cyclic voltammograms of Acetylcholine Chloride. The trend of these limiting steps seems to be similar to the conductivity data for the sample DES formulation, Figure 7b. a) Cathodic slope. b) Anodic slope

The similarity between the data suggests that the limiting processes of cyclic voltammetry are conductance limited. Even though the CV data shows features in its reverse scan, these can be avoided by reducing the upper limit of the voltage range in the measurement itself. This change was not implemented in this study as maintaining the same CV parameters was important to allow for parallel and high-throughput measurements between different DES sample conditions and compositions.

Looking at the combined experimental results, some general trends start to emerge. Samples containing AcChCl as their QAS show a very low melting point and most were found to be liquid at room temperature ($19 - 24$ ℃). Even though ChCl has a smaller cation structure, the addition of the acetyl functional group increases the asymmetry of the cation species and decreases the melting point of the salt (i.e., $146 - 150$℃, compared to 302 ℃ for ChCl).[61,62] This confirms that, for pure species with lower melting temperatures, the resulting DES are more likely to be liquid at lower temperatures. Yet even though TPAB melts at 270 ℃, it has a very limited number

of liquid samples when compared to those formulated using ChCl or TEAC, despite their higher melting points. This could be attributed to the influence of the Br^- anion. [63,64] In fact, it is known that DES form a complex solvation environment where, for Type III DES, the strongest interactions are between the halide species and the hydrogen bonding sites of both the HBD and the cation species of the QAS. [2,65] This can help explain why changing the halide from chlorine to iodine, while maintaining the cation structure intact, did not produce any liquid samples at room temperature.

Additionally, it was shown that for certain combinations of DES precursor materials, there can be a wide range of compositions that yield liquid samples at room temperature. While some of the measured electrochemical properties seem to not change with respect to the composition of the sample (i.e., potential window), others have a stronger relationship to the ratio of QAS/HBD and the molecular structure of the species. For example, these DES-based electrolytes tend to be electrochemically limited by viscosity, both in the conductivity and in the limiting processes on the CV. However, for the same combination of QAS and HBD, there are several samples which exhibit high conductivities, broad potential window and show electrochemical stability. This further motivates their potential use in energy-related applications. Moreover, it is important to also study DES systems outside of their eutectic point as it can help to understand the complex relationships between molecular structures, solvation, and transport coefficients (i.e., viscosity, diffusivity). This will also allow us to build better predictive models for DES materials, and to advance their design and application as green solvents. In fact, there are likely practical situations in which more favorable properties exist at compositions that fall outside of the eutectic point. Without more comprehensive studies of DES materials, advancement and practical applications will be hindered. The traditional route for the formulation of these solvents is prohibitively slow

and cumbersome to study their vast molecular design space. Thus, data-driven design of experiments, coupled with high-throughput workflows for synthesis and characterization are essential for their advancement. The results from the current and any subsequent experimental campaigns can also be integrated in the selection of new molecules, moving the workflow towards a closed-loop system for new material discovery in the field of deep eutectic solvents. This strategy can be used to both validate the initial selection of candidate molecules, as well as to build a more diverse and complete database of DES properties.

3.4 Conclusion & Future Directions

Deep eutectic solvents are considered inexpensive designer solvents with great appeal as electrolytes for energy-related applications thanks to their low-cost, green environmental footprint, wide potential window, and adequate ionic conductivity. Despite these benefits, identifying optimal DES is a challenging task due to the massive molecular design space that is associated with these materials. High-throughput and data-driven strategies provide an avenue towards developing DES electrolytes designed specifically for target applications. After selecting candidate molecules through a cheminformatic campaign, DES were then synthesized in high-throughput, to complete an experimental campaign spanning 50 QAS/HBD combinations and 12 molar ratios for a total of 600 unique samples. The systematic characterization of such a large number of DES-candidates is valuable and unique in the current literature, where data on DES electrolytes is still scarce and overwhelmingly focused on choline chloride samples. Importantly, the high-throughput electrochemical characterization reported in this chapter also identified promising electrolyte candidates with wide electrochemical potential windows (over 3 V) and ionic conductivities above 1 mS/cm. This suggests that there are likely numerous promising electrolyte materials within the vast molecular design space of DES that remain to be discovered.

While efforts to move this work closer towards an automated closed loop system are still underway, the methods outlined in this study could quickly increase the DES data that is available and openly shared for use with advanced statistical methods. Future work could focus on generating predictive Quantitative Structure-Property Relationship (QSPR) models to better understand which molecular features lead to ideal DES properties, as seen in Halder et al. [66] The use of advanced methods to predict DES properties from molecular features and formulation parameters will become essential elements in future investigations aiming to efficiently sample DES candidates. In addition, methods outlined in this chapter can also be extended beyond the analysis of DES-based electrolytes and can provide some inspiration for approaching other materials design problems with large design spaces. The MAP-based workflow showcased in this chapter could be implemented for the study of other systems where the thermodynamics of mixtures play an important role such as microemulsions, especially for drug delivery applications, or the phase transition temperature of lipid systems. Embracing these data-driven strategies and the use of low-cost, automatic, and open-source robotic systems will make the incorporation of AI-driven algorithms and iterative exploratory campaigns into the design of experiments (DoE) much more accessible to the scientific community. This will allow more efficiently learn these materials properties, which will facilitate the design of DES electrolytes with optimum properties or other multivariate material design spaces.

Given the appealing properties of these designer solvents, there has been recent efforts in incorporating them into redox flows batteries (RFBs) for the design of inorganic-base grid level energy storage systems. In the context of RFBs, there's also been a push for greener redox active species, such as redox-active organic molecules (ROMs), to replace expensive and resource limited earth metals currently in use. ROMs have low solubility in aqueous solvents, which limits

their current use. However, there have reports showing increased solubility of redox species in DES, which subsequently lead to increases in energy density capabilities and improved battery performance. [67,68] This topic will be the focus of Chapter 4.

3.5 REFERENCES

1. Martins, M. A. R., Pinho, S. P. & Coutinho, J. A. P. Insights into the Nature of Eutectic and Deep Eutectic Mixtures. *J Solution Chem* **48**, 962–982 (1234).
2. Smith, E. L., Abbott, A. P. & Ryder, K. S. Deep Eutectic Solvents (DESs) and Their Applications. *Chem Rev* **114**, 11060–11082 (2014).
3. Chakrabarti, M. H. *et al.* Prospects of applying ionic liquids and deep eutectic solvents for renewable energy storage by means of redox flow batteries. *Renewable and Sustainable Energy Reviews* **30**, 254–270 (2014).
4. Ortiz-Martínez, V. M., Gómez-Coma, L., Pérez, G., Ortiz, A. & Ortiz, I. The roles of ionic liquids as new electrolytes in redox flow batteries. (2020) doi:10.1016/j.seppur.2020.117436.
5. Abbott, A. P., Boothby, D., Capper, G., Davies, D. L. & Rasheed, R. K. Deep Eutectic Solvents formed between choline chloride and carboxylic acids: Versatile alternatives to ionic liquids. *J Am Chem Soc* **126**, 9142–9147 (2004).
6. Al-Murshedi, A. Y. M., Hartley, J. M., Abbott, A. P. & Ryder, K. S. Effect of water on the electrodeposition of copper on nickel in deep eutectic solvents. *https://doi.org/10.1080/00202967.2019.1671062* **97**, 321–329 (2019).
7. Popescu, A. M., Cojocaru, A., Donath, C. & Constantin, V. Electrochemical study and electrodeposition of copper(I) in ionic liquid-reline. *Chem Res Chin Univ* **29**, 991–997 (2013).
8. Abbott, A. P., Ttaib, K. el, Frisch, G., Ryder, K. S. & Weston, D. This journal is c the Owner Societies. *Phys. Chem. Chem. Phys* **14**, 2443–2449 (2012).
9. Abbott, A. P., Ttaib, E., Frisch, G., Mckenzie, K. J. & Ryder, K. S. Electrodeposition of copper composites from deep eutectic solvents based on choline chloride. (2009) doi:10.1039/b817881j.
10. Yuan, Z., Liu, H., Yong, W. F., She, Q. & Esteban, J. Green Chemistry CRITICAL REVIEW Status and advances of deep eutectic solvents for metal separation and recovery. (2022) doi:10.1039/d1gc03851f.
11. Abbott, A. P. Deep eutectic solvents and their application in electrochemistry. *Curr Opin Green Sustain Chem* **36**, (2022).
12. Karami, B., Ghaemi, A. & Shahhosseini, S. Eco-Friendly Deep Eutectic Solvents Blended with Diethanolamine Solution for Postcombustion CO2 Capture. *Energy and Fuels* **36**, 945–957 (2022).

13. Bi, Y. *et al.* Efficient CO2 capture by a novel deep eutectic solvent through facile, one-pot synthesis with low energy consumption and feasible regeneration. *Science of the Total Environment* **705**, (2020).
14. Li, X., Hou, M., Han, B., Wang, X. & Zou, L. Solubility of CO2 in a choline chloride + urea eutectic mixture. *J Chem Eng Data* **53**, 548–550 (2008).
15. Leron, R. B. & Li, M. H. Solubility of carbon dioxide in a eutectic mixture of choline chloride and glycerol at moderate pressures. *Journal of Chemical Thermodynamics* **57**, 131–136 (2013).
16. Gu, Y., Hou, Y., Ren, S., Sun, Y. & Wu, W. Hydrophobic Functional Deep Eutectic Solvents Used for Efficient and Reversible Capture of CO2. *ACS Omega* **5**, 6809–6816 (2020).
17. Zhang, Y. *et al.* Study on CO2 absorption by novel choline chloride-diethylenetriamine-water deep eutectic solvents in a rotor-stator reactor. *Chemical Engineering and Processing - Process Intensification* **184**, 109299 (2023).
18. Makoś-Chełstowska, P. VOCs absorption from gas streams using deep eutectic solvents – A review. *J Hazard Mater* **448**, 130957 (2023).
19. García, G., Aparicio, S., Ullah, R. & Atilhan, M. Deep eutectic solvents: Physicochemical properties and gas separation applications. *Energy and Fuels* **29**, 2616–2644 (2015).
20. del Mar Contreras-Gámez, M. *et al.* Deep eutectic solvents for improved biomass pretreatment: Current status and future prospective towards sustainable processes. *Bioresour Technol* **369**, 128396 (2023).
21. Patil, S. S. & Rathod, V. K. Extraction and purification of curcuminoids from Curcuma longa using microwave assisted deep eutectic solvent based system and cost estimation. *Process Biochemistry* **126**, 61–71 (2023).
22. Gurkan, B., Squire, H. & Pentzer, E. Metal-Free Deep Eutectic Solvents: Preparation, Physical Properties, and Significance. *J. Phys. Chem. Lett* **10**, 26 (2019).
23. Holbrey, J. D ; Seddon, K. R. Ionic Liquids. *Clean Technol. Environ. Policy* **1**, 223–236 (1999).
24. Kaul, M. J., Qadah, D., Mandella, V. & Dietz, M. L. Systematic evaluation of hydrophobic deep-melting eutectics as alternative solvents for the extraction of organic solutes from aqueous solution. *RSC Adv* **9**, 15798–15804 (2019).
25. Haghbakhsh, R., Parvaneh, K., Raeissi, S. & Shariati, A. A general viscosity model for deep eutectic solvents: The free volume theory coupled with association equations of state. *Fluid Phase Equilib* **470**, 193–202 (2018).
26. Lloret, J. O., Vega, L. F. & Llovell, F. Accurate description of thermophysical properties of Tetraalkylammonium Chloride Deep Eutectic Solvents with the soft-SAFT equation of state. *Fluid Phase Equilib* **448**, 81–93 (2017).
27. González De Castilla, A., Bittner, J. P., Müller, S., Jakobtorweihen, S. & Smirnova, I. Thermodynamic and Transport Properties Modeling of Deep Eutectic Solvents: A Review

on gE-Models, Equations of State, and Molecular Dynamics. *J Chem Eng Data* **65**, 943–967 (2020).
28. Dean, W., Klein, J. & Gurkan, B. Do Deep Eutectic Solvents Behave Like Ionic Liquid Electrolytes? A Perspective from the Electrode-Electrolyte Interface. *J Electrochem Soc* **168**, 026503 (2021).
29. Matsuda, S., Nishioka, K. & Nakanishi, S. High-throughput combinatorial screening of multi-component electrolyte additives to improve the performance of Li metal secondary batteries. *Sci Rep* **9**, 1–3 (2019).
30. Cheng, L. *et al.* Accelerating Electrolyte Discovery for Energy Storage with High-Throughput Screening. *Journal of Physical Chemistry Letters* vol. 6 283–291 Preprint at https://doi.org/10.1021/jz502319n (2015).
31. Sun, S. *et al.* Accelerated Development of Perovskite-Inspired Materials via High-Throughput Synthesis and Machine-Learning Diagnosis. *Joule* **3**, 1437–1451 (2019).
32. Whitacre, J. F. *et al.* An Autonomous Electrochemical Test Stand for Machine Learning Informed Electrolyte Optimization. *J Electrochem Soc* **166**, A4181 (2019).
33. Cummins, D. J. & Bell, M. A. Integrating Everything: The Molecule Selection Toolkit, a System for Compound Prioritization in Drug Discovery. *J. Med. Chem* **59**, 7010 (2016).
34. Nicolaou, C. A. & Brown, N. Multi-objective optimization methods in drug design. *Drug Discov Today Technol* **10**, (2013).
35. Cruz-Monteagudo, M., Borges, F. & Cordeiro, M. N. D. S. Desirability-Based Multiobjective Optimization for Global QSAR Studies: Application to the Design of Novel NSAIDs with Improved Analgesic, Antiinflammatory, and Ulcerogenic Profiles. (2008) doi:10.1002/jcc.20994.
36. Rodriguez, J., Politi, M., Adler, S., Beck, D. & Pozzo, L. High-throughput and data driven strategies for the design of deep-eutectic solvent electrolytes †. *Mol. Syst. Des. Eng* **7**, 933–949 (2022).
37. Rodriguez, J. Next Generation Materials and Strategies for the Advancement of Redox-Flow Batteries. (University of Washington, 2021).
38. formlabs. FLHTAM02- High Temp Resin. Preprint at (2020).
39. Ibrahim, R. K. *et al.* Physical properties of ethylene glycol-based deep eutectic solvents. *J Mol Liq* **276**, 794–800 (2019).
40. Gurkan, B., Squire, H. & Pentzer, E. Metal-Free Deep Eutectic Solvents: Preparation, Physical Properties, and Significance. *Journal of Physical Chemistry Letters* **10**, 7956–7964 (2019).
41. Rodriguez, J. *et al.* PhasIR: An Instrumentation and Analysis Software for High-throughput Phase Transition Temperature Measurements. *Journal of Open Hardware* **5**, (2021).
42. Politi, M. & Rodriguez, J. phasIR: Python modules for high-throughput measurement of melting point using IR bolometry. *GitHub* https://github.com/pozzo-research-group/phasIR (2021).

43. Murbach, M. D., Gerwe, B., Dawson-Elli, N. & Tsui, L.-K. impedance.py: A Python package for electrochemical impedance analysis. doi:10.21105/joss.02349.
44. Maugeri, Z. & Domínguez De María, P. Novel choline-chloride-based deep-eutectic-solvents with renewable hydrogen bond donors: Levulinic acid and sugar-based polyols. *RSC Adv* **2**, 421–425 (2012).
45. Abbott, A. P., Capper, G., Davies, D. L., Rasheed, R. K. & Tambyrajah, V. Novel solvent properties of choline chloride/urea mixtures. *Chemical Communications* 70–71 (2003) doi:10.1039/b210714g.
46. Abbott, A. P. *et al.* Glycerol eutectics as sustainable solvent systems. *Green Chemistry* **13**, 82–90 (2011).
47. Shahbaz, K., Mjalli, F. S., Hashim, M. A. & Al Nashef, I. M. Using deep eutectic solvents for the removal of glycerol from palm oil-based biodiesel. *Journal of Applied Sciences* vol. 10 3349–3354 Preprint at https://doi.org/10.3923/jas.2010.3349.3354 (2010).
48. Abbott, A. P., Capper, G., Davies, D. L., Rasheed, R. K. & Tambyrajah, V. Novel solvent properties of choline chloride/urea mixtures †. (2002) doi:10.1039/b210714g.
49. Biernacki, K., Souza, H. K. S., Almeida, C. M. R., Magalhães, A. L. & Goncąlves, M. P. Physicochemical Properties of Choline Chloride-Based Deep Eutectic Solvents with Polyols: An Experimental and Theoretical Investigation. *ACS Sustain Chem Eng* **8**, 18712–18728 (2020).
50. Abbott, A. P., Harris, R. C. & Ryder, K. S. Application of hole theory to define ionic liquids by their transport properties. *Journal of Physical Chemistry B* **111**, 4910–4913 (2007).
51. Abbott, A. P., Harris, R. C. & Ryder, K. S. Application of hole theory to define ionic liquids by their transport properties. *Journal of Physical Chemistry B* **111**, 4910–4913 (2007).
52. F.S. Ghareh Bagh, K. Shahbaz, F.S. Mjalli, I.M. AlNashef, M. A. H. Electrical conductivity of ammonium and phosphonium based deep eutectic solvents: Measurements and artificial intelligence-based prediction | Elsevier Enhanced Reader. *Fluid Phase Equilib* **356**, 30–37 (2013).
53. Chalamala, B. R. *et al.* Redox flow batteries: An engineering perspective. *Proceedings of the IEEE* **102**, 976–999 (2014).
54. Li, Q. *et al.* The electrochemical stability of ionic liquids and deep eutectic solvents. *Sci China Chem* **59**, 571–577 (2016).
55. Hou, Y. *et al.* Novel binary eutectic mixtures based on imidazole. *J Mol Liq* **143**, 154–159 (2008).
56. López, N., Delso, I., Matute, D., Lafuente, C. & Artal, M. Characterization of xylitol or citric acid:choline chloride:water mixtures: Structure, thermophysical properties, and quercetin solubility. *Food Chem* **306**, (2020).
57. García, G., Aparicio, S., Ullah, R. & Atilhan, M. Deep eutectic solvents: Physicochemical properties and gas separation applications. *Energy and Fuels* **29**, 2616–2644 (2015).

58. Haerens, K., Matthijs, E., Binnemans, K. & van der Bruggen, B. Electrochemical decomposition of choline chloride based ionic liquid analogues. (2009) doi:10.1039/b906318h.
59. Fuchs, D. *et al.* Electrochemical Behavior of Graphene in a Deep Eutectic Solvent. *Cite This: ACS Appl. Mater. Interfaces* **12**, 40948 (2020).
60. Sinclair, N. S., Shen, X., Guarr, E., Savinell, R. F. & Wainright, J. S. Electrochemical Decomposition of Primary Alcohol Groups in Deep Eutectic Solvents. *J Electrochem Soc* **168**, 106506 (2021).
61. Sigma-Aldrich. Acetylcholine Chloride; SDS A6625. 1–8 Preprint at (2021).
62. Acros-Organics. Choline Chloride ; SDS AC110290000. 1–7 Preprint at (2021).
63. Sigma-Aldrich. Tetraethylammonium Chloride ; SDS T2265. 1–9 Preprint at (2021).
64. Sigma-Aldrich. Tetrapropylammonium Brominde; SDS 225568. 1–8 Preprint at (2020).
65. Zhang, Y. *et al.* Liquid Structure and Transport Properties of the Deep Eutectic Solvent Ethaline. *J. Phys. Chem. B* **124**, 2021 (2020).
66. Halder, A. K., Ambure, P., Perez-Castillo, Y. & Cordeiro, M. N. D. S. Turning deep-eutectic solvents into value-added products for CO2 capture: A desirability-based virtual screening study. *Journal of CO2 Utilization* **58**, 101926 (2022).
67. Goeltz, J. C. & Matsushima, L. N. Metal-free redox active deep eutectic solvents. *Chemical Communications* **53**, 9983–9985 (2017).
68. Sinclair, N. S., Poe, D., Savinell, R. F., Maginn, E. J. & Wainright, J. S. A Nitroxide Containing Organic Molecule in a Deep Eutectic Solvent for Flow Battery Applications. *J Electrochem Soc* **168**, 020527 (2021).

Chapter 4. DESIGN OF ORGANIC, DEEP-EUTECTIC SOLVENTS-BASED ELECTROLYTES FOR REDOX FLOW BATTERIES

4.1 INTRODUCTION

Over the past few decades, improvements in energy technologies have allowed increased use of renewable energy sources to produce electricity. The combination of wind, solar and hydroelectric power has reached a third of the share of last year worldwide energy production. [1] These greener technologies are a key component in the reduction of greenhouse gases emission and mitigation of climate change. Unfortunately, the adaptation of low-carbon energy systems still cannot compete with traditional fossil fuel infrastructures, due to the intermittent and unpredictable nature of renewable energy sources. Grid-scale energy storage technologies can help meet the need of on-demand electricity. Among them, electrochemical energy storage systems (i.e., batteries) have been identified as a promising solution thanks to their efficiency, scalability and performance flexibility. [2] Redox flow batteries (RFBs) in particular, have shown to be the most promising solution thanks to the decoupled control of power capacity and energy storage. [3] A schematic for such a system can be found in Figure 4.1.

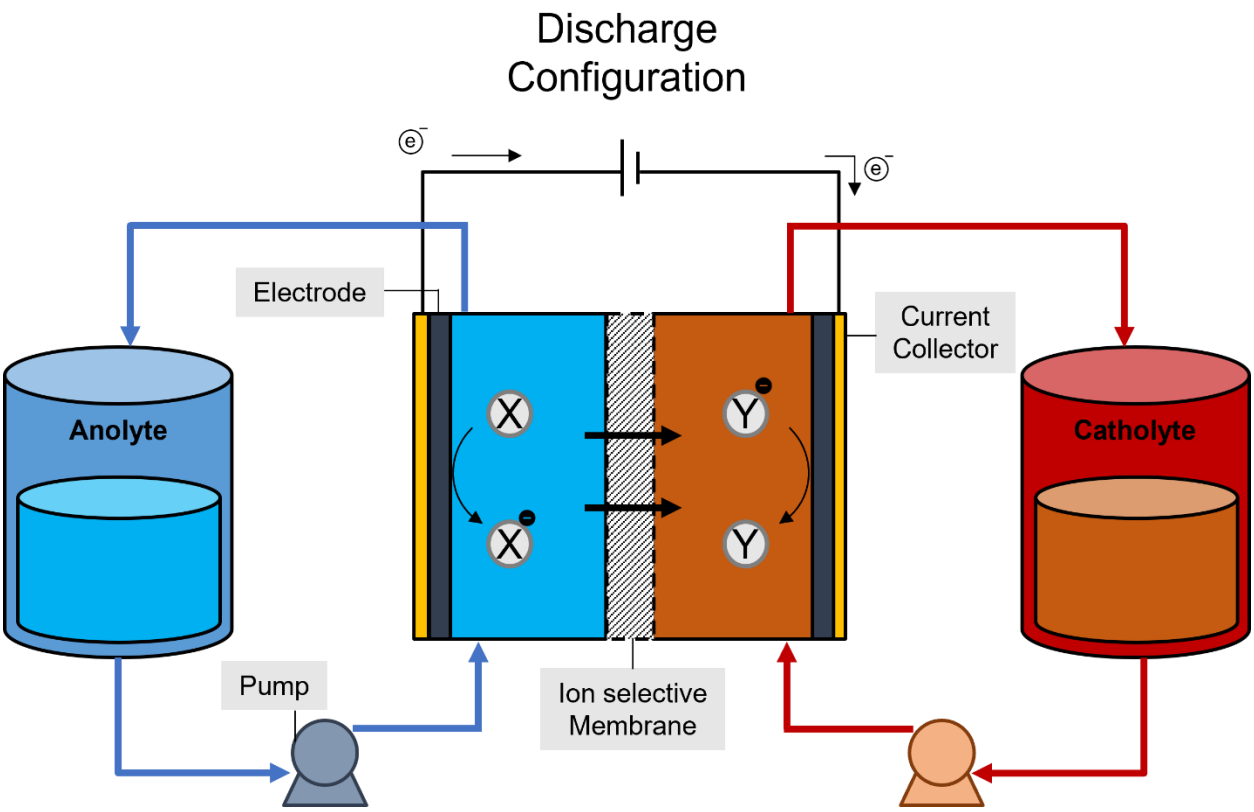

Figure 4.1 Schematic depicting a redox flow battery. The electrolyte and redox active species are store in outside tanks for the negative (anolyte) and positive (catholyte) side of the battery. These are pumped into the cell stack during the battery operations. The configuration depicted in this figure corresponds to the RFB in discharge mode.

Compared to conventional rechargeable batteries, such as lithium-ion or lead-acid based ones, which have been primarily tailored for small applications or transportation purposes, RFB offer better parameters in size scalability, durability, and stability during charge/discharge cycles.[4–8] The greater advantage of this battery technology stands in its ability to independently scale power, given by the size of the cell stack, and energy, limited by the overall active material concentration and size of external electrolyte storage tanks.[4] These features allow for a more stable storage solutions which require less maintenance and have longer service lives. The redox active materials in RFBs are found in the liquid phased electrolytes, known as anolyte and catholyte, which are stored in external reservoirs. The conversion of chemical energy into electrical one takes

place in flow-through electrodes contained in the cell. This is composed of two electrodes and an ion conductive membrane. [9] The current industry-leading system is the all-vanadium redox battery (VFB). The vanadium/vanadium couple is usually dissolved in concentrated sulfuric acid. However, the intrinsic low energy density and narrow stability window dictated by electrolysis ($\sim 1.23\ V$), coupled with concerns on the cost feasibility of the resource-limited active material and the hazards posed by its corrosive electrolyte, make their grid scale implementation limited. [6] Another factor preventing broader use of these systems is the high cost of materials of the current industry leading system based on Vanadium chemistries. In fact, these systems are still more than double ($\$250\ kWh^{-1}$) the US Department of Energy (DOE) performance target of $\$\ 100\ kWh^{-1}$ for utility applications. [10]

To mitigate these issues, research has been focused on new RFBs materials that are low-cost and more environmentally friendly. Organic electroactive species have been proposed as alternative candidates for flow batteries applications. [2,3,11–13] Organic families such as benzoquinones, 2,2,6,6-tetramethyl-1-piperidinyloxy (TEMPO), fluorenones or alkoxy benzenes have been identified as candidates of redox active materials [11,14–19]. These molecules can be easily synthesized, and their property can be tailored to the needs of their application. Their commercial availability makes them more cost effective compared to Vanadium, as molecules belonging to these families are used as dyes or are naturally occurring materials [19,20]. The selection of the redox active material for these batteries dictates their performance. In fact, factors such as the concentration of active material, the redox couple voltage difference and electrolyte can drastically impact the energy density and power density of the electrochemical storage system. In the past decade there have been several efforts demonstrating the use of these organic redox active molecules. However, the majority of these examples are still based on aqueous electrolytes. The

most common examples of ORAM are TEMPO, [16,21–24] methyl viologens, [21,24–28] , quinones, [29–31] phenazine, [16,32,33] as well as imide [34] and fluorenones. [35] Among the organic redox active materials (ORAMs) families indicated above, many of them present redox processing at negative potentials. To increase the availability of catholyte materials, there have been some efforts in the computation community to search for candidate molecules with positive redox potentials. While these examples have been promising in replacing rare earth metals in RFB systems, most of them only test electrolytes with active materials concentration at or below 0.5M, which is still not enough for improved energy density. In fact, it is known that the solubility of these organic groups is limited in water or aqueous systems. This prompted the shift towards all organic, non-aqueous RFBs. [5] The use of organic electrolytes will also allow for wider voltage ranges and increase the available design space of organic molecules that can be implemented for these energy storage systems.

As shown in Chapter 3 deep eutectic solvents are a new class of materials which have shown great potential in electrochemical applications. These solvents have also already been shown to be candidate in RFB systems as replacement for conventional organic electrolytes such as acetonitrile and propylene carbonate, which are generally toxic or flammable. In this regard, DESs have an advantage as possible candidate solvents as they are generally composed of inexpensive and widely available materials which are frequently biodegradable and non-hazardous.[36] In recent years, several studies have reported the use of DES as electrolytes in RFBs, however, the majority of them rely on metallic active species, including the use of choline chloride ethylene glycol -based DES as the electrolyte for an all copper RFB or in a zinc/cerium RFB. [37] In the last few years, there's also been examples of organic active materials being coupled with DES. Currently, systems have been focused on the use of TEMPO and its functionalization, quinones

and anthraquinones, but these systems generally tested either low concentrations of active species ($\leq 10mM$) or included water in their electrolyte.[23,38,39]

In this chapter the focus will be to integrate several organic redox active materials into deep eutectic solvents. To do so, two strategies were evaluated. First is the formation of a ternary system in which the active material is simply added to a deep eutectic solvent. Alternatively, given the large chemical variety that these organic molecules can achieve it might be possible to use these materials as the HBD of DES. In fact, several of the commercially available ORAM already present hydrogen bonding capabilities. In either case, different considerations needed to be addressed. First, the active species needs to be soluble in the DES electrolyte in both its reduced and oxidized state. For the case of binary system, both states of the molecule need to form a low melting eutectic with the QAS component. Second, the concentration of the active materials should be high ($> 1.0\ M$). Finally, the addition or use of the ORAM in the DES should not hinder the conductivity, viscosity, and melting point of the electrolytes. Due to grant end date, the majority of the work presented in this Chapter will only include some preliminary results, but suggestions for future directions will be provided.

4.2 Materials and Methods

4.2.1 *Chemicals*

To prepare the base deep eutectic solvents, the following materials were used. Choline Chloride (ChCl) (99%) was obtained from Acros Organics (Fair Lawn, NJ). Ethylammonium chloride ($\geq 98\%$) , 2-hydroxyethylammonium chloride, Acetylcholine Chloride (AcChCl) ($\geq$ 99%) were purchased from Millipore Sigma (Burlington, MA). All QASs were dried under vacuum for 24hr upon receipt and were then stored inside an airtight desiccator to prevent

significant water uptake. 4-Amino-4*H*-1,2,4-triazole (99%) was also purchased from Millipore Sigma (Burlington, MA). Ethylene Glycol (Certified) was purchased from Fisher Scientific (Hampton, NH). Urea (Ultrapure) was purchased from Thermo Scientific (Hampton, NH). These were all used as received and required no further processing.

The selected organic redox active molecules were as follows. 4-hydroxy-TEMPO (97%), 1,2-diaminoanthraquinone (≥ 100%), 2-hydroxy-1,4-napthoquinone (97%), 9-fluorenone (98%) were all purchased from Millipore Sigma (Burlington, MA). 9-fluorenone-1-carboxylic acid (> 98%), 9-fluorenone-1-carboxylic acid (98%), 9-fluorenone-2-carboxylic acid (> 96%), and Anthraquinone-2-carboxylic acid (> 99%) were al purchased from TCI (Tokyo, Japan). All materials were used as received and required no further processing.

I want to note that throughout this chapter the following short-hand notation for the chemicals used may be implemented. ChCl: choline chloride; AcChCl: acetylcholine chloride; EAC: ethylammonium chloride; 2HEAC: 2-hydroxyethylammonium chloride; EG: ethylene glycol; 4AT: 4-amino-1,2,4-triazole; 4HOT: 4-hydroxy TEMPO; 2H14NQ: 2-hydroxy-1,4-naphtoquinone; 12DAQ: 1,2-diaminoantraquinone; 9FL: 9-fluorenone; 9FLnCA: 9-fluorenone-n-carboxylic acid.

4.2.2 *Sample Preparation*

For ternary mixtures, corresponding to a base deep eutectic solvent with the addition of an ORAM, the organic compounds were added after a homogeneous solution was obtained between the DES components. In this case, the deep eutectic solvents were synthesized following the traditional experimental procedure mentioned in the introduction of Chapter 3. The selection of the based DES to use for this preliminary study was based on the experimental campaign described in Chapter 3, by looking at those combinations of materials that achieved the highest ionic

conductivity and widest potential window. The selected DES were the following: choline chloride and ethylene glycol at a 1:2 ratio, respectively. This is also known in literature as ethaline and can also be used to connect the results of this study to the broader collection of published DES. Next, acetylcholine chloride was mixed with ethylene glycol at 1:2 and a 1:4 ratio, respectively. Finally, acetylcholine chloride was also tested in combination with 4-amino-1,2,4-triazole at a 1:2 ratio.

For binary testing, the high-throughput protocol described in Chapter 3 was used to combine a 4-hydroxy tempo with four different quaternary ammonium salts, namely choline chloride, acetylcholine chloride, ethylammonium chloride and 2-hydroxyethylammonium chloride. These were tested at 6 different mole fractions between the two DES components, Table 4.1. The MAP-based protocol was also followed for the samples processing and characterization.

Table 4.1 Mole fractions tested between 4-hydroxy tempo and the selected quaternary ammonium salt for testing binary redox-DES.

QAS_{xf}	$4HOT_{xf}$
0.1	0.9
0.2	0.8
0.3	0.7
0.35	0.65
0.5	0.5
0.65	0.35

4.2.3 *Solubility Testing*

The maximum solubility of the active material was obtained spectroscopically through UV-Vis spectroscopy as all the organic molecules tested are colored. To do so, a stock solution of known concentration was prepared for each combination of DES and ORAM tested. Table 4.2 summarizes the concentration used for each stock. Only the ethylene glycol-based DES were tested for maximum solubility due to high-viscosities of the 4AT-based one.

Table 4.2 Table of stock concentration for each ORAM tested for maximum solubility in the ethylene glycol-based DES. The dilution factor was used to create a series of 5 sequential dilution for each stock.

ORAM	Stock Concentration [mM]	Dilution Factor
4HOT	100	3
12DAQ	2.5	5
2H14NQ	10	3
9FL	10	3
9F4CA	10	3

To obtain a calibration curve relating the concentration to the sample's peak absorbance, the procedure described in Chapter 2.2.1 was followed. The maximum solubility was tested by adding the organic active molecule to 1mL of DES in a 1.5mL centrifuge tube along with a stir bar. These were stirred overnight on a stir plate and later placed in an over at 65 ℃ for 6-8 hours to ensure that the maximum solubility was achieved. If all the ORAM added completely dissolved, additional one was added, and the processing of the samples repeated. This protocol was followed for all combinations of ORAM and DES tested for ternary mixtures. Next, the samples were centrifuged for 10 minutes. The supernatant was then tested spectroscopically, and the maximum achieved concentration was obtained using the calibration curve previously obtained. The supernatant was also diluted to a factor of 10 and 100 to avoid overwhelming of the UV-Vis detector.

4.3 Preliminary Results & Discussion

4.3.1 *Solubility of ORAM in Select DES*

The solubility of the redox active species dissolved in electrolytes is among the most important properties to achieve the best battery performance. In fact, this quantity will dictate the achievable energy density of the RFB. First, the active materials were tested at concentrations of

$100mM$ in all four selected DES. These were again ChCl:EG (1:2), AcChCl:EG (1:2), AcChCl:EG (1:4), and AcChCl:4AT (1:2). Figure 4.2 shows a qualitative comparison of the samples prepared. All formed a homogeneous mixture with the addition of the organic molecules and no change in the DES melting point or physical state was noticed. This is promising for the use of these solvents in combination with organic active materials. It is notable that the 9-fluorenone-4 carboxylic acid was only fully solubilized in the acetylcholine chloride at a 1:2 ratio between ethylene glycol and 4-amino-1,2,4-triaole. The remaining DES tested with 9F4CA remained cloudy and the crystal eventually precipitated out. Furthermore, other functionalized fluorenone molecules, namely 9-fluorenone-1-carboxylic acid, 9-fluorenone-4-carboxylic acid, as well as anthraquinone-2-carboxilic acid, were also tested in AcChCl:EG (1:2) DES at $100mM$, but none of these molecules were able to be dissolved in the selected solvent. These differences seem to be based on where the functionalization is placed on the fluorenone backbone and prompt further tests.

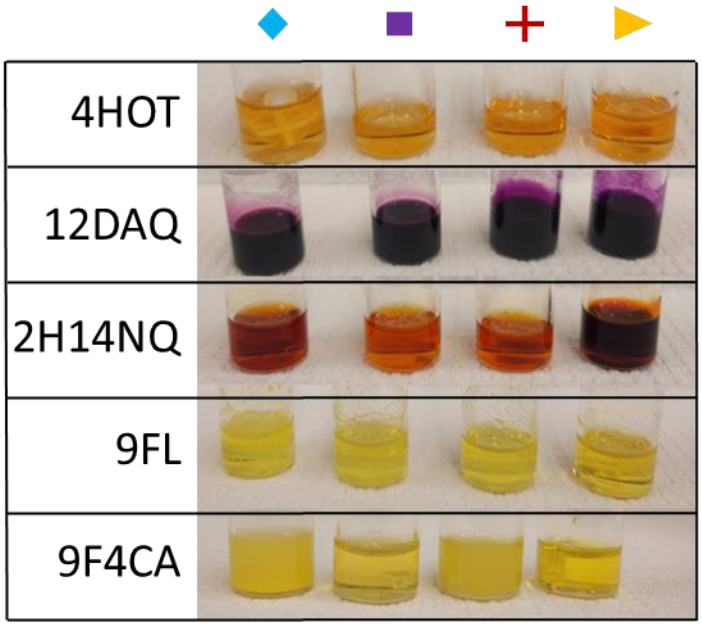

Figure 4.2 $0.1M$ solutions of the tested organic redox active molecules in the four DES tested. Diamon) ChCl:EG (1:2), Square) AcChCl:EG (1:2), Cross) AcChCl:EG (1:4), Triangle) AcChCl:4AT (1:2).

Since 4-hydroxy TEMPO has a high solubility in aqueous systems, about 2.1M, it was also tested at 0.5M and 1.0M in the three-ethylene glycol-based DES.[22] All three were able to fully solubilize the organic compound and formed uniform mixtures, Figure 4.3 shows the samples at $1M$. However, after approximately 2 days, the samples using choline chloride as its quaternary ammonium salt shows crystals in solution (see inset in Figure 4.3). A similar behavior was previously noted by Gurkan et al, where recrystallization was due to localized areas of higher concentration of choline chloride in the samples that cause the salt to re-crystalize.[40] In this case, since 4HOT is a small stable radical with hydrogen bonding capabilities, we hypothesize that it is able to be included in the complex hydrogen bonding network formed between the hydrogen bonding species and the quaternary ammonium salt. In this case, for higher concentration of the organic molecule it is possible that is creating areas on heterogeneity and forcing choline chloride to crash out. However, if the sample is placed on a hot plate in mild temperatures, ~ 40 ℃, the crystals resolubilized and the samples becomes homogeneous again. This could be a confirmation of the behavior previously noted.

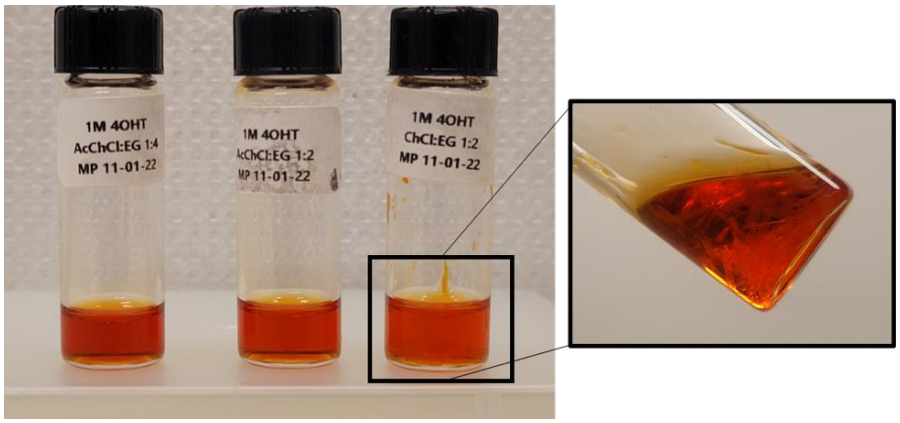

Figure 4.3 $1M$ solution of 4-hydroxy tempo in acetylcholine chloride: ethylene glycol (1:4) (left), acetylcholine chloride: ethylene glycol (1:2) (center) and choline chloride: ethylene glycol (1:2) (left). The onset highlights the presence of choline crystals in the samples. This photo was taken 3-months after the samples were originally prepared.

Additionally, it is noted that the photo depicting the samples in Figure 4.3 was taken after 3 months of the sample preparation. The acetylcholine chloride-based sample remained liquid and uniform, and the choline chloride-based sample did not fully solidify. This behavior shows promise for the use for the use of 4-hydroxy TEMPO in DES as a battery electrolyte.

Once again, the maximum solubility of the ORAM was tested for the ethylene glycol-based DES. In this case, as a comparison, the organic molecules were also dissolved in water and 0.5 $M\ NaCl_{aq}$. Figure 4.4 shows a qualitative comparison of the samples made using 4-HOT in water (B) and DES (A, C, D). In this case the sample water was not at its maximum solubility, and it is used for qualitative comparison. Once again, at these higher concentrations, the deep eutectic solvents show sign of recrystallization which is complete for the case of choline chloride (A) and only partial for the acetylcholine chloride (C, D). This is not surprising based on the behavior previously seen for the samples at $1M$. Again, after applying mild heating to the samples, a clear and uniform mixture is seen.

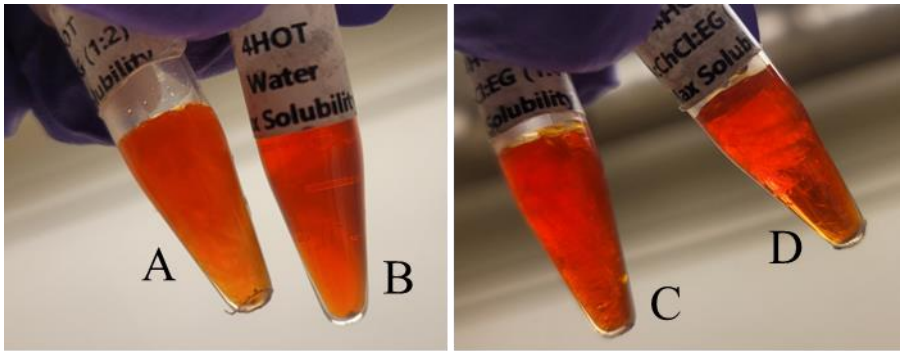

Figure 4.4 Maximum solubility of 4-hydroxy tempo in A) choline chloride: ethylene glycol (1:2), B) water, C) acetylcholine chloride: ethylene glycol (1:2) and D) acetylcholine chloride: ethylene glycol (1:4). Note that the sample in water was not at its maximum solubility and it is used for qualitative comparison.

On the other hand, Figure 4.5 show a comparison of the maximum solubility of 1,2-diaminoanthraquinone, 9-fluorenone, and 2-hydroxy-1,2-naphtaquinone. In all three panels of

Figure 4.5, the tube on the left represents samples dissolved in choline chloride: ethylene glycol (1:2), while the right tube the solvent is water. In this case, all these organic molecules are known to be poor soluble ($\leq 0.1\,mM$) or completely insoluble in water. These organic species are significantly more soluble in these aprotic systems compared to aqueous ones. In this case, no samples showed signs of recrystallization. This could be due to the significantly large size of these organic molecules compared to the TEMPO-based one.

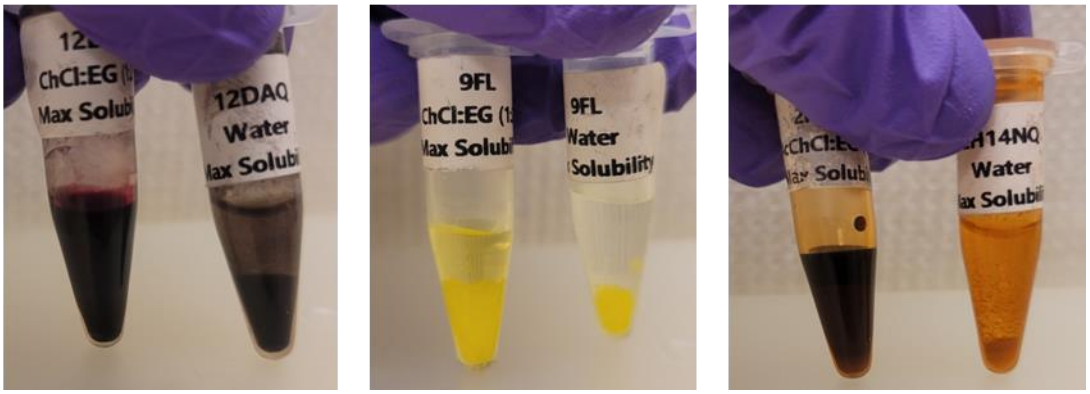

Figure 4.5 Maximum solubility of Left) 1,2-diaminoanthraquinone in DES and water, Center) 9-fluorenone in DES and water, Right) 2-hydroxy-1,2-naphtaquinone in DES and water. In all three panels, the tube on the left represents samples dissolved in choline chloride: ethylene glycol (1:2), while the right tube the solvent is water.

As mentioned previously, the maximum solubility was also quantified using UV-Vis spectroscopy and a calibration curve obtained using stock of known species concentration and their relative peak absorbance (see section 2.2.1). Figure 4.6 shows an example of absorption spectra and corresponding calibration curve for the 4-hydroxy TEMPO in AcChCl:EG at a 1:4 ratio. The maximum solubility obtained for all combinations of materials tested can be found in Table 4.3. As expected, the data follows the same trends from the qualitative assessment of the samples noted previously.

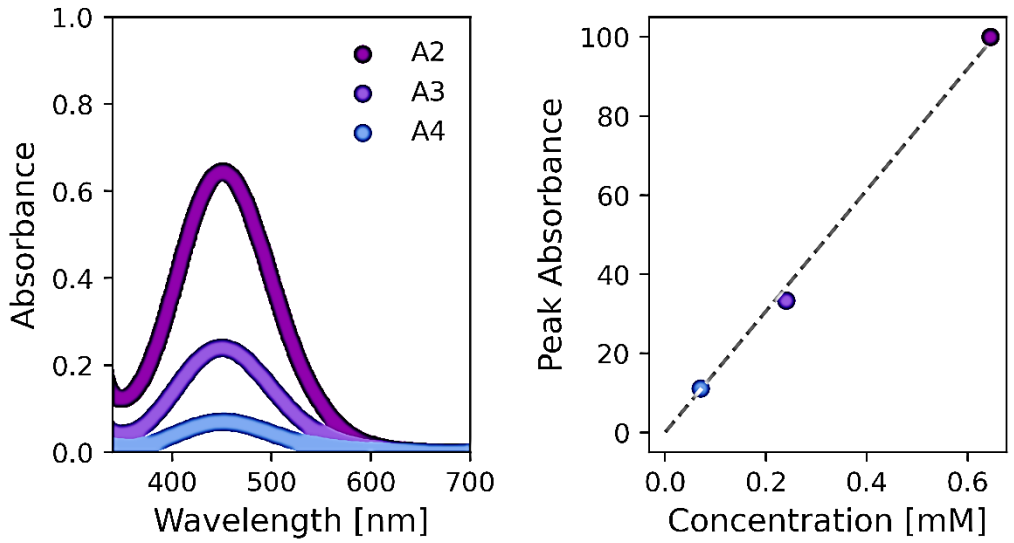

Figure 4.6 Example Uv-Vis absorption spectra for the determination of the maximum solubility of 4HOT in AcChCl:EG at a 1:4 ratio (Left) and resulting spectroscopic calibration curve (Right) obtained using *Beer's Law*.

Table 4.3 Table summarizing the maximum solubilities recorded for the tested organic redox active molecules in the 3 ethylene glycol-base DES. The maximum solubility was obtained spectroscopically.

ORAM	DES	Maximum Solubility [M]
4HOT	ChCl:EG (1:2)	3.2
	AcChCl:EG (1:2)	2.4
	AcChCl:EG (1:4)	4.2
12DAQ	ChCl:EG (1:2)	0.041
	AcChCl:EG (1:2)	0.030
	AcChCl:EG (1:4)	0.018
2H14NQ	ChCl:EG (1:2)	0.47
	AcChCl:EG (1:2)	0.31
	AcChCl:EG (1:4)	0.18
9FL	ChCl:EG (1:2)	0.071
	AcChCl:EG (1:2)	0.078
	AcChCl:EG (1:4)	0.10
9F4CA	ChCl:EG (1:2)	0.044
	AcChCl:EG (1:2)	0.078
	AcChCl:EG (1:4)	0.02

While the concentration of organic species in solution tends to be lower than $1M$, besides for the case of 4HOT, the data shows how these deep eutectic solvents can solubilize these bulky organic molecules much better than aqueous electrolytes. It might be possible to make use of additives to increase the concentration of these species in DES. However, given the large design space that these solvents belong to, it is also possible that certain combinations of hydrogen bond donors and quaternary ammonium salts could lead to increased solubilization of organic molecules.

These preliminary results on the solubility of organic redox active molecules show great promise for this class of materials in combination with these novel designer solvents. Unfortunately, no comparison with literature values can be made as these combinations of materials have not been studied. Further studies are also needed to better understand what molecular properties can lead to higher concentration of organic active species in these solvents.

4.3.2 *Electrochemical Characterization*

Given the target application for these materials, the electrochemical properties of the ORAM tested were characterized using the high-throughput protocol described in Chapter 3, as well as the same parameters unless otherwise noted. The tests were all performed at room temperature, $\sim 20℃$. Once again, the ionic conductivity was obtained by electrochemical impedance spectroscopy. Using the screen-printed electrode system. Figure 4.7 Left shows the result of the conductivity measurement for all the samples at $0.1M$ concentration of organic molecules. The addition of salt does not cause significant change in the sample's ionic conductivity. The value for the neat DES is noted on the graph (left-most markers). On the other hand, a more significant change in conductivity can be noted in Figure 4.7 Right. In this case, as more 4-hydroxy TEMPO is added, the conductivity of the sample starts to significantly decrease.

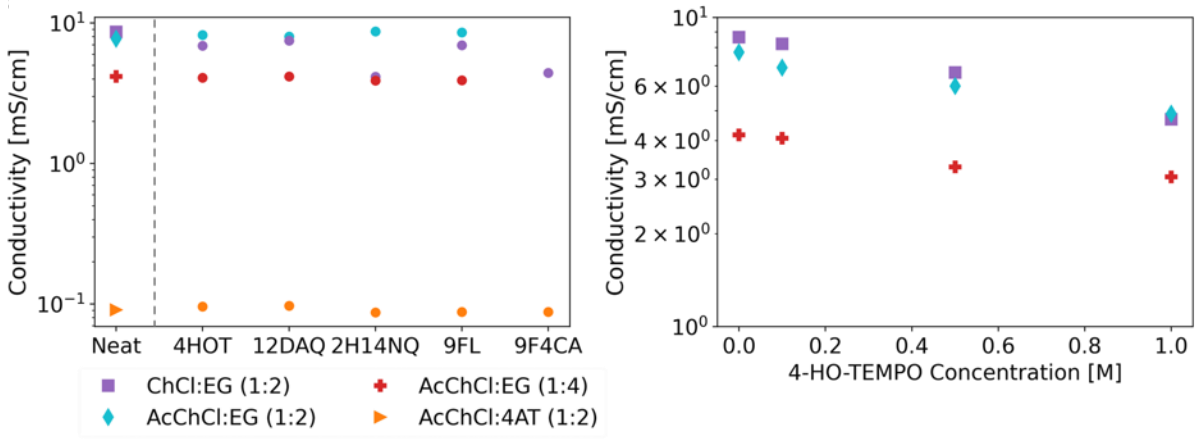

Figure 4.7 Ionic conductivity extracted using electrochemical impedance spectroscopy. Left) Conductivity of the neat DES and the ORAM dissolved at 0.1 M in DESs. Right) Conductivity of 4-Hot tempo at $0.1M, 0.5M$ and $1M$in DESs

This could be due to participation of the stable radical molecule in the hydrogen bonding network, further decreasing the species mobility. Further qualitative inspection of the samples at higher ORAM concentration, it is noted a higher viscosity for the $1M$ sample compared to the $0.1M$one. This is in line with the hypothesis just formulated. However, rheological studies could be used to quantitatively compare the physical change of the samples. However, it is possible to just use ionic conductivity as a proxy for the reduced species mobility.

The electrochemical characterization also involved the use of cyclic voltammetry to probe the redox processes of these organic molecules. At first, the CV scans were run at reduced potential window in the region in which these molecules showed signs of redox activity. First, the samples at the smaller concentration will be discussed. The two fluorenone-based shows irreversible redox processes at negative potentials, Figure 4.8. In fact, there is only the presence of a feature in the reverse scan, but none is observed on the forward scan for both systems in combination with all the DES tested.

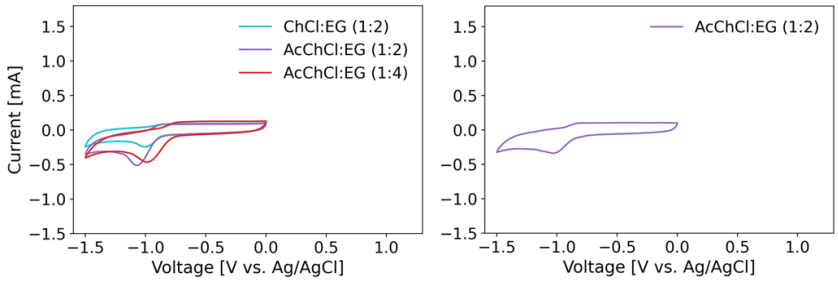

Figure 4.8 Cyclic voltammograms showing irreversible redox processes at negative potentials for 9FL and 9F4CA, respectively. Measurements were run at 100mV/s, for 5 cycles.

On the other hand, Figure 4.9 shows reversible redox processes for 2H14NQ, 12DAQ, and 4HOT, respectively. It is possible to observe the presence of two features, one on the reverse and one of the forward scans. Small variation in peak position can be noted for all organic molecules depending on the solvent used. However, the mid-point between the CV features is relatively constant in position, indicating that the redox species are undergoing the same electrochemical process in all three DES solvents tested.

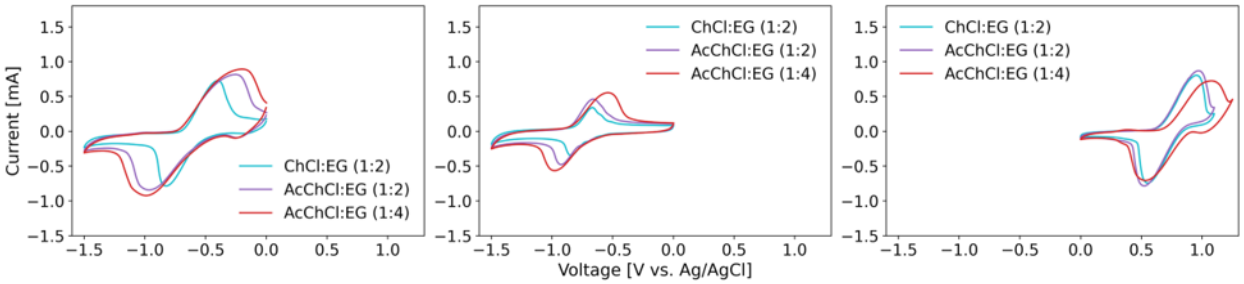

Figure 4.9 Cyclic voltammograms showing reversible redox processes for 2H14NQ, 12DAQ, and 4HOT, respectively. Measurements were run at 100mV/s, for 5 cycles.

The differences between the peak broadness and position potentially indicate differences in species mobility in the solvents tested. In these aprotic solvents, the organic species are most likely undergoing electron transfer reaction involving the formation of radicals. These are possible thanks to charge delocalization of over the cyclic, conjugated pi systems. [41] In fact, all the organic redox active molecules tested present cyclical structures which enable this delocalization of charges. This

behavior was also noted by Ghahremani et a., in which they provide a perspective for the use of these DES as electrolytes. [42]

To confirm possible diffusion limitation of the active species it is possible to conduct different simple CV measurements at different scan rates and compare the relative position and peak of the CV features. This will be part of the future steps of this study and therefore not included in this current report.

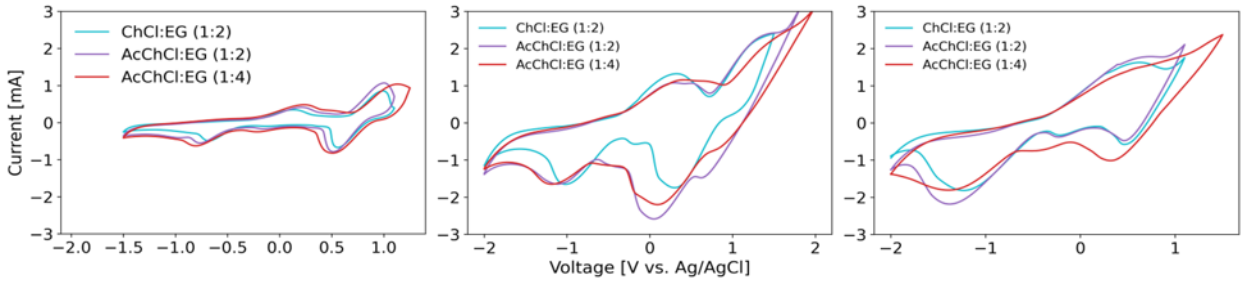

Figure 4.10 Cyclic voltammograms of the 4-hydroxy TEMPO at different concentrations. Left) $0.1M$; Center) $0.5M$; Right) $1M$. Measurements were run at room temperature (~ 20 ℃) with a scan rate of 100mV/s, for a total of 5 cycles.

Finally, Figure 4.10 shows the resulting cyclic voltammograms ran on the 4-hydroxy TEMPO samples at higher concentrations (increasing from left to right) and with wider potentials windows. Again, the electrochemical characterization was run at room temperature. When running the CV scan at a wider window, the samples at $0.1M$ molar shows signs of two distinct redox processes. This behavior was previously observed by Chen et al. in a $50mM$ TEMPO in ethaline. [38] Even though the system studied in this work is a hydroxy-functionalized TEMPO radical, the organic molecules is undergoing the same redox processes of oxidation into an aminoxyl anion and a reduction to an oxoammonium species. [38] The samples at higher concentration of the organic molecules show clear sign of species mobility limitations. In fact, the features in the voltammogram become broad and the two-electron transfer feature eventually merge into one. Since the window was extended to potential above $1.1V$, contribution from the upper limit of the

electrolyte stability starts also to appear. This once again corresponds to changes in oxidation states of the halide anion composing the quaternary ammonium salt, in this case Cl^-.

4.3.3 *MAP-based Protocol Testing using 4-Hydroxy TEMPO*

The protocol described in Chapter 3 was used to synthesize combinations of four different quaternary ammonium salts and the 4-hydroxy TEMPO organic molecules. In fact, given the small size, the hydrogen bonding site present in the molecule and its radical state were all promising feature for possible formation of binary DES samples. Out of 24 total samples prepared, only one of them, namely the acetylcholine choline chloride and 4-hydroxy TEMPO at a 2:1 ratio was found liquid at room temperature, Figure 4.11. This sample has a calculated concentration of active material of about $2.6\ M$, which is very promising.

Figure 4.11 Samples corresponding to acetylcholine choline chloride and 4-hydroxy TEMPO at a 2:1 ratio obtained using the MAP-based protocol.

The remaining samples were found in the solid phase. However, the majority formed uniform phases. The samples using 2-hydroxyethylammonium chloride as their quaternary ammonium salt showed non-homogenous phases.

The onset of melting for all molar ratios tested between 4-hydroxy TEMPO and acetylcholine chloride were obtained using the PhasIR system and the experimental characterization was run in a glove box to reduce water uptake from the samples. Again, the

samples were placed in the inert atmosphere for 1 day prior to characterization to allow further drying and remove possible residual water from the samples' preparation. The results of the physical characterization can be seen in Figure 4.12 (right). In this case, even though the sample at a 2:1 ratio was liquid at room temperature, the eutectic point was closer to a 1:1 ratio. It is also noted that all samples show onset of these phase transition behavior above 30℃, indicating that most likely some trace water was still trapped in the samples. Nevertheless, a melting point found slightly above room temperature should not be a limitation for use of these organic molecules in binary DES, as these are mild temperature that can be easily implemented, especially in energy storage applications.

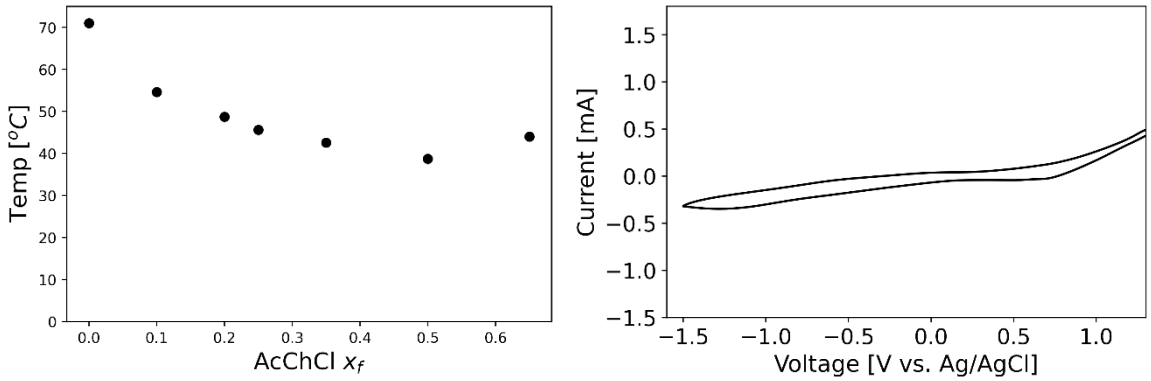

Figure 4.12 Left) Onset of melting for all molar ratios tested between 4-hydroxy TEMPO and acetylcholine chloride prepared using the MAP-based protocol. The temperatures were obtained using the PhasIR system. Right) Cyclic voltammogram of the 2:1 AcChCl: 4HOT sample found liquid at room temperature after processing of samples using the high-throughput protocol.

Finally, the conductivity of the binary DES found liquid at room temperature was found to be $0.64\, mS \cdot cm^{-1}$. The sample was viscous and therefore this low value was not surprising. Moreover, Figure 4.12(right) shows the resulting cyclic voltammogram recorded at room temperature for the sample. From the lack of any feature displayed in the voltammogram and the relatively low currents measured, it is clear that the redox active species have limited mobility. This was again not surprising given the high viscosity of the sample and the low ionic conductivity.

4.4 PROPOSED ELECTROCHEMICAL HARDWARE UPDATES

Organic redox active molecules show promise as alternatives to inorganic, resource limited metals currently used in redox flow batteries. Goeltz et al., have demonstrated the formation of a binary Type III DES between methyl viologens and two hydrogen bond donors which was able to achieve a $4.2M$ concentration and was found liquid at 30 ℃.[28] While that is a promising example, the current protocol implemented for the samples' characterization in this study, showcased in this Chapter and Chapter 3, is limited to room temperatures. It is to note that this is currently an artificial limitation posed by the choice of electrochemical cell for the high-throughput workflow developed. The proposed upgrades to the electrochemical set up will allow for increasing the throughput and automation of the synthesis and characterization of these samples. These additions include solutions to probe the electrochemical properties of both base DES, as well as binary and ternary redox-DES. Achieving a higher temperature will also aid in reducing the viscosity of the samples and hopefully allow for better probing of redox processes.

The high-throughput protocol described in Chapter 3 has been successful at synthesizing, processing, and analyzing several hundred samples in a matter of a month. This outcome would not have been possible without the aid of automation platforms and design of new labware/hardware solutions. While that is already a success, the use of single-use screen-printed electrode systems quickly became the bottleneck of this new synthesis protocol. In fact, even though it allows for use of small volumes (approximately $200\,\mu L$ per sample), and the characterization can be completed in less than 10 min per sample, it still requires manual changing of the sample and electrode cell. Finding a platform that can allow the parallel measurement of several samples would further increase the throughput capabilities of the workflow and reduce the time-intensive manual steps required by the researcher. The manufacturer of the screen-printed

electrodes, Metrohm (Herisau, Switzerland) offers a well-plate version of these 3-electrodes cells, the CONNECTYOR96X. A simplified schematic can be seen in Figure 4.13. In fact, the connector can be directly interfaced using a small RaspberryPi system, SYNCONN96X provided by the manufacturer, which requires a simple voltage signal to turn on and off the connection with each cell-well in the plate. This would allow the serialization of the measurements for up to 96 samples, removing the human intervention from this step of the workflow.

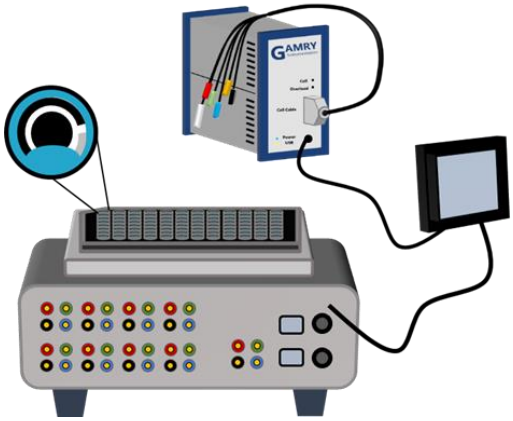

Figure 4.13 Example schematics of CONNECTOR96X from Metrohm USA for high-throughput electrochemical screening. Limitations of this system are current compatibility issues with the Gamry Potentiostat and room temperature operations.

The implementation of the CONNECTOR96X will aid in further speeding up the sample characterization, but not vary the physical conditions of the test itself. In fact, there is a need to test the electrochemical properties of both DES electrolytes, studied in Chapter 3, and organic active materials at higher temperatures. Unfortunately, there are no simple and cost-effective solutions for this characterization that are commercially available and allow for integration for high-throughput protocols. However, there are viable solutions that can be designed and fabricated in-house. For example, it would be possible to make use of the screen-printed electrodes and create a support to heat them while the electrochemical measurements are underway. For this application,

a copper tube and a variable-transformer controlled heating tape could be used to form a hot enclosure for the electrode cell. Concerns and limitations for this solution include non-uniform sample placement over the electrodes throughout the heating process and possible material incompatibility with the support of the electrochemical cell. An alternative design would be to use a dip version of the screen-printed electrodes. This design is already provided by the manufacturer and would not require further work on the cell prior to implementation. Furthermore, this could be combined with a well-plate heated block that can host the samples contained in glass vials instead. This solution could also be combined with a thermocouple probe to track possible temperature fluctuations throughout the sample measurement. A 3D printed case for the temperature and electrochemical probe can be easily designed and fabricated, which would allow for consistent placement of the measurement sets. This would also enable its application in the open-source and hardware Jubilee platform, discussed in Chapter 5 and 6, for further automation of this characterization step. A possible limitation to this design is the requirement for higher volumes of samples due to the size of the electrode cell and the opening of the glass vials.

All the modifications indicated are relatively small in cost and size. This latter property can also allow for the integration of these systems into a glove box for property characterization under dry and inert environments. As DES contain hygroscopic components, this solution would be beneficial to truly probe the electrolyte properties without any water uptake. This will become necessary for testing the stability of pure DES and redox-DES at longer cycling protocols.

4.5 CONCLUSIONS

The preliminary results shown in this chapter show a promising avenue for the use of DES as solvents for novel organic redox molecules. Aside from a very few species, mainly TEMPO and its derivatives, as well as methyl viologens, these organic compounds are generally poorly soluble

or completely insoluble in aqueous systems. Deep eutectic solvents are promising alternative for use as non-aqueous electrolytes and display 'greener' qualities and are safer alternatives to current organic solvents. Therefore, DES as electrolytes in RFBs is a promising area of research that has the potential to improve the performance and sustainability of energy storage systems. However, more research is needed to further understand and optimize the properties of DES-based RFBs.

In this Thesis, only a handful of ORAMs have been tested as proof of concept. However, most of them showed redox activity at negative potentials and only one resulted in a positive regime. The list of candidates can be easily expanded to include a broader variety of chemical structures, functionalization, and redox activity. These can include viologens, quinones, hydroquinones, and benzoquinones to name a few. A study from Er et al. has indicated several quinones and derivatives which show potential use as anolytes.[43] This study can be referenced during the selection on new ORAM to test. While limited, new molecules can also be chosen based on literature examples as a matter of comparison for the results obtained with this semi-automated protocol.

4.6 REFERENCES

1. *Renewable Capacity Highlights*. (2019).
2. Alotto, P., Guarnieri, M. & Moro, F. Redox flow batteries for the storage of renewable energy: A review. *Renewable and Sustainable Energy Reviews* **29**, 325–335 (2014).
3. Dunn, B., Kamath, H. & Tarascon, J. M. Electrical energy storage for the grid: A battery of choices. *Science (1979)* **334**, 928–935 (2011).
4. Weber, A. Z. *et al.* Redox flow batteries: A review. *J Appl Electrochem* **41**, 1137–1164 (2011).
5. Winsberg, J., Hagemann, T., Janoschka, T., Hager, M. D. & Schubert, U. S. Redox-Flow Batteries: From Metals to Organic Redox-Active Materials. *Angewandte Chemie - International Edition* **56**, 686–711 (2017).
6. Chalamala, B. R. *et al.* Redox flow batteries: An engineering perspective. *Proceedings of the IEEE* **102**, 976–999 (2014).

7. Chakrabarti, M. H., Dryfe, R. A. W. & Roberts, E. P. L. Evaluation of electrolytes for redox flow battery applications. *Electrochim Acta* **52**, 2189–2195 (2007).
8. Wang, W. *et al.* Recent Progress in Redox Flow Battery Research and Development. *Adv Funct Mater* **23**, 970–986 (2013).
9. Yang, Z. *et al.* Electrochemical energy storage for green grid. *Chem Rev* **111**, 3577–3613 (2011).
10. Tang, L. *et al.* Capital cost evaluation of conventional and emerging redox flow batteries for grid storage applications. *Electrochim Acta* **437**, (2023).
11. Wei, X. *et al.* Materials and Systems for Organic Redox Flow Batteries: Status and Challenges. (2017) doi:10.1021/acsenergylett.7b00650.
12. Darling, R. M., Gallagher, K. G., Kowalski, J. A., Ha, S. & Brushett, F. R. Pathways to low-cost electrochemical energy storage: A comparison of aqueous and nonaqueous flow batteries. *Energy Environ Sci* **7**, 3459–3477 (2014).
13. Dmello, R., Milshtein, J. D., Brushett, F. R. & Smith, K. C. Cost-driven materials selection criteria for redox flow battery electrolytes. *J Power Sources* **330**, 261–272 (2016).
14. Er, S., Suh, C., Marshak, M. P. & Aspuru-Guzik, A. Computational design of molecules for an all-quinone redox flow battery. *Chem Sci* **6**, 885–893 (2015).
15. Likit-Anurak, K., Uthaichana, K., Punyawudho, K. & Khunatorn, Y. The Performance and Efficiency of Organic Electrolyte Redox Flow Battery Prototype. *Energy Procedia* **118**, 54–62 (2017).
16. Winsberg, J. *et al.* TEMPO/Phenazine Combi-Molecule: A Redox-Active Material for Symmetric Aqueous Redox-Flow Batteries. *ACS Energy Lett* **1**, 976–980 (2016).
17. Tang, Y. *et al.* Organic Electroactive Molecule-Based Electrolytes for Redox Flow Batteries: Status and Challenges of Molecular Design. *Frontiers in Chemistry | www.frontiersin.org* **1**, 451 (2020).
18. Xing, X. *et al.* A nonaqueous all organic semisolid flow battery. *Chemical Communications* **55**, 14214–14217 (2019).
19. Liu, T., Wei, X., Nie, Z., Sprenkle, V. & Wang, W. A Total Organic Aqueous Redox Flow Battery Employing a Low Cost and Sustainable Methyl Viologen Anolyte and 4-HO-TEMPO Catholyte. *Adv Energy Mater* **6**, (2016).
20. Turcanu, A. & Bechtold, T. PH Dependent redox behaviour of Alizarin Red S (1,2-dihydroxy-9,10- anthraquinone-3-sulfonate) - Cyclic voltammetry in presence of dispersed vat dye. *Dyes and Pigments* **91**, 324–331 (2011).
21. Hu, B., Hu, M., Luo, J. & Liu, T. L. A Stable, Low Permeable TEMPO Catholyte for Aqueous Total Organic Redox Flow Batteries. (2021) doi:10.1002/aenm.202102577.
22. Zhou, W. *et al.* Fundamental properties of TEMPO-based catholytes for aqueous redox flow batteries: effects of substituent groups and electrolytes on electrochemical properties, solubilities and battery performance †. (2020) doi:10.1039/d0ra03424j.

23. Goeltz, J. C. & Carter, J. M. Finding balance with deep eutectic solvents: High concentrations and improved conductivities for the off-the-shelf nitroxide TEMPOL. *J Mol Liq* **338**, (2021).
24. Liu, T., Wei, X., Nie, Z., Sprenkle, V. & Wang, W. A Total Organic Aqueous Redox Flow Battery Employing a Low Cost and Sustainable Methyl Viologen Anolyte and 4-HO-TEMPO Catholyte. *Adv Energy Mater* **6**, (2016).
25. DeBruler, C. *et al.* Designer Two-Electron Storage Viologen Anolyte Materials for Neutral Aqueous Organic Redox Flow Batteries. *Chem* **3**, 961–978 (2017).
26. Hu, B., DeBruler, C., Rhodes, Z. & Liu, T. L. Long-Cycling Aqueous Organic Redox Flow Battery (AORFB) toward Sustainable and Safe Energy Storage. *J Am Chem Soc* **139**, 1207–1214 (2017).
27. Luo, J. *et al.* Unprecedented Capacity and Stability of Ammonium Ferrocyanide Catholyte in pH Neutral Aqueous Redox Flow Batteries. *Joule* **3**, 149–163 (2019).
28. Goeltz, J. C. & Matsushima, L. N. Metal-free redox active deep eutectic solvents †. *Chem. Commun* **53**, 9983 (2017).
29. Ji, Y. *et al.* A Phosphonate-Functionalized Quinone Redox Flow Battery at Near-Neutral pH with Record Capacity Retention Rate. *Advanced Science News* 1–17 (2019) doi:10.1002/aenm.201900039.
30. Hu, B., Luo, J., Hu, M., Yuan, B. & Liu, T. L. A pH-Neutral, Metal-Free Aqueous Organic Redox Flow Battery Employing an Ammonium Anthraquinone Anolyte. *Angewandte Chemie - International Edition* **58**, 16629–16636 (2019).
31. Huskinson, B. *et al.* A metal-free organic-inorganic aqueous flow battery. *Nature* **505**, (2014).
32. Romadina, E. I., Akkuratov, A. v., Simoska, O. & Stevenson, K. J. Phenazine-Based Compound as a Universal Water-Soluble Anolyte Material for the Redox Flow Batteries. *Batteries* **8**, (2022).
33. Zhang, C. *et al.* Phenothiazine-Based Organic Catholyte for High-Capacity and Long-Life Aqueous Redox Flow Batteries. *Advanced Materials* **31**, 1–8 (2019).
34. Medabalmi, V., Sundararajan, M., Singh, V., Baik, M.-H. & Byon, H. R. Naphthalene diimide as a two-electron anolyte for aqueous and neutral pH redox flow batteries †. *J Mater Chem A Mater* **8**, 11218–11223 (2020).
35. Feng, R. *et al.* Reversible ketone hydrogenation and dehydrogenation for aqueous organic redox flow batteries. *Science (1979)* **372**, 836–840 (2021).
36. Cruz, H., Jordão, N. & Branco, L. C. Deep eutectic solvents (DESs) as low-cost and green electrolytes for electrochromic devices. *Green Chemistry* **19**, 1653–1658 (2017).
37. Ji, Y. *et al.* Recent research progress of redox flow batteries based on deep eutectic solvents (DESs). *Int J Green Energy* (2022) doi:10.1080/15435075.2022.2079949.
38. Chen, B. *et al.* Feasibility of TEMPO-functionalized imidazolium, ammonium and pyridinium salts as redox-active carriers in ethaline deep eutectic solvent for energy storage. *Mol Syst Des Eng* **5**, 1147–1157 (2020).

39. Zhang, C., Zhang, L., Ding, Y., Guo, X. & Yu, G. Eutectic Electrolytes for High-Energy-Density Redox Flow Batteries. *ACS Energy Lett* (2018) doi:10.1021/acsenergylett.8b01899.
40. Gurkan, B., Squire, H. & Pentzer, E. Metal-Free Deep Eutectic Solvents: Preparation, Physical Properties, and Significance. *J. Phys. Chem. Lett* **10**, 26 (2019).
41. Smith, D. K. Exploring the Role of H-Bonding in Organic Electrochemistry – From Supramolecular Applications to Mechanistic Investigations. *Chemical Record* vol. 21 2488–2501 Preprint at https://doi.org/10.1002/tcr.202100186 (2021).
42. Ghahremani, R., Savinell, R. F. & Gurkan, B. Perspective-Hydrogen Bonded Concentrated Electrolytes for Redox Flow Batteries: Limitations and Prospects. *J Electrochem Soc* **169**, (2022).
43. Er, S., Suh, C., Marshak, M. P. & Aspuru-Guzik, A. Computational design of molecules for an all-quinone redox flow battery. *Chem Sci* **6**, 885–893 (2015).

Chapter 5. HIGH-THROUGHPUT WORKFLOW FOR THE SYNTHESIS OF CDSE NANOCRYSTALS USING A SONOCHEMICAL MATERIALS ACCELERATION PLATFORM

This chapter contains work from the following publication and the author would like to acknowledge the contributions of the coauthors:

Politi, M., Baum, F., Vaddi, K., Antonio, E., Vasquez, J., Bishop, B., Peek, N. Holmberg, V. & Pozzo, L. D. High-throughput Workflow for the Synthesis of CdSe Nanocrystals Using a Sonochemical Materials Acceleration Platform. Digital Discovery, 2023, Advance Article. DOI: https://doi.org/10.1039/D3DD00033H

5.1 INTRODUCTION.

Quantum dots (QDs) are materials with great scientific and technological interest, with applications in solar cells,[1] light-emitting diodes (LEDs),[2] biofluorescence tagging,[3] sensors[4] and recently in neuromorphic hardware.[5] They consist of semiconductor nanoparticles with size below the exciton Bohr radius. Their remarkable optical and electronic properties arise from quantum confinement effect, which is strongly dependent on the QDs size. Among the QDs, there is a special class of nanocrystals known as magic-sized clusters (MSCs). These are formed in thermodynamic local minimum conditions that favor the growth of species with a precise number of atoms (the magic size) instead of the continuous growth towards a large particle. Typically, CdSe MSCs show diameters below 2 nm. Their optical characterization presents narrow and sharp absorption peaks and broad photoluminescence peaks. These features limit the application of MSCs in devices that require color purity but enable them to be used as white-light emitters.[6] The optical properties of QDs and their subgroup, MSCs, are also strongly dependent on their surface functionalization. In this context, one possible method to improve surface passivation is the use of ligands through colloidal synthetic routes.[7]

The most widely used technique for the synthesis of QDs and MSCs is the hot injection method.[8] Its protocol includes the precursor solution preparation under inert atmosphere, followed by the injection step, which starts the decomposition of the organometallic species, leading to nucleation and growth processes. This synthesis usually involves the use of ligands with long carbon chains to stabilize the nanoparticle surface. This method presents great versatility and has been used to obtain metallic [9], chalcogenides [10], and perovskites nanocrystals [11] with various shapes and sizes. The advantage of this method is the relationship between QDs size and the reaction time, which can provide great size control. Additionally, the fast nucleation events generated in the injection step allows the formation of monodisperse particles.[8] However, this synthesis route requires high temperatures for precursors decomposition and the use of a Schlenk line to ensure an inert atmosphere. Under these conditions, only a single set of experimental parameters can be tested per batch, leading to lengthy procedures for exploration or property optimization tasks. Furthermore, this method is prone to batch-to-batch variability, as well as observational and random errors, leading to inconsistent outcomes for the same set of conditions.

Sonochemical synthesis is an interesting alternative technique for the fabrication of nanostructured materials. It was used to obtain noble metal nanostructures, [12–17] metal oxides, [18,19] metal sulfides,[20–23] and quantum dots.[24–26] This technique provides thermal energy to the reaction medium through acoustic cavitation: the formation, growth, and implosive collapse of bubbles in a liquid due to a perturbation in the form of pressure waves. As the ultrasonic waves travel through the solution, it generates cavitation bubbles, which increase in size and decrease in internal pressure. Finally, the bubbles reach a point of instability, culminating in their collapse. This process generates localized transient regions of extreme conditions in the solution, with temperatures around 5,000 K and pressures of 500 atmospheres, with cooling rates as high

as 10^9 °C $\cdot S^{-1}$. [27–29] Sonochemistry exploits these conditions to decompose the precursors and promote chemical reactions, leading to the target compound formation, followed by its nucleation and growth into a particle. Among the advantages of sonochemical synthesis, its single pot synthetic procedure facilitates the scalability and reproducibility of the experimental design. Furthermore, sonochemistry does not necessarily require inert conditions and the synthesis can be carried out at room temperature, significantly simplifying its implementation.

Considering its characteristics, sonochemical synthesis is a perfect match to combine high-throughput experimentation with low-cost fabrication techniques. Herein, a new workflow implementing an affordable liquid handling robot and an open-hardware sonication station is presented. The OT-2 Liquid Handling Robot, from Opentrons, is an affordable, open-source tool capable of preparing hundreds of precursor solutions to be synthesized and allows for flexible and reproducible protocols. The sonication station is based on a flexible tool-changing motion platform, called Jubilee, which is integrated with a sonication horn to allow for an array of automated sonochemical synthesis experiments. To demonstrate the implementation of these automation platforms, we explored how the combination of different experimental parameters affect the sonochemical synthesis of CdSe QDs and MSCs. CdSe is one of the most well-studied QD systems, with established relationships between optical properties, particle size, and surface passivation. Therefore, with simple characterization techniques, such as UV-Vis Extinction Spectroscopy and Photoluminescence Spectroscopy we could access information about particle shape, particle size, size distribution, particle concentration, surface passivation, and band gap energy to name a few.

In this context, in this Chapter we thoroughly investigate how the concentration of ligands (oleic acid and oleylamine) and precursors (cadmium acetate and elemental selenium), influence

the properties of the resulting CdSe QDs or MSCs. In our design of experiments (DOE), we explored 5 different conditions or 'levels' for these four parameters using a full factorial design (5^4), resulting 625 unique synthetic conditions. The experiments were repeated in triplicate to ensure repeatability of the workflow and to assess the reliability of results obtained from each campaign. This number of syntheses would be infeasible or extremely costly, both in time and resources, to perform using traditional low-throughput synthesis routes such as solvothermal methods. Furthermore, the automated workflow allows researchers to carry out experiments with sample volumes as small as $0.5\ mL$ per condition tested, significantly reducing the cost and the environmental impact of the experimental process. The UV-Vis extinction and photoluminescence spectra were obtained using microplate readers, which allowed fast characterization of up to 96 samples at a time. Design of experiments, data analysis, and visualization routines were created with Python scripts, which facilitated the handling of the large volume of data resulting from experimental campaigns.

5.2 Materials and Methods

5.2.1 *Chemicals*

Cadmium acetate anhydrous was purchased from Sigma Aldrich (99.995 %), elemental selenium pellets (99.99%), trioctylphosphine (97 %), oleic acid (90%, tech grade), oleylamine (70%, tech grade), 1-octadecene (90 %, tech grade), n-decane ($\leq$ 100 %), and hexanol ($\geq$ 98 %, FCC) were obtained from Sigma Aldrich. Ethanol (100 Proof) was purchased from Decon Laboratories. All chemicals were used as received.

5.2.2 *Labware & Robotic Platforms*

All stock solutions were prepared in 20 mL glass scintillation vials, supported in a customized 3D printed 12-vial plate. All files required to reproduce any custom labware described in this paper can be found in a GitHub repository. [30] All samples were synthesized into NEST 2.2 mL 96-Well deep well plates, with square wells and U-shaped bottom (Catalog number: 503002). The solutions for UV-Vis absorption spectroscopy were prepared into clear, flat-bottom FisherbrandTM 96-Well Polystyrene plates (360 µL, 12-565-501). Finally, the solutions for photoluminescence spectroscopy were prepared into black, flat-bottom FisherbrandTM 96-Well polystyrene plates (360 µL, 12-565-501).

An Opentrons OT-2 Liquid Handling Robot was used to mix the precursors for all the samples, as well as for performing all dilution procedures for measurements. The robot was equipped with a single-channel Opentrons P300 GEN2 pipette ($20\ \mu L$ - $300\ \mu L$) and a single-channel P20 GEN2 pipette ($2\ \mu L$ - $20\ \mu L$). The pipette tips were stored on Opentrons $300\ \mu L$ tip rack and Opentrons $20\ \mu L$ tip rack, respectively. To interface with the robotic platform, the Opentrons Python API was used to run commands through Jupyter Notebooks. An in-house developed open-source software, OT2-DOE, was used to define the design space and communicate with the OT-2 Liquid handling Robot.[31] The calibration files for the labware used in the experimental campaign are also available on the software's GitHub repository.

The second robotic platform was implemented for the sonochemical synthesis of the samples. The platform, called Sonication Station, is a configurable and open-source laboratory automation platform for sonochemical applications, based on the Jubilee motion control system. The original Jubilee design presents a modular tool-changing motion platform that accommodates user-created tools and beds.[32,33] The Sonication Station was assembled with a QSonica Q125

sonicator, equipped with a 5/64" (2 mm) sonication probe (#4423). The platform allows for automated single-point sonochemical processing of samples, for a maximum of six plates loaded on the platform's deck at a time. The sonication station was interfaced using a Python script and the machine's API. The Sonication Station design and control libraries are open-source and available on GitHub.[34] More discussion on this platform, specifically in the context of broader laboratory automation task is discussed in Chapter 6.

5.2.3 *Stock Solution Preparation*

The stock solutions were prepared under inert conditions in a glovebox due to air and water reactivity of trioctylphosphine (TOP). TOP was chosen as the solvent for the metal precursors due to the higher solubility of both anhydrous cadmium acetate and elemental selenium in this medium. For the chalcogenide precursor solution (0.5 M), 1.729 g of cadmium acetate anhydrous and 15 mL of TOP were added into a scintillation flask, heated to 125 ℃ and stirred until complete dissolution of the salt, usually around 4 hrs. For the selenium precursor solution (1 M), 1.201 g of selenium pellets and 15 mL of TOP were added into a scintillation flask and stirred at room temperature until complete dissolution, usually 10hrs. Both scintillation flasks were sealed and stored for use in the OT-2 robotic platform. All other components, namely oleic acid, oleylamine, and 1-octadecene, were used in their pure form and did not require any processing before use.

5.2.4 *Automated Sample Formulation*

The OT-2 Liquid Handling Robot was programmed to formulate different solutions containing a given amount of each of the four components under investigation in the square deep-well 96 well plates. Octadecene was added to the solution to reach a total sample volume of $0.5 mL$. Each component was tested at five different concentrations (Table 5.1), resulting in $5^4 =$

625 possible unique conditions. The synthesis was performed in batches of 96 samples in well plates, processed sequentially.

Table 5.1 Concentration values for each parameter used for the sonochemical synthesis of CdSe. The design space is composed of every unique combination of each of these parameters, for a total of 625 samples.

Parameter	Concentrations [M]				
Cadmium precursor	0	0.025	0.05	0.075	0.1
Selenium precursor	0	0.025	0.05	0.075	0.1
Oleic acid	0	0.125	0.25	0.375	0.5
oleylamine	0	0.125	0.25	0.375	0.5

5.2.5 *Sonochemical Synthesis*

After the solutions were prepared by the OT-2 robotic liquid handling platform, the 96 well plate was transferred to the Sonication Station. This station, depicted in Figure 5.1, automatically sonicated each well in the well plate for 5 minutes, with duty cycle of 0.5, pulse interval of 15s (7.5s on/off), with a total time per sample of 10 minutes, using 50% amplitude from the 100W source (20kHz). Between the sonication of each sample, the probe underwent a cleaning cycle using four hexanol baths and two ethanol baths, each at maximum sonication power for 30s, and finally was allowed to dry in air for 1 minute.

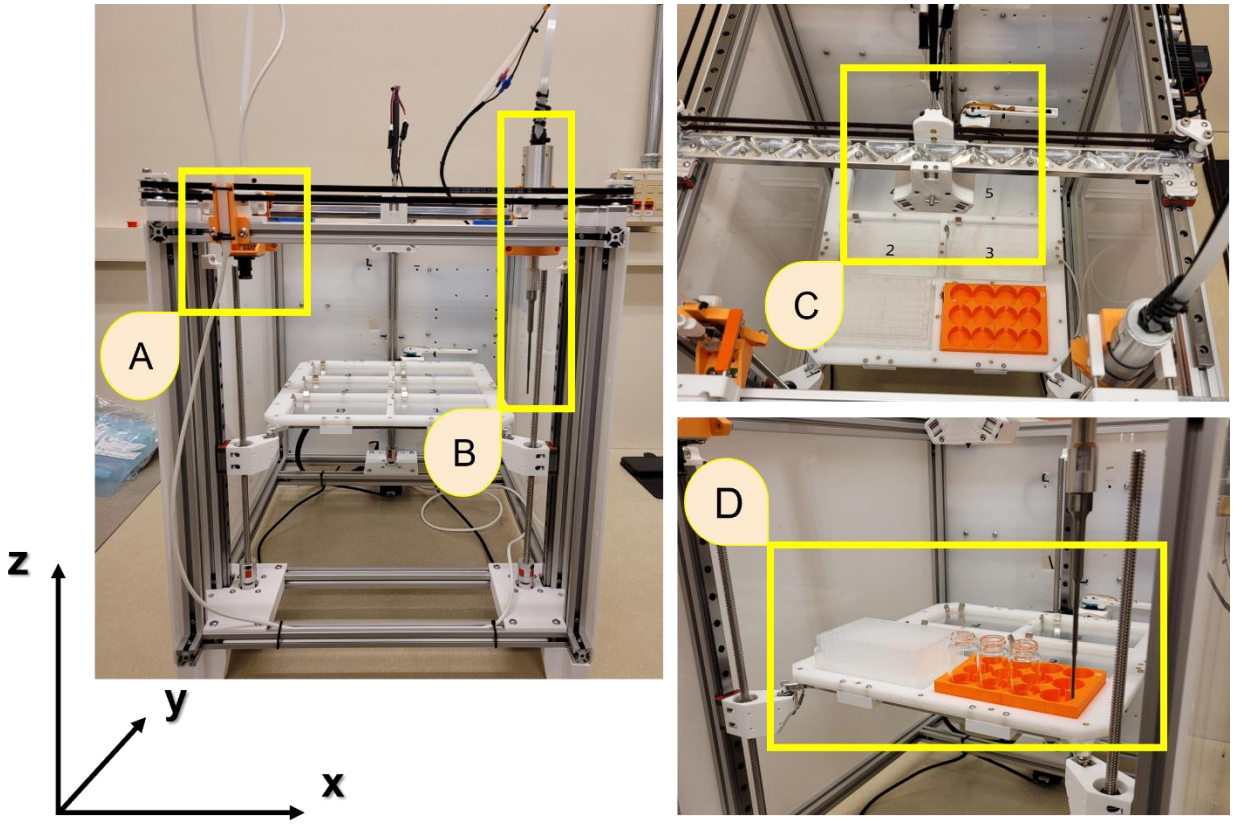

Figure 5.1 Sonication Station components representation. A) Camera tool. This is used to perform a calibration step for any labware implemented on the platform. B) Sonication horn tool used to process samples. C) Tool changer component. The t-shaped metal component is used to lock and secure the selected tool. The Tool changer arm moves in the x, y plane. D) Deck with 6 total slots which can house SLAS standard size labware

5.2.6 *Optical and Morphological Characterization*

The UV-Vis extinction spectroscopy was performed on a Biotek Epoch 2, using clear 96 well plates loaded with the as-synthesized CdSe solutions, diluted in a 1:10 fold with 1-octadecene. The measurement was performed from 300 to 700 nm, with a step of 1 nm. The measurements were performed 24 hours after the synthetic procedure was complete. For more information on this technique, please refer to Chapter 2, section 2.2.1 .

The photoluminescence spectroscopy was performed on a Biotek Synergy H1, using black 96 well plate, loaded with the crude CdSe solutions diluted in a 1:100 fold with 1-octadecene. The

measurement was performed with an excitation wavelength of 325 nm, from 30$ to 700 nm, with a reading step of 1 nm. Once again, the measurements were performed 24 hours after the synthetic procedure was complete. For more information on this technique, please refer to Chapter 2, section 2.2.2.

A subset of the experimental sample space was also reproduced and measured using a Xenocs Xeuss 3.0 (Grenoble, France) SAXS instrument. The samples were loaded into 1.5 mm diameter Boron-rich capillaries (Charles Supper, 15BG) and measured using WAXS, MAXS and SAXS instrumental configurations to cover a broad q-range. The measurement was obtained using a copper source and the combined configurations allow to investigate a scattering vector q range from $5 \cdot 10^{-3}$ to approximately 1 $Å^{-1}$. In this regime it is possible to obtain information about the particle size, polydispersity, and aggregation state after the data is adjusted by subtracting the scattering contribution from both the solvent and empty capillary. Absolute scaling was not possible due to small variations in the thickness of the sealed capillaries. Samples were run 'as-synthesized', as well as diluted 4-fold in n-decane to reduce interparticle correlations and to probe the dilute-limit form factor $P(q)$ that is associated to intrinsic particle shape. The data reduction and processing were completed using the XSACT software, while the data fitting was completed using the open-source McSAS software.[35,36]

5.3 Results & Discussion

The main appeal of using high-throughput platforms for materials synthesis is the speed at which large experimental spaces can be investigated. In fact, using the high-throughput synthesis and characterization workflow, all the 625 unique samples composing the design space were completed (from formulation to data analysis) in less than two weeks. To ensure that both the workflow and the experimental conditions were reproducible, the campaign was repeated two

more times, for a total of 1875 samples processed. The samples were prepared in a batch fashion, using commercially available 96-well plates to sonochemically synthesize the CdSe QDs. The use of 96-well ANSI/SLAS standards is convenient, as it is widely commercialized, and also requires no further customization of sample holders for characterization techniques in, for example, commercial microplate readers.The total time for the synthetic procedure was approximately 30 hours per plate (96 samples). This short experimental time was possible as most of the lengthier processing steps (e.g., the sonication of the samples) were fully automated and required no human intervention. On the other hand, even though the conventional hot-injection synthesis protocol is a more established synthesis route, it would have been prohibitive to implement for this type of experimental study, and the entire campaign ran in triplicates would have taken well more than a year to complete. The sonochemical material acceleration platform poses a great advantage compared to the traditional hot-injection synthesis route when comparing the required volumes of materials required to complete the experimental campaign. Table 5.2 summarizes the total volume of each stock solution required to formulate all 1875 samples. These values include excess stock, approximately 15% of the required amount for each component, to allow the use of the OT-2 pipetting robot. Values for the thermochemical route would be at least one order of magnitude higher, as its lowest working volume usually amounts to approximately $5mL$. Consequently, high-throughput platforms are generally more cost effective and environmentally friendly (i.e., significantly lower waste produced) for the same amount of information extraction.

Table 5.2 Total volume required for the sonochemical synthesis of all 625 samples in triplicates. All values are indicated in mL. Note: The indicated values also include a $\approx 15\%$ added volume as buffer for the liquid handling robot platform.

Component	Volume [mL]
Cadmium Acetate/ TOP [$0.5M$]	108.0
Selenium/ TOP [$1M$]	53.8
Oleic Acid	84.5

Oleylamine	88
1-Octadecine	742.4

5.3.1 *Effect of Ligands Concentration and Sample Composition on CdSe Size and Optical Properties*

To determine the effect of the synthetic conditions on the optical properties of the nanocrystals, we measured their absorption and emission spectra. Given the number of dimensions of the experimental space and the large amount of data generated the data visualization became a challenge. To address this challenge, the spectra were shown in two different groups: one based on precursor concentration, and the other was based on the ligand concentration. Even though it only allows one to analyze a subset of condition at a time, it still enables the extraction of general trends in the synthesis from UV-vis extinction and photoluminescence emission spectra. Figure 5.2 shows the UV-Vis absorption spectra for the samples synthesized with different $Cd(OAc)_2$ and elemental selenium precursor concentrations, at $0\ M$ and $0.25\ M$ for oleic acid and olylamine, respectively.

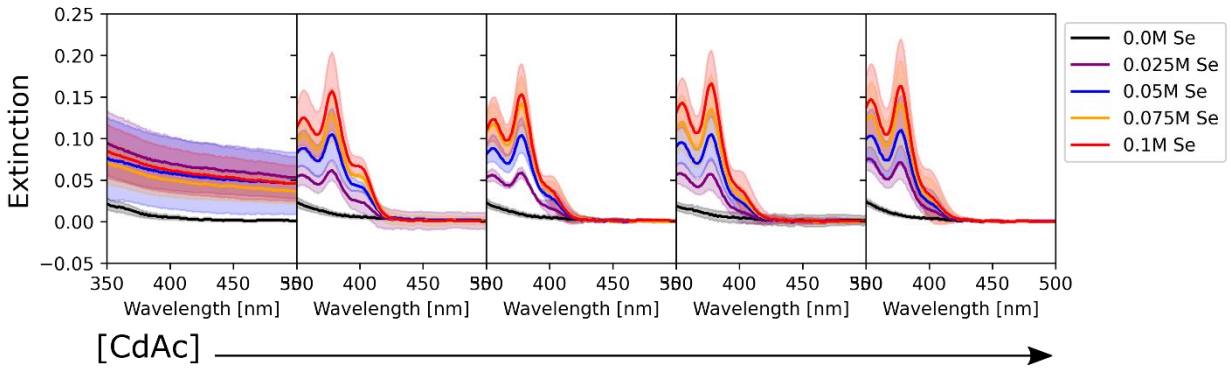

Figure 5.2 UV-Vis absorption spectra of the CdSe QDs synthesized at varying precursors conditions and with oleic acid and oleylamine concentration of 0 M and 0.25 M, respectively. The color of the spectra corresponds to different selenium conditions (see legend), whereas the concentration of cadmium acetate increases moving from left to right (0 M, 0.025 M, 0.05 M, 0.075 M, and 0.1 M, respectively). Since the data was collected in triplicates, the shaded area of the corresponding color shows the variation of response across the different batches tested.

As expected, when either cadmium or selenium precursors were absent, no optical signature from quantum dots was observed (e.g., left-most subplot in Figure 5.2). On the other hand, when both precursors are present, for this set of ligands' conditions, the absorption intensity tends to increase without variation in the peak number or peak position. This indicates that, at our experimental range, cadmium or selenium concentrations and ratio did not have an influence on the particle size, but only on the number of particles formed. This trend is in line with previous findings seen by Jiang et al.[37] Next, to obtain structural insight on the formed nanocrystals, the effective mass approximation equation, based on the first peak position in the absorption spectra, was used to estimate the particle size.[38] Furthermore, the size distribution of the particles was qualitatively estimated by the broadness of the absorption peaks, where broad peaks or “shoulders features” indicate particles with polydispersity.[39] The calculated QDs diameter obtained for all our experimental conditions ranged between 1.3 and 2.1 nm. Finally, looking at the shaded areas indicating the variation across the three repeats of the experimental procedure, we noticed good

repeatability of the syntheses and little to no variation in the peak position. This confirmed the fact that the tested experimental conditions are repeatable, which increases the validity of the results obtained. Small differences were only seen for the peak intensity, which could indicate some variability in the concentration of the QDs formed. However, these were mainly noticed in those samples that did not contain any stabilizing agent. This was expected as ligands not only play an important role in making the particles colloidally stable, but they can also be used for tuning the nucleation and growth of these nanocrystals.[40] However, these fluctuations are still within reason (most of them are below 5%) and did not affect the repeatability of the experimental outcomes. This once again confirms the great advantage of using an automated workflow for nanocrystals synthesis. This level of repeatability on such a large design space would not have been possible to complete following the traditional thermochemical route.

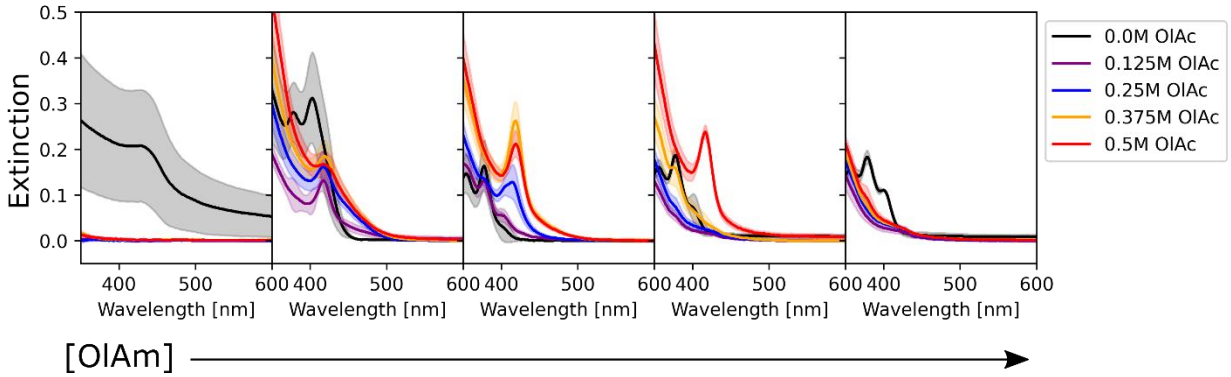

Figure 5.3 UV-Vis absorption spectra of the CdSe QDs synthesized at the highest precursor concentration (0.1 M for both components) with varying ligands concentration. The color of the spectra corresponds to different oleic acid conditions (see legend), whereas the concentration of oleylamine increases moving from left to right (0 M, 0.125 M, 0.25 M, 0.375 M, and 0.5 M, respectively). Since the data was collected in triplicates, the shaded area of the corresponding color shows the variation of response across the different batches tested.

As mentioned previously, the data was also grouped with respect to the metal precursors' conditions. Figure 5.3 presents the UV-Vis spectra of the samples with the highest precursor concentrations ($0.1\,M$ for both cadmium acetate and elemental selenium). This representation

allowed us to identify two main trends in the data. The former presents broad peaks or "shoulders" at longer wavelengths (≈450 nm) when oleylamine is absent or its concentration is exceeded by that of oleic acid. This is related to the formation of regular QDs. The latter showed sharp, narrow peaks at specific positions at shorter wavelengths (< 450 nm) indicating the formation of magic sized clusters, with absorption first peak position centered at wavelengths of 380, 405, and 417 nm. MSCs presenting such optical features were reported in the literature for 380, 405, and 417 nm. [41–43] Once the structure determination was out of the scope of this work, and we will refer to these structures as $CdSe_{380nm}$, $CdSe_{405nm}$, and $CdSe_{417nm}$. Magic-sized QDs with similar characteristics were previously reported, [41–44] obtained through the traditional hot-injection synthesis. This confirmed the ability of our platform to achieve nanocrystals of similar characteristics as the traditional synthetic route. In Figure 5.3, it was noticed that, as the concentration of oleylamine increases (left to right), the characteristics of magic size cluster formation were more predominant. This was only true if the amount of oleylamine was larger than oleic acid. In this case, primarily narrower and sharper absorption peaks were present, while as the fraction of oleic acid increased, the peaks became broader. The broadening of the absorption peak in QDs can be related to the widening of the size distribution. This behavior was previously reported in typical hot-injection syntheses of QDs.[39]At the concentrations studied in this paper, oleylamine was reported to act to stabilize the nuclei by reducing the solubility of the monomer (CdSe molecular units) in the solution and promoting nucleation of smaller nuclei.[45] This led to the formation of smaller QDs with increased monodispersity or even magic-sized QDs. [46] This was reinforced by the observation of the UV-Vis spectra of the samples prior the sonication step (Figure 5.4).

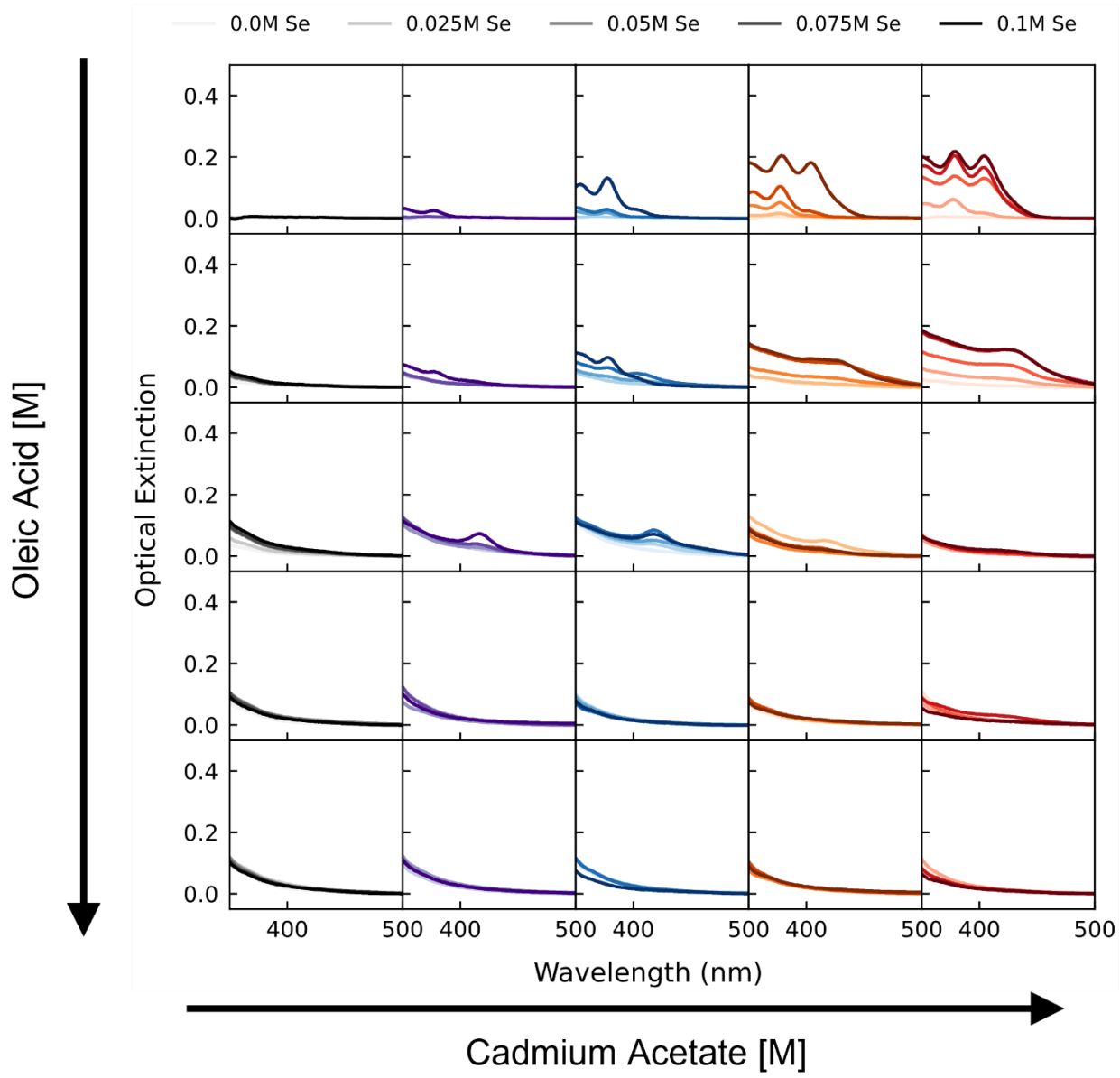

Figure 5.4 UV-Vis absorption spectra of the CdSe QDs synthesized at varying precursors and oleic acid conditions, prior to sonochemical processing. The concentration of oleylamine is 0.125 M. The color of the spectra corresponds to different selenium conditions (see legend), whereas the concentration of cadmium acetate increases moving from left to right (0 M, 0.025 M, 0.05 M, 0.075 M, and 0.1 M, respectively). Additionally, moving from top to bottom, the concentration of oleic acid increases from 0M to 0.1M

The samples containing higher amounts of oleylamine presented absorption spectra characteristic of magic-sized quantum dots even before undergoing sonochemical processing. On the other hand,

increasing the concentration of oleic acid was reported to increase the solubility of the monomer in the solution, de-stabilizing the nuclei, and generating less nucleation.[39] As expected, from Figure 5.3, it could also be noticed that generally the samples that did not contain any ligands, had a higher variation in intensity, compared to the surface stabilized samples.

To perform a high-level evaluation of the experimental effects on the synthesis, one needs to consider the entire set of data. However, given the high dimensionality of the experimental space and the large amount of data generated, it becomes impossible to visualize all the spectra at once.

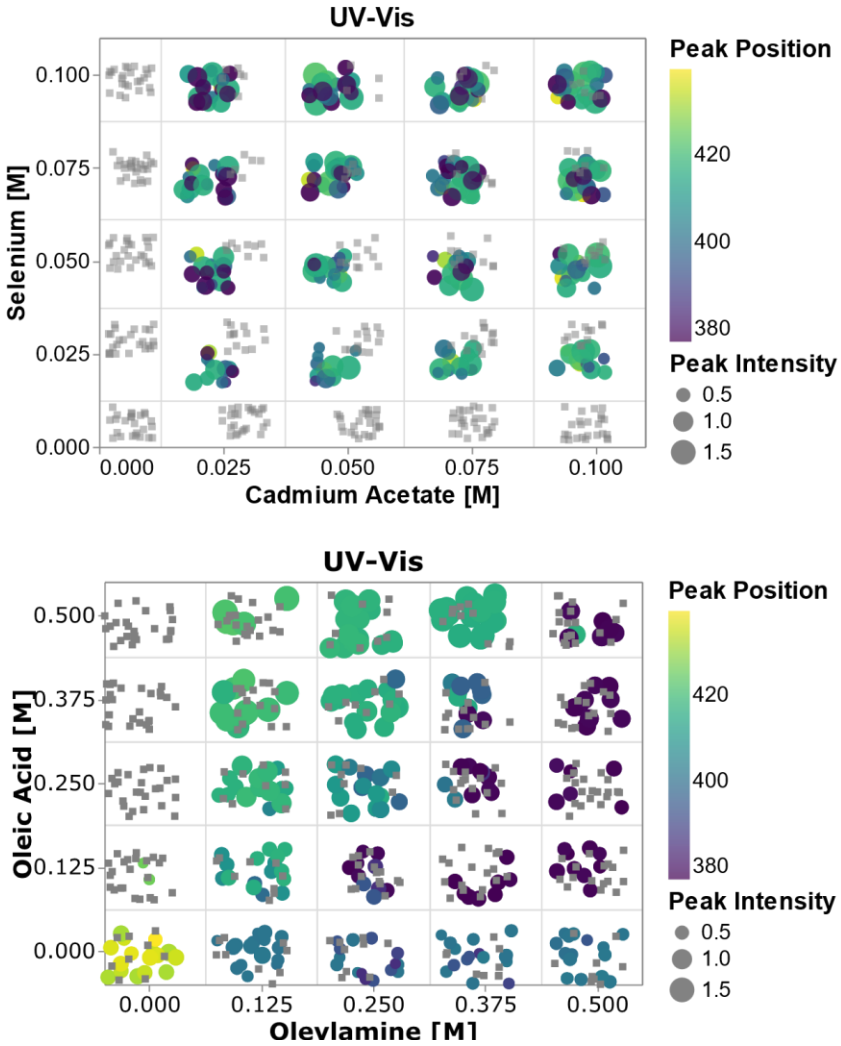

Figure 5.5 Scatter plot of the average intensity at 300, 320, and 340 nm and the first peak position against the precursor concentration (Top) and ligand concentration (Bottom). Since each combination of conditions yielded 25 samples, noise was added to the data for plotting purposes. The grey squares indicate that no extinction response was observed for those samples.

Therefore, the most important quantifiable parameters from the absorption spectra were summarized using a scatter plot. In Figure 5.5, the color of each point represents the first peak position, while the point size represents the average absorption intensity at 300, 320 and 340 nm, which is used as a proxy for the number of particles.[39,47] To prevent overlap of the data points and ease the visualization, jitter noise was added to the plot. Therefore, small spatial variations between points which fall into the same quadrant do not carry meaningful information. Each box inside the

plot is related to one combination of precursor and ligand concentrations indicated on the axis. When samples are grouped by precursor concentration, one cannot see a clear trend in the absorption peak position distribution. The absence of trends indicates that the absorption peak position, related to the QD size, is not greatly affected by the precursor concentration. Additionally, this visual representation confirms that no nanocrystals were formed when cadmium or selenium precursors were absent. In general, for the entire design space the data showed that increasing the concentration of the metal precursors only favored the formation of more particles of the same size, not the growth of the existing ones.[48] On the other hand, when grouped by ligand concentration, all the samples followed the trends previously observed. This can be discerned by the fact that each quadrant is dominated by a single color for its markers. Drawing a diagonal line from the origin to the top right, the plot can be split into two main regions, based on the ligand amount and proportion. The lower right diagonal region of the plot, in which samples contained higher concentrations of oleylamine and lower amounts of oleic acid, presented peaks below 415 nm. This value corresponds to a particle size of approximately 1.7nm. Additionally, samples in this region presented lower absorption intensity peaks when compared to the remaining experimental conditions. This was mainly related to the fact that alkylamines are reported to bind more strongly to theCd^{+2} ion than the carboxylic acids, slowing down the reaction to form CdSe monomer units. This led to a smaller number of nanocrystals formed and consequently lower absorption intensities.[46] In summary, increasing the amount of oleylamine or the OLAm/OAc ratio led to a lower concentration of smaller, monodispersed QDs, while the opposite yielded larger concentrations of bigger and QDs with polydispersity. This was confirmed by looking at the upper left diagonal region in the plot. Here, higher peak positions and generally higher intensities (i.e., larger marker size) were present, as well as peaks at wavelengths above 415 nm. It was also

interesting to notice that, for the case in which only oleic acid was present in the sample, no absorption feature was observed. It is possible that the cadmium salt contained in these samples formed a stable intermediate cadmium oleate species, therefore inhibiting the nucleation of CdSe nanocrystals. This would explain why these carboxylic acid-terminated ligand containing samples showed no or extremely small optical response.

We also studied the impact of synthetic parameters on the photoluminescence. Figure 5.6 shows the photoluminescence spectra of the CdSe QDs. The strong signal below 400 nm present in some of the samples is related to scattering of the excitation beam, possibly due to unreacted ligands in the solution. Analyzing the spectra, three main groups of samples were found: (i) samples with no emission or weak emission overwhelmed by the excitation beam scattering; (ii) samples with broad emission peaks between 600 and 700 nm; and (iii) samples with one sharp peak around 450 nm, with a small or absent secondary peak at higher wavelengths.

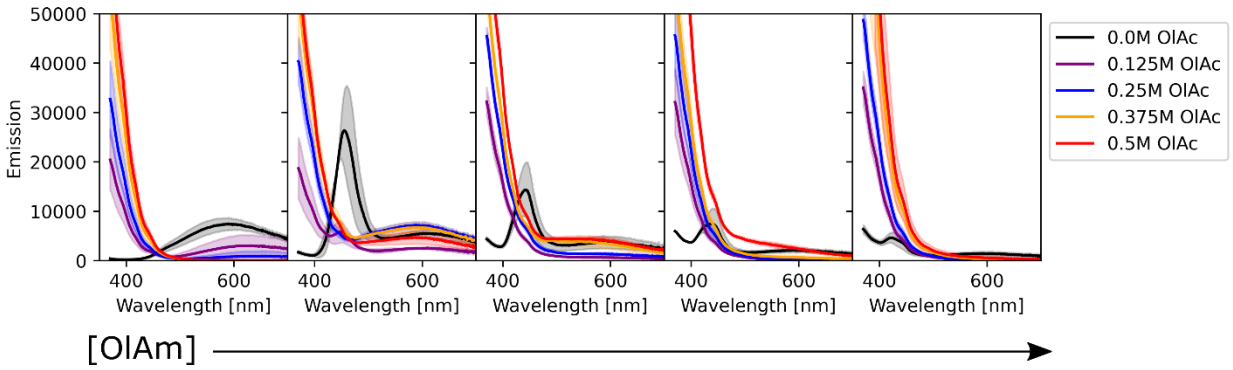

Figure 5.6 Photoluminescence spectra of the CdSe QDs synthesized at the higher precursor concentration (0.1 M for both components) with varying ligands concentration. The color of the spectra corresponds to different oleic acid conditions (see legend), whereas the concentration of oleylamine increases moving from left to right (0 M, 0.125 M, 0.25 M, 0.375 M, and 0.5 M, respectively). Since the data was collected in triplicates, the shaded area of the corresponding color shows the variation of response across the different batches tested.

The optical behavior of the first group of samples was related to the absence of QD formation or the formation of QDs with poor surface passivation, leading to non-radiative recombination. This behavior was more pronounced at higher concentration of oleic acid and oleylamine. The spectral characteristics of the second group were related to surface traps, which leads to recombination at a lower energy (higher wavelength) than the typical band gap of CdSe QDs.[49] This behavior was prominent when lower concentrations of oleic acid were employed or in TOP-only syntheses (i.e., no ligands added in the sample formulation). The samples with no ligands showed a similar behavior with those containing only oleic acid, with the surface trap recombination playing an important role on the light emission from the particles. Additionally, increasing the oleic acid concentration generally caused a decrease in the intensity of emission. These results might suggest that in this experimental setup, the presence of oleic acid was deleterious to surface passivation, leading to surface trap-based luminescence or surface trap related non-radiative recombination. A particular characteristic of our experimental setup was the cadmium precursor solution, consisting of cadmium acetate dissolved in trioctylphosphine instead of the commonly used cadmium oleate. This was again chosen as it allowed production of stock solutions with higher concentration of precursors, which in turn allowed the overall sample volume to be limited to $500\ \mu L$. Therefore, it is possible that the addition of oleic acid in the samples containing both ligands might not form cadmium oleate, which is known to play an important role in achieving surface passivation. Instead, this fatty acid would most likely bind as an uncharged type L ligand to the surface of CdSe nanocrystals, decreasing its capacity to passivate the QD's surface. Finally, the last identified trend was present in samples containing only oleylamine or oleylamine in higher amounts than oleic acid. These sample conditions showed a sharp, intense, and well-defined peak, typical of band-edge luminescence. In these samples, the surface-trap

luminescence had a small role compared to the main peak. However, as the concentration of oleylamine increased, the intensity of the peak started to decrease (black curves in Figure 5.6). Alkylamines are known as excellent surface passivators, and previous reports on syntheses of quantum dots reported their capacity to increase photoluminescence quantum yield.[50] In fact, they can coordinate with dangling bonds on the particle surface to mitigate surface trap states, enhancing the photoluminescence intensity. While phosphines, such as TOP, will passivate the selenium dangling bonds, the alkylamines will coordinate with the cadmium ones on the particle surface. [50] Finally, we note that there was little variation across the triplicate runs performed, once again confirming the reproducibility of the workflow across a wide range of conditions.

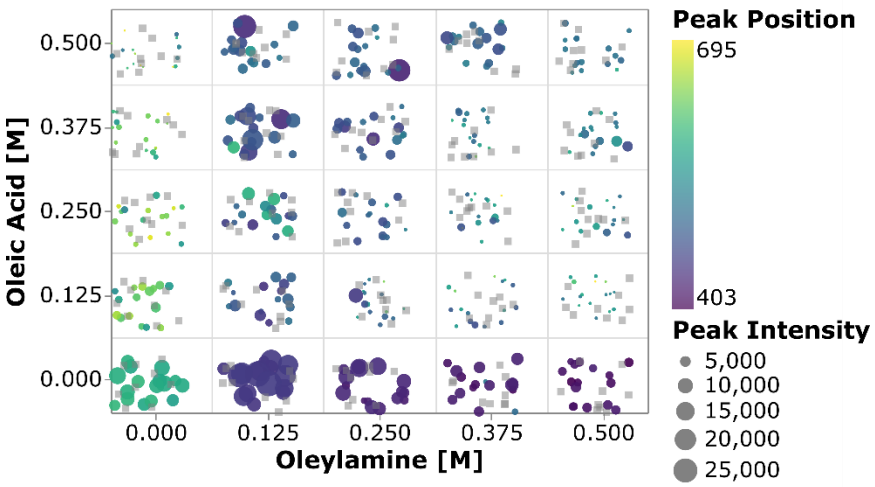

Figure 5.7 Scatter plot of emission intensity and peak position versus ligands concentration. Since each combination of conditions yielded 25 samples, noise was added to the data for plotting purposes. The grey squares indicate that no emission response was observed for those samples.

Figure 5.7 shows how the combination of oleylamine and oleic acid affected the photoluminescence intensity from band edge recombination for the entire collected dataset. It can be noticed that photoluminescence was stronger in the absence of oleic acid and for low concentrations of oleylamine. Most of the remaining samples showed either no feature in their

spectra, caused by scattering of unreacted ligands or low intensity peaks at wavelengths above 600nm, confirming the trends observed from the photoluminescence spectra.

Finally, a smaller subset of the samples was repeated and characterized using small-angle X-ray scattering, a non-destructive technique that allows for accessing structural and morphological information in materials across time scales which can range from angstrom to micrometers. Table 5.3 shows the sample compositions tested. Since the particle size had a higher dependence on the ligand concentration and composition, the samples were all tested at the highest metal precursors concentration, 0.1 M for both cadmium acetate and selenium.

Table 5.3 Sample composition for the subset of conditions characterized using Small Angle X-Ray Scattering.

Sample Name	Oleic Acid [M]	Oleylamine [M]	Cadmium Acetate [M]	Selenium [M]
CdSe 1	0	0	0.1	0.1
CdSe 2	0	0.125	0.1	0.1
CdSe 3	0.25	0.125	0.1	0.1
CdSe 4	0.5	0.125	0.1	0.1
CdSe 5	0	0.25	0.1	0.1
CdSe 6	0.25	0.25	0.1	0.1
CdSe 7	0.5	0.25	0.1	0.1
CdSe 8	0	0.375	0.1	0.1
CdSe 9	0.5	0.375	0.1	0.1
CdSe 10	0	0.5	0.1	0.1

Once again, these samples were measured 'as synthesized' and were not purified prior to characterization. SAXS was conducted before and after the sonication of the samples to gain more insights on the changes that occur during the processing step. In SAXS measurements, the intensity data is generally plotted as a function of the scattering vector 'q', which is related to the wavelength of the X-ray beam and the scattering angle.[51] This quantity can be inversely related to the characteristic dimensions of the sample, so smaller particles will present features at larger 'q'

values, the opposite is observed for larger particles. Figure 5.8 shows SAXS profiles for three samples having different ligand compositions. The panel on the left had no ligands in solutions and presents signs of particle aggregation. In fact, the sample profile post sonication (dark blue markers) shows several upturns features at different 'q' values and the slope of the SAXS curve keeps increasing towards lower 'q' values without reaching a plateau. This feature is not present, or not as prominent as in this sample, in the remainder of the samples tested using this technique, see Figure 5.8. This behaviour is in line with the UV-Vis spectroscopy data, which showed larger batch-to-batch variation and the formation of large particles for samples synthesized without addition of extra stabilizing ligands.

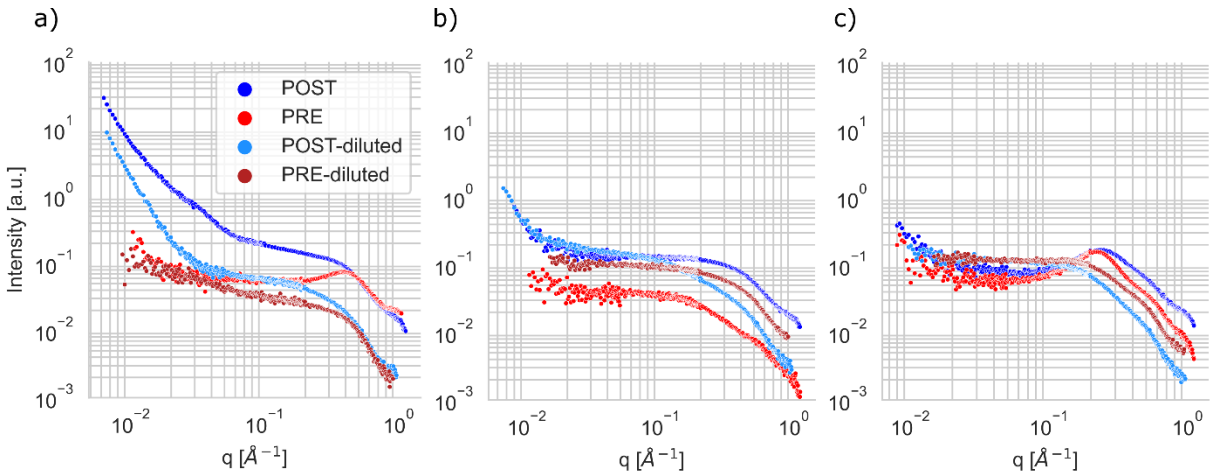

Figure 5.8 SAXS profiles of CdSe QDs sonochemically synthesized. SAXS profiles were collected for samples before and after sonochemical processing. Furthermore, to gain better insight on the particle size distribution, the samples were also diluted 4-fold in n-decane, see legend. a) SAXS profile for CdSe samples containing no ligands and metal precursors at 0.1 M each. b) SAXS profile for CdSe samples containing only oleylamine at 0.125M and metal precursors at 0.1 M each. c) SAXS profile for CdSe samples containing oleylamine at 0.375M, oleic acid at 0.5M and metal precursors at 0.1 M each.

Another feature that can be noticed on the SAXS profile is the presence of a structure factor, which appears as a local peak in the intensity curve in the proximity of the turnover point

instead of a plateau. This attribute is related to spatial interactions between particles. In this case, as expected, this behavior is more pronounced in the samples prior to sonication and for those samples containing higher concentrations of ligands, especially oleic acid (Figure 5.8c). Additionally, this can also be observed in samples post-sonication, again predominantly in those containing larger amounts of coordinating ligands. This dependency on the spatial interactions among samples is minimized or removed by diluting the samples prior to SAXS characterization.

The diluted samples were characterized and fitted using a polydisperse sphere model to extract the particle size distribution through the McSAS software. This is an open-source Monte-Carlo regression package that allows for the determination of model parameter distributions, such as the particle size distribution, which allows to assess polydispersity of the samples more quantitatively.[36] It is evident that the samples prior to sonication show coordination of the precursors. This can be confirmed by the fact that all samples tested show scattering contributions at 'high-q' values in the same range, between 4.5 $Å^{-1}$ and 6 $Å^{-1}$ regardless of samples composition (see Figure 5.8). It is noticeable that some of the samples show small scattering contributions at very high 'q' values (over 7 $Å^{-1}$). This feature is caused by slight variations in the diameter of the capillaries that were used to hold the samples during the SAXS measurements, so it was ignored during the fitting protocol. When fitting the data, it was possible to assign a target χ^2 parameter, which specifies how well the model function needs to match the experimental data. A low χ^2 indicates a good fit, while higher values imply larger uncertainties. A significant difference was noticed when fitting the pre- and post-sonication data, as the software was able to converge to a final fit when target χ^2 values were set between 1.5-5 for the former set of samples, while the processed samples were all able to obtain a good fit at a target χ^2 of 1.25 or below. Once again, the McSAS provides a histogram with particle size distribution that is useful to assess differences

in synthesis outcomes. The three panels in Figure 5.9 show the UV-Vis spectra, SAXS profiles and respective fit outcomes for diluted samples, as well as the size distribution for samples with no ligands (a), 0.125 M oleylamine and no oleic acid (b), and 0.125 M oleylamine and 0.25 M oleic acid (c), respectively.

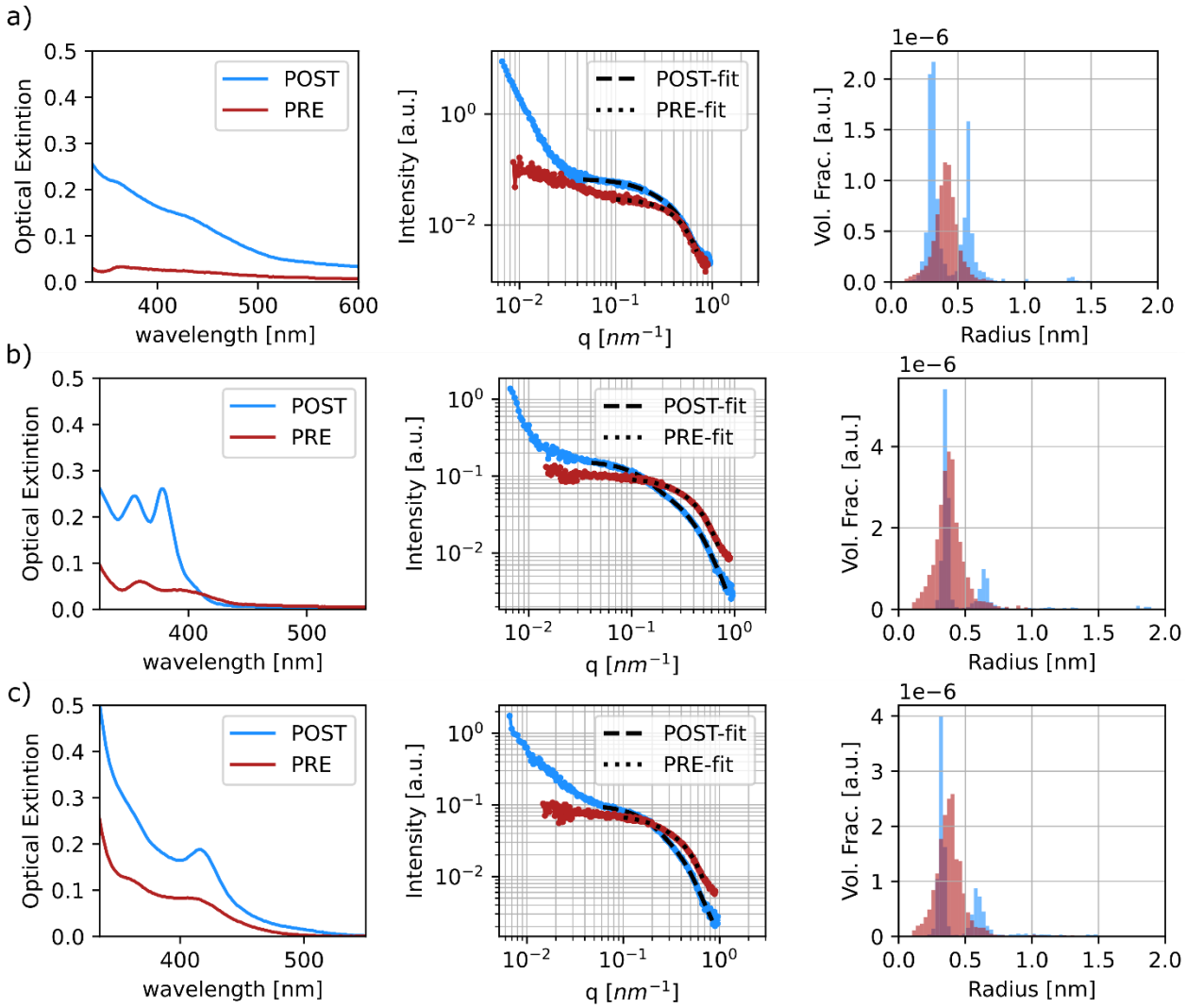

Figure 5.9 Summary of results for the characterization of samples CdSe 1 (no ligands) [a], CdSe 2 (oleylamine 0.125M) [b], and CdSe 3 (0.25M oleic acid and 0.125M oleylamine) [c]. All samples had 0.1M for both CdAc and Se precursors. In all the plots displayed, the red colored dataset represents the sample in its pre-sonicated state, whereas the blue dataset depicts the samples in its post-sonication state. Left) Uv-Vis spectra for the samples diluted in Octadecene (1:10). Center) Reduced SAXS profiles. Both curves represent the samples diluted 25% in n-decane for better data resolution. Right) Histogram of particle sized obtained from fitting the SAXS data (center) using the McSAS software.

All samples show at least two populations of particles in their profiles, with the first centering around 0.35 nm in radius. Again, looking at the distribution of sizes obtained from the

pre-sonicated samples, it is clear that this population can be attributed to precursors' coordination in solution prior to nanoparticle formation. The second and larger size population can be instead attributed to the formation of quantum dots and MSCs. Based on radius size found at the peak position of the histograms obtained from the fitting, the final particle size was approximated. For samples displaying three clusters of particle size, the value of the latter two groups were extracted and presented as a range. Table 5.4 summarizes and compares the findings of particle size based on both spectroscopic and SAXS techniques.

Table 5.4 Comparison of approximate particle size based on both UV-Vis spectroscopy and small-angle X-Ray scattering. The sphere diameter from the former technique is obtained through the effective mass approximation equation from Yu et al., whereas the particle size from the latter technique is obtained from the spherical model fitting through the McSAS GUI, specifically the radius distribution histogram.[36,52]

Sample Name	UV-Vis		SAXS
	Peak Position	D_{sphere}	D_{sphere}
CdSe 1	432	1.82	1.16
CdSe 2	379	1.36	1.3
CdSe 3	416	1.69	1.3
CdSe 4	409	1.63	1.2-1.7
CdSe 5	379	1.36	1.4
CdSe 6	413	1.67	1.3-2.1
CdSe 7	411	1.65	1.1-2.1
CdSe 8	360	1.18	1.1-2.0
CdSe 9	414	1.67	1.2-2.1
CdSe 10	363	1.21	1.4-2.6

The data generally shows good agreement for the particle size. While perfect matching of sizes was not expected, the data seems to show similar trends in the size obtained. For example,

the samples containing only oleylamine (CdSe 2,5,8,10) show the formation of smaller particles with diameters below 1.5 nm, in agreement with the trends observed using the effective mass approximation based on the peak position of the sample's UV-Vis spectrum. It is notable that the sample containing no ligand was fit to a restricted 'q-range' as the fitting protocol was not able to converge when smaller 'q' values were included. In this region the sample showed signs of aggregation and therefore the particle size presented in Table 5.4 is not fully representative of the actual particle sizes found in the samples. In this instance, agreement with the UV-Vis data was not expected based on the fitting estimation. Finally, samples that contain higher amounts of ligand, especially oleic acid, tend to present a higher variation of particle sizes. This could also be attributed to possible intermediate particles being formed during synthesis, therefore leading to higher polydispersity. This trend is in line with the findings observed from the UV-Vis data for the entirety of the design space investigated previously.

5.3.2 *Data Analysis - Impacts of Design Variables on Spectral Characteristics*

Once again, the challenges posed by the high dimensionality of the experimental space and the large amount of data generated by the experimental campaign, not only can affect the visualization of the results, but also their holistic interpretation. To address this obstacle, we implemented a model-based approach to better understand the dependencies of the design variables (i.e., concentrations of precursors and ligands) on the optical properties of the samples. The first step involves the selection of a model to predict the feature of interest. This can then be inspected to understand several parameter trends. However, the model can be selected from a variety of classes, from the simple linear model to a more complex, non-linear one. In the first type of models, the value to be predicted (e.g., the absorption peak position of the UV-Vis spectrum) is assumed to be a weighted combination of design variables. Given the linearity of the model, the

coefficients associated with each design variable can be used to interpret its relative `impact' or `importance' on the predicted feature. However, these models very seldom are able to capture the complexity of phenomena such as the synthesis of nanocrystals studied in this work. Another approach is to use a class of non-linear models, more commonly associated with the machine learning and statistics community to improve the predictive accuracy and use a separate explanation model to interpret the data. In fact, given the large amount of data that the proposed workflow generated, it is possible to fit complex and highly accurate models such as a gradient boosting algorithm like xgboost [53,54]. To make the outputs of a framework more interpretable, typical explanation models use a proxy set of simplified inputs (e.g., a binary variable indicating whether a given input is present or missing) and map them to original inputs. In this work, we make use of SHAP analysis, a strategy based on shapely values from coalition game theory via additive feature attributions. [55] At a higher level, the explanation model used in SHAP attributes feature importance based on the change (positive, zero, or negative) to the output of the predictive model relative to its average (over the training data), when conditioned on a particular feature value. The feature attribution values explain how to get from the predictive model average to the actual predicted value of any given input. This is done by averaging over all possible combinations of the input ordering sequence. One of the advantages of using SHAP is that it is locally accurate, and it can match the model prediction to the explanation prediction for each input. Next, it has missingness, so that if a feature has a value of zero or is missing data, it will have no impact on the model outcome. Finally, SHAP has the property of consistency, meaning that for two different predictive models, the impact of the inputs should follow that of the predictive models. This means that if the marginal contribution of a feature changes (i.e., decreases), its shapely value should change in the same manner (i.e., smaller shapely value) [55]

In this study, we defined the predictive model inputs to be the concentration of the precursors and ligands, as well as their respective indicator variables (i.e., a binary variable indicating whether a specie is present in the sample or not). Several models were fitted for predicting manually annotated features from the spectral data and indicator variables were used to interpret for the presence of a peak. Table 5.5 shows the accuracy of an xgboost model (trained using the python version in Chen et al. [56]) for an 80-20 train-test split.

Table 5.5 Summary of predictive model accuracy for different features of interest. The indicator features are trained using a binary logistic loss while the rest are trained using the root-mean-square-error as the loss function.

Feature to be predicted	Test Accuracy
UV-Vis peak indicator [UV_{ind}]	0.135
UV-Vis peak position [UV_{PP}]	0.433
Photoluminescence peak indicator [PL_{ind}]	0.013
Photoluminescence peak position [PL_{PP}]	0.583
Photoluminescence peak intensity [PL_{PI}]	0.781

All training data features were standardized to have a mean of zero and a standard deviation of 1. Thanks to this feature transformation, each value of the feature that is modeled represents a change from the mean (i.e. a peak shift or intensity shift from the mean), instead of the absolute values. Furthermore, to avoid data leakage, the test data was only transformed using the corresponding training data before computing the test loss. The design variable values were also transformed similarly to the features, but used a quantile transformation instead where the concentrations are binned into 5 groups, corresponding to the tested conditions All the data transformations and plotting tasks were performed using Python scripts. A total of five features were modeled, namely the absorption peak position and peak presence, as well as the photoluminescence peak presence, position, and intensity. Figure 5.10 shows the average absolute

SHAP values of the different design variables for a given predictive model using a bar chart. The design variables on the y-axis are annotated and ordered (top to bottom) based on their `global' importance in the predictive task. However, we note that each panel in Figure 5.10 corresponds to a particular predictive task where we used the exact computation of shapely values since the number of input variables is small (8) and the results would not be sensitive to a random seed used. As expected, the formation of a UV-Vis absorption peak is mainly dependent on the presence of the metal precursors, $CdAc$ and Se, but not by their concentration. This confirms what was previously noted from the spectroscopic characterization. Again, changes to the UV-Vis pea position, which can be related to the size of the QDs or MSCs formed, are mainly driven by the concentration and presence of the coordinating ligands, oleylamine and oleic acid. However, there is no dependence on the concentration of the metal precursors. Looking at the photoluminescence features, the presence of a peak is mainly observed in the presence of $CdAc$ and Se, but the actual concentration was not a significant factor in predicting whether a sample will have photoluminescence emission or not. Again, changes to photoluminescence peak position (d) and peak intensity (e) are mainly influenced by the presence of oleic acid and the concentration of oleylamine. It is important to consider the fact that the samples were measured 'as synthesized' and not cleaned prior to the spectroscopic characterization. Therefore, only a few of the samples presented a feature in their emission spectra. However, the trends learned from SHAP do match with the spectroscopic characterization.

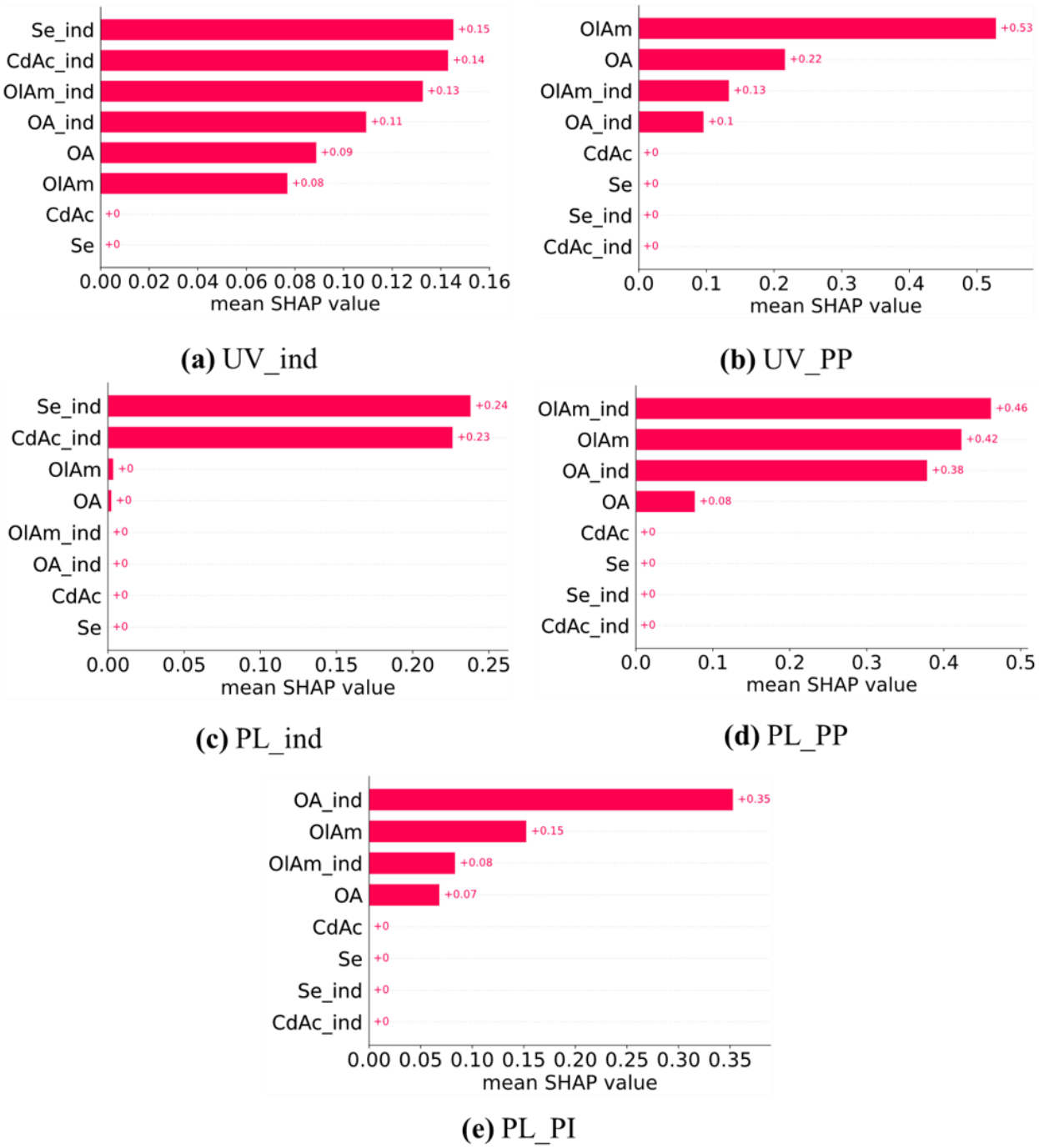

Figure 5.10 Average absolute SHAP values of different design variables for a given predictive model displayed using a bar chart. Each panel corresponds to a particular predictive task annotated in the figure caption. The design variables on the y-axis are annotated and ordered based on their `global' importance in the predictive task. Design variables are denoted as $CdAc$ for Cadmium Acetate, Se for selenium, $OlAm$ for oleylamine, and OAc for oleic acid. The features are denoted using UV for the UV-Vis extinction spectrum and PL for the photoluminescence spectrum. PP corresponds to a peak position; PI corresponds to peak intensity. In both design variables and features, the suffix '$\_ind$' corresponds to the respective indicator variable.

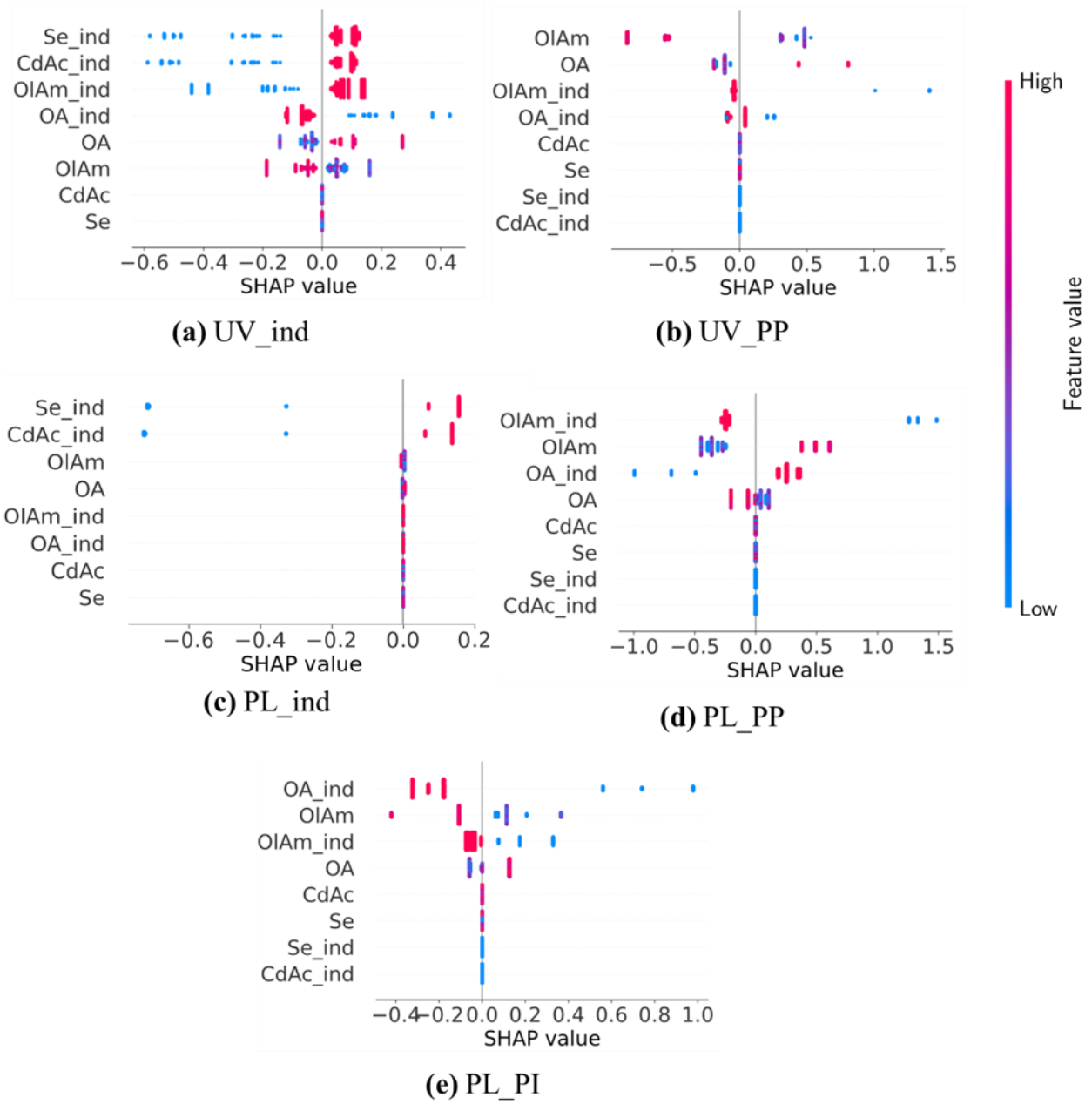

Figure 5.11 A `bee swarm' plot describing the sample distribution of influence of design variables with panels arranged and annotated in the same manner as Figure 5.10.

While the averages shown in Figure 5.10 summarize insights into the major contributions of different design variables to different features of interest, it is also useful to understand how the prediction of a particular feature changes between different samples and the nature of influence (i.e., linear vs non-linear or if it has any `interaction' effects with other variables). Individual SHAP

values are visualized using a `bee swarm' plot shown in Figure 5.11. Here the distribution of SHAP values is shown using a scatter plot, one per each design variable in the predictive model. Once again, each panel in Figure 5.11 corresponds to a model predicting a feature annotated using the title beneath it. For any given design variable in the model, we plot the SHAP value for all samples on the x-axis, and the value of the design variable is assigned a color code shown on the color bar: high (red) to low (blue) for a continuous variable and 1 (red) and 0 (blue) for an indicator variable. The distribution along the x-axis represents how the design variable's importance changes between different samples studied, while a vertical distribution shows no change, and it is used for data interpretation purposes. Once again, the design variables are ordered on the y-axis using their `global' importance. Analyzing each panel in Figure 5.11 and looking at the scatter plot distribution, the following conclusions could be drawn. First, the dependence of both UV-Vis and photoluminescence peak appearance on the presence of both cadmium acetate and elemental selenium is confirmed. This was expected as it is unlikely that we expect a peak corresponding to a $CdSe$ $q$uantum dot formation without any traces of either metal precursors. Next, the UV-Vis peak shift is strongly correlated to the specific concentration of oleylamine and oleic acid and there appears to be a non-linear effect. However, it is to note that the model is only trained (and tested) on samples that present an absorption peak since the presence of a peak is already modeled using the indicator function shown in panel (a). Nonetheless, the dependence on the ligand concentration is confirmed to have opposite trends. For higher concentrations of oleylamine, the absorption peak moves towards smaller wavelengths, while the opposite happens for higher concentration of oleic acid. Finally, the photoluminescence peak shift also shows a competing influence between the presence of oleylamine and oleic acid where a red shift is more likely in the presence of oleic acid and the absence of oleylamine and vice-versa. The position and intensity of features in the emission

spectra show no dependence on the metal precursors concentration, but mainly on the presence and concentration of ligands. Additionally, the presence of ligands shows a stronger correlation with the modeled features, compared to their respective concentrations.

5.4 CONCLUSION

The workflow for a material acceleration platform based on a sonochemical synthesis is demonstrated to enable the investigation of large experimental designs, which is extremely costly and time consuming by traditional synthetic methods. This platform provides a flexible, open-hardware, and affordable solution that can be implemented for a diverse set of chemical systems. Furthermore, given the speed and simplicity of the proposed workflow, it makes it possible to close the loop and more easily implement AI-driven strategies for achieving a certain spectral target or optimizing materials properties. These self-driving lab solutions can allow for a drastic increase of available data on these nanocrystals systems and aid in the discovery of new materials with desired chemical and physical properties.

We employed an open-source and open-hardware materials acceleration platform to study the formation of CdSe quantum dots using a sonochemical synthesis route. The range of concentrations of selenium and cadmium precursors in this Chapter only affected the number of particles generated but did not play an important role in the absorption peak position, related to particle size. On the other hand, the concentration of the ligands was the most important factor to control the particle size. The role of the ligands is related to the binding energy with the cadmium ion, which ultimately controls the nucleation rate of the synthesis. Regarding the photoluminescence emission, a similar trend was perceived. However, we found that while the presence of oleylamine favors the increase of photoluminescence intensity, the addition of oleic

acid has the opposite effect. This effect is related to the different capabilities of surface passivation between the two ligands.

Finally, a model-agnostic analysis strategy was implemented not only to confirm the trends observed in the scatter plot representation of the spectra, but to provide a quantitative breakdown of which experimental parameter contributed most to the changes in the properties analyzed. The strategy of coupling the proposed high-throughput workflow to a data-driven approach for the interpretation of the results provides a holistic view of the design space investigated. In fact, given the limitation of the traditional representation of the data (i.e., spectra) for this four-dimensional experimental space, the identification of quantitative fingerprints from the data was crucial to the generalization and understanding of how the chosen experimental conditions affected the growth and optical properties of CdSe nanocrystals.

While successful, the workflow presented in this Chapter represents a human-in-the-loop type of self-driving lab, in which the automation of the experimental procedure still relies on a researcher moving sample plates between the different workflow stations. Chapter 6 will dive deeper in how the Sonication Station, the robotic platform which allowed for the automation of sample processing, was reconfigured and its capabilities expanded to allow for a more flexible and modular system for broader laboratory automation applications.

5.5 REFERENCES

1. Carey, G. H. *et al.* Colloidal Quantum Dot Solar Cells. (2015) doi:10.1021/acs.chemrev.5b00063.
2. Dai, X. *et al.* Solution-processed, high-performance light-emitting diodes based on quantum dots. *Nature* **515**, 96–99 (2014).
3. Bruchez, M., Moronne, M., Gin, P., Weiss, S. & Alivisatos, A. P. Semiconductor nanocrystals as fluorescent biological labels. *Science* **281**, 2013–2016 (1998).

4. Sakaue, H., Aikawa, A. & Iijima, Y. Anodized-aluminum as quantum dot support for global temperature sensing from 100 to 500 K. *Sens Actuators B Chem* **150**, 569–573 (2010).
5. Lv, Z. *et al.* Semiconductor Quantum Dots for Memories and Neuromorphic Computing Systems. *Chem Rev* **120**, 3941–4006 (2020).
6. Sadeghi, S., Khabbaz Abkenar, S., Ow-Yang, C. W. & Nizamoglu, S. Efficient White LEDs Using Liquid-state Magic-sized CdSe Quantum Dots. *Scientific Reports 2019 9:1* **9**, 1–9 (2019).
7. Kumari, K. *et al.* Effect of surface passivating ligand on structural and optoelectronic properties of polymer : CdSe quantum dot composites. *J Phys D Appl Phys* **41**, 235409 (2008).
8. de Mello Donegá, C., Liljeroth, P. & Vanmaekelbergh, D. Physicochemical evaluation of the hot-injection method, a synthesis route for monodisperse nanocrystals. *Small* **1**, 1152–1162 (2005).
9. Liu, Z., Shamsuzzoha, M., Ada, E. T., Reichert, W. M. & Nikles, D. E. Synthesis and activation of Pt nanoparticles with controlled size for fuel cell electrocatalysts. *J Power Sources* **164**, 472–480 (2007).
10. Pan, D. *et al.* Synthesis of Cu-In-S ternary nanocrystals with tunable structure and composition. *J Am Chem Soc* **130**, 5620–5621 (2008).
11. Protesescu, L. *et al.* Nanocrystals of Cesium Lead Halide Perovskites (CsPbX3, X = Cl, Br, and I): Novel Optoelectronic Materials Showing Bright Emission with Wide Color Gamut. *Nano Lett* **15**, 3692–3696 (2015).
12. Nemamcha, A., Rehspringer, J. L. & Khatmi, D. Synthesis of palladium nanoparticles by sonochemical reduction of palladium(II) nitrate in aqueous solution. *Journal of Physical Chemistry B* **110**, 383–387 (2006).
13. Okitsu, K., Ashokkumar, M. & Grieser, F. Sonochemical synthesis of gold nanoparticles: effects of ultrasound frequency. *J Phys Chem B* **109**, 20673–20675 (2005).
14. Xu, H. & Suslick, K. S. Sonochemical synthesis of highly fluorescent Ag nanoclusters. *ACS Nano* **4**, 3209–3214 (2010).
15. Mizukoshi, Y. *et al.* Preparation of platinum nanoparticles by sonochemical reduction of the Pt(IV) ions: role of surfactants. *Ultrason Sonochem* **8**, 1–6 (2001).
16. Su, C.-H., Wu, P.-L. & Yeh, C.-S. Sonochemical Synthesis of Well-Dispersed Gold Nanoparticles at the Ice Temperature. (2003) doi:10.1021/jp035451v.
17. Kristl, M. & Drofenik, M. Preparation of Au2S3 and nanocrystalline gold by sonochemical method. *Inorg Chem Commun* **12**, 1419–1422 (2003).
18. Jung, S. H. *et al.* Sonochemical preparation of shape-selective ZnO nanostructures. *Cryst Growth Des* **8**, 265–269 (2008).
19. Yin, L., Wang, Y., Pang, G., Koltypin, Y. & Gedanken, A. Sonochemical synthesis of cerium oxide nanoparticles-effect of additives and quantum size effect. *J Colloid Interface Sci* **246**, 78–84 (2002).

20. Wang, H., Lu, Y. N., Zhu, J. J. & Chen, H. Y. Sonochemical fabrication and characterization of stibnite nanorods. *Inorg Chem* **42**, 6404–6411 (2003).
21. Wang, G., Li, G., Liang, C. & Zhang, L. Sonochemical Synthesis and Phase Control of Nanocrystalline CdS. *http://dx.doi.org/10.1246/cl.2001.344* 344–345 (2002) doi:10.1246/CL.2001.344.
22. Peng, Z. A. & Peng, X. Formation of high-quality CdTe, CdSe, and CdS nanocrystals using CdO as precursor [6]. *J Am Chem Soc* **123**, 183–184 (2001).
23. Kristl, M. & Drofenik, M. Sonochemical synthesis of nanocrystalline mercury sulfide, selenide and telluride in aqueous solutions. *Ultrason Sonochem* **15**, 695–699 (2008).
24. Hobson, R. A., Muivaney, P. & Grieser, F. *Formation of Q-state CdS Colloids using Ultrasound*. *J. CHEM. SOC., CHEM. COMMUN* (1994).
25. Kastilani, R., Bishop, B. P., Holmberg, V. C. & Pozzo, L. D. On-Demand Sonochemical Synthesis of Ultrasmall and Magic-Size CdSe Quantum Dots in Single-Phase and Emulsion Systems. *Langmuir* **35**, 16583–16592 (2019).
26. Murcia, M. J. *et al.* Facile sonochemical synthesis of highly luminescent ZnS-shelled CdSe quantum dots. *Chemistry of Materials* **18**, 2219–2225 (2006).
27. Suslick, K. S. Sonochemistry. *Science (1979)* **247**, 1439–1446 (1990).
28. Suslick, K. S. The Chemical Effects of Ultrasound. *SCIENTIFIC AMERlCAN* 80–86 (1989).
29. Yu, C.-L., Yu, J. C., He, H.-B. & Zhou, W.-Q. Progress in Sonochemical Fabrication of Nanostructured Phptocatalysts. *Rare Metals* **35**, 211–222 (2016).
30. pozzo-research-group. Automation-Hardware: Pozzo Group OT2 Hardware. *GitHub* https://github.com/pozzo-research-group/Automation-Hardware (2021).
31. Antonio, E. & Politi, M. pozzo-research-group/OT2-DOE. https://github.com/pozzo-research-group/OT2-DOE (2022).
32. Vasquez, J., Twigg-Smith, H., Tran O'leary, J. & Peek, N. Jubilee: An Extensible Machine for Multi-tool Fabrication. doi:10.1145/3313831.3376425.
33. Vasquez, J. machineagency/jubilee. *GitHub* https://github.com/machineagency/jubilee (2021).
34. Vasquez, J. & Peek, N. machineagency/sonication_station. *GitHub* https://github.com/machineagency/sonication_station (2020).
35. Breßler, I., Pauw, B. R. & Thünemann, A. F. McSAS: A tool for extracting form-free size distributions of small-angle scattering (SAS) patterns using a Monte-Carlo method. *GitHub* Preprint at https://github.com/BAMresearch/McSAS (2022).
36. Bressler, I., Pauw, B. R. & Thünemann, A. F. McSAS: Software for the retrieval of model parameter distributions from scattering patterns. *J Appl Crystallogr* **48**, 962–969 (2015).
37. Jiang, Y. *et al.* Synthesis of CdSe Nanoplatelets without Short-Chain Ligands: Implication for Their Growth Mechanisms. *ACS Omega* **3**, 6199–6205 (2018).

38. Yu, W. W., Qu, L., Guo, W. & Peng, X. Experimental determination of the extinction coefficient of CdTe, CdSe, and CdS nanocrystals. *Chemistry of Materials* **15**, 2854–2860 (2003).
39. Abe, S., Capek, R. K., de Geyter, B. & Hens, Z. Reaction chemistry/nanocrystal property relations in the hot injection synthesis, the role of the solute solubility. *ACS Nano* **7**, 943–949 (2013).
40. Heuer-Jungemann, A. *et al.* The Role of Ligands in the Chemical Synthesis and Applications of Inorganic Nanoparticles. (2019) doi:10.1021/acs.chemrev.8b00733.
41. Zhu, D. *et al.* Interpreting the Ultraviolet Absorption in the Spectrum of 415 nm-Bandgap CdSe Magic-Size Clusters. *J Phys Chem Lett* **9**, 2818–2824 (2018).
42. Harrell, S. M., McBride, J. R. & Rosenthal, S. J. Synthesis of ultrasmall and magic-sized CdSe nanocrystals. *Chemistry of Materials* **25**, 1199–1210 (2013).
43. Dai, Q. *et al.* Facile synthesis of magic-sized CdSe and CdTe nanocrystals with tunable existence periods. *Nanotechnology* **18**, 405603 (2007).
44. Pun, A. B., Mule, A. S., Held, J. T. & Norris, D. J. Core/Shell Magic-Sized CdSe Nanocrystals. (2021) doi:10.1021/acs.nanolett.1c02412.
45. Huang, X., Parashar, V. K. & Gijs, M. A. M. Nucleation and Growth Behavior of CdSe Nanocrystals Synthesized in the Presence of Oleylamine Coordinating Ligand. *Langmuir* **34**, 6070–6076 (2018).
46. García-Rodríguez, R. & Liu, H. Mechanistic insights into the role of alkylamine in the synthesis of CdSe nanocrystals. *J Am Chem Soc* **136**, 1968–1975 (2014).
47. Karel Čapek, R. *et al.* Optical properties of zincblende cadmium selenide quantum dots. *Journal of Physical Chemistry C* **114**, 6371–6376 (2010).
48. Bootharaju, M. S. *et al.* Magic-Sized Stoichiometric II-VI Nanoclusters. *Small* **17**, (2021).
49. Hill, N. A. & Whaley, K. B. A theoretical study of the influence of the surface on the electronic structure of CdSe nanoclusters. *J Chem Phys* **100**, 2831 (1994).
50. Kim, W., Lim, S. J., Jung, S. & Shin, S. K. Binary amine-phosphine passivation of surface traps on CdSe nanocrystals. *Journal of Physical Chemistry C* **114**, 1539–1546 (2010).
51. Li, T., Senesi, A. J. & Lee, B. Small Angle X-ray Scattering for Nanoparticle Research. (2016) doi:10.1021/acs.chemrev.5b00690.
52. Yu, W. W., Qu, L., Guo, W. & Peng, X. Experimental Determination of the Extinction Coefficient of CdTe, CdSe, and CdS Nanocrystals. (2003) doi:10.1021/cm034081k.
53. Friedman, J., Hastie, T. & Tibshirani, R. *Additive Logistic Regression: a Statistical View of Boosting*. *The Annals of Statistics* vol. 28 (2000).
54. Friedman, J. H. Greedy Function Approximation: A Gradient Boosting Machine on JSTOR. *The Annals of Statistics* **29**, 1189–1232 (2001).
55. Lundberg, S. M., Allen, P. G. & Lee, S.-I. A Unified Approach to Interpreting Model Predictions. *Proceedings of the 31st International Conference on Neural Information Processing Systems* (2017).

56. Chen, T. & Guestrin, C. XGBoost: A Scalable Tree Boosting System. *Proceedings of the 22nd ACM SIGKDD International Conference on Knowledge Discovery and Data Mining* 785–794 (2016) doi:10.1145/2939672.2939785.

Chapter 6. SCIENCE JUBILEE, A LOW-COST, OPEN-HARDWARE SELF-DRIVING LAB

This chapter partly contains work from the following publication and the author would like to acknowledge the contributions of the coauthors:

Lo, S., Baird, S., Schrier, J., Blaiszik, B., Carson, N., Foster, I., Aguilar-Granda, A., Kalini, S., Maruyama, B., **Politi, M.,** Tran, H., Sparks, T., Aspuru-Guzik, A. Review of Low-cost Self-driving Laboratories: The "Frugal Twin" Concept. *Digital Discovery,* 2024. DOI: https://doi.org/10.1039/D3DD00223C

6.1 INTRODUCTION & MOTIVATION

Traditional materials science and chemistry workflows rely heavily on labor- and time-intensive steps. While these experimental protocols can provide significant insights into the system under investigation, they can also significantly impede the pace of new materials discovery and their successive applications. Within the past five years, the advent of a new science paradigm has the potential to accelerate the pace of materials discovery. [1] The key to this paradigm is not based solely on the advancement of a key technology, but how heterogeneous capabilities cooperate to achieve greater and better advancements.[2] In fact, this novel approach to science combines autonomous robotic systems, designed to conduct scientific experiments and research, with minimal to no human intervention. Furthermore, it integrates both computation and physical cutting-edge technologies such as artificial intelligence, robotics, and advanced sensors to perform tasks traditionally carried out by scientists. These ecosystems not only incorporate automation and artificial intelligence (AI), but also include several data and communication orchestration strategies, data management, and scheduling along with human creativity and intuition.[3] All of these are crucial components required for accelerating the pace of discovery, optimization, and implementation of new materials. The combination of these features has been called many names, including self-driving laboratories (SDLs), [1,4–8] materials acceleration platforms (MAPs), [3,9–11] Lab

4.0, [12,13] Robot Scientist, [14,15] autonomous research system (ARES), [16] and autonomous experimentation systems. [17] One note to make is that while these terms have been used almost interchangeably in the community, in particular the first two in the list, there can be slight differences in emphasis between them. For example, MAP conveys a more specific focus on materials research and innovation within the broader context of self-driving labs. Nonetheless, in this Chapter, the terms are used synonymously to describe an autonomous, experiment-performing system. Additionally, I will define "autonomy" as the ability of a system to make decisions and perform all manual experimental steps completely independently, without the need for human interaction. Systems that are autonomous perform what are defined as "closed-loop" workflows, in which the AI-agent drives all aspects of the experimental campaign. On the other hand, "automation" implies a human-in-the-loop type of approach in which the researcher will be tasked to complete some actions (e.g., move samples from one platform to another) to "close the loop."

Self-driving labs can streamline experimental processes, enhance efficiency, and reduce human error in experimental campaigns. These autonomous laboratories have the potential to revolutionize various fields by enabling round-the-clock experimentation without the limitations of human availability. In fact, not only is the researcher not required to perform manual tasks, but with the automation of data collection, handling, interpretation, and storage, the time between execution and decision-making for the next iteration of conditions to test gets significantly shortened. Moreover, the use of robotic platforms also promises to eliminate batch variability due to human errors, allowing to track and quantify systematic errors, leading to more reproducible and shareable procedures. The main advantage of these platforms is the possibility to investigate broader experimental spaces for both synthesis and parameter optimization. Robotic platforms have been successfully applied to synthesize organic compounds of pharmaceutical interest [18–20],

nanomaterials[21–28], materials science [29], chemistry [18,30,31], and biotechnology [20,32,33], among others. However, materials acceleration platforms still present some limitations, such as 'rigid' designs (i.e., only intended for use of specific materials, reaction models, or applications) and high upfront costs of implementation in the laboratory. This limits incentives to integrate such platforms, and most wet-lab researchers still rely on low-throughput, time intensive workflows. [34] The highest benefit of SDLs will be achieved by closed-loop design approaches, in which the experimental campaign is conducted completely without human intervention by relying on AI agents for data analysis and decision-making, and robotic platforms for all the physical sample manipulation and characterization.

There are several approaches that can be taken to design a self-driving lab or automated workflow. These options stem from unique design solutions to automating the different manual tasks involved in an experimental procedure. There are three main categories: human-inspired, hardware-centric, and human-in-the-loop designs. [35] The first class relates to the interface of traditional instrumentation with a robotic arm that can mimic human behavior. This can be significantly advantageous as it can be directly integrated with conventional infrastructures for materials characterization without the need to integrate into a single workstation. [8] These robotic arms can be either stationary or mobile. One of the most prominent examples of an SDL based on human-inspired design is the work conducted by Burger et al. at the University of Liverpool. [36] Their "Mobile Robotic Chemist" consists of a KUKA Mobile Robot and platform base, which was tasked with evaluating several sample conditions to improve photocatalysis for hydrogen generation form water. The robot was coupled with a Bayesian Optimization algorithm to autonomously complete the task by varying up to 10 parameters over the course of 8 days. [36] Unfortunately, while appealing, these mobile robotic arms can have prohibitive costs.

Additionally, they can require the modification of a physical laboratory space to be adapted to the robot's movement paths and elimination of any obstacles, and most of the time this includes human researchers as well. Moreover, this can also require a single dedicated space which cannot be achieved by academic groups due to lack of resources and space. The use of these mobile robots will also require extensive routine and position calibration, which can be tedious and time-intensive. [35] Another approach to using these human-inspire robot arms is to use stationary ones. For example, MacLeod et al. showcased one such example for the optimization of optical and electronic properties of thin-films. [6,37] In this case, the robotic arm acts as a central connection point in between different experimental components, such as the film synthesis platform, the film annealing one and other characterization stations. Wagner et al. showcased another example of a SDL in which the robotic arm is placed on rail along the length of the platform, in this case contained within a glove box for air- or water-sensitive chemistries, to have access to all the stations required for the experimental workflow. [11] These flexible solutions can be easily reconfigured as new components can be added, or existing ones rearranged to adapt the workflow to other materials synthesis. Including modularity in the initial SDL design can provide significant advantages over rigid designs. Furthermore, this strategy can reduce the overall implementation cost and maintenance of the instrument in the inevitable case that one of the components needs repair or substitution. [35] Consideration for these robotic arms are their maximum payload and the ability to reach all components of an SDL. They can also require custom grippers to facilitate or enable specific sample or labware handling, which will in turn increase the overall cost of the tool.

The second design approach is a hardware-centric one. In this case, the experimental process does not rely on procedures that mimic human behavior, but instead focuses on leveraging the hardware capability to complete the design task. A simple example of this would be to use a

pipette to mix a solution by sequential aspiration and dispense steps instead of relying on a stir bar and magnetic plate. [35] Another such approach is the use of microfluidic systems, a combination of pumps and tubing for transferring the samples between the different workstations composing the SDL. [8] There are already successful examples of this approach in the literature. The SDL designed by Bateni et al., Smart Dope, builds on a flow chemistry platform for the formulation, in-situ monitoring, and subsequent characterization of reactions for the synthesis of colloidal lead halide perovskites quantum dots. [38] While flexible and extensible to other chemistries, this type of approach can only work for liquid-based synthesis and can have limitation with high-viscosity samples. Finally, the third design approach is the human-in-the-loop one. Sometimes, it is simpler to keep the researcher in the loop to take care for example of moving the samples from the synthesis to the characterization instruments, than implementing a robotic arm. This strategy was displayed for example by Vaddi et. al. who combined an Opentrons OT-2 liquid handling robot to a plate reader for the synthesis of gold-nanorods [39] or the workflow described in Chapter 5.

The application of high-throughput experimentation systems and automation platforms has been more limited at the broader academic scale primarily due to economic reasons and significant initial time and resource investment. However, this trend was present at the beginning of the development of this new way of carrying out experiments in the biochemistry and medical field.[40] As more and more companies designing materials science tools and instruments adopt these strategies, the cost of technology and instrumentation costs will progressively decrease, allowing further accessibility of automation solutions by groups from diverse academic institutions, both at research and educational levels. It is known that industry plays a crucial role in addressing the challenges posed by the required hardware and software for SDLs. Currently, experimental automation has been more commonly implemented in biological science and medicinal chemistry

thanks to a larger commercial push on technological development. [8] Unfortunately, the realm of inorganic chemistry and materials science is still lagging as their characterization techniques still rely on high-fidelity, single-sample type of protocols. Nonetheless, there has been a recent increase in manufacturers that offer off-the shelf automated instrumentation for a variety of processing and materials characterization. These products span a large cost range, starting from $10,000 USD to upwards of $1 million USD, as they can be configured as single benchtop workstation, such as an Opentrons OT-2 liquid handling robot, or as a full integrated solution for product development such as those offered by Chemspeed or Unchained Labs. The implementation of these solutions in completely autonomous systems is still a work in progress, but there are already successes in literature that provide a notable example of the impact that these SDLs can have on the scientific community. Platforms from Chemspeed have been implemented by Christensen et al. to optimize Suzuki-Miyaura cross-coupling reaction,[41] as well as IBM's RoboRxn for chemistry, which can also be accessed remotely.[42] Both of these implemented a hardware-centric design. As they were mentioned before, the SDL implementing commercial mobile robotic arms can be found in MacLeod et al. [6,37] and Burger et al. [36] Next, Vapourtech provides an example of a commercial flow reactor which was used by Jeraal et al. for reaction conditions optimization. [43] While commercial solutions do not require upfront time dedicated to their design and orchestration, it can be challenging to reconfigure them for workflows for new materials spaces. In fact, they can still be difficult to integrate in current workflow architectures or even in the lab. For example, a mobile robot might require a dedicated room to accommodate or simplify the movement paths. Unfortunately, most academic research groups and institutions still rely on very few simple semi-automated equipment. These workflows fall under the human-in-the-loop design category. In fact, they currently seem to be the most common in literature as with most flow-based syntheses the

combination of a liquid handling robot with a plate reader can automate the majority of the time-intensive steps. Nonetheless, the focus of the automation task is usually on the sample formulation, while the processing and characterization can still cause a bottleneck, as most high-fidelity instrumentation still requires single-sample protocols.

Flexible and reconfigurable automated workflows have the potential to encourage the transition from conventional laboratories to a new paradigm of science. To address their limitations and lower the barrier of entry to these SDL technologies for a more wide-spread use of automation systems, academic groups have been making use of open-source hardware (OSH) systems to creatively provide an alternative to expensive platforms. [44,45] These are physical devices whose designs are made publicly available for anyone to replicate, modify, distribute, and manufacture. This emphasizes transparency and collaboration among both research groups and industry. It also allows individuals and organizations to freely access, improve, and share hardware products without restrictive licenses or proprietary constraints. The openness of these designs fosters innovation and promotes interoperability among different hardware components and systems. [46] Examples of open-hardware tools in the research context include solutions such as the adaptation of 3D printers and platforms, [47–49] platforms for modular automated workflows, [34] pipetting robot platforms, pipettes, and autosamplers, [49–56] and imaging [57–60]. There are also examples of open-hardware materials acceleration platforms. For example, the automated titrator LEGOLAS, built from LEGO by Saar et al., can perform liquid dispensing and measure pH. The design involves a combination of 3D-printed parts, Raspberry Pi components, and metal extrusions, along with the modular toy parts.[61] Next, a light mixing demo composed of a Raspberry Pi Pico microcontroller and a light sensor designed by Baird & Sparks, makes a simple and complete SDL for autonomous color-mixing tasks.[62] Another example is the automation of the synthesis of metal-organic

frameworks conducted by Xie et al. using a reconfigured 3D printer. [63] A successful demonstration of a fully autonomous, open-source, and open-hardware workflow was developed at the National Institute of Standards and Technology (NIST) by Beaucage and Martin. [64] The developed an autonomous formulation laboratory implementing commercial off-the-shelf components (i.e., an Opentrons OT-2 liquid-handling robot, syringe pumps, and flow selectors), along with custom components, all orchestrated using a Python-based microservice software solution. This experimental set up can also be integrated into the x-ray and neutron scattering instrumentation found at their facility. Moreover, their physical and software set up allows for reconfigurability and the addition of new in-line or secondary measurements devices. These examples of automated and semi-automated tools with multi-use and application-agnostic features make for a more accessible and affordable system for increasing the throughput of material discovery.

Although laboratory automation increases precision and the efficiency of science experiments, a one-size-fits-all solution does not necessarily exist for science experiments. As mentioned, the maker movement has introduced open-source hardware toolkits for computer-controlled tasks, enabling low-cost, customizable, and extensible technologies for automation. [65] These toolkits have so far predominantly been used for digital fabrication applications such as 3D printing. However, these technologies are increasingly customized by scientists for laboratory automation tasks. This Chapter will describe the development of an open-source and open-hardware, modular, and closed-loop laboratory automation platform based on a repurposed, tool-changing 3D printer. Next, it will briefly cover the structure of a new Python-based high-level control software to facilitate machine control, as well as the steps required when implementing a new tool onto the robotic platform. Its implementation for autonomous workflows will be evaluated based on a benchmarking protocol for SDLs, an autonomous color-mixing problem.

Finally, discussion of the current limitations and potential future solutions to them will be provided, along with an outlook to how low-cost, open-hardware laboratory automation design can impact materials science research, as well as enabling automation tools to be included in hands-on educational curricula.

6.2 The Robotic Platform

6.2.1 *The Original Jubilee Design*

Jubilee is an open-hardware and software 3D printing platform developed by Vasquez et al. [66] Originally, Jubilee was designed for multi-tool digital fabrication tasks and more. Examples of its initial application ranged from multi-head 3D printing, multi-pen plotting, and image stitching applications. Jubilee presents a modular, automatic tool-changing design allowing the platform to be tool-agnostic. This key feature allows for simple inclusion of user-designed tools, as well as beds. One of the main design principles of this platform is defined as "fabricatability", the instance in which all parts required to build a Jubilee can be readily sourced in low volume, readily 3D printed and assembled using commonly available maker tools (i.e., screwdrivers, hex keys, metric screws, etc.). [66,67] The platform can be purchased as a kit, but it still requires the user to build the machine and its tools themselves. The availability of purchasing the kit for less than $\$\,2{,}000\ USD$, including a few customizable options, significantly lowers the barrier of entry to this tool by eliminating time-intensive and frustrating tasks to source each build component individually through the project's bill of materials (BOM). [67] Additionally, Jubilee comes with a variety of documentation and resources to support users during the building phase, such as a project Wiki containing visual instructions and videos, machine tuning procedures, and tool template designs. Furthermore, there is an active Discord channel for informal communication, which also allows for prompt help for any machine related issue or even for tool (re)design. [68] All of these

features were the reason that Jubilee was selected to be a new laboratory automation tool. As shown in Chapter 5, the inclusion of new tools can allow for solutions which are not readily available for purchase. The sonicator probe used for the sonochemical synthesis of nanoparticles discussed before required no modification to the existing platform. Moreover, both the processing tool and Jubilee can be individually used in other contexts as they do not have any hardware or software constraints. This is not the case for other commercially available laboratory automation platforms, which will only allow instrumentation developed by the same manufacturer to be used. The flexibility and modularity of Jubilee are another advantage of this technology.

Currently, documented applications using this platform mostly fall in the category of digital fabrication, with few instances that make use of cameras for monitoring samples or others simple liquid-handling/gel printing tasks using a syringe tool. The application of more complex workflows is still lagging. However, it is possible to integrate all necessary tools to create a closed-loop experimental system. Nonetheless, before these platforms which originated from the digital fabrication space can be safely implemented in chemistry and materials science laboratories, they might require additional hardening of the frame and alternative to PLA-based parts to broaden their material compatibility. This Chapter will focus on the initial efforts made to broaden the tool library available to use with Jubilee, as well as the creation of a new python-based control language to allow scientist and researchers to use higher-level commands for interfacing with the machine. Solutions stemming from the open-hardware community can significantly lower the barrier of entry to laboratory automation. They have the potential to support community-driven projects for the co-creation and maintenance of new, modular, and flexible platforms for chemistry and materials science self-driving laboratories. By openly sharing designs and ideas, the efforts to

develop new tools can be shared among the community which avoids duplication of efforts and can lead to the creation of new standards for these fields.

6.2.2 *Jubilee for Science Applications*

Autonomous laboratories hold the potential to streamline experimental processes, enhance efficiency, and mitigate human errors. However, these physical systems require an advanced control language and architecture that allow straightforward communication with the machine. A new Python-based repository was created to develop science protocols using this reconfigured 3D printing platform. This new instance of Jubilee was named Science Jubilee, and it stems from a further collaboration with Machine Agency, the group of Dr. Nadya Peek, a professor in the Human Centered Design and Engineering department at the University of Washington, who supervised the original Jubilee design. [69] As Jubilee becomes more of a community tool, the structure of the control language repository and the tools available for implementation on the platform will evolve and improve. The content of this section aims to provide a starting point and a gentle introduction to the work completed so far.

6.2.2.1 A Python-based Control Language

When designing a new machine control language, there are considerations that need to be addressed. One consideration revolves around the intended user of this product. Out of the box, Jubilee is controlled using a Duet3D main board, which is implemented and designed for additive/subtractive manufacturing machines. [70] The programming language this board expects to receive is `g-code`, a domain-specific language primarily used in 3D printing and CNC machines. [71] Most users from the digital fabrication space will use slicers, software dedicated to generating the sequence of `g-code` the machine will need to perform for the task at hand. In this case, the user is not required to auto-generate the protocol files and does not need to know programming

language to use the machine. In fact, the slicer takes care of the task abstraction and allows the user to define their instrument parameters and tools directly from a GUI. The slicer software is also machine-agnostic and can be configured to be used with any brand and model of 3D printer. Unfortunately, such computational tools do not exist for laboratory automation. However, there was a need to have a high-level language that can be research and human oriented, to remove the domain-specific knowledge, and to make the system more accessible to a broader audience. An immediate choice was Python, a ubiquitous programming language, especially in the materials and chemical sciences. Figure 6.1 displays a simplified schematic of the Science Jubilee repository. This project is a new instance of the original Jubilee repository on GitHub, specific to running autonomous/automated experimental workflows using Jubilee. [72]

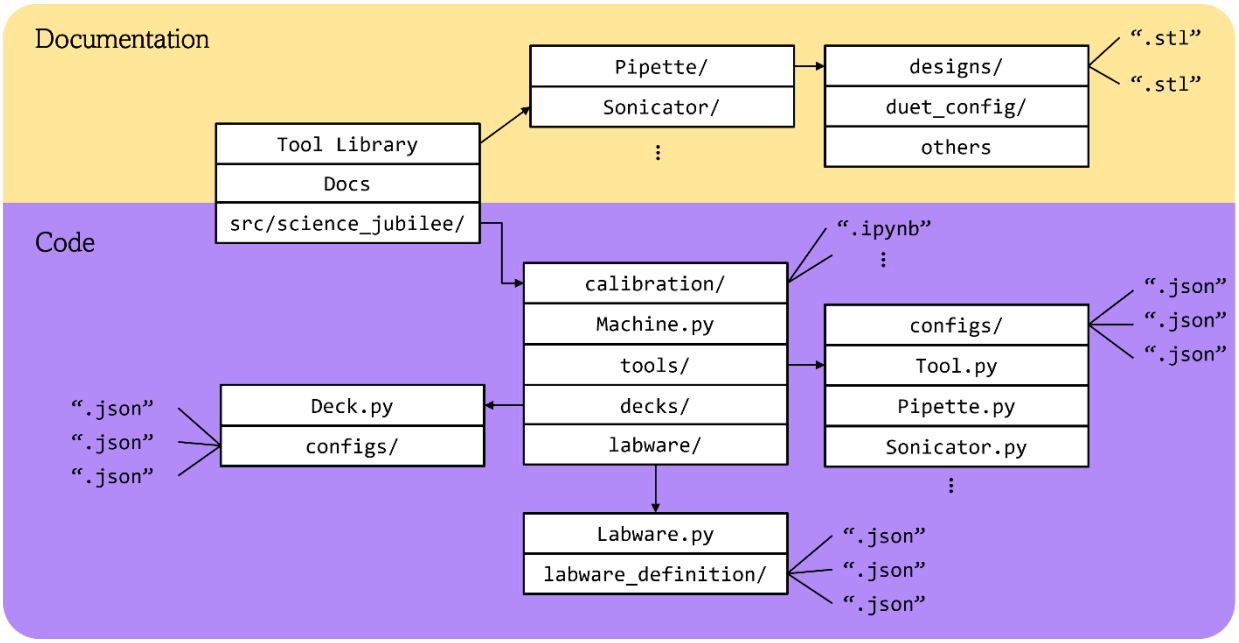

Figure 6.1 A simplified schematics of the Science Jubilee repository showcasing the different components. The top level is divided into a Documentation and a Code section. The former is composed of a Tool Library which contains the design files and instructions on how to build and integrate each tool onto a Jubilee. Next, the documentation folder contains all the files used to compile the project's readthedocs.io page. The latter section contains all the code required to control your platform (i.e., Machine.py), your tools (i.e., the tool-specific `.py` modules), as well as the deck and labware modules and definitions. This modular structure allows for flexible workflows to be integrated both physically and computationally.

At the highest level, the repository can be divided into two sections: Documentation and Code. The former is composed of a t*ool library* which contains the design files and instructions (Figure 6.2) on how to build and integrate each tool onto a Jubilee. Next, the *documentation* folder contains all the files used to compile the project's readthedocs.io page. The latter section contains all the code required to control your platform (i.e., `Machine.py`), your tools (i.e., the tool-specific `.py` modules), as well as the deck and *labware definitions* and *configuration files*. This modular structure allows for flexible workflows to be integrated both physically and computationally. There

are example Jupyter Notebook files in the *calibration* folder to walk users through machine/tool calibration routines and example protocol set-up.

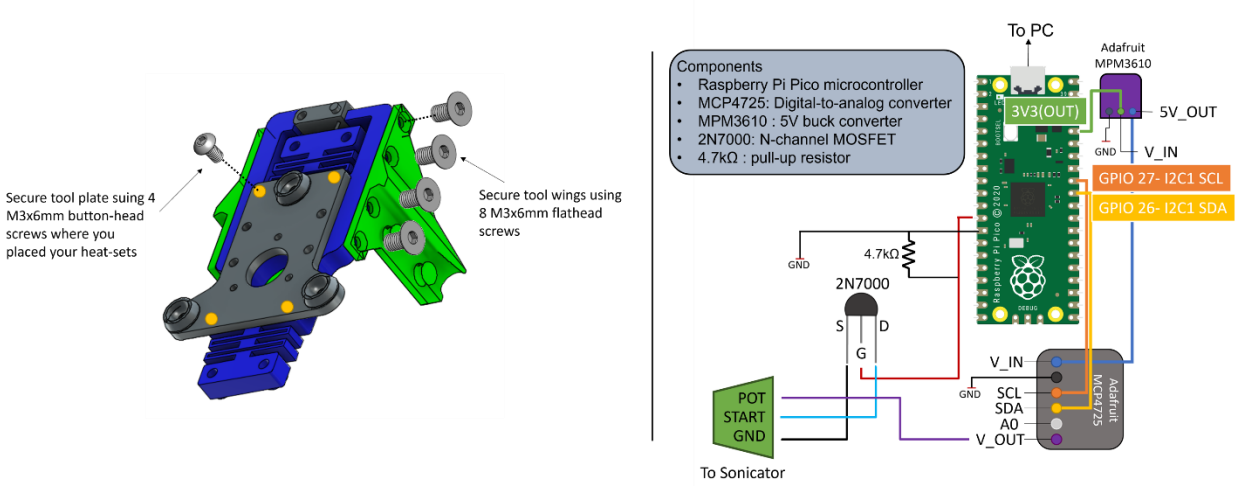

Figure 6.2 Example documentation files: a snipped from building instructions of the OT-2 Pipette tool plate (Left) and the schematic to reproduce the microcontroller that runs the sonicator tool board. (Right)

Another important consideration is to correctly identify the initial scope of the instrument, while also embedding features to ensure flexibility and modularity of the control language. In this case, the intended use of Jubilee is to perform generalizable science tasks involving synthesis, processing, and characterization of samples. The platform is interfaced through the `machine.py` module with a python interpreter of choice. This module takes care of all the elementary machine-oriented operations such as motion control of the platform components, sending `g-code` commands to the Duet3D board, and the tool handling commands such as (i.e., `machine.pickup_tool("tool_name")` and `machine.park_tool()`). To allow for more modularity, the definition and control of any tool is contained in individual `.py` modules. Each tool will have its own associated module containing all the possible actions each tool can complete, e.g., `camera.capture_image()` or `pipette.pickup_tip()`. This structure allows for easier tool integration and separates the machine movement and tool actions tasks,

which allows for tool modules to be more machine-agnostic and require only small (if any) modifications to be used in other laboratory contexts.

Figure 6.3 shows an example protocol set up based on the Science Jubilee repository. The structure is intended to mimic the physical machine set up and to add some redundancy as a high-level safety check. In fact, the user is required to define all the components needed to conduct the desired workflow. First, the connection to the Jubilee machine is established. The interface of the Duet3D board can be done in standalone mode, using a PC or computer via ethernet cable or Wi-Fi. A second option exists by using a single board computer (SBC), such as a Raspberry Pi board. Next, the deck can be defined using a configuration file. This contains geometric details, dimensions, and any unique features of the selected bed, such as number of slots and their coordinate points. The labware can then be defined by their definition file and the index of the deck's slot it will be placed on. It is to note that the labware definition files and the *`Labware.py`* file were heavily inspired by those designed by Opentrons for their liquid-handling platforms. [73] Finally, the tools can be defined by utilizing their respective *`.py`* modules, as well as their index as they are indicated in the Jubilee's *`config.g`* file, tool name, as well as any tool configuration file. The use of configuration files for the tool definition allows the same module to be used for different tool models, for example two pipettes with different liquid-handling capabilities. Each tool will need to be associated with the digital machine object by the *`machine.load("tool_name")`*

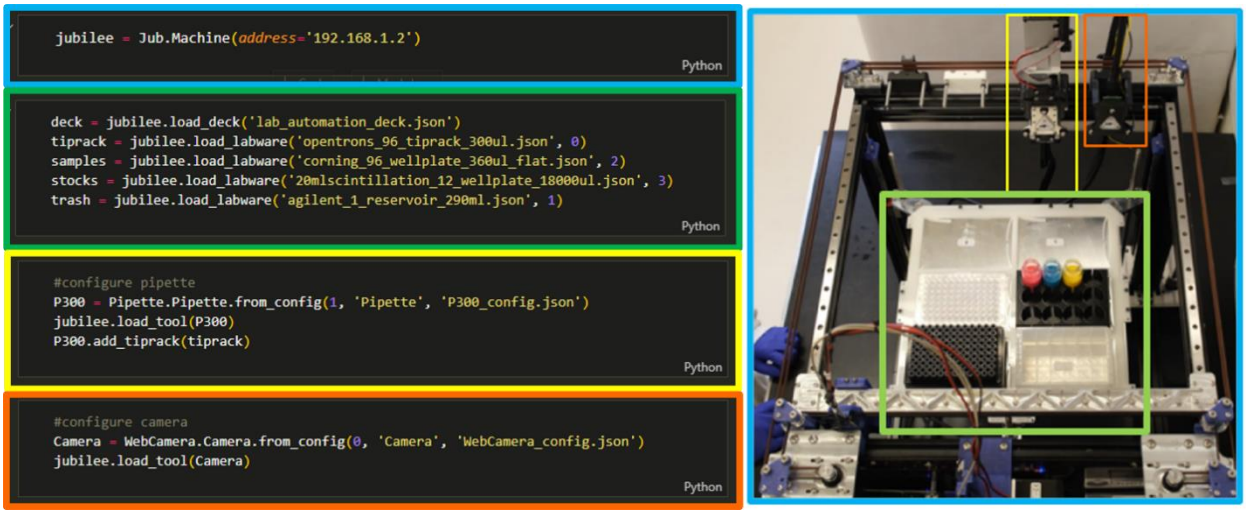

Figure 6.3 Example protocol set up based on the Science Jubilee project repository. Similarly to the physical machine set up (right), the user is required to define all the components needed to conduct the desired workflow. First, it needs to establish a connection with the machine. Next the deck design and labware are instantiated. Finally, the tools can be defined by utilizing their respective `.py` modules, as well as their index (as indicated in the machine's `config.g` file), tool name, and any tool configuration files.

The project's repository is open-source and community members can access directly on GitHub, clone it, and use it to design their own SDL protocols. This can incentivize the sharing of designs, promote reproducibility and the formation of new open-hardware ecosystems for laboratory automation tools and platforms.

6.2.2.2 Tool Integration

The ability to host and operate vastly different tools within its frame gives Jubilee the ability for end-to-end workflow designs. These refer to the complete design that can complete all the required steps in an experimental protocol. [35] In fact, the application-agnostic feature of this platform allows for more flexible tool implementation, where these can be easily swapped out, without the need to reconfigure the entire machine. The mechanism for tool pick-up is straightforward, where the combination of the locking mechanism, found on the tool carriage

component of the platform, and the base tool-holder template implementing ball-bearings allows for consistent and constant tool positioning. This is an important workflow reproducibility and standardization. Once the tool completes the set of actions it was tasked with, the tool carriage can automatically park it back onto the machine's frame and proceed to use a different tool, without any human-intervention.

Tools can be classified in four categories: tools which require a motor to be controlled by the Duet3D main board, tools which require an I/O logic connected to a GPIO pin on the Duet3D board, tools which require an external trigger (i.e., not controlled by the Duet3D), and peripheral tools such as tools placed on the deck of a Jubilee and not on the tool changer (e.g., a mix/stir plate or a hot plate). Examples of the first category are the OT-2 pipette, the syringe tool, peristaltic pumps, or the filament extruder. The electromagnet tool, lights, or a heater for the deck fall under the category of GPIO actuated tools. Next, the sonicator or any tool interfaced using a microcontroller can be categorized as external trigger one. Finally, a peripheral tool is one that is used within the robotic platform, but not connected to the tool changer component. A stir plate for example is one tool that will be placed on the deck of the Jubilee. The base `Tool` c*lass*, contained in the project's repository, is used to associate the tool with machine's specific properties, such as the offset that the tool center has with respect to the tool carriage and the tool's parking position, among others. Currently, this information is stored onto Jubilee's Duet3D main board, but a user can easily define their own or modify the class to accommodate their physical setup requirements. This enables the tools used by Jubilee to retain some platform agnostic features and ensures shareable products that other community members can replicate and implement on their own instrumentation with minimal modifications.

To integrate a new tool, there are a few steps that a researcher should follow. First, there needs to be a set of documentation containing the BOM to source the parts and step-by-step (visual) instructions on how to build the tool. The tool parking post and tool holder should follow the design requirements provided on the original Jubilee's Wiki. [74] If a tool is directly connected to the machine's Duet3D board, instructions on how to modify the core `config.g` file should be indicated as well. Next, a python module containing the set of actions that the tool can perform should be added to the repository's `/tool/` folder. [72] Physically, the tools need to be connected to the appropriate pins and ports. Their parking post positions need to be recorded in files with a Duet3D defined naming convention and structure after aligning the tool changer's locking mechanism with aperture on the tool's wedge plate. The final steps would be to measure and record the tool's offset with respect to the tool changer reference point into the machine's `config.g` file. Finally, to ensure that a new tool can be integrated onto this platform, its control should not depend on proprietary software, graphical user interface (GUI), or human intervention (i.e., click a button or turn a nob). Instead, this should be interfaced directly, ideally with Python or other scripting languages.

6.2.2.3 Tool Development

There is a wide variety of tools required to complete an experimental workflow. These can include those required for sample formulation, sample characterization, and processing. However, there is also an array of peripheral tools required to maintain sample conditions constant throughout the experiment or to replace actions that a researcher would need to complete. An example would be to place a cap or a lid over sample containers to avoid evaporation or to move samples between different instruments. This task can be completed in a human-inspired manner by using a robotic arm, equipped with a gripper tool to mimic the twisting. However, there are also

creative solution that can take advantage of hardware-centric designs to complete similar tasks. For example, a simple and inexpensive solution is the use of an electromagnet (Adafruit, 5V Electromagnet , Adafruit Product ID: 3872) and metal washers attached to a lid. Figure 6.4 depicts such a tool while removing the lid from an SLAS 96 wellplate labware.

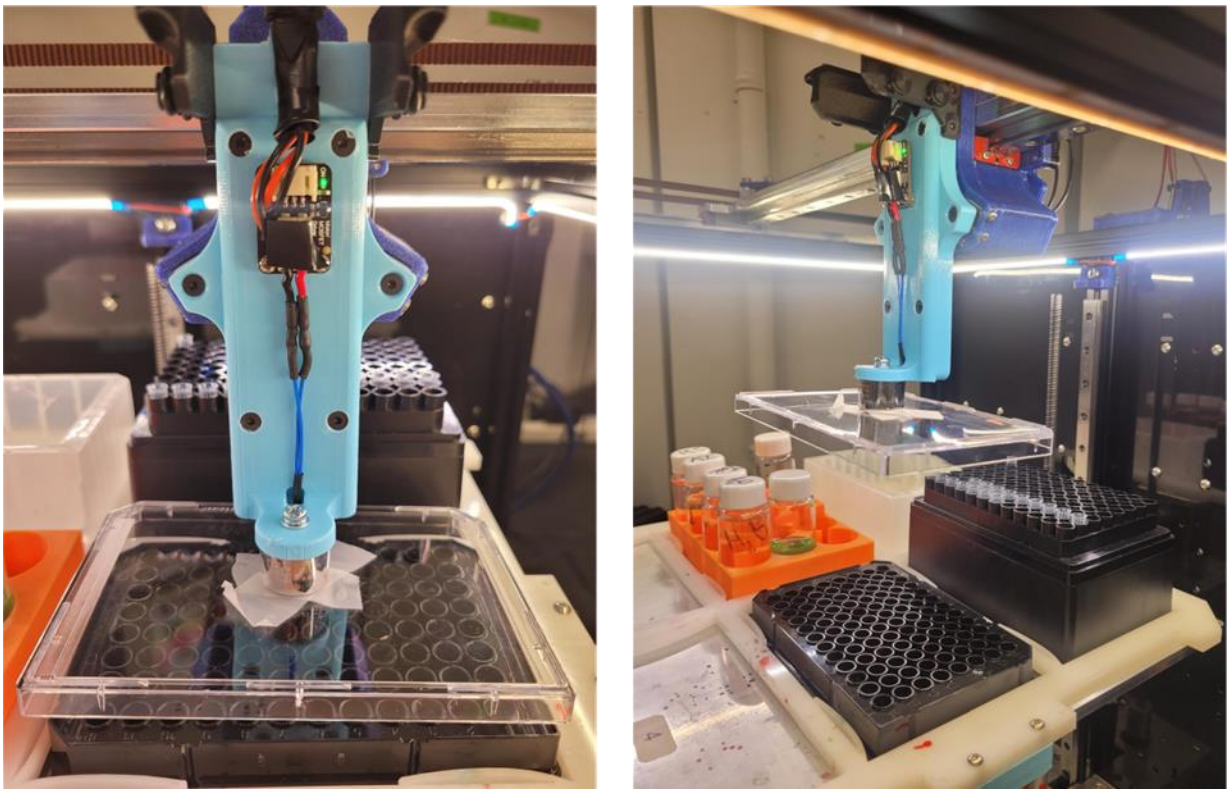

Figure 6.4 Electromagnet tool while lidding(left) and de-lidding (right) a 96-well plate

In this case, the tool is first connected to a MOSFET driver (Adafruit STEMMA MOSFET driver) to ensure safe operations, then directly interfaced by the Jubilee's Duet board using one of the 5V GPIO pins. The electromagnet can be engaged by simply turning on its pin, this will allow for picking up the lid. To disengage the lid, the pin connected to the tool can be simply turned off. Another peripheral tool that can play an important role in ensuring the samples are well mixed throughout the entire process. Traditional stir plates use magnets inside the sample's container to continuously agitate the solution. However, this same task can be challenging to complete for

labware with sample volumes of 300 μL or less, such as wellplates. A solution to limitation given by traditional tools is to build a mix plate based on haptic motors (Vybronics LRA motor, DigiKey 1670-VG0832012-ND). These are vibrating motors which can allow for agitating samples. These motors require a driver board (Adafruit, DRV2605L Haptic Motor Controller board, Adafruit Product ID: 2305) for their control and to allow for modulating the vibration patterns. While this tool is currently still under development, any updates and final documentation will be included in the `science_jubilee/tool_library/` folder on GitHub. [72]

To complete more experimental relevant tasks, there is a need for higher-fidelity tools, especially for characterization. Spectroscopic techniques, such as those discussed in Chapter 2, section 2.2, can provide qualitative and quantitative information on sample's morphology, concentration, and optical properties, all in a non-destructive way. A spectroscopic tool was developed implementing a reflection/backscattering probe (Ocean Insights, Reflection probe UV/VIS, QR400-7-UV-BX), a detector (Ocean Insight , Ocean HDX-XR UV to NIR) and two different light sources: a white light (Ocean Insight, DH 2000-BAL, 210-2500nm) for reflection and transmittance measurements, as well as an LED light source (Ocean Insight, LSM-365A) for photoluminescence measurements. Figure 6.5 shows a simplified schematics of the spectroscopic probe set up.

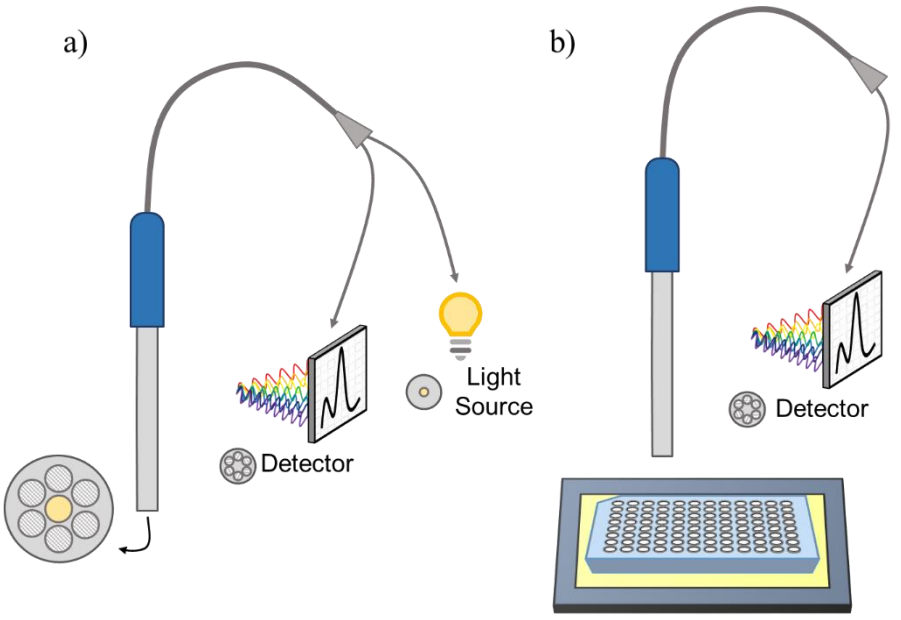

Figure 6.5 Example schematics for the Ocean Insight spectroscopic probe. a) Depiction of the base reflection/backscattering probe set up. The fiber optics array is shown on the bottom left corner. The central fiber carries the light, while the outer array measures the sample's response. b) An alternative proposed configuration to allow for transmittance measurements in which the light source is placed below the sample labware instead of being carried inside the fiber optic probe.

The light sources can be interchangeably used depending on the type of measurement of interest. The photoluminescence can use the configuration shown in Figure 6.5 a). In this case, the light source will be the LED light without any modification to the design and has been already integrated into the science Jubilee tool library. On the other hand, to determine other spectroscopic properties such as extinction or light absorbance, for example to determine the color of a sample, the set up requires further design. In fact, while reflectance can be used to assess color for solid samples, this becomes more complicated for liquid ones. The surface properties of a material can influence their reflectance response. To calibrate the probe to quantitatively measure reflectance, a reflectance standard was purchased (Labsphere, AS-01160-060). However, the surface of the standard is opaque, while the liquid samples of interest in most experimental procedures, especially those implementing autonomous system, tend to be transparent and shiny. In this case, the solution is to

place the light source in line with the measuring probe while the sample is placed in the middle. This approach could be obtain using the current probe and detector, but changing the measurement design, where instead of using the middle fiber optic probe to carry the light from the source, this latter one can be placed below the sample, see Figure 6.5 b). Unfortunately, this would require the fabrication of a "light-box" with enough light intensity to ensure high-fidelity measurements and therefore further work needs to be completed before the spectroscopic probe can be used to characterize sample's light absorbance or transmittance.

Finally, a list of all current tools that have been successfully integrated onto a jubilee machine for materials science applications are as follows. For materials handling examples include a syringe extrusion tool, an Opentrons OT-2 pipette implemented without mechanical modifications to the original design, peristaltic pumps, and an inoculation loop tool. Raspberry pi cameras and a spectroscopic tool from Ocean Optics, with both Halogen and LED light sources can be used for sample monitoring or characterization. For sample processing, a dip probe sonicator and a mix/stir plate have been developed. Finally, an electromagnet tool has been designed for moving objects such as vial caps and lids for capping protocols.

6.3 Autonomous Color Matching

Up to this point, this Chapter has focused on the software and new tool integration on Jubilee to transform it into a laboratory automation tool for self-driving labs. As a proof of concept for materials science application, the new capabilities were evaluated on what is becoming the new benchmarking task for SDL, an autonomous color matching problem. [62,75]

6.3.1 *Experimental Design*

This autonomous color matching task combines the use of different skills required to translate a low-throughput workflow into an autonomous one and has high educational value when working in this new science paradigm approach. In fact, it requires experimental planning, orchestration, and use of laboratory automation solutions to complete the manual experimental steps, and by including an AI agent for the decision-making process, the workflow readily becomes a straightforward working example of a self-driving lab. There are a handful of examples of this approach in the literature, involving liquid-handling,[75,76] and light mixing. [62] The task consists of mixing arbitrary stock colors to match as close as possible a provided target color , indicated as a set of `[R,G,B]` values, in the least number of iterations. Ginsburg et al. have run this SDL example using the facility at Argonne National Laboratory, implemented their modular science factory architecture. [75,77] While successful, this implementation makes use of four individual devices, connected by a central robotic arm to form an autonomous workflow. [75] The high level of complexity can discourage replication of this system, as well as the prohibitive cost associated with each of the instruments implemented to ensure a closed-loop approach. Next, the light mixing example described by Baird and Sparks provides a low-cost (< 100 $ USD) entry point to SDL and autonomous workflow design and orchestration. [62] The example allows the user to assess different optimization algorithms and it is intended to be more of a pedagogical tool than an extensible scientific tool. Science Jubilee can function as a middle ground for low-cost development of this autonomous SDL task. In fact, while seemingly trivial, this color matching task can be directly translated into scientific workflows, where instead of paint, nanoparticle precursors can be used to optimize the particle's optical properties by using a higher-fidelity tool, such as a spectroscopic probe. The set up and optimization remain virtually unchanged.

6.3.2 *Preliminary Results*

To conduct this color matching task using a Jubilee, the tools, labware and initial machine set up depicted in Figure 6.3 were used. These are namely an OT-2 P300 pipette, a Raspberry Pi Camera V3 equipped with a ring light, a 96-well flat-bottom plate, 20mL scintillation glass vials, an Opentrons P300 tip rack and a tip trash container. The color stocks used were red, blue, and yellow instead of cyan, magenta, yellow, and black as used by Ginsburg et al. [75] For the decision-making algorithm, a single-objective Bayesian Optimization algorithm was implemented as described in Chapter 2, section 2.4.1. The platform and its deck were set up and configured with tools and labware required to conduct the experimental steps in the color matching campaign. Figure 6.6 shows an Opentrons OT-2 pipette (attached to the carriage tool) performing a liquid transfer from a stock container to a sample well. The camera tool can be found in the top left corner of the picture. All the remaining computational steps are conducted on a PC orchestrating the SDL task.

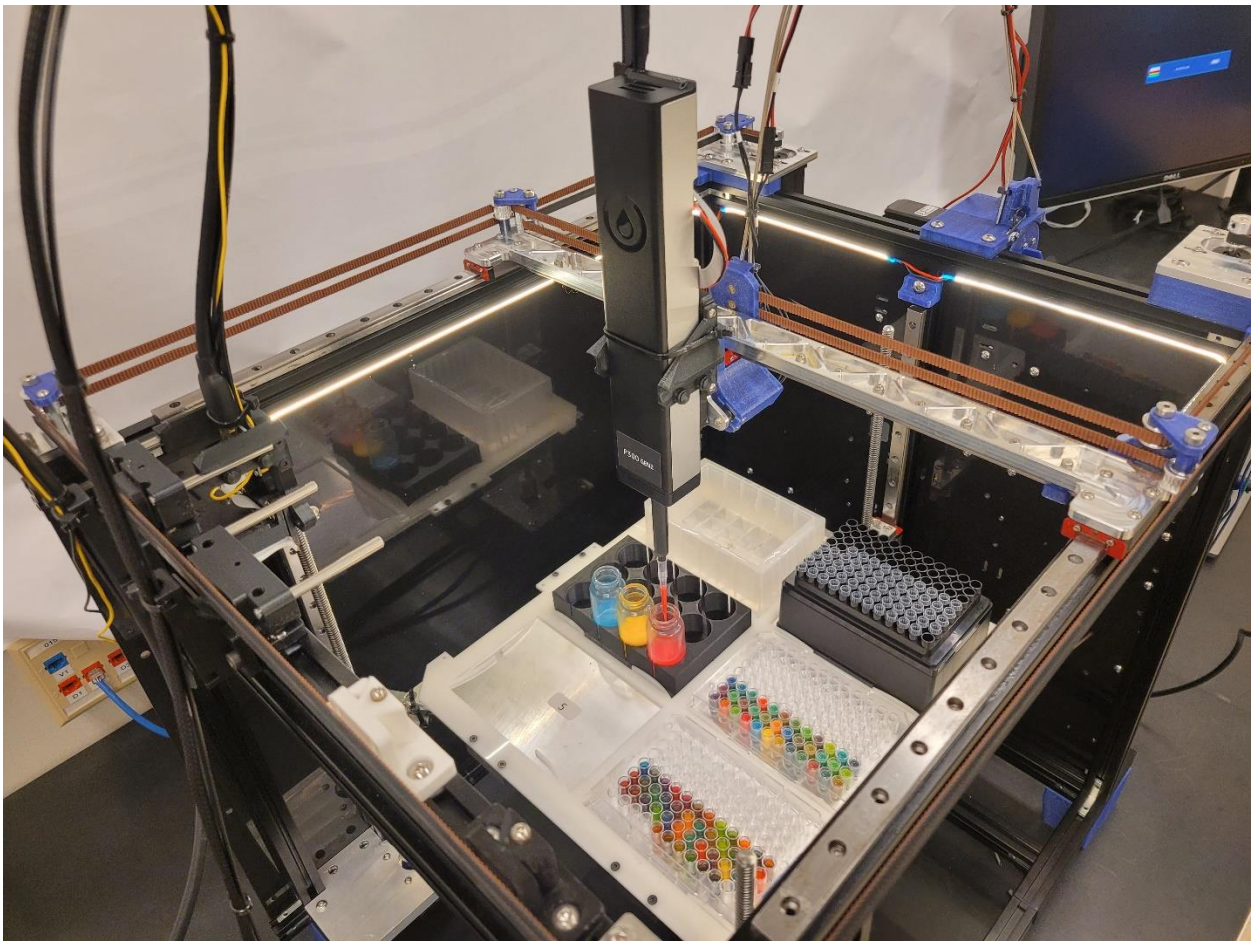

Figure 6.6 A photo depicting a Jubilee platform and its deck configured with tools and labware to carry out the experimental steps required in the color matching campaign. An Opentrons OT-2 pipette (attached to the carriage tool) while performing a liquid transfer from a stock container to a sample well. The camera tool can be found in the top left corner of the picture. All other steps are carried out on a PC orchestrating the SDL task.

The iterative steps for the autonomous campaign are as follows:

- The optimizer suggests a sample to test by providing a list of volume fractions, one for each stock provided,
- Jubilee uses the `Pipette` tool to distribute and mix the indicated volumes of the color stocks,
- The `Camera` tool is then equipped onto the tool carriage, which will be used to capture an image of the sample. Using image analysis, the `[R,G,B]` values of the color made are extracted,

- A scoring function, such as a Euclidean distance, evaluates how close the current point is with respect to the target color,
- The score is then fed back into the optimizer, which will then propose a new set of conditions to test based on the results of the previous iterations.

The workflow was designed in a modular fashion by developing a *ColorMatcher* Python class, made openly available in a GitHub repository, which acts as an orchestrator to communicate the results obtained using the physical experimental systems with the AI-agent, initiate the successive iteration, and a visualization panel to monitor the progression of the optimization task. [78] Both the optimizer class and the experimental protocols were purposefully defined in separate `.py` modules to allow flexibility and adaptability of the class to other robotic platforms or new decision-making algorithms, without the need to significantly modify the python code. Figure 6.7 showcases the results of an experimental campaign in which the Optimizer was tasked with reproducing a target color with `[81, 184, 93]` as its RGB values. The algorithm had no previous knowledge of the color stocks or of color mixing theory. Only the first point in this campaign was randomly generated. All subsequent iterations were proposed by the algorithm's acquisition function.

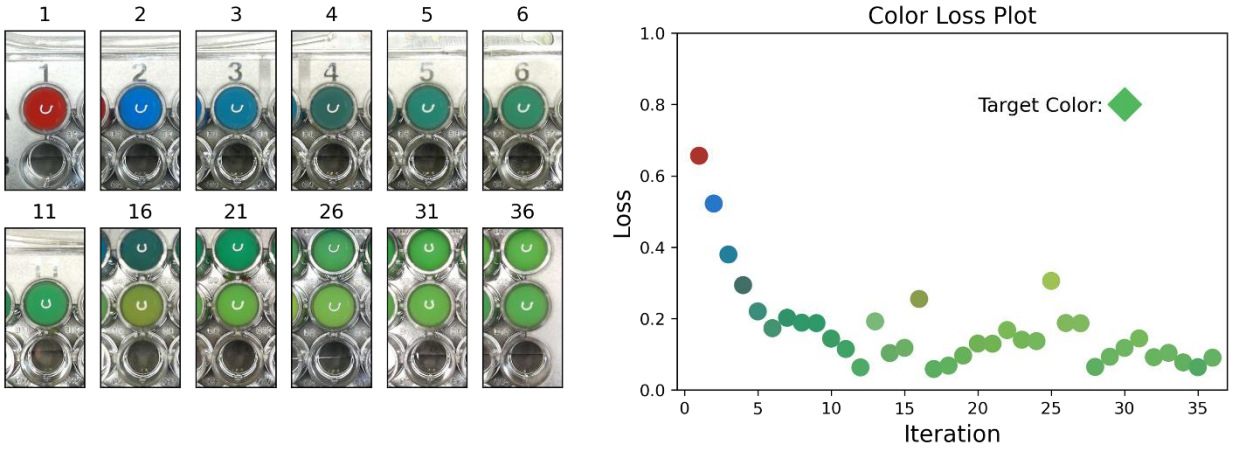

Figure 6.7 A summary of results of an autonomous color matching campaign with target color of RGB: [81,184,93] (depicted in the top right corner of this figure). The images on the left graph were captured during the experimental workflow, where the iteration number is indicated on top of each panel. The plot on the right shows the score that each color obtained using a Euclidean distance metric where 0 is a perfect match. The color of each marker corresponds to the RGB value measured by the Camera tool.

The images in each panel on the left side of Figure 6.7 were captured during the experimental workflow by the camera, where the iteration number is indicated on top of each image. The plot on the right shows the score that each color obtained, based on the Euclidean distance metric where 0 is a perfect match. The color of each marker corresponds to the RGB value measured by the Camera tool. Even with only 36 total iterations, the optimizer was able to readily reach a color very close to the target, approximately after 6 iterations. The rest of the allotted tries, the algorithm tries to vary the sample composition to minimize the distance and reach a score as close to zero as possible. This workflow can be easily repeated adapted to implement with varying number of stocks, for example including white and black paint to allow for a broader color space to be accessed. This new approach will not require any modification to the experimental set up or the *ColorMatche*r class, demonstrating the adaptability of the proposed approach to this problem. Furthermore, once higher-fidelity tools are available and configured to be implemented on the

Jubilee platform, the experimental protocol can be simply modified by simply changing a few lines of code, but no modification to the orchestrator class

6.3.3 *An interactive Dashboard*

Inspired by a recent outreach event in which this autonomous color-matching problem was showcased, a dashboard to simulate the same task was created to use as an interactive pedagogical tool to teach students about these tools. This can also be used as a simulation tool for testing new AI-based algorithms to complete this optimization task. The dashboard was created using a Python-based app building software called Dash. [79] A similar strategy to the *ColorMatcher* class was taken, where the optimizer is defined separately from the main dashboard code and can be interchanged with other active learning algorithms. The only requirement for a new algorithm is the presence two methods:

1. `` `optimizer.update(array(inputs), array(output))` ``: a method to provide the algorithm with the results of the new queried data. In this example the input will be the volume fractions of stock colors composing each queried sample; the output will be the color score of each formulated sample.
2. `` `optimizer.ask()`: a method that returns the acquisition function's suggested next sample to test, provided as a list on stock volume fractions to test. ``

A preliminary implementation of the dashboard can be seen in Figure 6.8. The dashboard is interactive, allowing a user to "challenge" the optimizer's performance and try and converge towards the target color first.

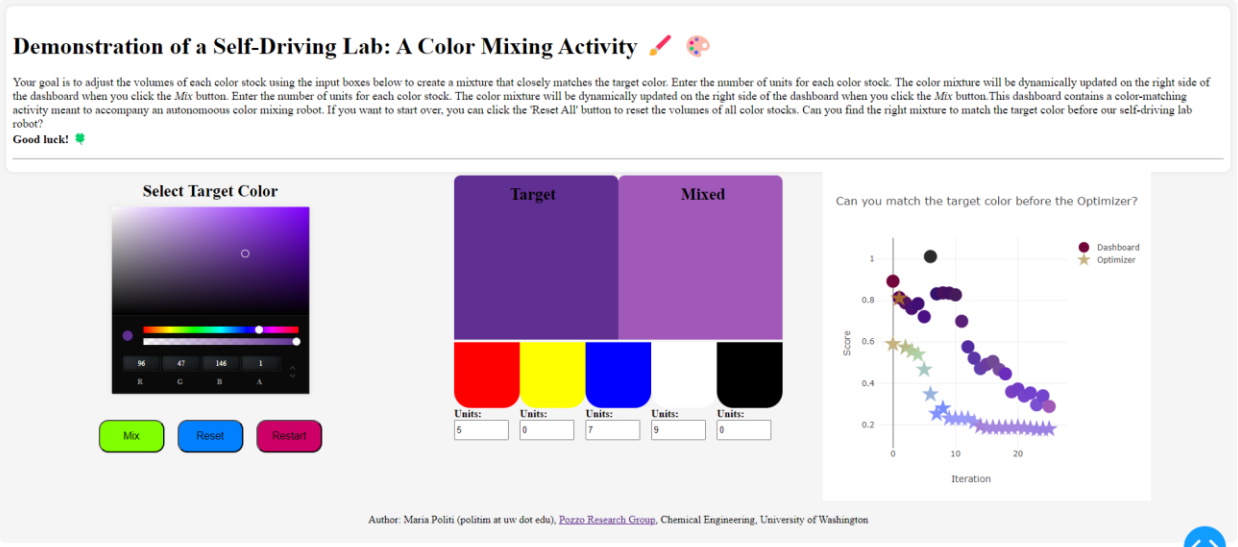

Figure 6.8 Example dashboard for simulating an autonomous color matching task. In this case, the dashboard is interactive, allowing a user to "challenge" the optimizer's performance and try and converge towards the target color first.

The target color can be varied directly from the dashboard using the color-picker widget found on the left panel. Below the left panel, there are three buttons used to mix the color stocks at the desired ratio, reset the color stocks values, or restart the optimization task from scratch, respectively. The "*Restart*" button will also instantiate a new optimizer object. The central panel allows the user to try new color formulations by indicating how many units of each base stock to use. The *Target* panel is updated based on the selection manel using the widget, while the *Mixed* panel showcases the user indicated color , after the mix button is clicked. Finally, the right most panel contains a plot used to monitor the progression of the optimization task, both for the user and optimizer. The algorithm queried point is generated every time the *Mix* button is pressed, ensuring a 1-to-1 point generation for every guess the user makes. While simple, this dashboard can be used as a simple, digital version of the autonomous color-matching task.

6.4 SUGGESTED FUTURE WORK

While the addition of this higher-level control language and the inclusion of new synthesis, processing, and characterization tools have significantly increased the number of science laboratory tasks able to be completed with Jubilee, there is still more work to be done before it can be deployed at larger scale. The project originates from the Maker Movement and retains lots of features from it. Unfortunately, there needs to be more safety checks in place before this platform can be trusted with more complex chemistry and materials science spaces. Possible upgrades include the use of sensors to ensure that a tool gets correctly picked up by the central carriage arm. In fact, the machine will continue to perform the sequential list of actions it has received, independently if it is in the correct state (e.g., a tool is attached). This can be easily achieved by either including computer vision algorithms that have learned the expected machine actions. Another solution is to make use of the metal parts composing the tool plate and the carriage arm. In fact, the same three ball bearings used to ensure consistency in tool position, could be used to close an electric circuit, triggering to the machine that the tool pick-up or parking was correctly executed. Next, hardening of the platform's frame and components is required to improve the material compatibility of this platform. For example, it is possible to purchase a metal version of the tool carriage component, as well as other metal components upgrades already designed by the original Jubilee community. Nonetheless, there are still several parts made of PLA plastic that can be more sensitive to organic solvents. These can be simply printed using more compatible materials using a resin-printer; this would require no modification or redesign of the components. Next, strategies for spilling containment are necessary. As more and more liquid handling task are integrated in the machine, the risk of contamination or accidents that can result in solvents dripping onto mechanical components is high. This can be avoided by attaching a collection tray at the

bottom of the jubilee frame. An additional upgrade will concern the frame to improve its long-term stability. The use of panels and bulkier frame masks is suggested to ensure longer lasting axis and position calibrations. The community-driven approach of the original Jubilee project can be extended to its science-based counterpart. To ensure broader implementation of this tool, the library of available tools needs to be expanded to accommodate more complex tasks. Some new tools might include a hot-plate with an SLAS standard footprint, a solid dispenser tool, and an autosampler tool able to connect samples formulated and processed on this platform with existing materials science characterization instrumentation (e.g., a small angle x-ray scattering instrument). These new tools should originate from the community at large by enforcing platform-agnosticism in the initial design. This can also motivate the formulation of tool and communication standards for these hardware systems, which has the advantage of increasing their implementation in broader science contexts.

One final, but equally important upgrade, would be a digital twin version of this laboratory automation platform. This would allow for testing and simulation of a workflow without the dependence of the physical machine or tools. This can ensure success of the workflow and can be a straightforward way of catching possible set-up errors, labware/tool inconsistencies, and safer protocol development.

6.5 CONCLUSION

Ecosystems for open-source hardware are less well established and have a nascent movement when compared than their open-source software counterparts. This Chapter highlighted an open-source hardware laboratory automation platform, Jubilee, reconfigured for scientific tasks. This platform can be produced with off-the-shelf hardware and common makers tools. A new python-based control library for Jubilee was developed to ensure high-level communication with

the physical machine. This allows for experimental protocols to be written in more research and human oriented terms and removes the domain-specific knowledge to increase accessibility of Jubilee. The library of tools was grown to allow for new synthesis, processing , and characterization tasks to be completed with this automation platform. It was demonstrated that Science Jubilee can function as a low-cost solution for autonomous SDL task. This can be achieved only thanks to the automatic, tool-changing capabilities of the machine. An autonomous color-matching campaign was used to benchmark the SDL capability of Jubilee with other system present in the literature. This task combines the use of different skills required to translate low-throughput protocols into an autonomous workflow and has high educational value when working in this new science paradigm approach. The color-matching campaign was completed using common laboratory labware, an OT-2 P300 pipette and a Raspberry Pi camera, all loaded onto a single Jubilee. The physical system was combined with a single-objective Bayesian Optimization algorithm to close the loop of this experimental design. While seemingly trivial, this task can be directly translated into other scientific workflows without redesign or modification to the approach.

Community-driven mechanisms that can be developed in the context of open-hardware designs drastically lower the barrier of entry to laboratory automation. Jubilee provides a flexible and affordable design that can be implemented for a diverse set of chemical systems. Furthermore, given the speed and simplicity of workflow development that can be achieved using this platform, closing-the-loop can be achieved by implementing AI-driven strategies. The autonomous color matching campaign successfully showcases the potential of this platform for becoming a more ubiquitous tool in materials science spaces. These self-driving lab solutions allow for a drastic increase of available data on new materials, the ease in reproducibility can also improve data

fidelity and shareability. Finally, increased access through lower costs will broaden the application space, enabling a larger number of scientists to take advantage of the precision of automation and enabling automation tools to be included in hands-on educational curricula. However, to truly achieve the ubiquitous use of SDLs in chemistry and materials science laboratories, there is a need for the development of standardized hardware designs and equipment communication protocols, as well broader availability of easily reproducible, openly available designs

6.6 REFERENCES

1. Delgado-Licona, F. & Abolhasani, M. Research Acceleration in Self-Driving Labs: Technological Roadmap toward Accelerated Materials and Molecular Discovery. *Advanced Intelligent Systems* **5**, (2023).
2. Pyzer-Knapp, E. O. *et al.* Accelerating materials discovery using artificial intelligence, high performance computing and robotics. *NPJ Comput Mater* **8**, (2022).
3. Flores-Leonar, M. M. *et al.* Materials Acceleration Platforms: On the way to autonomous experimentation. *Curr Opin Green Sustain Chem* **25**, 100370 (2020).
4. Bennett, J. A. *et al.* Autonomous reaction Pareto-front mapping with a self-driving catalysis laboratory. *Nature Chemical Engineering* **1**, 240–250 (2024).
5. Epps, R. W., Volk, A. A., Ibrahim, M. Y. S. & Abolhasani, M. Universal self-driving laboratory for accelerated discovery of materials and molecules. *Cell Press* **7**, 2541–2545 (2021).
6. MacLeod, B. P. *et al.* Self-driving laboratory for accelerated discovery of thin-film materials. *Sci Adv* **6**, (2020).
7. Seifrid, M. *et al.* Autonomous Chemical Experiments: Challenges and Perspectives on Establishing a Self-Driving Lab. *Acc Chem Res* **55**, 2454–2466 (2022).
8. Abolhasani, M. & Kumacheva, E. The rise of self-driving labs in chemical and materials sciences. *Nature Synthesis* **2**, 483–492 (2023).
9. Aspuru-Guzik, A. & Persson, K. *Materials Acceleration Platform: Accelerating Advanced Energy Materials Discovery by Integrating High-Throughput Methods and Artificial Intelligence*. https://www.cifar.ca/wp-content/uploads/MissionInnovationIC6Report.pdf (2018).
10. Seifrid, M., Hattrick-Simpers, J., Aspuru-Guzik, A., Kalil, T. & Cranford, S. Reaching critical MASS: Crowdsourcing designs for the next generation of materials acceleration platforms. *Matter* **5**, 1972–1976 (2022).
11. Wagner, J. *et al.* The evolution of Materials Acceleration Platforms: toward the laboratory of the future with AMANDA. *J. Mater Sci* **56**, 16422–16446 (2021).

12. What is Laboratory 4.0? Labmate Online. https://www.labmate-online.com/news/laboratory-products/3/breaking-news/what-is-laboratory-40/57352.
13. What is lab 4.0? - Automata. https://automata.tech/blog/what-is-lab-4-0/.
14. Williams, K. *et al.* Cheaper faster drug development validated by the repositioning of drugs against neglected tropical diseases. *J. R. Soc. Interface* **12**, (2015).
15. King, R. D. *et al.* The robot scientist adam. *Computer (Long Beach Calif)* **42**, 46–54 (2009).
16. Deneault, J. R. *et al.* Toward autonomous additive manufacturing: Bayesian optimization on a 3D printer. *MRS Bull* **46**, (2021).
17. Stach, E. *et al.* Autonomous experimentation systems for materials development: A community perspective. *Matter* **4**, 2702–2726 (2021).
18. Coley, C. W. *et al.* A robotic platform for flow synthesis of organic compounds informed by AI planning. *Science* **365**, 1–9 (2019).
19. Chan, C. Y. *et al.* Accelerating drug discovery via organs-on-chips. *Lab Chip* **13**, 4697 (2013).
20. Caschera, F. *et al.* Automated Discovery of Novel Drug Formulations Using Predictive Iterated High Throughput Experimentation. *PLoS One* **5**, (2010).
21. Li, J. *et al.* Autonomous discovery of optically active chiral inorganic perovskite nanocrystals through an intelligent cloud lab. *Nature Communications 2020 11:1* **11**, 1–10 (2020).
22. Chan, E. M. *et al.* Reproducible, High-Throughput Synthesis of Colloidal Nanocrystals for Optimization in Multidimensional Parameter Space. *Nano Lett* **10**, 1874–1885 (2010).
23. Vikram, A., Brudnak, K., Zahid, A., Shim, M. & Kenis, P. J. A. Accelerated screening of colloidal nanocrystals using artificial neural network-assisted autonomous flow reactor technology. *Nanoscale* **13**, 17028–17039 (2021).
24. Epps, R. W., Felton, K. C., Coley, C. W. & Abolhasani, M. Automated microfluidic platform for systematic studies of colloidal perovskite nanocrystals: towards continuous nano-manufacturing. *Lab Chip* **17**, 4040–4047 (2017).
25. Abdel-Latif, K. *et al.* Self-Driven Multistep Quantum Dot Synthesis Enabled by Autonomous Robotic Experimentation in Flow 2000245 (1 of 13). *Adv. Intell. Syst* **3**, (2021).
26. Salley, D. *et al.* A nanomaterials discovery robot for the Darwinian evolution of shape programmable gold nanoparticles. doi:10.1038/s41467-020-16501-4.
27. Zhao, H. *et al.* A robotic platform for the synthesis of colloidal nanocrystals. *Nature Synthesis* **2**, 21 (2023).
28. Li, J., Tu, Y., Liu, R., Lu, Y. & Zhu, X. Toward "On-Demand" Materials Synthesis and Scientific Discovery through Intelligent Robots. *Advanced Science* **7**, (2020).
29. Ren, F. *et al.* Accelerated discovery of metallic glasses through iteration of machine learning and high-throughput experiments. *Sci Adv* **4**, (2018).
30. Coley, C. W., Eyke, N. S. & Jensen, K. F. Autonomous Discovery in the Chemical Sciences Part I: Progress. *Angewandte Chemie - International Edition* **59**, 22858–22893 (2020).

31. Caramelli, D. *et al.* Discovering New Chemistry with an Autonomous Robotic Platform Driven by a Reactivity-Seeking Neural Network. *ACS Cent Sci* **7**, 1821–1830 (2021).
32. King, R. D. *et al.* The automation of science. *Science (1979)* **324**, 85–89 (2009).
33. Coutant, A. *et al.* Closed-loop cycles of experiment design, execution, and learning accelerate systems biology model development in yeast. *PNAS* (2019) doi:10.1073/pnas.1900548116.
34. Eggert, S., Mieszczanek, P., Meinert, C. & Hutmacher, D. W. OpenWorkstation: A modular open-source technology for automated in vitro workflows. *HardwareX* **8**, e00152 (2020).
35. Lo, S. *et al.* Review of Low-cost Self-driving Laboratories in Chemistry and Materials Science: The 'Frugal Twin' Concept. *Digital Discovery* (2024) doi:10.1039/d3dd00223c.
36. Burger, B. *et al.* A mobile robotic chemist. *Nature* **583**, 237–241 (2020).
37. MacLeod, B. P., Parlane, F. G. L., Brown, A. K., Hein, J. E. & Berlinguette, C. P. Flexible automation accelerates materials discovery. *Nat Mater* **21**, 722–726 (2022).
38. Bateni, F. *et al.* Smart Dope: A Self-Driving Fluidic Lab for Accelerated Development of Doped Perovskite Quantum Dots. *Adv Energy Mater* (2023) doi:10.1002/aenm.202302303.
39. Vaddi, K., Chiang, H. T. & Pozzo, L. D. Autonomous retrosynthesis of gold nanoparticles via spectral shape matching. *Digital Discovery* **1**, 502–510 (2022).
40. Borman, S. Combinatorial chemistry. *Chem. Eng. News* **76**, 47–67 (1998).
41. Christensen, M. *et al.* Data-science driven autonomous process optimization. *Commun Chem* **4**, (2021).
42. O'neill, S. AI-Driven Robotic Laboratories Show Promise. *Engineering* **7**, 1351–1353 (2021).
43. Jeraal, M. I., Sung, S. & Lapkin, A. A. A Machine Learning-Enabled Autonomous Flow Chemistry Platform for Process Optimization of Multiple Reaction Metrics. *Chemistry - Methods* **1**, 71–77 (2021).
44. Powell, A. Democratizing production through open source knowledge: From open software to open hardware. *Media Cult Soc* **34**, 691–708 (2012).
45. Blow, N. Lab automation: tales along the road to automation. *Nature Methods 2008 5:1* **5**, 109–112 (2008).
46. Definition (English) - Open Source Hardware Association. https://www.oshwa.org/definition/.
47. Jones, R. *et al.* RepRap-The Replicating Rapid Prototyper Proof for review only RepRap-The Replicating Rapid Prototyper. : *Robotica* **29**, 177–191 (2011).
48. Zhang, C., Wijnen, B. & Pearce, J. M. Open-Source 3-D Platform for Low-Cost Scientific Instrument Ecosystem. *SLAS Technol* **21**, 517–525 (2016).
49. Baas, S. & Saggiomo, V. Ender3 3D printer kit transformed into open, programmable syringe pump set. *HardwareX* **10**, e00219 (2021).
50. Carvalho, M. C. & Murray, R. H. Osmar, the open-source microsyringe autosampler. *HardwareX* **3**, 10–38 (2018).

51. Keesey, R., LeSuer, R. & Schrier, J. Sidekick: A Low-Cost Open-Source 3D-printed liquid dispensing robot. *HardwareX* **12**, e00319 (2022).
52. Nejatimoharrami, F., Faina, A. & Stoy, K. New Capabilities of EvoBot: A Modular, Open-Source Liquid-Handling Robot. *SLAS Technol* **22**, 500–506 (2017).
53. Bravo-Martinez, J. Open source 3D-printed 1000 lL micropump. *Hardware X* (2018) doi:10.1016/j.ohx.2017.08.002.
54. Faiña, A., Nejati, B. & Stoy, K. EvoBot: An Open-Source, Modular, Liquid Handling Robot for Scientific Experiments. doi:10.3390/app10030814.
55. Open-Source Liquid Handler | OTTO. https://openliquidhandler.com/.
56. Yoshikawa, N., Darvish, K., Vakili, M. G., Garg, A. & Aspuru-Guzik, A. Digital pipette: open hardware for liquid transfer in self-driving laboratories. *Digital Discovery* **2**, 1745–1751 (2023).
57. Bhom, A. AMi: A GUI-based, open-source system for imaging samples in multi-well plates. *Acta Crystallogr F Struct Biol Commun* **75**, 531–536 (2019).
58. Pineda, D., Pérez, J., Gaviria, D., Ospino-Villalba, K. & Camargo, O. MEDUSA: An open-source and webcam based multispectral imaging system. (2022) doi:10.1016/j.ohx.2022.e00282.
59. Regan, B., Kinahan, D., Daly, P., O'kennedy, R. & Collins, D. Design and fabrication of a low-cost wireless camera imaging system for centrifugal microfluidics. *HardwareX* **11**, e00259 (2022).
60. Jonveaux, L. Arduino-Like Development Kit for Single-Element Ultrasound Imaging. *Journal of Open Hardware* (2017) doi:10.5334/joh.2.
61. Saar, L. *et al.* The LEGOLAS Kit: A low-cost robot science kit for education with symbolic regression for hypothesis discovery and validation. *MRS Bull* **47**, 881–885 (2022).
62. Baird, S. G. & Sparks, T. D. Building a "Hello World" for self-driving labs: The Closed-loop Spectroscopy Lab Light-mixing demo. *STAR Protoc* **4**, 102329 (2023).
63. Xie, Y. *et al.* Accelerate Synthesis of Metal−Organic Frameworks by a Robotic Platform and Bayesian Optimization. *ACS Appl. Mater. Interfaces* **13**, 53485–53491 (2021).
64. Beaucage, P. A. & Martin, T. B. The Autonomous Formulation Laboratory: An Open Liquid Handling Platform for Formulation Discovery Using X-ray and Neutron Scattering. doi:10.1021/acs.chemmater.2c03118.
65. Browder, R. E., Aldrich, H. E. & Bradley, S. W. The emergence of the maker movement: Implications for entrepreneurship research. *J Bus Ventur* **34**, 459–476 (2019).
66. Vasquez, J., Twigg-Smith, H., Tran O'leary, J. & Peek, N. Jubilee: An Extensible Machine for Multi-tool Fabrication. (2020) doi:10.1145/3313831.3376425.
67. Dunn, K., Feng, C. & Peek, N. Jubilee: A Case Study of Distributed Manufacturing in an Open Source Hardware Project. *Journal of Open Hardware* **7**, 1–15 (2023).
68. Jubilee. https://jubilee3d.com/index.php?title=Main_Page.
69. Machine Agency. https://depts.washington.edu/machines/.
70. Duet3D . https://www.duet3d.com/.

71. Latif, K., Adam, A., Yusof, Y. & Kadir, A. Z. A. A review of G code, STEP, STEP-NC, and open architecture control technologies based embedded CNC systems. *International Journal of Advanced Manufacturing Technology* vol. 114 2549–2566 Preprint at https://doi.org/10.1007/s00170-021-06741-z (2021).
72. Politi, M. *et al.* machineagency/science-jubilee: Controlling Jubilees for Science! *GitHub* https://github.com/machineagency/science-jubilee (2023).
73. Opentrons/opentrons: Software for writing protocols and running them on the Opentrons Flex and Opentrons OT-2. https://github.com/Opentrons/opentrons.
74. Tools - Jubilee. https://jubilee3d.com/index.php?title=Tools.
75. Ginsburg, T. *et al.* Exploring Benchmarks for Self-Driving Labs using Color Matching. *ACM International Conference Proceeding Series* 2147–2152 (2023) doi:10.1145/3624062.3624615.
76. Roch, L. M. *et al.* ChemOS: An orchestration software to democratize autonomous discovery. *PLoS One* **15**, (2020).
77. Vescovi, R. *et al.* Towards a modular architecture for science factories. *Digital Discovery* **2**, 1980–1998 (2023).
78. Pelkie, B. & Politi, M. pozzo-research-group/jubilee_pipette_BOdemo: Color matching bayesian optimization with jubilee, rewritten to use pipette. *GitHub* https://github.com/pozzo-research-group/jubilee_pipette_BOdemo (2024).
79. Dash Documentation & User Guide | Plotly. https://dash.plotly.com/.

Chapter 7. SUMMARY & OUTLOOK

While laboratory automation holds immense promise for accelerating scientific progress, it is essential to acknowledge the diverse needs and challenges of different scientific experiments. The ultimate objective of MAPs is to achieve autonomous experimentation through the combination of artificial intelligence with high-throughput robotic systems without requiring human intervention. The main advantage of these platforms is the possibility to investigate broader experimental spaces for both synthesis and parameter optimization. Open-source hardware (OSH) principles have made the use of these materials' acceleration platforms more accessible and more easily implemented. However, there are still efforts required to achieve a broader community utilization of these high-throughput solutions.

In Chapter 3, a combination of commercially available and custom automation solutions was presented to systematically study the inexpensive designer solvents, deep eutectic solvents (DES). These have great appeal as electrolytes for energy-related applications thanks to their low-cost, green environmental footprint, wide potential window, and adequate ionic conductivity. Despite these benefits, the massive molecular design space associated with these materials has hindered their use. The study presented high-throughput and data-driven strategies as an avenue to investigate new candidate DES. After a cheminformatic campaign, DES were then synthesized in high-throughput, to complete an experimental campaign spanning 50 QAS/HBD combinations and 12 molar ratios for a total of 600 unique samples. This systematic characterization was valuable and unique in the current literature, where data on DES electrolytes is still scarce and overwhelmingly focused on choline chloride samples. Importantly, the high-throughput electrochemical characterization reported identified several promising electrolyte candidates with wide electrochemical potential windows (over 3 V) and ionic conductivities above 1 mS/cm. This

suggests that there are likely numerous promising electrolyte materials within the vast molecular design space of DES that remain to be discovered. While efforts to move this work closer towards an automated closed loop system are still underway, the methods outlined in this study could quickly increase the DES data that is available and openly shared for use with advanced statistical methods. The use of advanced methods to predict DES properties from molecular features and formulation parameters will become essential elements in future investigations aiming to efficiently sample DES candidates. In addition, methods outlined in this chapter can also be extended to other materials design problems with large design spaces. The MAP-based workflow showcased in this chapter could be implemented for the study of other systems where the thermodynamics of mixtures play an important role such as microemulsions, especially for drug delivery applications, or the phase transition temperature of lipid systems. Given the numerous appealing properties of DES solvents, Chapter 4 explores their incorporating them into redox flows batteries (RFBs) for the design of inorganic-base grid level energy storage systems. The push for greener redox active species for use in electrochemical storage technologies, such as redox-active organic molecules (ROMs), to replace expensive and resource limited earth metals currently in use. Preliminary results highlight good solubility of these organic species in DES, however, at higher concentrations their electrochemical performance is hindered by poor species mobility, due to high viscosity. This prompts novel automation approaches for higher temperature studies of these systems.

In Chapter 5, the investigation of a large experimental design space for the ligand mediated sonochemical synthesis of CdSe nanoparticles was presented. The workflow was developed as a human-in-the-loop type of approach by implementing a combination of a liquid handling robot, a custom automation platform equipped for single point sonochemical processing of samples, and a

plate reader for characterization tasks. A total of almost two thousand samples in less than two months, which would not have been achievable using traditional synthesis approaches. In was found that the range of concentrations of selenium and cadmium precursors implemented in this study did not play a role in the samples' absorption peak position, related to particle size. The role of the ligands was related to the binding energy with the cadmium ion, which ultimately controls the nucleation rate of the synthesis and more strongly affected the particle size. Regarding the photoluminescence emission, the presence of oleylamine favored the increase of photoluminescence intensity, while the addition of oleic acid had the opposite effect, due to differences in surface passivation of the two ligands. The use of data-driven and model-agnostic analysis strategies confirmed data trends previously observed, as well as provided a quantitative breakdown of the most influential experimental parameters. The strategy of coupling the proposed high-throughput workflow to a data-driven approach for the interpretation of the results provides a holistic view of the design space investigated. The modular nature of the protocol makes the workflow adaptable to a variety of future studies, including other nanocrystal design spaces, emulsification processes, and nanoparticle re-dispersion or exfoliation.

In Chapter 6, the development of an open-source and open-hardware, modular laboratory automation platform based on the tool-changing 3D printer Jubilee is demonstrated in the context of low-cost SDLs. The application-agnostic feature of this platform allows for more flexible tool implementation, where these can be easily swapped out, without the need to reconfigure the entire machine. A new, python-based control interface for the machine allows for high-level, machine-readable, but also research, and human oriented protocols. By removing the domain-specific knowledge Jubilee can become more accessible to a broader audience. This platform provides a flexible and affordable design that can be implemented for a diverse set of chemical systems. It is

now possible to achieve close-loop workflows with Jubilee by combining AI-driven strategies, the new high-level control language and the broadened library of open-science tools integrated in it. The autonomous color matching campaign successfully showcases the potential of this platform for becoming a more ubiquitous tool in materials science spaces. This shows how the development of open-science laboratory automation platforms can jumpstart the democratization of laboratory automation tools, impacting materials science research and educational curricula alike.

These self-driving lab solutions hold immense scientific and educational value for both new materials discovery and more interdisciplinary skill development. These tools also allow for a drastic increase of available data on new materials, the ease in reproducibility can also improve data fidelity and shareability. The increased access through low-costs solution will broaden the application space of this new science paradigm, empowering a larger number of (materials) scientists to take advantage of the precision of automation, and enabling automation tools to be included in hands-on educational curricula. However, to truly achieve the ubiquitous use of SDLs in chemistry and materials science laboratories, there is a need for the development of standardized hardware designs and equipment communication protocols, as well broader availability of easily reproducible, openly available designs. This can only be achieved through community-driven and community-maintained ecosystems, developed in the context of open-hardware designs. Embracing these data-driven strategies and the use of low-cost, automatic, and open-source robotic systems will make the incorporation of AI-driven algorithms and iterative exploratory campaigns into the design of experiments much more accessible to the scientific community. This will allow the community to discover new materials, optimize known ones, and more readily achieve innovative solutions to global challenges more efficiently.

Chapter 8. OPEN-SOURCE SOFTWARE FOR AIDED HIGH-THROUGHPUT DATA CLASSIFICATION USING CONVOLUTIONAL NEURAL NETWORKS

8.1 BACKGROUND

To create a more streamlined process for experimental design with minimum user interaction, it is paramount to combine high-throughput experimentation with reliable and efficient data analysis strategies. High-throughput experimentation (HTE) and high-throughput testing (HTT) have exponentially increased the volume of experimental data available to scientists. However, one of the major bottlenecks in their implementation is the data analysis. Without the aid of faster and automated data classification, the bottleneck of the high-throughput sample screening process would simply be shifted form the experimental tasks, to the feature recognition and modeling steps. Machine learning algorithms are effective tools that can aid the performance of the classification task and increase its efficiency. The need for autonomous binning and classification has seen an increase in the employment of machine learning approaches in discovery of catalysts, energy materials and process parameters for design of experiment. [1,2] However, these solutions rely on specific sets of hyperparameters for their machine learning models to achieve the desired purpose. Furthermore, numerical data from experimental characterization of materials carries diversity in features and magnitude. These features are traditionally extracted using deterministic models based on empirical relationships between variables of the process under investigation. As an example, X-ray diffraction (XRD) data is easier to characterize in linear form as compared to small angle X-ray scattering data, which requires transformation of axis to log-log scale.

One of the most widely applied strategy to enhance the performance of machine learning model is Combined Automatic Machine Learning (AutoML) for combined alogrithm selection and hyperparameter optimization (CASH), [3] However, these packages are only limited to hyper-parameter tuning and data features remain untouched. To improve the effectiveness of machine learning models, some of the popular feature engineering strategies used for simple numerical data include binning, binarization, normalization, and Box-Cox transformations are popular feature engineering strategies for simple numerical data like ratings vs. reviews.[4] Moreover, Deep Feature Synthesis has shown promising results. Here features are generated from relational databases by performing multi-layer mathematical transformation operations. [5] Another package employs transformation of data in Quantile Sketch Array (QSA) to improve the effectiveness of machine learning model. [6].

Another aspect often ignored during evaluation of machine learning model is kernel methods based on feature engineering. Feature engineering has demonstrated the importance of presenting the data in the correct form, order, and structure can significantly dictate how well a machine learning model can perform. [5,6] In fact, after being collected, the data may also require further processing or visualization through multiple transformations. By refining the way data is represented to the ML model, features can be extracted effectively and efficiently. It is also possible to code data into the red, green and blue (RGB) channels of a color image, thus constructing a pattern which could be easily distinguishable by the algorithm. To implement high-throughput analysis to a variety of data, an open source python-based package named HARDy, which stands for “Handling Arbitrary Recognition of Data in Python”, was developed in collaboration with two other graduate students, Abdul Moeez and David Hurt, from the Materials Science and Engineering department and the Chemical Engineering department, respectively. The

package can be described as a feature extraction and data representation algorithm which applies mathematical transformations to raw data as part of feature engineering and then evaluates the performance of ML classification algorithm through application of kernel methods by encoding data in RGB patterns. The package provides an extension to machine learning by adding layers of feature transformation and representation. HARDy` presents an infrastructure which aids in the identification of the best combination of numerical and visual transformations to improve data classification through convolutional neural networks (CNN). `HARDy` exploits the difference between human-readable images of experimental data (i.e. Cartesian representation) and computer-readable plots, which maximizes the data density presented to an algorithm and reduces superfluous information. `HARDy` uses configuration files, fed to the open-source package `Keras-tuner`, removing the need for the user to manually generate unique parameters combinations for each neural network model to be investigated. The workflow of the package is as follows:

- *`Configuration:`* Sets attributes for user-defined transformations, machine learning hyperparameters, or hyperparameter space.
- *`Handling`*: Imports pre-labeled data from `.csv` files and loads it into the catalog. Later, the data will be split into training and testing sets.
- *`Arbitrage`*: Applies user-defined numerical and visual transformations to all the loaded data.
- *`Recognition`*: A machine learning module that applies user-defined hyperparameter search space for training and evaluation of the model.
- *`Data-Reporting`*: Imports the results of machine learning models and reports them into dataframes and plots.

8.2 Description and Use Case

The python-based package HARDy is a modularly structured package which classifies data using 2D convolutional neural networks. A schematic for the package can be found in Figure 8.1.

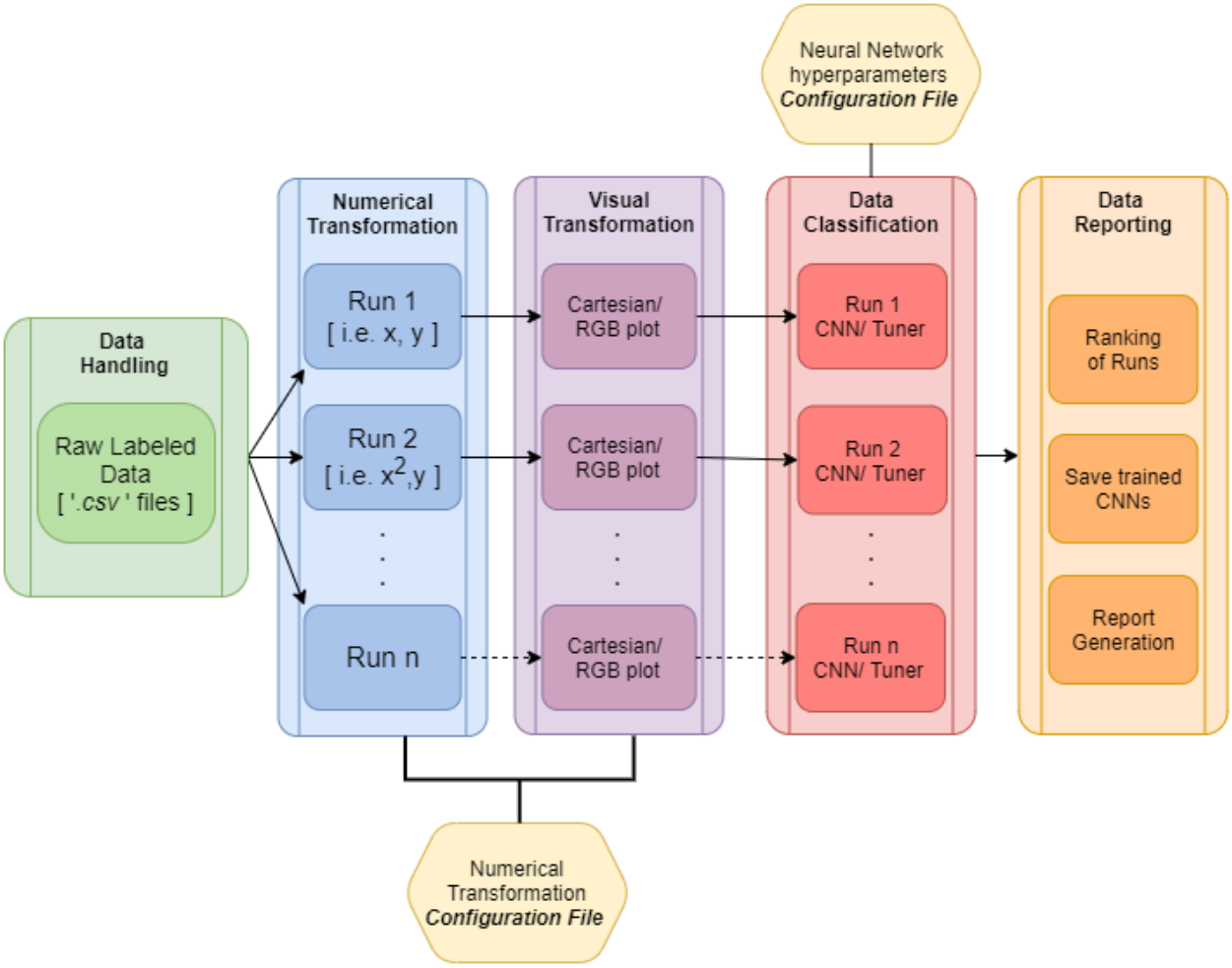

Figure 8.1 Information flow for HARDy

The package was tested on a set of simulated small angle scattering (SAS) data to be classified into four different particle models: spherical, ellipsoidal, cylindrical and core-shell spherical. A total of ten thousand files were generated for each model. The data was generated using sasmodels, a python-based software for modeling and fitting of SAS data. [7] The geometrical and physical parameters used to obtain each spectrum were taken from a published work

discussing a similar classification task. [8]. The name of each SAS model was used as label for the data, allowing for further validation of the test set results. These models were selected as they present similar parameters and data features, which at times make it challenging to distinguish between them.

First, the pre-labelled data was loaded. A subset of the files, three thousand files in total, is identified as the testing set. It is to note that all the ML models initialized in the same code run are validated using the same testing set. A user-provided list of transformations, input through a configuration file, is applied to the data. Different trials can be specified, so that multiple sets of transformations can be investigated. Both Cartesian and RGB plots representations were compared. The latter visualization option was obtained by encoding the data into the pixel values of each channel composing a color image, for a total of six-channels available (i.e., 3 RGB channels in horizontal/vertical orthogonal directions). Figure 8.2 shows an example of numerical and visual transformation applied to a spherical model data.

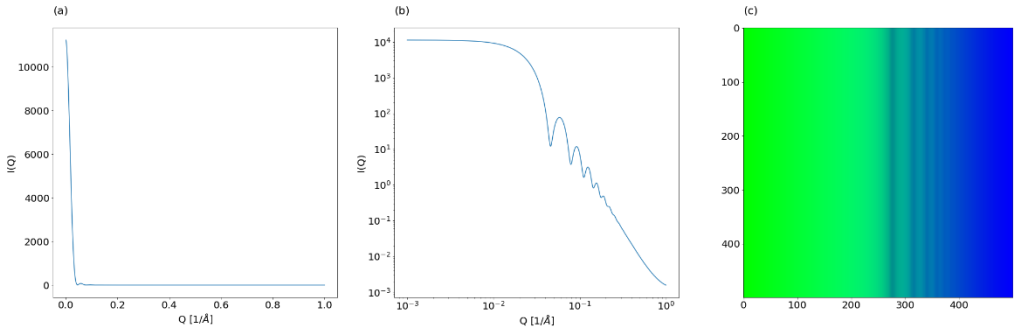

Figure 8.2 Comparison between numerical and visual transformations on the same dataset. Panel (a) show the data visualized in cartesian coordinates in a lin-lin manned. Panel (b) represents the same data after both the scattering length q and the intensity I(q) have been logarithmically transformed. Panel (c) show the log-log data plotted in the blue and green channel of an RGB image

The data is then fed into a convolutional neural network, whose hyperparameters and structure were defined using another configuration file. Alternatively, it is also possible to train multiple classifiers for a single transformation trial through the use of a tuner, by instead providing a hyperparameter space and a search method. The classification results, as well as the best performing trained model were saved for each transformation run. The package also allows the user to visually compare, through a parallel coordinates plot (see documentation), the performance of each transformation and, in the case of a tuning session, which hyperparameter combination yielded higher classification accuracy. Figure 8.3 shows a summary of a few runs comparing the two visualization strategies.

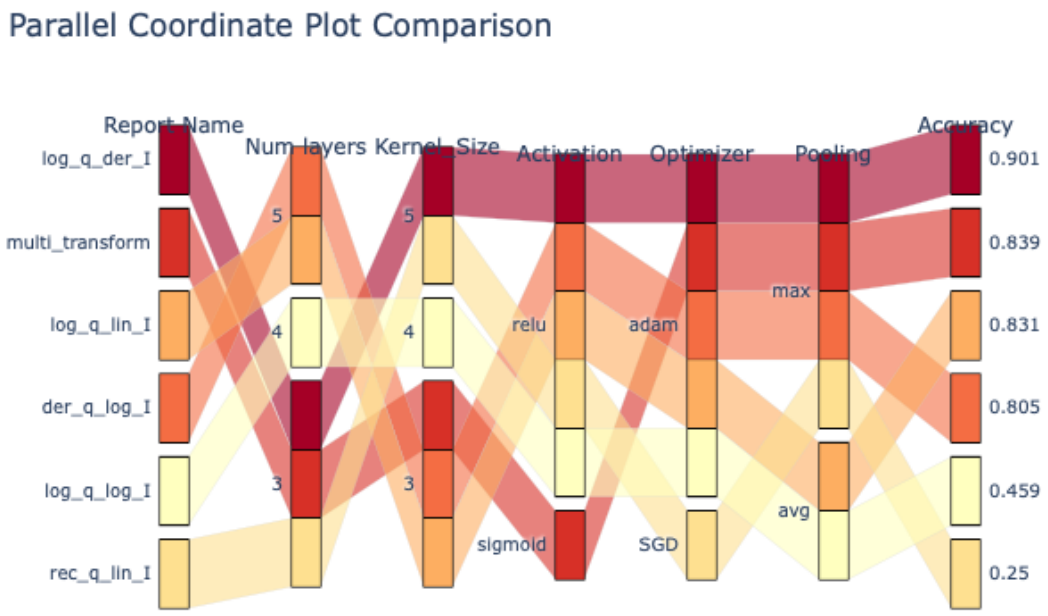

Figure 8.3 Parallel Coordinate Plot for the classification of SAS data into four models: spherical, cylindrical, ellipsoidal and core-shell sphere. The name of each run corresponds to the transformation applied to the scattering length q and intensity I. These results visualized the data in RGB plot. Only a limited number of transformations tested is shown here (see documentation)

Comprehensive results for all transformations tested are available in the documentation. It can be noticed that data representation using Cartesian coordinate plots yielded a higher number of instances in which the accuracy of the trained machine learning model was ~25%. This value corresponds to machine learning model's inability to recognize differences in a four-class classification task. On the other hand, the RGB plots show, on average, higher accuracy for the same combinations of numerical transformations. To further validate the results, mathematical fitting was performed on a test set using the SASmodels package. The fitting was based on probabilities determined by the ML model for each label. In scenarios where the output probability was below 70\%, the data was also fitted using the second highest possible SAS model.

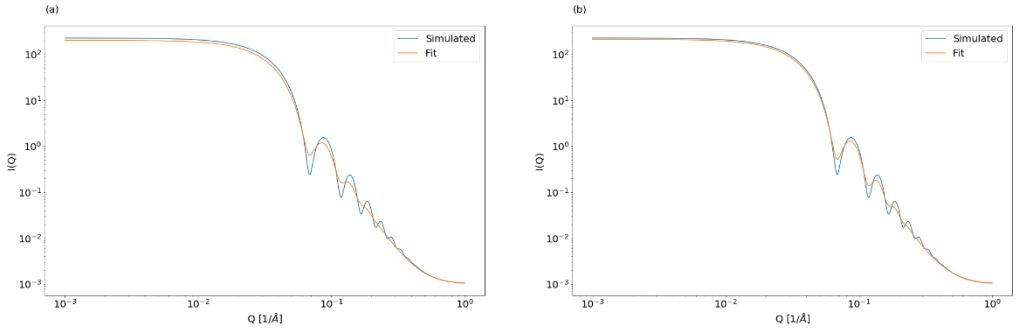

Figure 8.4 Comparison of spherical fit (a) and core-shell sphere fit (b) on a file generated using the latter model. The machine learning model incorrectly labeled the data with a spherical model, however both models seem to fit the data similarly well.

The average chi-square parameter of the fitted data was determined to be 7.5. Approximately 11 % of the data had a probability lower than 70\%. In all cases, if the neural network was not able to correctly label the data with the highest probability label, the second highest probability label was the correct one.

In conclusion, we have demonstrated reliability in the classification task provided by `HARDy`. The code can also be used to guide modeling of data and will help identify the most probable model(s) to use, decreasing significantly the time spent on data analysis. Finally, the minimal user interaction required by the package allows for deployment of the task on a supercomputing cluster system, possibly removing the limitations given by the high computational power required to run these ML algorithms. All configuration files and scripts used to run the example presented in this paper can be found in the package documentation.[9]

8.3 References

1. Williams, T., McCullough, K. & Lauterbach, J. A. Enabling Catalyst Discovery through Machine Learning and High-Throughput Experimentation. *Chemistry of Materials* **32**, 157–165 (2020).

2. Becker, P. *et al.* Low Temperature Synthesis of Stable γ-CsPbI3 Perovskite Layers for Solar Cells Obtained by High Throughput Experimentation. *Adv Energy Mater* **9**, 1900555 (2019).
3. Hutter, F., Kotthoff, L. & Vanschoren, J. *Automated Machine Learning*. (Springer International Publishing, Cham, 2019). doi:10.1007/978-3-030-05318-5.
4. Zheng, A. & Casari, A. *Feature Engineering for Machine Learning*. (2018).
5. Kanter, J. M. & Veeramachaneni, K. Deep feature synthesis: Towards automating data science endeavors. *Proceedings of the 2015 IEEE International Conference on Data Science and Advanced Analytics, DSAA 2015* (2015) doi:10.1109/DSAA.2015.7344858.
6. Nargesian, F., Samulowitz, H., Khurana, U., Khalil, E. B. & Turaga, D. Learning Feature Engineering for Classification. (2017).
7. sasmodels package — SasView 5.0.6 documentation. https://www.sasview.org/docs/dev/sasmodels-api/sasmodels.html.
8. Archibald, R. K. *et al.* Classifying and analyzing small-angle scattering data using weighted k nearest neighbors machine learning techniques. *J Appl Crystallogr* **53**, 326–334 (2020).
9. Politi, M., Moeez, A. & Hurt, D. HARDy. *GitHub* https://github.com/EISy-as-Py/hardy (2020).

BIBLIOGRAPHY

Abbott, A. P. Deep eutectic solvents and their application in electrochemistry. *Curr Opin Green Sustain Chem* **36**, (2022).

Abbott, A. P. *et al*. Glycerol eutectics as sustainable solvent systems. *Green Chemistry* **13**, 82–90 (2011).

Abbott, A. P., Boothby, D., Capper, G., Davies, D. L. & Rasheed, R. K. Deep Eutectic Solvents formed between choline chloride and carboxylic acids: Versatile alternatives to ionic liquids. *J Am Chem Soc* **126**, 9142–9147 (2004).

Abbott, A. P., Capper, G., Davies, D. L., Rasheed, R. K. & Tambyrajah, V. Novel solvent properties of choline chloride/urea mixtures. *Chemical Communications* 70–71 (2003) doi:10.1039/b210714g.

Abbott, A. P., Capper, G., Davies, D. L., Rasheed, R. K. & Tambyrajah, V. Novel solvent properties of choline chloride/urea mixtures †. (2002) doi:10.1039/b210714g.

Abbott, A. P., Harris, R. C. & Ryder, K. S. Application of hole theory to define ionic liquids by their transport properties. *Journal of Physical Chemistry B* **111**, 4910–4913 (2007).

Abbott, A. P., Ttaib, E., Frisch, G., Mckenzie, K. J. & Ryder, K. S. Electrodeposition of copper composites from deep eutectic solvents based on choline chloride. (2009) doi:10.1039/b817881j.

Abdel-Latif, K. *et al.* Self-Driven Multistep Quantum Dot Synthesis Enabled by Autonomous Robotic Experimentation in Flow 2000245 (1 of 13). *Adv. Intell. Syst* **3**, (2021).

Abe, S., Capek, R. K., de Geyter, B. & Hens, Z. Reaction chemistry/nanocrystal property relations in the hot injection synthesis, the role of the solute solubility. *ACS Nano* **7**, 943–949 (2013).

Abolhasani, M. & Kumacheva, E. The rise of self-driving labs in chemical and materials sciences. *Nature Synthesis 2023 2:6* **2**, 483–492 (2023).

Acros-Organics. Choline Chloride ; SDS AC110290000. 1–7 Preprint at (2021).

Adams, F., Mcdannald, A., Takeuchi, I. & Gilad Kusne, A. Human-in-the-loop for Bayesian autonomous materials phase mapping. doi:10.1016/j.matt.2024.01.005.

Al-Murshedi, A. Y. M., Hartley, J. M., Abbott, A. P. & Ryder, K. S. Effect of water on the electrodeposition of copper on nickel in deep eutectic solvents. *https://doi.org/10.1080/00202967.2019.1671062* **97**, 321–329 (2019).

Alotto, P., Guarnieri, M. & Moro, F. Redox flow batteries for the storage of renewable energy: A review. *Renewable and Sustainable Energy Reviews* **29**, 325–335 (2014).

Antonio, E. & Politi, M. pozzo-research-group/OT2-DOE. https://github.com/pozzo-research-group/OT2-DOE (2022).

Aspuru-Guzik, A. & Persson, K. *Materials Acceleration Platform: Accelerating Advanced Energy Materials Discovery by Integrating High-Throughput Methods and Artificial Intelligence*. https://www.cifar.ca/wp-content/uploads/MissionInnovationIC6Report.pdf (2018).

Baas, S. & Saggiomo, V. Ender3 3D printer kit transformed into open, programmable syringe pump set. *HardwareX* **10**, e00219 (2021).

Baird, S. G. & Sparks, T. D. Building a "Hello World" for self-driving labs: The Closed-loop Spectroscopy Lab Light-mixing demo. *STAR Protoc* **4**, 102329 (2023).

Bard, A. J., Faulkner, L. R. & White, H. S. *Electrochemical Methods*. (Wiley, 2022).

Bateni, F. *et al.* Smart Dope: A Self-Driving Fluidic Lab for Accelerated Development of Doped Perovskite Quantum Dots. *Adv Energy Mater* (2023) doi:10.1002/aenm.202302303.

Bennett, J. A. *et al.* Autonomous reaction Pareto-front mapping with a self-driving catalysis laboratory. *Nature Chemical Engineering* **1**, 240–250 (2024).

Bera, D., Qian, L., Tseng, T.-K. & Holloway, P. H. Quantum Dots and Their Multimodal Applications: A Review. *Materials* 2260–2345 Preprint at https://doi.org/10.3390/ma3042260 (2010).

Bhom, A. AMi: A GUI-based, open-source system for imaging samples in multi-well plates. *Acta Crystallogr F Struct Biol Commun* **75**, 531–536 (2019).

Bi, Y. *et al.* Efficient CO2 capture by a novel deep eutectic solvent through facile, one-pot synthesis with low energy consumption and feasible regeneration. *Science of the Total Environment* **705**, (2020).

Biernacki, K., Souza, H. K. S., Almeida, C. M. R., Magalhães, A. L. & Goncąlves, M. P. Physicochemical Properties of Choline Chloride-Based Deep Eutectic Solvents with Polyols: An Experimental and Theoretical Investigation. *ACS Sustain Chem Eng* **8**, 18712–18728 (2020).

Bing, Y. & Zhang, B. Analytical Issues in Combinatorial Chemistry. in *Analytical Methods in Combinatorial Chemistry* 1–11 (2010).

Blow, N. Lab automation: tales along the road to automation. *Nature Methods 2008 5:1* **5**, 109–112 (2008).

Bootharaju, M. S. *et al.* Magic-Sized Stoichiometric II-VI Nanoclusters. *Small* **17**, 1–16 (2021).

Borman, S. Combinatorial chemistry. *Chem. Eng. News* **76**, 47–67 (1998).

Bravo-Martinez, J. Open source 3D-printed 1000 lL micropump. *Hardware X* (2018) doi:10.1016/j.ohx.2017.08.002.

Breßler, I., Pauw, B. R. & Thünemann, A. F. McSAS: A tool for extracting form-free size distributions of small-angle scattering (SAS) patterns using a Monte-Carlo method. *GitHub* Preprint at https://github.com/BAMresearch/McSAS (2022).

Breßler, I., Pauw, B. R. & Thünemann, A. F. McSAS: Software for the retrieval of model parameter distributions from scattering patterns. *J Appl Crystallogr* **48**, 962–969 (2015).

Browder, R. E., Aldrich, H. E. & Bradley, S. W. The emergence of the maker movement: Implications for entrepreneurship research. *J Bus Ventur* **34**, 459–476 (2019).

Bruchez, M., Moronne, M., Gin, P., Weiss, S. & Alivisatos, A. P. Semiconductor nanocrystals as fluorescent biological labels. *Science* **281**, 2013–2016 (1998).

Burger, B. *et al.* A mobile robotic chemist. *Nature* **583**, 237–241 (2020).

Caramelli, D. *et al.* Discovering New Chemistry with an Autonomous Robotic Platform Driven by a Reactivity-Seeking Neural Network. *ACS Cent Sci* **7**, 1821–1830 (2021).

Carey, G. H. *et al.* Colloidal Quantum Dot Solar Cells. (2015) doi:10.1021/acs.chemrev.5b00063.

Carvalho, M. C. & Murray, R. H. Osmar, the open-source microsyringe autosampler. *HardwareX* **3**, 10–38 (2018).

Caschera, F. *et al.* Automated Discovery of Novel Drug Formulations Using Predictive Iterated High Throughput Experimentation. *PLoS One* **5**, (2010).

Chakrabarti, M. H. *et al.* Prospects of applying ionic liquids and deep eutectic solvents for renewable energy storage by means of redox flow batteries. *Renewable and Sustainable Energy Reviews* **30**, 254–270 (2014).

Chakrabarti, M. H., Dryfe, R. A. W. & Roberts, E. P. L. Evaluation of electrolytes for redox flow battery applications. *Electrochim Acta* **52**, 2189–2195 (2007).

Chalamala, B. R. *et al.* Redox flow batteries: An engineering perspective. *Proceedings of the IEEE* **102**, 976–999 (2014).

Chan, C. Y. *et al.* Accelerating drug discovery via organs-on-chips. *Lab Chip* **13**, 4697 (2013).

Chan, E. M. *et al.* Reproducible, High-Throughput Synthesis of Colloidal Nanocrystals for Optimization in Multidimensional Parameter Space. *Nano Lett* **10**, 1874–1885 (2010).

Chen, B. *et al.* Feasibility of TEMPO-functionalized imidazolium, ammonium and pyridinium salts as redox-active carriers in ethaline deep eutectic solvent for energy storage. *Mol Syst Des Eng* **5**, 1147–1157 (2020).

Chen, T. & Guestrin, C. XGBoost: A Scalable Tree Boosting System. *Proceedings of the 22nd ACM SIGKDD International Conference on Knowledge Discovery and Data Mining* 785–794 (2016) doi:10.1145/2939672.2939785.

Cheng, L. *et al.* Accelerating Electrolyte Discovery for Energy Storage with High-Throughput Screening. *Journal of Physical Chemistry Letters* vol. 6 283–291 Preprint at https://doi.org/10.1021/jz502319n (2015).

Christensen, M. *et al.* Data-science driven autonomous process optimization. *Commun Chem* **4**, (2021).

Coley, C. W. *et al.* A robotic platform for flow synthesis of organic compounds informed by AI planning. *Science* **365**, 1–9 (2019).

Coley, C. W., Eyke, N. S. & Jensen, K. F. Autonomous Discovery in the Chemical Sciences Part I: Progress. *Angewandte Chemie - International Edition* **59**, 22858–22893 (2020).

Coutant, A. *et al.* Closed-loop cycles of experiment design, execution, and learning accelerate systems biology model development in yeast. *PNAS* (2019) doi:10.1073/pnas.1900548116.

Cruz, H., Jordão, N. & Branco, L. C. Deep eutectic solvents (DESs) as low-cost and green electrolytes for electrochromic devices. *Green Chemistry* **19**, 1653–1658 (2017).

Cruz-Monteagudo, M., Borges, F. & Cordeiro, M. N. D. S. Desirability-Based Multiobjective Optimization for Global QSAR Studies: Application to the Design of Novel NSAIDs with Improved Analgesic, Antiinflammatory, and Ulcerogenic Profiles. (2008) doi:10.1002/jcc.20994.

Cummins, D. J. & Bell, M. A. Integrating Everything: The Molecule Selection Toolkit, a System for Compound Prioritization in Drug Discovery. *J. Med. Chem* **59**, 7010 (2016).

Dai, Q. *et al.* Facile synthesis of magic-sized CdSe and CdTe nanocrystals with tunable existence periods. *Nanotechnology* **18**, 405603 (2007).

Dai, X. *et al.* Solution-processed, high-performance light-emitting diodes based on quantum dots. *Nature* **515**, 96–99 (2014).

Darling, R. M., Gallagher, K. G., Kowalski, J. A., Ha, S. & Brushett, F. R. Pathways to low-cost electrochemical energy storage: A comparison of aqueous and nonaqueous flow batteries. *Energy Environ Sci* **7**, 3459–3477 (2014).

Dave, A. *et al.* Autonomous Discovery of Battery Electrolytes with Robotic Experimentation and Machine Learning. *Cell Rep Phys Sci* **1**, (2020).

de Mello Donegá, C., Liljeroth, P. & Vanmaekelbergh, D. Physicochemical evaluation of the hot-injection method, a synthesis route for monodisperse nanocrystals. *Small* **1**, 1152–1162 (2005).

Dean, W., Klein, J. & Gurkan, B. Do Deep Eutectic Solvents Behave Like Ionic Liquid Electrolytes? A Perspective from the Electrode-Electrolyte Interface. *J Electrochem Soc* **168**, 026503 (2021).

DeBruler, C. *et al.* Designer Two-Electron Storage Viologen Anolyte Materials for Neutral Aqueous Organic Redox Flow Batteries. *Chem* **3**, 961–978 (2017).

Definition (English) - Open Source Hardware Association. https://www.oshwa.org/definition/.

del Mar Contreras-Gámez, M. *et al.* Deep eutectic solvents for improved biomass pretreatment: Current status and future prospective towards sustainable processes. *Bioresour Technol* **369**, 128396 (2023).

Delgado-Licona, F. & Abolhasani, M. Research Acceleration in Self-Driving Labs: Technological Roadmap toward Accelerated Materials and Molecular Discovery. *Advanced Intelligent Systems* **5**, (2023).

Deneault, J. R. *et al.* Toward autonomous additive manufacturing: Bayesian optimization on a 3D printer. *MRS Bull* **46**, (2021).

Dmello, R., Milshtein, J. D., Brushett, F. R. & Smith, K. C. Cost-driven materials selection criteria for redox flow battery electrolytes. *J Power Sources* **330**, 261–272 (2016).

Duet3D . https://www.duet3d.com/.

Dunn, B., Kamath, H. & Tarascon, J. M. Electrical energy storage for the grid: A battery of choices. *Science (1979)* **334**, 928–935 (2011).

Dunn, K., Feng, C. & Peek, N. Jubilee: A Case Study of Distributed Manufacturing in an Open Source Hardware Project. *Journal of Open Hardware* **7**, 1–15 (2023).

Eggert, S., Mieszczanek, P., Meinert, C. & Hutmacher, D. W. OpenWorkstation: A modular open-source technology for automated in vitro workflows. *HardwareX* **8**, e00152 (2020).

Elgrishi, N. *et al.* A Practical Beginner's Guide to Cyclic Voltammetry. (2017) doi:10.1021/acs.jchemed.7b00361.

Epps, R. W., Felton, K. C., Coley, C. W. & Abolhasani, M. Automated microfluidic platform for systematic studies of colloidal perovskite nanocrystals: towards continuous nano-manufacturing. *Lab Chip* **17**, 4040–4047 (2017).

Epps, R. W., Volk, A. A., Ibrahim, M. Y. S. & Abolhasani, M. Universal self-driving laboratory for accelerated discovery of materials and molecules. *Cell Press* **7**, 2541–2545 (2021).

Er, S., Suh, C., Marshak, M. P. & Aspuru-Guzik, A. Computational design of molecules for an all-quinone redox flow battery. *Chem Sci* **6**, 885–893 (2015).

Er, S., Suh, C., Marshak, M. P. & Aspuru-Guzik, A. Computational design of molecules for an all-quinone redox flow battery. *Chem Sci* **6**, 885–893 (2015).

F.S. Ghareh Bagh, K. Shahbaz, F.S. Mjalli, I.M. AlNashef, M. A. H. Electrical conductivity of ammonium and phosphonium based deep eutectic solvents: Measurements and artificial intelligence-based prediction | Elsevier Enhanced Reader. *Fluid Phase Equilib* **356**, 30–37 (2013).

Faiña, A., Nejati, B. & Stoy, K. EvoBot: An Open-Source, Modular, Liquid Handling Robot for Scientific Experiments. doi:10.3390/app10030814.

Feng, R. *et al.* Reversible ketone hydrogenation and dehydrogenation for aqueous organic redox flow batteries. *Science (1979)* **372**, 836–840 (2021).

Flores-Leonar, M. M. *et al.* Materials Acceleration Platforms: On the way to autonomous experimentation. *Curr Opin Green Sustain Chem* **25**, 100370 (2020).

formlabs. FLHTAM02- High Temp Resin. Preprint at (2020).

Friedman, J. H. Greedy Function Approximation: A Gradient Boosting Machine on JSTOR. *The Annals of Statistics* **29**, 1189–1232 (2001).

Friedman, J., Hastie, T. & Tibshirani, R. *Additive Logistic Regression: A Statistical View of Boosting*. *The Annals of Statistics* vol. 28 (2000).

Fuchs, D. *et al.* Electrochemical Behavior of Graphene in a Deep Eutectic Solvent. *Cite This: ACS Appl. Mater. Interfaces* **12**, 40948 (2020).

Gallagher, P. K. *Handbook of Thermal Analysis and Calorimetry*. vol. 1 (1998).

García, G., Aparicio, S., Ullah, R. & Atilhan, M. Deep eutectic solvents: Physicochemical properties and gas separation applications. *Energy and Fuels* **29**, 2616–2644 (2015).

García-Rodríguez, R. & Liu, H. Mechanistic insights into the role of alkylamine in the synthesis of CdSe nanocrystals. *J Am Chem Soc* **136**, 1968–1975 (2014).

Ghahremani, R., Savinell, R. F. & Gurkan, B. Perspective-Hydrogen Bonded Concentrated Electrolytes for Redox Flow Batteries: Limitations and Prospects. *J Electrochem Soc* **169**, (2022).

Ginsburg, T. *et al.* Exploring Benchmarks for Self-Driving Labs using Color Matching. *ACM International Conference Proceeding Series* 2147–2152 (2023) doi:10.1145/3624062.3624615.

Goeltz, J. C. & Carter, J. M. Finding balance with deep eutectic solvents: High concentrations and improved conductivities for the off-the-shelf nitroxide TEMPOL. *J Mol Liq* **338**, (2021).

Goeltz, J. C. & Matsushima, L. N. Metal-free redox active deep eutectic solvents. *Chemical Communications* **53**, 9983–9985 (2017).

Gómez-Bombarelli, R. *et al.* Automatic chemical design using a data-driven continuous representation of molecules. *ACS Cent. Sci.* **4**, 268–276 (2018).

González De Castilla, A., Bittner, J. P., Müller, S., Jakobtorweihen, S. & Smirnova, I. Thermodynamic and Transport Properties Modeling of Deep Eutectic Solvents: A Review on gE-Models, Equations of State, and Molecular Dynamics. *J Chem Eng Data* **65**, 943–967 (2020).

Gu, Y., Hou, Y., Ren, S., Sun, Y. & Wu, W. Hydrophobic Functional Deep Eutectic Solvents Used for Efficient and Reversible Capture of CO2. *ACS Omega* **5**, 6809–6816 (2020).

Gurkan, B., Squire, H. & Pentzer, E. Metal-Free Deep Eutectic Solvents: Preparation, Physical Properties, and Significance. *J. Phys. Chem. Lett* **10**, 26 (2019).

Gurkan, B., Squire, H. & Pentzer, E. Metal-Free Deep Eutectic Solvents: Preparation, Physical Properties, and Significance. *Journal of Physical Chemistry Letters* **10**, 7956–7964 (2019).

Haerens, K., Matthijs, E., Binnemans, K. & van der Bruggen, B. Electrochemical decomposition of choline chloride based ionic liquid analogues. (2009) doi:10.1039/b906318h.

Haghbakhsh, R., Parvaneh, K., Raeissi, S. & Shariati, A. A general viscosity model for deep eutectic solvents: The free volume theory coupled with association equations of state. *Fluid Phase Equilib* **470**, 193–202 (2018).

Halder, A. K., Ambure, P., Perez-Castillo, Y. & Cordeiro, M. N. D. S. Turning deep-eutectic solvents into value-added products for CO2 capture: A desirability-based virtual screening study. *Journal of CO2 Utilization* **58**, 101926 (2022).

Harrell, S. M., McBride, J. R. & Rosenthal, S. J. Synthesis of ultrasmall and magic-sized CdSe nanocrystals. *Chemistry of Materials* **25**, 1199–1210 (2013).

Harris, D. C. & Bertolucci, M. D. *Symmetry and Spectroscopy- An Introduction to Vibrational and Electronic Spectroscopy*. (Oxford University Press, Inc., 1978).

Heuer-Jungemann, A. *et al.* The Role of Ligands in the Chemical Synthesis and Applications of Inorganic Nanoparticles. **119**, 4819–4880 (2019).

Hey, T., Tansley, S. & Tolle, K. *The Fourth Paradigm: Data-Driven Discovery*. (2009).

Hill, N. A. & Whaley, K. B. A theoretical study of the influence of the surface on the electronic structure of CdSe nanoclusters. *J Chem Phys* **100**, 2831 (1994).

Hobson, R. A., Muivaney, P. & Grieser, F. Formation of Q-state CdS Colloids using Ultrasound. *J. CHEM. SOC., CHEM. COMMUN* 823–824 (1994).

Holbrey, J. D ; Seddon, K. R. Ionic Liquids. *Clean Technol. Environ. Policy* **1**, 223–236 (1999).

Hou, Y. *et al.* Novel binary eutectic mixtures based on imidazole. *J Mol Liq* **143**, 154–159 (2008).

Houben, C. & Lapkin, A. A. Automatic discovery and optimization of chemical processes. *Curr. Opin. Chem. Eng.* **9**, 1–7 (2015).

Hu, B., DeBruler, C., Rhodes, Z. & Liu, T. L. Long-Cycling Aqueous Organic Redox Flow Battery (AORFB) toward Sustainable and Safe Energy Storage. *J Am Chem Soc* **139**, 1207–1214 (2017).

Hu, B., Hu, M., Luo, J. & Liu, T. L. A Stable, Low Permeable TEMPO Catholyte for Aqueous Total Organic Redox Flow Batteries. (2021) doi:10.1002/aenm.202102577.

Hu, B., Luo, J., Hu, M., Yuan, B. & Liu, T. L. A pH-Neutral, Metal-Free Aqueous Organic Redox Flow Battery Employing an Ammonium Anthraquinone Anolyte. *Angewandte Chemie - International Edition* **58**, 16629–16636 (2019).

Huang, X., Parashar, V. K. & Gijs, M. A. M. Nucleation and Growth Behavior of CdSe Nanocrystals Synthesized in the Presence of Oleylamine Coordinating Ligand. *Langmuir* **34**, 6070–6076 (2018).

Huskinson, B. *et al.* A metal-free organic-inorganic aqueous flow battery. *Nature* **505**, (2014).

Ibrahim, R. K. *et al.* Physical properties of ethylene glycol-based deep eutectic solvents. *J Mol Liq* **276**, 794–800 (2019).

Jeraal, M. I., Sung, S. & Lapkin, A. A. A Machine Learning-Enabled Autonomous Flow Chemistry Platform for Process Optimization of Multiple Reaction Metrics. *Chemistry - Methods* **1**, 71–77 (2021).

Ji, Y. *et al.* A Phosphonate-Functionalized Quinone Redox Flow Battery at Near-Neutral pH with Record Capacity Retention Rate. *Advanced Science News* 1–17 (2019) doi:10.1002/aenm.201900039.

Ji, Y. *et al.* Recent research progress of redox flow batteries based on deep eutectic solvents (DESs). *Int J Green Energy* (2022) doi:10.1080/15435075.2022.2079949.

Jiang, Y. *et al.* Synthesis of CdSe Nanoplatelets without Short-Chain Ligands: Implication for Their Growth Mechanisms. *ACS Omega* **3**, 6199–6205 (2018).

Jones, D. R., Schonlau, M. & Welch, W. J. Efficient Global Optimization of Expensive Black-Box Functions. *Journal of Global Optimization* **13**, 455–492 (1998).

Jones, R. *et al.* RepRap-The Replicating Rapid Prototyper Proof for review only RepRap-The Replicating Rapid Prototyper. : *Robotica* **29**, 177–191 (2011).

Jonveaux, L. Arduino-Like Development Kit for Single-Element Ultrasound Imaging. *Journal of Open Hardware* (2017) doi:10.5334/joh.2.

Jubilee. https://jubilee3d.com/index.php?title=Main_Page.

Jung, S. H. *et al.* Sonochemical preparation of shape-selective ZnO nanostructures. *Cryst Growth Des* **8**, 265–269 (2008).

Karami, B., Ghaemi, A. & Shahhosseini, S. Eco-Friendly Deep Eutectic Solvents Blended with Diethanolamine Solution for Postcombustion CO2 Capture. *Energy and Fuels* **36**, 945–957 (2022).

Karel Čapek, R. *et al.* Optical properties of zincblende cadmium selenide quantum dots. *Journal of Physical Chemistry C* **114**, 6371–6376 (2010).

Kastilani, R., Bishop, B. P., Holmberg, V. C. & Pozzo, L. D. On-Demand Sonochemical Synthesis of Ultrasmall and Magic-Size CdSe Quantum Dots in Single-Phase and Emulsion Systems. *Langmuir* **35**, 16583–16592 (2019).

Kaul, M. J., Qadah, D., Mandella, V. & Dietz, M. L. Systematic evaluation of hydrophobic deep-melting eutectics as alternative solvents for the extraction of organic solutes from aqueous solution. *RSC Adv* **9**, 15798–15804 (2019).

Kawakami, K. Parallel thermal analysis technology using an infrared camera for high-throughput evaluation of active pharmaceutical ingredients: A case study of melting point determination. *AAPS PharmSciTech* **11**, 1202–1205 (2010).

Keesey, R., LeSuer, R. & Schrier, J. Sidekick: A Low-Cost Open-Source 3D-printed liquid dispensing robot. *HardwareX* **12**, e00319 (2022).

Kim, W., Lim, S. J., Jung, S. & Shin, S. K. Binary amine-phosphine passivation of surface traps on CdSe nanocrystals. *Journal of Physical Chemistry C* **114**, 1539–1546 (2010).

King, R. D. *et al.* The automation of science. *Science (1979)* **324**, 85–89 (2009).

King, R. D. *et al.* The robot scientist adam. *Computer (Long Beach Calif)* **42**, 46–54 (2009).

Kirkpatrick, P. & Ellis, C. Chemical space. *Nature* **432**, 823 (2004).

Kristl, M. & Drofenik, M. Preparation of Au2S3 and nanocrystalline gold by sonochemical method. *Inorg Chem Commun* **12**, 1419–1422 (2003).

Kristl, M. & Drofenik, M. Sonochemical synthesis of nanocrystalline mercury sulfide, selenide and telluride in aqueous solutions. *Ultrason Sonochem* **15**, 695–699 (2008).

Kulik, H. J. & Sigman, M. S. Advancing Discovery in Chemistry with Artificial Intelligence: From Reaction Outcomes to New Materials and Catalysts. *Acc Chem Res* **54**, 2335–2336 (2021).

Kumari, K. *et al.* Effect of surface passivating ligand on structural and optoelectronic properties of polymer : CdSe quantum dot composites. *J Phys D Appl Phys* **41**, 235409 (2008).

Latif, K., Adam, A., Yusof, Y. & Kadir, A. Z. A. A review of G code, STEP, STEP-NC, and open architecture control technologies based embedded CNC systems. *International Journal of Advanced Manufacturing Technology* vol. 114 2549–2566 Preprint at https://doi.org/10.1007/s00170-021-06741-z (2021).

Leron, R. B. & Li, M. H. Solubility of carbon dioxide in a eutectic mixture of choline chloride and glycerol at moderate pressures. *Journal of Chemical Thermodynamics* **57**, 131–136 (2013).

Li, J. *et al.* Autonomous discovery of optically active chiral inorganic perovskite nanocrystals through an intelligent cloud lab. *Nature Communications 2020 11:1* **11**, 1–10 (2020).

Li, J., Tu, Y., Liu, R., Lu, Y. & Zhu, X. Toward "On-Demand" Materials Synthesis and Scientific Discovery through Intelligent Robots. *Advanced Science* **7**, (2020).

Li, Q. *et al.* The electrochemical stability of ionic liquids and deep eutectic solvents. *Sci China Chem* **59**, 571–577 (2016).

Li, T., Senesi, A. J. & Lee, B. Small Angle X-ray Scattering for Nanoparticle Research. (2016) doi:10.1021/acs.chemrev.5b00690.

Li, X., Hou, M., Han, B., Wang, X. & Zou, L. Solubility of CO2 in a choline chloride + urea eutectic mixture. *J Chem Eng Data* **53**, 548–550 (2008).

Liang, Q. *et al.* Benchmarking the performance of Bayesian optimization across multiple experimental materials science domains. *NPJ Comput Mater* **7**, (2021).

Likit-Anurak, K., Uthaichana, K., Punyawudho, K. & Khunatorn, Y. The Performance and Efficiency of Organic Electrolyte Redox Flow Battery Prototype. *Energy Procedia* **118**, 54–62 (2017).

Liu, J. & Hein, J. E. Automation, analytics and artificial intelligence for chemical synthesis. *Nature Synthesis* **2**, (2023).

Liu, T., Wei, X., Nie, Z., Sprenkle, V. & Wang, W. A Total Organic Aqueous Redox Flow Battery Employing a Low Cost and Sustainable Methyl Viologen Anolyte and 4-HO-TEMPO Catholyte. *Adv Energy Mater* **6**, (2016).

Liu, T., Wei, X., Nie, Z., Sprenkle, V. & Wang, W. A Total Organic Aqueous Redox Flow Battery Employing a Low Cost and Sustainable Methyl Viologen Anolyte and 4-HO-TEMPO Catholyte. *Adv Energy Mater* **6**, (2016).

Liu, Z., Shamsuzzoha, M., Ada, E. T., Reichert, W. M. & Nikles, D. E. Synthesis and activation of Pt nanoparticles with controlled size for fuel cell electrocatalysts. *J Power Sources* **164**, 472–480 (2007).

Lloret, J. O., Vega, L. F. & Llovell, F. Accurate description of thermophysical properties of Tetraalkylammonium Chloride Deep Eutectic Solvents with the soft-SAFT equation of state. *Fluid Phase Equilib* **448**, 81–93 (2017).

Lo, S. *et al.* Review of Low-cost Self-driving Laboratories in Chemistry and Materials Science: The 'Frugal Twin' Concept. *Digital Discovery* (2024) doi:10.1039/d3dd00223c.

López, N., Delso, I., Matute, D., Lafuente, C. & Artal, M. Characterization of xylitol or citric acid:choline chloride:water mixtures: Structure, thermophysical properties, and quercetin solubility. *Food Chem* **306**, (2020).

Lundberg, S. M., Allen, P. G. & Lee, S.-I. A Unified Approach to Interpreting Model Predictions. *Proceedings of the 31st International Conference on Neural Information Processing Systems* (2017).

Luo, J. *et al.* Unprecedented Capacity and Stability of Ammonium Ferrocyanide Catholyte in pH Neutral Aqueous Redox Flow Batteries. *Joule* **3**, 149–163 (2019).

Lv, Z. *et al.* Semiconductor Quantum Dots for Memories and Neuromorphic Computing Systems. *Chem Rev* **120**, 3941–4006 (2020).

Machine Agency. https://depts.washington.edu/machines/.

MacLeod, B. P. *et al.* Self-driving laboratory for accelerated discovery of thin-film materials. *Sci Adv* **6**, (2020).

MacLeod, B. P., Parlane, F. G. L., Brown, A. K., Hein, J. E. & Berlinguette, C. P. Flexible automation accelerates materials discovery. *Nat Mater* **21**, 722–726 (2022).

Maier, W. F., Stowe, K. & Sieg, S. Combinatorial and high-throughput materials science. *Angewandte Chemie - International Edition* **46**, 6016–6067 (2007).

Makoś-Chełstowska, P. VOCs absorption from gas streams using deep eutectic solvents – A review. *J Hazard Mater* **448**, 130957 (2023).

Martins, M. A. R., Pinho, S. P. & Coutinho, J. A. P. Insights into the Nature of Eutectic and Deep Eutectic Mixtures. *J Solution Chem* **48**, 962–982 (1234).

Matsuda, S., Nishioka, K. & Nakanishi, S. High-throughput combinatorial screening of multi-component electrolyte additives to improve the performance of Li metal secondary batteries. *Sci Rep* **9**, 1–3 (2019).

Maugeri, Z. & Domínguez De María, P. Novel choline-chloride-based deep-eutectic-solvents with renewable hydrogen bond donors: Levulinic acid and sugar-based polyols. *RSC Adv* **2**, 421–425 (2012).

McCullough, K., Williams, T., Mingle, K., Jamshidi, P. & Lauterbach, J. High-throughput experimentation meets artificial intelligence: A new pathway to catalyst discovery. *Physical Chemistry Chemical Physics* **22**, 11174–11196 (2020).

Medabalmi, V., Sundararajan, M., Singh, V., Baik, M.-H. & Byon, H. R. Naphthalene diimide as a two-electron anolyte for aqueous and neutral pH redox flow batteries †. *J Mater Chem A Mater* **8**, 11218–11223 (2020).

Miguel Hernández-Lobato, J., Requeima, J., Pyzer-Knapp, E. O. & Aspuru-Guzik, A. *Parallel and Distributed Thompson Sampling for Large-Scale Accelerated Exploration of Chemical Space*. (2017).

Mizukoshi, Y. *et al.* Preparation of platinum nanoparticles by sonochemical reduction of the Pt(IV) ions: role of surfactants. *Ultrason Sonochem* **8**, 1–6 (2001).

Murbach, M. D., Gerwe, B., Dawson-Elli, N. & Tsui, L.-K. impedance.py: A Python package for electrochemical impedance analysis. doi:10.21105/joss.02349.

Murcia, M. J. *et al.* Facile sonochemical synthesis of highly luminescent ZnS-shelled CdSe quantum dots. *Chemistry of Materials* **18**, 2219–2225 (2006).

Nejatimoharrami, F., Faina, A. & Stoy, K. New Capabilities of EvoBot: A Modular, Open-Source Liquid-Handling Robot. *SLAS Technol* **22**, 500–506 (2017).

Nemamcha, A., Rehspringer, J. L. & Khatmi, D. Synthesis of palladium nanoparticles by sonochemical reduction of palladium(II) nitrate in aqueous solution. *Journal of Physical Chemistry B* **110**, 383–387 (2006).

Nicolaou, C. A. & Brown, N. Multi-objective optimization methods in drug design. *Drug Discov Today Technol* **10**, (2013).

O'neill, S. AI-Driven Robotic Laboratories Show Promise. *Engineering* **7**, 1351–1353 (2021).

Okitsu, K., Ashokkumar, M. & Grieser, F. Sonochemical synthesis of gold nanoparticles: effects of ultrasound frequency. *J Phys Chem B* **109**, 20673–20675 (2005).

Open-Source Liquid Handler | OTTO. https://openliquidhandler.com/.

Opentrons/opentrons: Software for writing protocols and running them on the Opentrons Flex and Opentrons OT-2. https://github.com/Opentrons/opentrons.

Orazem, M. E. & Tribollet, B. *Electrochemical Impedance Spectroscopy*. (Wiley, 2008).

Ortiz-Martínez, V. M., Gómez-Coma, L., Pérez, G., Ortiz, A. & Ortiz, I. The roles of ionic liquids as new electrolytes in redox flow batteries. (2020) doi:10.1016/j.seppur.2020.117436.

Pan, D. *et al.* Synthesis of Cu-In-S ternary nanocrystals with tunable structure and composition. *J Am Chem Soc* **130**, 5620–5621 (2008).

Patil, S. S. & Rathod, V. K. Extraction and purification of curcuminoids from Curcuma longa using microwave assisted deep eutectic solvent based system and cost estimation. *Process Biochemistry* **126**, 61–71 (2023).

Pelkie, B. & Politi, M. pozzo-research-group/jubilee_pipette_BOdemo: Color matching bayesian optimization with jubilee, rewritten to use pipette. *GitHub* https://github.com/pozzo-research-group/jubilee_pipette_BOdemo (2024).

Peng, Z. A. & Peng, X. Formation of high-quality CdTe, CdSe, and CdS nanocrystals using CdO as precursor [6]. *J Am Chem Soc* **123**, 183–184 (2001).

Pineda, D., Pérez, J., Gaviria, D., Ospino-Villalba, K. & Camargo, O. MEDUSA: An open-source and webcam based multispectral imaging system. (2022) doi:10.1016/j.ohx.2022.e00282.

Politi, M. & Rodriguez, J. phasIR: Python modules for high-throughput measurement of melting point using IR bolometry. *GitHub* https://github.com/pozzo-research-group/phasIR (2021).

Popescu, A. M., Cojocaru, A., Donath, C. & Constantin, V. Electrochemical study and electrodeposition of copper(I) in ionic liquid-reline. *Chem Res Chin Univ* **29**, 991–997 (2013).

Powell, A. Democratizing production through open source knowledge: From open software to open hardware. *Media Cult Soc* **34**, 691–708 (2012).

pozzo-research-group. Automation-Hardware: Pozzo Group OT2 Hardware. *GitHub* https://github.com/pozzo-research-group/Automation-Hardware (2021).

Protesescu, L. *et al.* Nanocrystals of Cesium Lead Halide Perovskites (CsPbX3, X = Cl, Br, and I): Novel Optoelectronic Materials Showing Bright Emission with Wide Color Gamut. *Nano Lett* **15**, 3692–3696 (2015).

Pun, A. B., Mule, A. S., Held, J. T. & Norris, D. J. Core/Shell Magic-Sized CdSe Nanocrystals. (2021) doi:10.1021/acs.nanolett.1c02412.

Pyzer-Knapp, E. O. *et al.* Accelerating materials discovery using artificial intelligence, high performance computing and robotics. *NPJ Comput Mater* **8**, (2022).

Regan, B., Kinahan, D., Daly, P., O'kennedy, R. & Collins, D. Design and fabrication of a low-cost wireless camera imaging system for centrifugal microfluidics. *HardwareX* **11**, e00259 (2022).

Ren, F. *et al.* Accelerated discovery of metallic glasses through iteration of machine learning and high-throughput experiments. *Sci Adv* **4**, (2018).

Renewable Capacity Highlights. (2019).

Richards, P. L. Bolometers for Infrared and Millimeter Waves. *J Appl Phys* **76**, 1 (1994).

Roch, L. M. *et al.* ChemOS: An orchestration software to democratize autonomous discovery. *PLoS One* **15**, (2020).

Rodriguez, J. *et al.* PhasIR: An Instrumentation and Analysis Software for High-throughput Phase Transition Temperature Measurements. *Journal of Open Hardware* **5**, (2021).

Rodriguez, J., Politi, M., Adler, S., Beck, D. & Pozzo, L. High-throughput and data driven strategies for the design of deep-eutectic solvent electrolytes †. *Mol. Syst. Des. Eng* **7**, 933–949 (2022).

Romadina, E. I., Akkuratov, A. v., Simoska, O. & Stevenson, K. J. Phenazine-Based Compound as a Universal Water-Soluble Anolyte Material for the Redox Flow Batteries. *Batteries* **8**, (2022).

Saar, L. *et al.* The LEGOLAS Kit: A low-cost robot science kit for education with symbolic regression for hypothesis discovery and validation. *MRS Bull* **47**, 881–885 (2022).

Sadeghi, S., Khabbaz Abkenar, S., Ow-Yang, C. W. & Nizamoglu, S. Efficient White LEDs Using Liquid-state Magic-sized CdSe Quantum Dots. *Scientific Reports 2019 9:1* **9**, 1–9 (2019).

Sakaue, H., Aikawa, A. & Iijima, Y. Anodized-aluminum as quantum dot support for global temperature sensing from 100 to 500 K. *Sens Actuators B Chem* **150**, 569–573 (2010).

Salley, D. *et al.* A nanomaterials discovery robot for the Darwinian evolution of shape programmable gold nanoparticles. doi:10.1038/s41467-020-16501-4.

Schmidt, J., Marques, M. R. G., Botti, S. & Marques, M. A. L. Recent advances and applications of machine learning in solid-state materials science. *npj Computational Materials* vol. 5 Preprint at https://doi.org/10.1038/s41524-019-0221-0 (2019).

scipy.signal.find_peaks.
https://docs.scipy.org/doc/scipy/reference/generated/scipy.signal.find_peaks.html.

Seifrid, M. *et al.* Autonomous Chemical Experiments: Challenges and Perspectives on Establishing a Self-Driving Lab. *Acc Chem Res* **55**, 2454–2466 (2022).

Seifrid, M., Hattrick-Simpers, J., Aspuru-Guzik, A., Kalil, T. & Cranford, S. Reaching critical MASS: Crowdsourcing designs for the next generation of materials acceleration platforms. *Matter* **5**, 1972–1976 (2022).

Settles, B. *Active Learning*. (2012).

Shahbaz, K., Mjalli, F. S., Hashim, M. A. & Al Nashef, I. M. Using deep eutectic solvents for the removal of glycerol from palm oil-based biodiesel. *Journal of Applied Sciences* vol. 10 3349–3354 Preprint at https://doi.org/10.3923/jas.2010.3349.3354 (2010).

Shahriari, B., Swersky, K., Wang, Z., Adams, R. P. & De Freitas, N. Taking the human out of the loop: a review of Bayesian optimization. *Proc. IEEE* **104**, 148–175 (2016).

Sigma-Aldrich. Acetylcholine Chloride; SDS A6625. 1–8 Preprint at (2021).

Sigma-Aldrich. Tetraethylammonium Chloride ; SDS T2265. 1–9 Preprint at (2021).

Sigma-Aldrich. Tetrapropylammonium Brominde; SDS 225568. 1–8 Preprint at (2020).

Sinclair, N. S., Poe, D., Savinell, R. F., Maginn, E. J. & Wainright, J. S. A Nitroxide Containing Organic Molecule in a Deep Eutectic Solvent for Flow Battery Applications. *J Electrochem Soc* **168**, 020527 (2021).

Sinclair, N. S., Shen, X., Guarr, E., Savinell, R. F. & Wainright, J. S. Electrochemical Decomposition of Primary Alcohol Groups in Deep Eutectic Solvents. *J Electrochem Soc* **168**, 106506 (2021).

Slautin, B. N. *et al.* Bayesian Co-navigation: Dynamic Designing of the Materials Digital Twins via Active Learning.

Smith, D. K. Exploring the Role of H-Bonding in Organic Electrochemistry – From Supramolecular Applications to Mechanistic Investigations. *Chemical Record* vol. 21 2488–2501 Preprint at https://doi.org/10.1002/tcr.202100186 (2021).

Smith, E. L., Abbott, A. P. & Ryder, K. S. Deep Eutectic Solvents (DESs) and Their Applications. *Chem Rev* **114**, 11060–11082 (2014).

Stach, E. *et al.* Autonomous experimentation systems for materials development: A community perspective. *Matter* **4**, 2702–2726 (2021).

Su, C.-H., Wu, P.-L. & Yeh, C.-S. Sonochemical Synthesis of Well-Dispersed Gold Nanoparticles at the Ice Temperature. *J. Phys. Chem. B* **107**, 14240–14243 (2003).

Sun, S. *et al.* A data fusion approach to optimize compositional stability of halide perovskites. *Matter* **4**, 1305–1322 (2021).

Sun, S. *et al.* Accelerated Development of Perovskite-Inspired Materials via High-Throughput Synthesis and Machine-Learning Diagnosis. *Joule* **3**, 1437–1451 (2019).

Suslick, K. S. Sonochemistry. *Science (1979)* **247**, 1439–1446 (1990).

Suslick, K. S. The Chemical Effects of Ultrasound. *SCIENTIFIC AMERlCAN* 80–86 (1989).

Tang, L. *et al.* Capital cost evaluation of conventional and emerging redox flow batteries for grid storage applications. *Electrochim Acta* **437**, (2023).

Tang, Y. *et al.* Organic Electroactive Molecule-Based Electrolytes for Redox Flow Batteries: Status and Challenges of Molecular Design. *Frontiers in Chemistry | www.frontiersin.org* **1**, 451 (2020).

Tools - Jubilee. https://jubilee3d.com/index.php?title=Tools.

Turcanu, A. & Bechtold, T. PH Dependent redox behaviour of Alizarin Red S (1,2-dihydroxy-9,10- anthraquinone-3-sulfonate) - Cyclic voltammetry in presence of dispersed vat dye. *Dyes and Pigments* **91**, 324–331 (2011).

Vaddi, K., Chiang, H. T. & Pozzo, L. D. Autonomous retrosynthesis of gold nanoparticles via spectral shape matching. *Digital Discovery* **1**, 502–510 (2022).

Vasquez, J. & Peek, N. machineagency/sonication_station. *GitHub* https://github.com/machineagency/sonication_station (2020).

Vasquez, J. machineagency/jubilee. *GitHub* https://github.com/machineagency/jubilee (2021).

Vasquez, J., Twigg-Smith, H., Tran O'leary, J. & Peek, N. Jubilee: An Extensible Machine for Multi-tool Fabrication. (2020) doi:10.1145/3313831.3376425.

Vescovi, R. *et al.* Towards a modular architecture for science factories. *Digital Discovery* **2**, 1980–1998 (2023).

Vikram, A., Brudnak, K., Zahid, A., Shim, M. & Kenis, P. J. A. Accelerated screening of colloidal nanocrystals using artificial neural network-assisted autonomous flow reactor technology. *Nanoscale* **13**, 17028–17039 (2021).

Wagner, J. *et al.* The evolution of Materials Acceleration Platforms: toward the laboratory of the future with AMANDA. *J. Mater Sci* **56**, 16422–16446 (2021).

Wang, G., Li, G., Liang, C. & Zhang, L. Sonochemical Synthesis and Phase Control of Nanocrystalline CdS. *Chem Lett* **30**, 344–345 (2001).

Wang, H., Lu, Y. N., Zhu, J. J. & Chen, H. Y. Sonochemical fabrication and characterization of stibnite nanorods. *Inorg Chem* **42**, 6404–6411 (2003).

Wang, W. *et al.* Recent Progress in Redox Flow Battery Research and Development. *Adv Funct Mater* **23**, 970–986 (2013).

Weber, A. Z. *et al.* Redox flow batteries: A review. *J Appl Electrochem* **41**, 1137–1164 (2011).

Wei, X. *et al.* Materials and Systems for Organic Redox Flow Batteries: Status and Challenges. (2017) doi:10.1021/acsenergylett.7b00650.

What is lab 4.0? - Automata. https://automata.tech/blog/what-is-lab-4-0/.

What is Laboratory 4.0? Labmate Online. https://www.labmate-online.com/news/laboratory-products/3/breaking-news/what-is-laboratory-40/57352.

Whitacre, J. F. *et al.* An Autonomous Electrochemical Test Stand for Machine Learning Informed Electrolyte Optimization. *J Electrochem Soc* **166**, A4181 (2019).

Williams, K. *et al.* Cheaper faster drug development validated by the repositioning of drugs against neglected tropical diseases. *J. R. Soc. Interface* **12**, (2015).

Winsberg, J. *et al.* TEMPO/Phenazine Combi-Molecule: A Redox-Active Material for Symmetric Aqueous Redox-Flow Batteries. *ACS Energy Lett* **1**, 976–980 (2016).

Winsberg, J., Hagemann, T., Janoschka, T., Hager, M. D. & Schubert, U. S. Redox-Flow Batteries: From Metals to Organic Redox-Active Materials. *Angewandte Chemie - International Edition* **56**, 686–711 (2017).

Xie, Y. *et al.* Accelerate Synthesis of Metal−Organic Frameworks by a Robotic Platform and Bayesian Optimization. *ACS Appl. Mater. Interfaces* **13**, 53485–53491 (2021).

Xie, Y., Sattari, K., Zhang, C. & Lin, J. Toward autonomous laboratories: Convergence of artificial intelligence and experimental automation. *Prog Mater Sci* (2022) doi:10.1016/j.pmatsci.2022.101043.

Xing, X. *et al.* A nonaqueous all organic semisolid flow battery. *Chemical Communications* **55**, 14214–14217 (2019).

Xu, H. & Suslick, K. S. Sonochemical synthesis of highly fluorescent Ag nanoclusters. *ACS Nano* **4**, 3209–3214 (2010).

Xue, D. *et al.* Accelerated search for materials with targeted properties by adaptive design. *Nat. Commun.* **7**, (2016).

Yang, Z. *et al.* Electrochemical energy storage for green grid. *Chem Rev* **111**, 3577–3613 (2011).

Yin, L., Wang, Y., Pang, G., Koltypin, Y. & Gedanken, A. Sonochemical synthesis of cerium oxide nanoparticles-effect of additives and quantum size effect. *J Colloid Interface Sci* **246**, 78–84 (2002).

Yoshikawa, N., Darvish, K., Vakili, M. G., Garg, A. & Aspuru-Guzik, A. Digital pipette: open hardware for liquid transfer in self-driving laboratories. *Digital Discovery* **2**, 1745–1751 (2023).

Yu, C.-L., Yu, J. C., He, H.-B. & Zhou, W.-Q. Progress in Sonochemical Fabrication of Nanostructured Phptocatalysts. *Rare Metals* **35**, 211–222 (2016).

Yu, W. W., Qu, L., Guo, W. & Peng, X. Experimental determination of the extinction coefficient of CdTe, CdSe, and CdS nanocrystals. *Chemistry of Materials* **15**, 2854–2860 (2003).

Yu, W. W., Qu, L., Guo, W. & Peng, X. Experimental Determination of the Extinction Coefficient of CdTe, CdSe, and CdS Nanocrystals. (2003) doi:10.1021/cm034081k.

Yuan, Z., Liu, H., Yong, W. F., She, Q. & Esteban, J. Green Chemistry CRITICAL REVIEW Status and advances of deep eutectic solvents for metal separation and recovery. (2022) doi:10.1039/d1gc03851f.

Zhang, C. *et al.* Phenothiazine-Based Organic Catholyte for High-Capacity and Long-Life Aqueous Redox Flow Batteries. *Advanced Materials* **31**, 1–8 (2019).

Zhang, C., Wijnen, B. & Pearce, J. M. Open-Source 3-D Platform for Low-Cost Scientific Instrument Ecosystem. *SLAS Technol* **21**, 517–525 (2016).

Zhang, C., Zhang, L., Ding, Y., Guo, X. & Yu, G. Eutectic Electrolytes for High-Energy-Density Redox Flow Batteries. *ACS Energy Lett* (2018) doi:10.1021/acsenergylett.8b01899.

Zhang, Y. *et al.* Liquid Structure and Transport Properties of the Deep Eutectic Solvent Ethaline. *J. Phys. Chem. B* **124**, 2021 (2020).

Zhang, Y. *et al.* Study on CO2 absorption by novel choline chloride-diethylenetriamine-water deep eutectic solvents in a rotor-stator reactor. *Chemical Engineering and Processing - Process Intensification* **184**, 109299 (2023).

Zhao, H. *et al.* A robotic platform for the synthesis of colloidal nanocrystals. *Nature Synthesis* **2**, 21 (2023).

Zhou, W. *et al.* Fundamental properties of TEMPO-based catholytes for aqueous redox flow batteries: effects of substituent groups and electrolytes on electrochemical properties, solubilities and battery performance †. (2020) doi:10.1039/d0ra03424j.

Zhu, D. *et al.* Interpreting the Ultraviolet Absorption in the Spectrum of 415 nm-Bandgap CdSe Magic-Size Clusters. *J Phys Chem Lett* **9**, 2818–2824 (2018).

Maria Politi

+ 1 (360)- 813 4846 pltmra@gmail.com

in linkedin.com/in/maria-politi-97a631170/ github.com/MariaPolit

INTEREST STATEMENT

Automation and data orchestration are revolutionizing the way people do science and more. In my current role, I design and implement open-software and -hardware tools for self-driving laboratories to rapidly design and test new materials. I thrive in cross-disciplinary teams, come up with novel research directions, and communicate science to varied-skilled audiences. I am motivated by the impact of open-science in making science more accessible and democratized.

EDUCATION

University of Washington: PhD, Chemical Engineering (Data Science) - June 2024

Oregon State University: BS, Chemical Engineering - June 2019

RESEARCH EXPERIENCE

Graduate Research Assistant, **University of Washington** 9/2019-Present

Thesis Title: *"Open-Science Materials Acceleration Platforms for Clean Energy Material Design Spaces"*

<u>High-throughput and Data-driven Strategies for the Design of Deep Eutectic Solvent Electrolytes</u>

- Development and implementation of high-throughput sample formulation & physico-chemical properties characterization for over 1000 samples in less than one year and < $ 15k
- Development of multiple open-source software packages for automation in materials cheminformatics, data collection, analysis, and data feature recognition

<u>High-throughput Sonochemical Synthesis of Nanoscale Semiconductors</u>

- Protocol and workflow development for high-throughput nanocrystals formulation and optimization, sample characterization and data analysis for over 2000 samples in less than 2 months
- Development of Python-based open-source software for experimental orchestration
- 3D Design and development of custom labware and hardware

<u>Close-Loop, Low-cost, and Open-hardware Science Automation</u>

- Development of Python API for modular tools and science automation platforms
- Design and development of novel open-hardware for formulation and characterization of materials
- Organizer of workshops and creator of resources and documentation for science automation

Teaching Assistant, University of Washington & Oregon State University 9/2018- Present

- Development of interactive activities in remote learning to stimulate and aid student learning
- Independent development of lecture material and related activity contents for introductory coding/data-science courses
- Assist with class and laboratory management of junior level courses in Chemical Engineering
- Independent development of activities and topics for recitation session
- Independent development of assignments and successive grading and feedback.
- Independent leading of help session and office hours

HONORS AND AWARDS

UW Clean Energy Institute – Clean Energy Scientific Achievement Award	2024
UW WE Rise - Certificate of Achievement	2024
UW Chemical Engineering – Outstanding Service Award	2023

Barbara Krieger-Brockett Travel Award	2022
Acceleration Consortium - Accelerate - Digital Discovery Poster Award	2022
UW Clean Energy Institute Travel Grant	2022
AIChE NSEF 2021- Nanoscale Science & Engineering Forum 2nd Place - Poster award	2021
UW Graduate School Conference Presentation Awards	2021
Erik Muehlenkamp Memorial Leadership Award (CBEE, Oregon State University)	2019

GRANTS AND FELLOWSHIPS

UW CEI Graduate Fellowship	2022-23
UW Chemical Engineering IDEA Funds, "Peer Mentorship for a More Accessible Graduate Experience"	2022
UW Diversity and Inclusion SEED Grant, "Peer Mentorship for a More Accessible Graduate Experience"	2022

CONFERENCE TALKS AND POSTERS

*"A Low-cost, Closed-loop Nanomaterials Synthesis Automation Platform", C*uriosities of Chemistry Lecture Series, MilliporeSigma	2024
"A Low-cost, Closed-loop Nanomaterials Synthesis Automation Platform", 2024 MRS Spring Meeting	2024
"Chemistry in a Digital Age", Merck & Acceleration Consortium Webinar	2023
"Jubilee, a community-driven Multitool Motion Platform", Acceleration Consortium - Accelerate 2023 Conference (Workshop)	2023
"New Tools to Enable the Scientific Maker Movement", Acceleration Consortium - Accelerate 2023 Conference (Poster)	2023
"Creating Figures for Papers and Poster Presentations", UW MEM-C 2023 Annual All-Hands (Workshop)	2023
"High-Throughput Screening of Binary and Ternary Organic Redox Active Materials-Based Deep Eutectic Solvents", 2022 AIChE Annual Meeting	2022
"Development of a High-Throughput Workflow for the Synthesis of CdSe Nanocrystals Using a Sonochemical Materials Acceleration Platform", 2022 AIChE Annual Meeting	2022
"Sonochemical Method for High-Throughput Synthesis of Inorganic Nanostructures", 2022 AIChE Annual Meeting	2022
"*Open-Hardware Materials Acceleration Platforms for Accessible and Democratized Materials Discovery",* Acceleration Consortium - Accelerate 2022 Conference (Poster)	2022

"*Development of a High-Throughput Workflow for the Synthesis of CdSe Nanocrystals Using a Sonochemical Materials Acceleration Platform*", 2022 MRS Spring Meeting (Poster)	2022
"High-Throughput Electrochemical Screening of Deep Eutectic Solvents for Use in Redox Flow Batteries", 2021 AIChE Annual Meeting	2021
"Development of a High-Throughput Workflow for the Synthesis of CdSe Nanocrystals Using a Sonochemical Materials Acceleration Platform", 2021 AIChE Annual Meeting (Poster)	2021
"*High-Throughput and Data-Driven Strategies for the Design of Deep Eutectic Solvent Electrolytes*", 2021 Virtual MRS Spring Meeting (Poster)	2021

LEADERSHIP, BROADER EDUCATION AND COMMUNITY OUTREACH

Pathways to Open-Source Hardware for Laboratory Automation Workshop, Workshop Organizer & Moderator	2024
Acceleration Consortium - Accelerate, Training workshop on Low-cost self-driving labs for education and research, Session Organizer & Moderator	2023
UW STEM Pals, Coding Workshop Organizer & Facilitator	2023
UW Chemical Engineering Department- Faculty Search Committee, Graduate Student Representative	2023
Foundation for International Understanding Through Students (FIUTS), Facilitator	2022-2023
Graduate Consulting Club @ University of Washington, Head of Communications	2022-2023
UW Chemical Engineering- Graduate Mentoring Program. Project Lead	2022-
UW C-Hack, Event Facilitator	2021-2022
UW Chemical Engineering- Distinguished Young Scholars Seminar, Review Panel	2021-2022
Undergraduate Student Mentor	2021-
Albers Marcovina Vista Gardens Foundation, Secretary	2020-2023
UW Chemical Engineering: Diversity, Equity and Inclusion Committee, Graduate Student Representative	2020-2022
UW Association of Chemical Engineering Students (ACES), Graduate Student Symposium Chair	2020 - 2021

PUBLICATIONS

* Indicates Co-First Authorship

Lo, S., Baird, S., Schrier, J., Blaiszik, B., Carson, N., Foster, I., Aguilar-Granda, A., Kalini, S., Maruyama, B., **Politi, M.,** Tran, H., Sparks, T., Aspuru-Guzik, A. Review of Low-cost Self-driving Laboratories: The "Frugal Twin" Concept. *Digital Discovery*, 2024. DOI: DOI: https://doi.org/10.1039/D3DD00223C

Politi, M., Baum, F., Vaddi, K., Antonio, E., Vasquez, J., Bishop, B., Peek, N. Holmberg, V. & Pozzo, L. D. High-throughput Workflow for the Synthesis of CdSe Nanocrystals Using a

Sonochemical Materials Acceleration Platform. *Digital Discovery*, 2023, Advance Article. DOI: https://doi.org/10.1039/D3DD00033H

Rodriguez, J *., **Politi, M.***, Adler, S., Beck, D., & Pozzo, L. D. High-Throughput and Data Driven Strategies for the Design of Deep-Eutectic Solvent Electrolytes - *Mol. Syst. Des. Eng*., 2022,7, 933-949. DOI: https://doi.org/10.1039/D2ME00050D

Rodriguez, J *., **Politi, M.***, Scheiwiller, S., Bonageri, S., Adler, S., Beck, D., & Pozzo, L. D. (2021). PhasIR: An Instrumentation and Analysis Software for High-throughput Phase Transition Temperature Measurements. *Journal of Open Hardware*, 5(1), 6. DOI: http://doi.org/10.5334/joh.39

Politi, M.*, Moeez, A.*, Adler, S., Beck, D., & Pozzo, L. D. (2022). HARDy: Handling Arbitrary Recognition of Data in Python. *Journal of Open-Source Software*, 7(71), 3829, https://doi.org/10.21105/joss.03829

SKILLS

Programming	Python | C | shell (bash) | MATLAB | SQL | G-Code | LaTeX | OOP
Software	Fusion360 | Tableau | Python Data Science Stack (Keras, Scikit-learn, Pandas, etc.) | Microsoft Office Suite | ChemDraw | Aspen Plus | COMSOL | Multiphysics |
Laboratory Techniques	Electrochemistry | Electrochemical Impedance Spectroscopy | Spectroscopy | Thermal analysis | Rheology | 3D printing | Resin printing | Sonochemistry | Electronics | Automation Platforms | Soldering | Analytical Chemistry | Inorganic Chemistry |

REFERENCES

Dr. Lilo D. Pozzo: University of Washington, Department of Chemical Engineering
✉: dpozzo@uw.edu

Dr. Jim Pfaendtner: North Carolina State University, Dean of Engineering
✉: pfaendtner@ncsu.edu

Dr. David Beck: University of Washington, Department of Chemical Engineering & eScience Institute
✉: dacb@uw.edu